THE CALIBRATION OF RECOIL PROTON PROPORTIONAL

SPECTROMETERS AND THE MEASUREMENT OF NEUTRON

SLOWING DOWN SPECTRA IN A LITHIUM FLUORIDE ASSEMBLY

by

Ian Brearley

A Thesis submitted in fulfilment

of the requirements for the Degree of

Doctor of Philosophy

Department of Physics

University of Birmingham

UNIVERSITYOF
BIRMINGHAM

University of Birmingham Research Archive

e-theses repository

SYNOPSIS

Growing concern about the world's future energy resources has led to an interest in neutronic behaviour in proposed fusion reactor materials. In this case the neutron slowing down spectra in lithium fluoride are examined at various distances from the neutron source. From the several methods available for measuring neutron spectra the recoil proton proportional counter was chosen.

The calibration of these counters is then discussed; in particular, the common assumption that the average energy loss per ionisation (W) is constant over the counter's energy range is shown to be invalid. In the calibration measurements it was found that the behaviour of W with energy was markedly different for the two hydrogen fillings. This difference was attributed to the influence of electronegative impurities in the gas in the counter. Further, a model assuming that the specific energy loss per ionisation (ω) was constant was found to be valid over the counter's energy ranges.

The response function shape, although sensitive to scattered neutrons, was found to be determined by the counter's dimensions, gas filling and known electric field distortion.

Finally, the calibrated counters were used to measure neutron slowing down spectra in a spherical lithium fluoride assembly over an energy range of 60 KeV to 2.5 MeV. The spectra were compared with calculated spectra and good agreement in shape was found although discrepancies existed in their absolute values. These discrepancies were attributed to a secondary neutron source and its contribution was assessed using a continuous flow water bath to measure the total neutron yield.

ACKNOWLEDGEMENTS

CONTENTS

CHAPTER I: INTRODUCTION

1.1   The World's Energy Problem

The population of the world is growing at a rate between

2% and 3% per annum;   assuming this growth continues, the world

population of over 3,000 million in 1970 will increase to 6,000

million by the end of this century (Meadow et al, 1972).   Thus,

even if there is no increase in per capita energy consumption –

an unacceptable premise for the developing nations – the world's

energy requirements will rise from over 8×10^9 tce/yr (tons of

coal equivalent per year) in 1970 to 16×10^9 tce/yr at the end

of the century (Bainbridge, 1975).   This energy usage will

almost certainly lead to a shortage of certain fossil fuels in

the early part of the next century;   for example, world proven

oil reserves at 1.6×10^{11} tce will last for little more than

30 years at the present rate of extraction of approximately

5×10^9 tce/yr (Bainbridge, 1975).   In the years ahead

discoveries of oil fields comparable in magnitude to those of

the North Sea and Alaska will be required almost annually to

prevent this occurring.

Thus to alleviate this shortage of fuel and to allow for

growth in energy use alternative non-fossil fuels must be

increasingly exploited.   Alternative non-fossil fuels include

nuclear energy (both fission and fusion) and renewable fuel

resources such as solar radiation, geothermal, tidal, wind and

wave energy.   These alternative fuels only supply at present

approximately 3% of the industrial nations' total fuel usage.

Further, only nuclear fission has been exploited to any great

extent;   for example, it is currently supplying 10% of the

British electricity demand. However, without a breeder reactor programme the usable energy content of the present world uranium supplies (at a price of below $66 per Kg in 1975) is only in the same order of magnitude as that of oil reserves (Bainbridge, 1975 and Dale, 1975). With a breeder programme, the energy attainable from these supplies may be increased by a factor of approximately 50, by converting fertile ^{238}U into fissile ^{239}Pu in the breeder reactor. However, there are some important environmental and safety questions to be publicly resolved before the use of breeder reactors will be allowed to become widespread. These problems are more likely to be political than technological and economic.

Many problems associated with nuclear fission would be appreciably reduced or removed if power was generated instead by controlled thermonuclear fusion. With fusion, there is no equivalent of criticality accidents and the bulk of its radio-active waste products are short lived. The scientific feasibility of a self-sustaining controlled fusion reaction has not yet been proven and there are many technological problems to surmount before it becomes a reality. It is, however, very attractive because world supplies of deuterium are virtually unlimited and lithium supplies for tritium breeding are estimated to be capable of supplying our energy needs at our present rate of use for many centuries.

1.2   The Concept of Fusion

From the shape of the well known binding energy versus atomic mass curve (see Burcham, 1963) it is clear that a vast amount of nuclear energy is potentially available from ordinary

matter.   As the maximum of this curve occurs at iron-56, this energy may be obtained by breaking up heavy isotopes (i.e. with mass number > 56) or by "fusing" lighter isotopes (with mass number < 56).   The first process where heavy nuclei are broken up is called fission and the second process is called fusion.

Nuclear fission has already been proved not only to be possible but also commercially viable, the latter being an important criterion for any power generating system.   So far, only uncontrolled nuclear fusion, in the form of the "H-bomb", has been demonstrated.

To exploit fusion energy is difficult as the particles involved in the process repel one another since both are positively charged nuclei.   Thus the coulomb barrier must be surmounted or penetrated;   hence only the lighter nuclei (normally isotopes of hydrogen) have been considered as fuel for fusion reactors as their coulomb barriers are small.   It is necessary that these nuclei be made to collide with sufficient energy that there is a significant probability that the coulomb barrier is overcome.   Although using electric fields charged particles may be readily accelerated to adequate energies it does not seem possible to exploit this idea because of the very poor energy return;   i.e. the net energy obtained from the process is less than that required to accelerate and transport the particles. To overcome this difficulty the nuclei involved may be strongly heated and the plasma so created confined long enough to enable the fusion process to take place with an adequate energy return. In this process the nuclei must be heated to a temperature in the range 10^7 to 10^9 Kelvin (corresponding to energies between 1 and 100 keV).   The process is referred to as thermo-

nuclear fusion because of the high temperatures involved.

Thermonuclear fusion may be classified according to both the reactions used (i.e. the fuel cycle) and the confinement method employed to hold the plasma together. Confinement methods may be broadly classified as gravitational, inertial or magnetic. Examples of gravitational confinement are the stars, where the energy is obtained principally by the proton-proton cycle in cold stars and by the carbon cycle in hot stars. Intermediate stars, such as our own sun, obtain their energy from both cycles. Obviously on earth gravitational confinement is not practical and so the associated fuel cycles will not be discussed further.

The fusion reactions of primary interest, due to their comparatively small couloumb barriers, are given below, together with their Q values. The two deuterium-deuterium branches occur with approximately equal probability over the temperature range of interest.

$$D + T \rightarrow {}^4He + n, \quad Q = + 17.6 \text{ MeV}$$

$$D + D \rightarrow {}^3He + n, \quad Q = + 3.27 \text{ MeV}$$

$$D + D \rightarrow T + H, \quad Q = + 3.03 \text{ MeV}$$

$$D + {}^3He \rightarrow {}^4He + H, \quad Q = + 18.3 \text{ MeV}$$
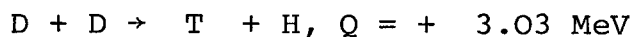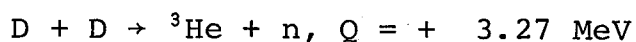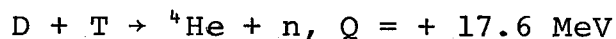
With these reactions there are several possible fuel cycles but, due to the nuclear cross-sections involved, it is generally considered that the first reaction above is the most likely candidate for the first generation of fusion reactors. In this reaction 80% of the energy released escapes from the plasma region in the form of a 14.1 MeV neutron. This neutron must be slowed down and absorbed in a blanket surrounding the plasma in order that its kinetic energy may be utilised. Tritium is radio-active with a half-life of 12.3 years and since it is

not naturally present in sufficient quantities, it must be bred
in the blanket.   The following neutron induced reactions are
used for this:

$${}^{6}\text{Li} + n \rightarrow T + {}^{4}\text{He}, \qquad Q = + 4.8 \text{ MeV}$$

$${}^{7}\text{Li} + n \rightarrow T + {}^{4}\text{He} + n, \qquad Q = - 2.5 \text{ MeV}$$
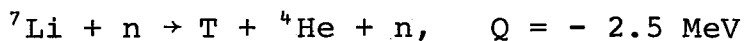
where the natural abundance of ${}^{6}\text{Li}$ is 7.4% and of ${}^{7}\text{Li}$ is 92.6%.
Thus to regenerate tritium, lithium must be present in the
blanket.   Therefore, lithium and deuterium are the primary fuels
in this D - T - Li fuel cycle.

In order that useful amounts of energy may be obtained
from nuclear fusion using the D - T reaction Lawson, 1957, derived
the following breakeven containment criterion for a magnetically
confined plasma which relates the density of the plasma (whose
temperature must exceed 5 keV) to the containment time in order
that the net energy output exceeds zero.   It may be expressed as

$$n \, \tau_{c} \gtrsim 10^{14} \text{ cm}^{-3} \text{ s} \qquad (1.1)$$

where n is the plasma number density and τ_{c} is the plasma
containment time.   A similar criterion also exists for inertia
confined fusion systems such as laser implosion.   For over two
decades the major proportion of controlled nuclear fusion research
has been directed towards the achievement of the plasma conditions
of density, temperature and containment times necessary to produce
significant amounts of power.   In the first part of this time
period the early optimistic forecasts were unfulfilled because
of the discovery of classical plasma instabilities.   However,
in the late sixties verification that significant progress in
several experimental facilities had been achieved led to
renewed enthusiasm.   Even so, a fusion reactor in which the net
energy output exceeds zero is still many tens of years in the

future.

Thus central to any proposed fusion reactor is the confinement problem, where the plasma must be contained so that the Lawson criterion is satisfied. The two types of confinement envisaged are magnetic, where the kinetic pressure of the plasma is balanced by a magnetic pressure for long enough for the reaction to occur, and inertial confinement, where a pellet of deuterium and tritium is uniformly and strongly heated in a nanosecond or so and the resulting implosion heats and condenses the matter at the centre of the pellet to a density several orders of magnitude greater than ordinary solid matter. The pellet in this latter method may be strongly heated by several methods including lasers, heavy ions and electron beams. Magnetic confinement, is expected to operate with plasma number densities, n, in the range 10^{13} to 10^{16} cm^{-3} with containment times, τ_c, in the range 100 to 0.1 seconds respectively, whilst inertial confinement would operate with n $\gtrsim 10^{26}$ cm^{-3} and $\tau_c \gtrsim 10^{-9}$ seconds.

Various magnetic confinement systems have been devised and three types: the mirror, theta-pinch and Tokamak are described in detail by Steiner, 1975. To date, Tokamak devices which are toroidal have been the most successful and have obtained the highest temperature, plasma density and containment times. A schematic diagram of the principles of the Tokamak confinement system is shown in figure 1.1 and a conceptual Tokamak reactor in figure 1.2a. The Tokamak concept employs a toroidal (closed) magnetic confinement scheme. The axial current is induced in the plasma by a changing magnetizing flux

(Φ_m) to provide a pulsed poloidal magnetic field (B_p) that works together with a steady-state toroidal field (B_t) to confine the plasma. The current also gives rise to ohmic heating within the plasma ring, which results in initial plasma heating. Further a Tokamak reactor requires a pulsed transverse field ($B_\perp$) to control the position of the plasma column and it is probable that the toroidal magnet coil system must be super-conducting to limit ohmic heating losses to acceptable levels. It is generally assumed (Steiner, 1975 and Ribe, 1975) that ohmic heating of the plasmas is not sufficient alone to heat the plasma to mean temperatures exceeding 10 KeV as required for power reactors. Thus, once the ohmic heating stage of the plasma heating cycle is completed, energetic neutral deuterium and tritium atoms may be injected in to the plasma to increase its temperature. Other methods of heating include adiabatic compression, radio-frequency heating and turbulent heating through the application of very large electrical fields. The major radius of a Tokamak reactor is expected to be 10 to 13 m and the minor (first wall) radius is expected to be 3 to 5 m.

In figure 1.2b a schematic diagram of a laser fusion reactor is shown. A D - T - Li fuel cycle with a laser confinement system is used. In this reactor there is no first wall as the laser cavity is provided by the formation of a vortex in the swirling liquid lithium. The vortex extends for virtually the full length of the pressure vessel, thereby permitting almost uniform laser irradiation of the solid deuterium-tritium pellet. As the laser implosion of this pellet is typically 100 MJ (Ribe, 1975), which corresponds in energy to approximately 23 kg of high explosive being detonated, some of this force to the pressure

vessel is reduced by introducing inert gas bubbles in the swirling lithium to absorb the shock wave. It should be noted that the momentum of this fusion blast is smaller by 2 to 3 orders of magnitude than that of the high explosive blast because of the smaller mass of the fusion debris. The major problems with this confinement scheme are associated with the lasers: the required combination of size (10 to 100 kJ/pulse), efficiency (at least 10%) and repetition rate (greater than 1 Hz) has yet to be achieved; further, the optic components of the laser beam transport system must be capable of handling laser light densities of approximately 3×10^4 J/m^2 or greater.

As can be seen from both designs, a blanket in which tritium is bred and the neutron energy is absorbed surrounds the plasma or pellet. The blanket will often contain, in addition to the breeding material, structural material, a coolant, a neutron moderator and further, beryllium is sometimes included to provide neutron multiplication by (n,2n) reactions. In some designs the breeding material, for example liquid lithium, also acts as the coolant. A list of possible materials for fusion reactor blankets is given in table 1.1. It should be noted that some conceptual reactor designs (especially those employing laser induced fusion) include fissile material in the blanket to increase the power output of the reactor system. However, this also increases the complexity, safety requirements and cost of the reactor, and results in the production of long-lived radioactive by-products.

There are many technological factors apart from containment problems associated with fusion reactors, which have to be considered in a complete system. First, the breeding

ratio (the number of tritium atoms produced per fusion reaction)
of the blanket must be in the order of 1.1.   Neutronic
calculations show that in most blanket designs this ratio can be
achieved without difficulty.   However, problems do arise with
the tritium, for example the recovery of tritium from the
blanket and the prevention of tritium diffusion into conventional
plant and the environment (Steiner, 1975).

Another problem is the large amount of energy deposited
in the first containment wall.   This comes from three sources,
viz. neutron induced reaction products including gamma rays,
plasma radiation and plasma particle fluxes.   The neutron wall
loading for most reactor designs lies in the region of
1 to 3 MW/m^2, but the energy deposited in the first wall depends
upon the reactor design.   The effect of this energy deposition
is to cause a large degree of enbrittlement, gas bubble formation
and surface erosion in the first wall which leads, in most
conceptual reactor designs, to the need to replace this wall
several times during the reactor's lifetime of twenty years or
more.   This is obviously not a problem in the laser system
outlined above.

Engineering problems also exist in producing the large
superconducting magnets (an order of magnitude greater in size
than those currently produced) which are required in magnetic
confinement schemes.   A further problem is that the super-
conducting coils will require that a radiation shield in the
range 0.5 to 1 m thick be placed between them and the blanket to
protect the coils from heating and/or radiation damage.   More
generally, design problems with high-field magnet systems may
limit the size of the superconducting magnets.   Further problems

concern the compatibility of the blanket materials (lithium or lithium beryllium fluoride) and the associated structural materials. These are intensified by the presence of impurities, radiation damage, neutron induced products and the high temperatures in the blanket ($\gtrsim 500^{\circ}C$).

Originally, fusion reactors were considered to be a "clean" and safe power source in comparison to fission reactors. This was because the concept of criticality is not applicable and there are no long-lived radioactive waste problems, as associated with fission reactors. However, neutron induced reactions cause some problems associated with nuclear afterheat and biological hazards associated with the radio-nuclei. Steiner, 1975, has estimated that first wall afterheat power density at shutdown in a fusion reactor is 1 or 2 orders of magnitude less than that of the fuel in a fast fission reactor (such as the LMFBR), and the total afterheat is generally in the range 0.2 to 2% of the reactor's thermal power. Thus, although the percentage afterheat in a fusion reactor can approach that of a fission reactor, it is considered to be less of a problem in loss of coolant accidents because of the lower afterheat power densities. (It should be noted that the afterheat power density is normally greatest in the first wall of a fusion reactor and in the fuel of a fission reactor.) The induced activity at equilibrium is estimated in most fusion reactor designs to lie in the region of 10^9 to 10^{10} Ci for a 1,000 MW(e) plant. However, the biological hazard potential[1]

---

(1) The biological hazard potential is defined as the activity divided by the maximum permissable concentration (MPC) for the radionuclide dispersed in air.

associated with the activated material in a fusion reactor will be 1 to 3 orders of magnitude less than that associated with plutonium isotopes in a fast fission reactor. Thus, safety requirements in the event of an accident in a fusion reactor may be less stringent than those of a fission reactor. Also, due to the short half-lives of the induced radio nuclei in the structural materials of a fusion blanket, these materials may be recycled after relatively short cooling periods (less than 10 years for aluminium, silicon carbide or vanadium structural materials but at least 50 years for iron or nickel based structures).

In conclusion, the ultimate goal of fusion research is to produce an economic and socially acceptable power source. As there are many technological difficulties yet to overcome, estimates of the cost per unit of power from fusion reactors based upon projections of present costs and designs will obviously prove unreliable. This was the case with the original estimates of cost for fission reactors. However, most projections of the cost per unit of electricity from fusion (see for example Carruthers, 1967) are approximately equal to that from a fast fission reactor. These estimates and the lure of plentiful energy supplies have encouraged research into fusion technology and the physical data required.

TABLE 1.1:   POSSIBLE BLANKET CONSTITUENTS

Purpose	Material
Breeding	Liquid lithium Molten salts (Li_2 Be F_4, Li F) Ceramic compounds (Li_2 O, Li_2 C_2) Aluminium compounds (Li Al, Li Al O_3)
Structure	Refectory based materials (Nb, V, Mo) Iron based alloys Nickel based alloys Aluminium based materials Carbon m based materials (SiC)
Coolant	Liquid lithium and Potassium Molten salts Helium
Moderator	The breeding materials Graphite
Neutron multiplication	Beryllium

1.3   Relevance of Cross-Section Determination

Central to the estimation of the performance of any proposed nuclear reactor system is the knowledge of the behaviour of neutrons as a function of direction, position, energy and time within that reactor system.   This enables many parameters such as, in the case of a fusion reactor, the tritium breeding rate, heat generation, radiation damage and induced radioactivity to be calculated.

In order to estimate the behaviour of a neutron in a reactor system the nuclear differential cross-sections of the materials in the system must be known, so that the neutron balance equation may be solved (see chapter V);   therefore, in any reactor programme the relevant cross-section data must be provided.

Compilations of such data exist for a number of nuclei in several national nuclear data libraries (for example, the British UKAEA Nuclear Data Library and the American ENDF/B - I to IV Nuclear Data Libraries).   Data for these compilations can be obtained from differential cross-section measurements, but these are complicated by their large angular and energy dependence.   Thus, the lack of direct differential cross-section measurements has led to the use of nuclear models to predict theoretically the differential cross-sections in some cases or to interpolate or extrapolate between measurements in others, in order to provide cross-section estimates for these libraries.   This can lead to errors, particularly in cases where the nuclear model used is inadequate.   For example, the secondary neutron spectra for the ^{6}Li(n,n^1d) and ^{7}Li(n,n^1t) reactions have been represented by an evaporation model in the

ENDF/B library. This leads to the prediction of an emitted neutron spectra which is too hard especially at back angles (see figure 1.3a and figure 1.3b). Stewart and Young, 1976, have shown that a nuclear model utilizing pseudo levels and phase-space arguments gives a much better agreement with the experimental neutron spectra of Hopkins et al, 1968. In this library similar difficulties exist in the representation of the neutron spectra from other three body reactions in light elements such as deuterium, beryllium-9 and carbon-12.

Errors such as these lead to the need to test the compiled nuclear cross-sections experimentally. Two types of reactor experiments (mock-up and bench-mark) may be performed to test this data. The first is where, for example, a "mock-up" of the fusion blanket is constructed with the breeding material and structural material in the same form as in a proposed reactor. Here an accelerator neutron source using the $T(d,n)^4He$ reaction may be employed to simulate the fusion source. In this simulated blanket the neutron spectra and tritium breeding may be measured as a function of position. This type of experiment is only really useful to assess the performance of a particular blanket configuration, as discrepancies between measured and calculated quantities may arise from errors in the calculational method and/or the nuclear data used; for example, the calculational method may be in error due to the geometric complexity of the blanket.

Thus the second type of experiment, the integral bench-mark experiment is often employed instead to test the nuclear data. In this type of experiment the geometric complexity and the number of materials used is considerably reduced. Thus the

uncertainties associated with the approximations made in the
calculational method can be minimised, and the experiment used
to check the accuracy of the nuclear data.   In this class of
experiment one of the most important integral parameters is the
neutron spectrum.   Further, if the total neutron source
strength can be measured then the measured and calculated neutron
spectra may be compared directly without the need for arbitrary
normalisation.

In this work it was decided to employ lithium fluoride
(a possible blanket constituent) in a spherical container using
an accelerator neutron source to simulate the fusion reaction.
Here, as the geometric arrangement is simple and only one type
of material is present, the system fulfills the criteria for a
bench-mark type of experiment.   Further, the neutron source
strength may be measured by detecting the associated alpha
particle from the $T(d,n)^4He$ reaction.   As tritium may be bred
from thermal neutrons via the $^6Li(n,T)^4He$ reaction then the
energy region of interest for neutron spectra measurements
extends from about 15 MeV down to thermal energies.

1.4   Neutron Spectroscopy

Neutron spectroscopy is difficult because neutrons can
only be detected when they interact with matter to produce
charged particles or photons, which may then be detected with
a conventional radiation detector such as a proportional
counter or an ionisation chamber.   A prerequisite of any
interaction which is to be used to detect neutrons is that its
cross-section be well known, so that the detector's efficiency
may be calculated.   This cross-section, in general, should be

smoothly varying as any resonance structure complicates the analysis. However, even if the cross-section, and hence the efficiency, of the detector is known there still remains the problem of measuring the neutron energy. This can be accomplished either by timing or by measuring the energy of the charged particles or photons resulting from the interaction.

Unfortunately, there is no one method, with the exception of the time-of-flight technique, which is capable of measuring neutron spectra over the range of interest from thermal energies to 15 MeV. This method is mainly applicable to transmission experiments (Alfieri et al, 1973), as only angular fluxes may be measured. This is a serious problem as the scalar flux is often required for comparison with the calculated flux. Another problem is that any attempt to perform neutron spectrum measurements in a localised region requires the extraction of a beam of neutrons from that region resulting in a serious perturbation to the measured system. Finally, timing problems limit the energy region of this method to one where the flight time is long compared with the time uncertainties associated with the production of source neutrons, the slowing down of neutrons and the detection of neutrons.

Other methods of fast neutron spectra measurements are outlined below. The lithium-6 semiconductor spectrometer is based upon measuring the energy of one or both of the reaction products from the following reaction

$$^6Li + n \rightarrow {}^4He + T + 4.78 \text{ MeV}.$$
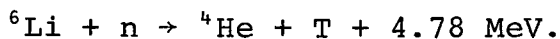
This spectrometer is capable of measuring neutron spectra from a few KeV to about 6 MeV, the upper limit being governed by competing (n,α) reactions in the silicon diode detectors. The

disadvantages are that the cross-section of the ^{6}Li(n,T)^{4}He reaction is not well known around and above the resonance at approximately 250 KeV, and that the semiconductor detector's lifetime is short due to neutron induced radiation damage.

Secondly, there are helium-3 spectrometers, where the following reaction:

$$^3He + n \rightarrow p + T + 764 \text{ keV}$$

is employed in either a proportional counter or as a gas filling between two semiconductor detectors. When helium-3 is used in a proportional counter, its accuracy is limited by the accuracy to which both the wall and electric field distortion may be determined and by the ability to distinguish between the competing reactions and the desired reaction.   (See Shalev et al, 1973).   The competing reactions are ^{3}He(n,pn)D, and ^{3}He(n,D)D, as well as electrons from gamma induced interactions in the walls.   The range of these counters is approximately from 150 KeV to 4 MeV depending upon the gas pressure.

The helium-3 semiconductor spectrometer covers the energy range from about 2 MeV to 10 MeV (the lower limit being governed by competing gamma induced background).   The upper limit is greater than with the lithium-6 semiconductor spectrometer as the ratio of the number of primary reactions to the number of competing (n,α) reactions is considerably better.

There are numerous counters in which the neutron energy is determined from the energy of a recoil proton, the result of an elastic collision between a neutron and proton.   First, there is the nuclear emulsion technique, where the track length of the recoil proton in a photographic film determines its energy.   This is limited to neutron energies above 500 KeV

from considerations of track length (approximately 5 μm) and grain size (approximately 0.2 μm). Its main disadvantage is the long scanning time required to measure each track length.

Secondly, there are organic scintillation spectrometers, where the recoil proton results in light emission from the scintillation material (e.g. anthracene, stilbene and liquid scintillators) and the intensity of the light, measured by a photomultiplier tube, is dependent upon the recoil proton's energy. The resolution of such a spectrometer is poor at 15% or greater and its efficiency is difficult to estimate accurately, but its energy range with gamma discrimination is from about 500 KeV to 16 MeV or more. These detectors have been reviewed recently by Perkins, 1975, and their unfolding techniques and operation by Jowett, 1975.

Finally, there are recoil proton proportional counters, where a proportional counter is filled with a hydrogenous gas and the ion pairs produced by the recoil protons are detected in the conventional method. As with all proton recoil counters this method fulfils some of the criteria for a spectrometer, namely that the hydrogen cross-section is well known and smoothly varying. Providing the active volume of the proportional counter is known accurately, then the efficiency of the detector may be determined to a similar accuracy. The recoil proton's energy can be simply estimated from the pulse height. The upper energy limit of recoil proton proportional counters is governed by the diameter of the counter and the stopping power of the gas filling, whilst the lower limit is governed by competing reactions. These come from both recoils from the heavy atoms in the gas and from gamma interactions in the walls

of the counter, although this may be circumvented by careful
choice of gas fillings as discussed in chapter VI. Thus, using
a series of counters of different gas fillings, the energy range
of this method extends from a few KeV to about 2.5 MeV for in
situ measurements.

Neutron energy spectra may be also measured by resonance
foil sandwich detectors as used by Hatton, 1970 and fission
threshold detectors with solid state recorders, as used by
Khadduri, 1973, but these methods are limited by the lack of
suitable nuclei. Further details of all the spectrometers
described above are given by Jones, 1970, Bore, 1973, and
Roberts, 1973.

It was decided to use recoil proton proportional counters
for neutron spectrum measurements in the bench-mark experiment
described in chapter V. Some of the advantages of this
spectrometer are that its efficiency may be easily calculated,
its resolution is adequate to resolve the resonance structure in
lithium fluoride and the unfolding technique and mode of operation
are comparatively simple. As the principles of proportional
counter operation and pulse formation are well known and may be
found in standard texts, such as Wilkinson, 1950, no attempt will
be made here to describe this aspect of the counter operation.

The development of this spectrometer technique has
followed two branches: one in which cylindrical counters were
used (mainly in the United States) and the other where a
spherical counter design was developed in Britain. Cylindrical
counters filled with either hydrogen or methane to measure neutron
spectra in the energy range 1 KeV to 1 MeV were developed by
Bennett, 1967a. He and his associates refined this technique

to predict and measure the counter's response to monoenergetic neutrons over an extended energy range. As mentioned above, the upper energy limit is determined by the need to confine the recoil protons within the sensitive volume of the counter. Failure to do this leads to an apparent increase in low energy recoil protons, as some of their energy is lost to the counter walls instead of to the gas of the counter. Clearly, this would lead to a distortion in the recoil proton distribution of monoenergetic neutrons (commonly called a response function) and the distortion so caused is called the wall and end effect. Further distortion can be caused by a non-uniform electric field resulting in non-uniform gas multiplication for similar energy events in different regions of the counter. The shape of the response function is discussed in more detail in chapters II and III. Gold and Bennett, 1968, and Bennett and Yule, 1972, have corrected for these distortions by considering the analytically determined path length distributions derived by Snidow and Warren, 1967 and by computing the electric field everywhere in the counter. Their analytical response functions were compared with experimentally measured ones and the agreement was found to be within experimental error. The unfolding technique they used with the above cylindrical counters was to correct the measured distorted recoil proton distribution to give one that corresponded to an undistorted recoil distribution, which was then differentiated to give the neutron flux.

The other branch of recoil proton proportional counters was developed by Benjamin et al, 1964a, who produced a spherical counter in which the electric field distortion was minimised.

This was achieved by balancing the electric field distortion caused by the spherical cathode with that caused by the insulators supporting the anode wire. In these counters, the spherical sensitive volume implies that the counter's response to a beam of monoenergetic neutrons is independent of the orientation of the anode wire to this beam unlike the cylindrical counter whose geometry means that a response function measured with a beam of monoenergetic neutrons is dependent upon the orientation of the anode wire to this beam. This follows from the fact that n-p scattering is forward peaked in the laboratory system although isotropic in the centre of mass system. The response function measurements of Broomfield et al, 1970, and Bore, 1973, have indicated that the electric field distortion, although much smaller than that of the cylindrical counter is still present, especially at low energies, and is greater than expected. Further, Bore's results have indicated that the exact response was dependent upon the filling gas employed. The unfolding code used with these spherical counters (see Benjamin et al, 1968a), calculates the incident neutron flux by unscambling from the differentiated recoil proton distribution a matrix of differentiated response functions derived analytically from the Snidow and Warren expressions, 1967. Later versions of this unfolding code, SPEC4, (see Kemshall, 1973), allow for electric field distortion by modifying the shape of the analytical response functions.

In this work the Benjamin type SP2 spherical counters manufactured by 20th Century Electronics Limited were used. This was partly because the Department of Physics of the University of Birmingham has had experience of these counters

through the work of Jones, 1970 and Bore, 1973, and partly
because spherical counters can measure the scalar neutron flux
in situations where there is a marked degree of anisotropy in
the angular flux - a hard task in cylindrical counters.   A
schematic diagram of a spherical counter is given in figure 1.4.
The need for and methods of calibration of these counters are
discussed in chapter II and the calibration results given in
chapter III.   The neutron source strength calculation for the
bench-mark experiment is discussed in chapter IV and the
experiment and results are described in chapter V.

Chapter II   NEUTRON FLUX MEASUREMENT AND COUNTER CALIBRATION

The purpose of this chapter is to describe the theory and background underlying the experimental work which is to follow. The first sections consider the theory of neutron flux measurements in hydrogen proportional counters and the need for counter calibration. A discussion of possible calibration methods follows and finally the chosen method, calibration by mono-energetic neutrons from accelerator targets, is discussed more fully.

2.1   Neutron Flux Measurement

In neutron spectroscopy work, hydrogen is frequently used as a gas filling for proportional counters, because its cross-section is well known and varies smoothly. We shall now consider the energy distribution of recoil protons in hydrogen, as a result of being bombarded by neutrons.

First consider the case of ϕ monoenergetic neutrons, all incident at energy E_n. If the counter was infinitely large (i.e. with no walls), then it has been shown that the recoil proton distribution is a rectangular distribution in the range 0 to E_n. Clearly the height of the rectangular distribution increases as ϕ, the number of neutrons, increases. This result follows from the conservation laws of momentum and energy, and from the fact that neutron-proton elastic scattering is isotropic in its centre of mass; it is valid for incident neutron energies below 14 MeV or so (Garber et al, 1970).

From this rectangular distribution of recoil proton energies, $M_\phi (E, E_n)$, can be found the probability of a recoil proton having a particular energy:-

$$P (E) = \frac{M_\phi (E, E_n)}{\phi . \sigma (E_n) N} \qquad (2.1)$$

where N is the number of hydrogen atoms in the counter and $\sigma (E_n)$ is the cross-section of the neutron-proton scattering.

Clearly, this probability distribution is also rectangular in the range O to E_n, and so it must be the case that

$$P (E) = \frac{1}{E_n} \quad \text{for } O \leqslant E \leqslant E_n \qquad (2.2)$$

and $P (E) = O$ for $E > E_n$

Thus there is an equal probability of a recoil proton having any energy in the range O to E_n.

Next, consider the case of a continuous range of neutron energies. Let the neutron flux be $\phi (E_n)$ and let the overall energy distribution of recoil protons per unit energy be M(E). Then since each neutron energy E_n results in a rectangular proton energy distribution:

$$M_\phi (E, E_n) = \phi (E_n) \quad \sigma (E_n) . N . P(E) \quad dE_n \qquad (2.3)$$

$$= \frac{\phi (E_n) \quad \sigma (E_n) \quad N \quad dE_n}{E_n} \qquad (2.4)$$

The overall proton energy distribution M(E) is simply obtained by summing together all values of $M_\phi (E, E_n)$ for

$E_n \geqslant E:-$

$$M(E) = \int_{E}^{\infty} \frac{\phi(E_n) \; \sigma(E_n) \; N}{E_n} \; dE_n \qquad (2.5)$$

and hence

$$\phi(E) = -\frac{dM(E)}{dE} \cdot \frac{E}{\sigma(E)N} \qquad (2.6)$$

which establishes the relationship between neutron flux and the recoil proton spectrum. Thus, for an infinite counter with no secondary scattering the neutron flux can be simply obtained by differentiation of M(E), the recoil proton spectrum.

Unfortunately in real counting systems a number of problems hinder direct application of equation (2.6). First, the above rectangular energy distribution of recoil protons, in the mono-energetic case, is distorted due to wall and end effects. That is, some of the recoil proton tracks are truncated by interaction with the walls of the counter, leading to an increase of apparently low energy recoil protons and a corresponding decrease in the number of high energy recoil protons, whilst other proton tracks may terminate in the region of electric field distortion at the ends of the anode. Further distortion in the electric field may be caused by variations in the diameter of the anode wire. Therefore, overall there may be non uniform gas multiplication (see Figure 2.1).

From this new energy distribution of recoil protons can be found the probability of observing a recoil proton at a particular energy, as before. This probability distribution is the response of the counter to a monoenergetic neutron and

is called a "response function". As a result of this distortion,
equation (2.6) is not valid in practice. Monoenergetic neutrons
with energy E_n give rise to a distorted recoil proton distri-
bution $M_o(E,E_n)$ which is zero for $E > E_n$ and non-zero for
$0 \leq E \leq E_n$, as in Figure 2.1. The problem then is to determine
the neutron flux $\phi(E_n)$ which gave rise to an observed recoil
distribution $M(E)$.

Let $N_o(E,E_n) = M_o(E,E_n) / \phi(E_n)$ $\qquad\qquad$ (2.7)

and so the distribution $M(E)$ is simply given by:

$$M(E) = \int_E^{E_{max}} N_o(E,E_n)\, \phi(E_n)\, dE_n \qquad\qquad (2.8)$$

where it is assumed that $\phi(E_n) = 0$ for $E_n > E_{max}$. In practice
because of the experimental and unfolding procedures, we divide
the neutron energy range into z equal lethargy groups, where
the numbering begins at E_n and runs backwards towards the origin;
thus, $E_1 = E_{max}$, $E_z = 0$ and the ith group runs from E_{i+1} to
E_i where $E_{i+1} = k E_i < E_i$, and $0 < k < 1$. Using this notation,
$M(E)$ is not observed as a continuous function but is discrete.
Let the discrete observations be:

$$M^i = \int_{E_{i+1}}^{E_i} M(E)\, dE \qquad\qquad (2.9)$$

Using (2.8)

$$M^i = \int_{E_{i+1}}^{E_i} \int_E^{E_{max}} \phi(E_n)\, N_o(E,E_n)\, dE_n \cdot dE \qquad (2.10)$$

Providing either $\phi(E_n)$ or $N_o(E,E_n)$ is virtually independent
of E_n over each energy group then (2.10) may be re-written in
discrete form as:

$$M^i = \sum_{j=1}^{i} N_O^{ij} \phi^j \qquad \text{where } i = 1, 2, \ldots, z \qquad (2.11)$$

where

$$\phi^j = \int_{E_{j+1}}^{E_j} \phi(E_n) \, dE_n \qquad (2.12)$$

and

$$N_O^{ij} = \frac{1}{E_j - E_{j+1}} \int_{E_{i+1}}^{E_i} \int_{E_{j+1}}^{E_j} N_O(E, E_n) \, dE_n \, dE \qquad (2.13)$$

Thus the set of equations given by (2.11) may be readily solved for the ϕ^j by back substitution. However in practice unknown errors on the observed values of M^i can lead to associated errors growing in the back substitution. This can be reduced (see Benjamin et al 1968a) by differentiating equation (2.8) with respect to E and following a similar analysis; hence it can be found that:

$$D M^i = \sum_{j=1}^{i} D N_O^{ij} \phi^j \qquad (2.14)$$

where D denotes differentiation with respect to E. A further problem in the application of equations (2.11) or (2.14) is the non-linearity of ionisation versus recoil proton energy. Moreover if heavy atoms are added to the gas to increase the stopping power, heavy ion recoils caused by neutrons can also distort the recoil proton distribution. As a result of all these factors the number of electrons collected on the anode wire of a recoil proton proportional counter does not give a direct measure of M(E), the recoil proton spectrum, but rather of M(I), the ionisation spectrum per unit ionisation.

Thus before this analysis can proceed it is necessary to transform the ionisation spectrum, M(I) to the recoil proton spectrum, M(E). The average energy loss per ion pair, W, is:

$$W = {}^E/_I \qquad (2.15)$$

where I is the number of ionisations (or ion pairs) formed by a proton of energy E. The specific energy loss per ion pair, ω, is:

$$\omega = {}^{dE}/_{dI} \qquad (2.16)$$

and so the ionisation spectrum M(I) may be transformed to the recoil proton spectrum by:

$$M(E) = M(I) / \omega \qquad (2.17)$$

There appears to be a certain amount of confusion in the literature about whether W and ω are functions of E or I. On the one hand, in a theoretical context it makes sense to think of a proton energy E giving rise to ionisation I and so one thinks of I as a function of E, i.e.

$$I = f(E) \qquad (2.18)$$

In this case W and ω may also be regarded as functions of E:

$$W(E) = {}^E/_I = {}^E/_{f(E)} \qquad (2.19)$$

$$\omega(E) = {}^{dE}/_{dI} = {}^1/_{f'(E)} \qquad (2.20)$$

so that

$$I = \int_0^E \left({}^1/_{\omega(E')} \right) dE' = f(E) \qquad (2.21)$$

and hence W and ω are related by the integral equation:

$$W(E) = E / \int_0^E \left({}^1/_{\omega(E')} \right) dE' \qquad (2.22)$$

On the other hand, in experimental work it is sometimes preferable to think in terms of the inverse relationship between E and I:

$$E = f^{-1}(I) \qquad (2.23)$$

i.e. the proton energy that must have given rise to a particular observed value of I. In this case, W and ω may be regarded as functions of I.

$$W(I) = E/I = f^{-1}(I) / I \qquad (2.24)$$

$$\omega(I) = \frac{dE}{dI} = df^{-1}(I) / dI \qquad (2.25)$$

so that

$$E = \int_O^I \omega(I') \, dI' = f^{-1}(I) \qquad (2.26)$$

and the relationship between ω and W is:

$$W(I) = \int_O^I \omega(I') \, dI' / I \qquad (2.27)$$

It will be convenient to use both interpretations below, depending on whether the discussion relates to a theoretical or experimental situation. To avoid ambiguity, the argument of the function is specified where necessary.

Returning to the problem of transforming M(I) to M(E) via equation (2.17), it is clearly important to know the behaviour of W(I) and ω(I) before this is executed. The parameter W(I) is particularly important to spectrum unfolding because it gives the correct energy scale by:

$$E = W(I) I \qquad (2.28)$$

A simplifying assumption about the behaviour of W(I) and

ω(I) that is frequently made is that they both remain constant

everywhere:

$$W(I) \ = \ \omega \ (I) \ = \ k \tag{2.29}$$

In this case, the ionisation spectrum M(I) is simply

proportional to the recoil proton spectrum M(E)

i.e. $M(E) \ = \ ^1/_k \ . \ M(I)$ (2.30)

Care must, however, be exercised over this simplifying assumption.

In the following section the expected theoretical behaviour

of W and ω is discussed in more detail, and is contrasted with

experimental evidence.

2.2 The Relationship between an Initial Particle's Energy

and the Resulting Ionisation

In the past few decades under the influence of Bohr (1948)

and later Lindhard et al (1963) there has been a considerable

development in the theoretical understanding of the penetration

of atomic particles through matter. This penetration starts a

complex chain of phenomena, but fortunately there are only a few

comparatively simple processes that play a central role in ioni-

sation.

An ion penetrating matter loses the greater part of its

energy by both inelastic collisions with the electrons of the

medium and, principally, elastic collisions with the nuclei.

In the former, the electrons become either excited and/or

ionised, while in the latter kinetic energy is transferred
to the recoil nucleus. The secondary particles from these
two processes, electrons from inelastic collisions and recoil
nuclei from elastic collisions, may themselves suffer further
collisions both elastic and inelastic, resulting in further
ionisation and/or excitations of electrons, and production of
recoil nuclei.

Because the mass of the electron is small in comparison
to that of the nucleus, it can be seen that very little of the
energy of the secondary electrons will be transferred to the
nuclei, and so secondary electrons play an insignificant role
in nuclear motion. On the other hand, the recoil nuclei will
contribute significantly to further ionisation and excitation of
the electrons. Therefore, for an incident ion of energy E,
it can be seen that part of its initial energy will add to atomic
motion, while part is gained by the electrons. These two effects
account for the majority of initial energy, E. The remaining
energy is lost in processes such as near thermal excitation and
the escape of light quanta.

Lindhard et al (1963) showed that the proportions of
initial energy going to the atoms and to the electrons were
dependent on the nuclear and electronic stopping power. These
stopping powers are approximately equal at 0.25 keV for protons
in hydrogen, but at lower energies, the nuclear stopping power
is larger than the electronic stopping power which gradually
falls. On the other hand, for energies greater than 0.25 keV,
the electronic stopping power is greater than the nuclear stop-
ping power and reaches a maximum in the region of 13 keV.

At energies greater than 1·0 keV the fraction of the initial
ion energy going to the nuclear motion falls from tens of per-
cent to a few tenths of a percent.

Clearly the average energy loss per ion pair, $\dot{W}$ is depend-
ent upon the relative amounts of the initial ion energy going
to the electrons. For high initial ion energies, nuclear
stopping is insignificant in comparison to electronic stopping
and so W, the average energy loss per ion pair, is expected
to be virtually independent of the initial ion's energy.
If the relative amount of energy going to ionisation is a
constant then W will be a constant.

At lower initial ion energies, the nuclear stopping
plays a more significant role; more energy is dissipated in
producing recoil nuclei and there is less to cause ionisation.
There exist several models to explain the behaviour of W at
low ion energies, and all are based upon the theory expounded
by Lindhard et al (1963) (See Dennis 1973, 1971 and Boring
et al 1965). Generally they all predict that W rises as the
initial ion energy, E, falls (i.e. $^{dW}/dE < o$) and that W is
dependent upon the type of initial ion. Clearly the correspond-
ing behaviour of ω may be inferred via the integral relation-
ship (2.22) or (2.27). These predictions apply to most media,
including the case of protons in hydrogen. They have had
reasonable success in the case of semi-conductor detectors
(Haines et al 1966) but poor success in the case of gases,
probably due to other processes, such as charge exchange.
Experimental evidence relating to the behaviour of W and ω in
hydrogen at low E is summarised later.

At high ion energies, the assumption is often made that ω
is a constant. However, Fano, 1946, found by considering
ionisation and excitation cross-sections for hydrogen, that W(E)
could be shown to be weakly dependent on the initial ion's
energy and mass. Some of the assumptions he made were that
particles of different mass, velocity and charge were equally
efficient in producing ionisations and that collisions in the
medium could be classified as either grazing or head on.
The model predicts that W(E) increases as energy increases,
because the relative frequencies of grazing and head-on collis-
ions are energy dependent. Care should be exercised not to
extend these results to low energies since the assumptions
employed gradually become less valid as energy decreases -
especially for energies below 100 keV. In particular, at low
ion energies the energy transferred to nuclear motion, and hence
its effect on W(E), is obviously dependent upon the mass,
energy and charge of the initial ion. Also the effect of charge
exchange and/or pick-up, which is more and more probable as the
proton energy falls below 100 KeV in hydrogen (Stier et al,
1954), is not considered by his model and could have an apprec-
iable effect on the relative amount of energy lost in excitations.
To summarise, Fano's model predicts that, at high energies, W
may be expected to rise slowly as energy increases and to
approach a constant level as $E \rightarrow \infty$. This prediction about
the behaviour of W implies that ω lies above W for all E over
which W is rising. It seems unlikely that ω could be constant
over any significant energy range and still be compatible with
rising W.

Despite this, in high energy experimental work $(E > 30 \text{ keV})$ $\omega = {}^{dE}/_{dI}$ is often postulated to be a constant and a linear relationship estimated between energy and ionisation. If the true ω is really not a constant but a linear relationship between E and I is still assumed, then obviously the relationship obtained will vary according to the energy range over which it is measured. When the experimental evidence is discussed below it is indeed found that the straight line fits do vary. Another possible explanation of this variation is electro-negative impurities which could reduce the observed ionisation significantly.

There is a certain amount of experimental evidence relating to the properties of W and ω in hydrogen. The experimental data fall broadly into two main groups, one in which W has been measured at low ion energies, less than 25 keV, and the other where W has been measured over an extended energy range. The low energy data is discussed first.

Bennett (1967a) obtained some indirect evidence using cylindrical hydrogen filled proportional counters, which indicated that a suitable model to describe the behaviour of ω (I) is:

$$\omega (I) = 1 + Fe^{-GI} \tag{2.31}$$

where for convenience ω (I) is expressed relative to the "effective Q value" of the $^{14}N (n,p) {}^{14}C$ reaction (used for calibration), I is in Kev and F and G are constants.

This model for ω does indeed imply that $^{dW}/_{dE} < 0$, as predicted theoretically. He found that F = 0.6, G = 1 gave a good fit to his data.

In a later paper, Bennett (1967b) chooses a large value for G in expression (2.31) so that ω (I) exhibits an effective "cut-off" behaviour. That is, ω (I) is constant at unity for E $\geq$ 0.2 keV and infinite for E $<$ 0.2 keV.

When ω(I) is equal to unity then using equation (2.26)

$$E = \int_0^I \omega(I') \, dI' = I + I_0 \qquad (2.32)$$

where I_0 is a constant. His experimental measurements indicated that any model with ω constant above 2 keV would fit his data well.

Werle (1969) found that at low ion energies ω decreased but W increased with decreasing ion energy, in hydrogen-filled proportional counters. In this experiment, quasi-monoenergetic neutrons were produced by a slowing down spectrometer, and both spherical and cylindrical counters were used to measure the ionisation caused by recoil protons. He proposed a model to be used at high energies based on his results:

E = I + 0.41   where E and I are in keV   (2.33)

Finally Werle used his model to reduce discrepancies in fast reactor neutron spectrum measurements.

Verbinski et al (1974) also measured ionisation, and maximum recoil proton energies in the range 2 to 200 keV, with both cylindrical and spherical hydrogen filled counters. He found

that W and ω were constant for energies 25 - 200 keV and below this energy, W and ω increased as E decreased. In the range 3 to 25 keV W changed by 25% and ω by 7%. If the model assumes that W and ω are constant at all energies he estimated the following errors in a neutron spectrum measurement at energies below 25 keV:

E range (kev)	Error in a neutron flux
1.5 - 3	15 - 40 %
3 - 9	8 - 15 %
9 - 14	4 - 8 %
14 - 25	2 - 4 %

Powell and Rogers (1970) measured transmitted neutrons from iron and scandium filters and applied a similar linear model, $E = I + I_o$ over the range 2 kev - 120 kev. They found that $W(E)$ was constant above 2 keV with $I_o = 0$ so that $E = I$ above 2 keV. They discovered that if other types of model were used it could lead to errors in the unfolded spectrum below 30 kev.

These low proton energy measurements excluding Werle's show that as the proton energy falls the ω and W values increase, as is expected from theory. But there seems to be a large discrepancy between measurements for example, Bennett (1967a) showed that above 2 keV ω was a constant whilst Verbinski et al (1974) showed that ω rose by 7% as E fell from 9 to 2 keV, and Werle showed that ω fell as E fell.

At high energies ω is often assumed to be a constant so that a linear relationship $E = KI + I_o$ (or $I = K^*E + E_o$) can be found. One should obtain the same estimate of I_o or E_o

for a particular gas filling no matter over which high energy regions measurements are made. However, experimental evidence over different energy ranges give different estimations of I_O indicating ω is not necessarily a constant over the whole range. In hydrogen, in the range 2 kev to 1 MeV Rogers (1970) found E_O approximately equal to zero, while Bore (1973) found E_O equal to - 8.2 $\pm$.3 keV over the range 200 to 500 keV. Carter's (1976) data revealed a further discrepancy in the value of E_O which was found to be -3.2 $\pm$ 1 keV in the energy range 25 to 550 keV for a 3 atmosphere filled hydrogen counter. Thus it might be expected that W and ω do vary slightly over the energy range 25 to 1000 keV but in most cases it is sufficient to regard ω as a constant.

The estimation of E_O for methane filled counters over an extended energy range has similarly produced a variety of results. For example, Allen and Ferguson (1957) showed that for E $<$ 250 keV $E_O \approx$ 8 keV whilst for E $>$ 250 keV their data gave E_O a value of 20 - 40 keV. This is in agreement with the methane measurements of Bore (1973) and Broomfield et al (1970), who both found that $E_O \approx$ 30 keV for E $>$ 300 keV. However, Bore later found E_O = 0 gave more consistent results with resonance structure, when using the same counter in filter measurements. On the other hand Kemshall (1973) found E_O = 43 $\pm$ 10 keV and 73 keV in an energy range 0.4 to 3 MeV for two different fillings of the same counter shell with 8 atmospheres of methane. However he attributed this discrepancy to electro-negative impurities in the gas, as the resolution of the helium-3 peak was considerably worse than that of a lower pressure filling.

These high energy measurements in both hydrogen and methane have shown that estimates of E_o are dependent on the energy region chosen although effects of electronegative impurities in the gas may also play an important role.

Argon and hydrogen gas mixtures have also been used in recoil proton counters. There is very little experimental data relating to the W value for energetic protons in this gas mixture. However measurements in argon by Phipps et al (1964), Lowery et al (1958) and Larson (1958) have shown that protons in the energy range 30 to 1860 keV have a constant W value. Below 30 keV the data of Phipps indicates an increase in W as energy decreases, as expected. This evidence on the behaviour of W in argon and the previous evidence on the behaviour of W and ω in hydrogen leads one to expect that in an argon-hydrogen mixture the assumption of constant ω is reasonable above 30 Kev.

In conclusion, for accurate neutron spectroscopy work a knowledge of the behaviour of W and ω (i.e. the relationship between ionisation and energy) is essential. This enables the ionisation spectrum to be transformed to the recoil-proton energy spectrum via equation (2.17), as required for neutron flux estimation. There are several possible methods of estimating the E - I relationship for a counter (i.e. calibrating it); in the following section these various methods and their merits are discussed.

2.3 Methods of Counter Calibration

Before neutron flux measurements can be made using a
particular counter, it needs to be calibrated. This entails
assigning an energy scale to the ionisation spectrum measured
by the counter. Ideally the calibration method should be simple
to apply and should result in an ionisation spectrum which has
easily recognisable characteristics, such as well defined
peaks or troughs whose energy values are already known. Further,
it is an advantage if these base energy values cover the whole
energy range over which the counter is to be used. However,
not one of the methods available fulfills all these require-
ments; they are outlined below together with their advantages
and disadvantages.

In the first method the helium-3 reaction (^{3}He (n,p)T)
is used to deposit energy in the counter. The gas of the
counter contains a small amount of helium-3 (less than 0.1%)
which, when exposed to thermal or fast neutrons undergoes a
positive Q reaction. For a single thermal neutron this reaction
releases a proton and a triton with a combined energy of
764 kev. Helium-3 reactions induced by fast neutrons occur
infrequently due to the large difference in cross-sections
(64,000 barns for thermals and 0.7 barns for fast neutrons of
1.0 MeV).

Alternatively the ^{14}N(n,p)^{14}C reaction could be used, but
there are two main disadvantages associated with it. First, the
thermal cross-section for the nitrogen reaction (14 barns) is
considerably less than that for the helium-3 reaction so that
more nitrogen is required in the counter (of the order of 5%).
Thus to maintain the same overall impurity level in the counter

one must be more wary of impurities in the nitrogen. Secondly the recoil carbon-14 nucleus has a velocity which is considerably less than its associated proton so that more of the carbon-14's energy goes to nuclear motion as the nuclear stopping power is greater, implying that the average energy loss per ion pair, W , is larger for carbon-14 than for its associated proton. The result is that the full energy (627 keV) of the original $^{14}N(n,p)^{14}C$ reaction is not seen, as some of it is lost to nuclear motion.

From these considerations the helium-3 reaction is the better choice, when using this "positive Q" method for counter calibration.

The main advantages of this method are that it is very simple to use and also that it produces an ionisation spectrum which has a very easily recognisable structure. The peak produced is readily apparent and can be accurately determined, and its resolution is a good measure of the counter's resolution. The reaction also occurs uniformly throughout the counter, so that the ionisation spectrum produced is a good measure of the underlying energy and counter processes. Another advantage is that the energy deposited by the reaction is within, or close to, the energy range of the counter.

However there are some disadvantages. The method results in a single observed (E,I) point, so that, in order to obtain the complete relationship between energy and ionisation, an assumption of strict proportionality is usually made as W and ω are normally unknown. Secondly, this method is applicable

only to those counters which contain sufficient gas to stop
the majority of the protons produced by the reaction before
they reach a wall. Otherwise, wall and end effects seriously
distort the ionisation spectrum produced.

Thirdly, once the counter has been calibrated and is in
use measuring neutron fluxes, the very (n,p) reaction which
was used in calibration now causes problems in the measurement
of fluxes with a large thermal component.

Finally, this method of calibration relies on the assumption
that all the reaction energy dissipated in the counter will
actually be observed. This may be unrealistic because several
processes are at work to cause a discrepancy between the reaction
energy and the observed energy. The major factors here are the
presence of electronegative impurities, space-charge effects,
recombination of the ions and electrons formed and possible
differences in the average energy loss per ion-pair for the
two charged particles produced by the reaction.

The second method of counter calibration entails irrad-
iating the counter with mono-energetic neutrons. This produces
a well defined ionisation spectrum and hence a single (E,I)
point. A series of these measurements using mono-energetic
neutrons of various energies can be used to find the whole
relationship between energy and ionisation from which a series
of response functions may be derived.

These experimental response functions may be compared with
theoretical ones (Snidow and Warren (1967)) in order to deter-
mine the errors in the theoretical response functions.

Furthermore, once the energy-ionisation relationship has been found for the counter, one of the other calibration methods may be used thereafter to estimate the overall gain of the system.

The major advantage of this method is that it produces the complete relationship between energy and ionisation without any additional proportionality assumptions. As with the first method discussed above, the ionisation spectrum has an easily recognisable form and is a good measure of the underlying processes, because the recoil protons occur uniformly throughout the counter.

This method undoubtedly calibrates the counter most accurately, but is unfortunately a costly procedure. It requires a variable energy accelerator capable of producing accelerated particles over a reasonable energy range, as well as a large experimental area in order to obtain response functions that are not distorted by room returns. Finally, the measurement procedure and analysis is very time consuming.

A third method of counter calibration uses a small alpha particle source situated at the centre of the anode wire in the counter. The alpha source produces an ionisation spectrum which has a well defined peak, whose energy may be calculated from range-energy tables. In this way a single E - I point is obtained and the assumption of strict proportionality between E and I enables the complete relation between alpha energy and ionisation to be specified.

When using the counter in neutron flux measurements, this relationship between alpha energy and ionisation must be transformed so that it is applicable to proton energies. If the W values for protons · and alphas are not known, then an assumption about their relative ionisation efficiencies must be made, and the calibration scale adjusted accordingly. Also, care must be taken that ionisation caused by the alpha source does not interfere with the ionisation spectrum produced by the neutrons. The energy lost by the alphas is often well outside the counter's energy range, so reducing the risk of such interference, but increasing the possible errors in energy calibration.

Another problem with this method is that the alphas are emitted from a localised source and so their ionisation spectrum does not give a true representation of the counter processes normally occurring. This method is rarely used on its own to calibrate a counter, but is frequently used as the first stage in the filter measurement method described next.

Finally a counter may be calibrated by filter measurements. This method involves transmitting fast neutrons through a material which has large, preferably symmetric, widely-spaced resonances at well known energies. Such materials as iron, PTFE, lithium carbonate and fluoride, boron and aluminium oxide have been used by various workers including Bore (1973), Broomfield et al (1970) and Powell and Rogers (1970). The neutrons then enter the counter as usual. This procedure modifies the initial neutron spectrum so that the neutrons entering the counter have a spectrum with dips and peaks associated with the resonances and anti-resonances of the material.

An ionisation spectrum is measured as normal but unfortunately this spectrum has no easily recognisable structure. This means that it must be unfolded in order to see the detail in the transmitted neutron spectrum. In the unfolding process, a rough energy calibration is required and this is normally provided by the use of either the helium-3 reaction or a localised alpha source, combined with the assumption of strict proportionality between energy and ionisation. The dips and peaks in the unfolded neutron spectrum are then compared with those in the expected neutron spectrum, predicted from the material's resonances. If there is any discrepancy in the energies at which these valleys and peaks occur, then the simple energy-ionisation assumed earlier is modified so that the two spectra agree. The final energy-ionisation relation completes the calibration process.

This is one of the most complex and time consuming methods of calibration as the ionisation spectrum has to be unfolded before the final energy-ionisation relationship can be obtained. Further, the unfolding process itself is subject to errors. However, it does provide a good measure of counter processes and a useful cross-check on any other calibration method employed.

In conclusion, the best method of calibrating a counter would appear to be the second method described, where the counter is bombarded by mono-energetic neutrons. In addition filter measurements may also be made to check the calibration, and then either the helium-3 reaction or an alpha source may be used to check the overall gain and resolution of the system. This

advocated procedure is indeed the one followed in the experimental work of chapter 3. Clearly, it requires the production of mono-energetic neutrons which is discussed in the following section.

2.4 Mono-Energetic Neutron Sources

In the method of counter calibration to be used, monoenergetic neutrons are required to measure the relationship between energy and ionisation and hence to determine the behaviour of W and ω . There are two main sources which produce mono-energetic neutrons: photoneutrons and neutrons from certain accelerator targets. In addition, quasi-monoenergetic neutrons may be produced by another method involving timing. These are discussed in turn.

Photoneutron sources make use of such reactions as D(γ ,n)p, whose Q value is -2.225 MeV and ^{9}Be (γ ,n)^{8}Be whose Q value is -1.666 MeV. If either deuterium or beryllium is exposed to a mono-energetic gamma source, then these reactions will produce vitually mono-energetic neutrons, provided that the gamma energy exceeds the relevant Q-value.[*] However, the very low gamma to neutron cross-section of these reactions results in a high gamma to neutron ratio. For example, 25 KeV neutrons can be produced by an antimony gamma source in beryllium, but the gamma to neutron ratio is approximately 10^4 : 1. Consequently, when a counter is exposed to such sources, it becomes

---

*Note that neutron energy is dependent on the angle between the paths of the neutron and of the incident gamma - but neutrons at a given angle are mono-energetic.

necessary to distinguish between ionisation caused by recoil protons and by electrons resulting from gamma interactions in the wall of the counter. This can be done by the use of rise-time discrimination (see Bennett 1967a).

Another problem is that both deuterium and beryllium are light elements and therefore degrade the energy of the neutrons, so that the resulting neutrons are no longer mono-energetic. Furthermore, in practice it is difficult to produce mono-energetic neutrons with a range of energies because gamma sources with a suitably wide range of energies are not readily available. All these factors mean that this method is rarely applied in the energy calibration of recoil proton counters.

Alternatively, bombarding certain nuclei with accelerated particles may result in mono-energetic neutrons. Again the neutron energy is dependent upon the angle between the neutron and incident particle's paths. For example, fast protons may be used with tritium, lithium and vanadium, while deuterons may be used with deuterium. In these cases the production of mono-energetic neutrons relies on the following reactions respectively,

$$T(p,n)^3He \quad \text{with} \quad Q = -0.764 \text{ MeV}$$
$$^7Li(p,n)^7Be \quad \text{with} \quad Q = -1.6441 \text{ MeV}$$
$$^{51}V(p,n)^{51}Cr \quad \text{with} \quad Q = -1.535 \text{ MeV}$$
$$D(d,n)T \quad \text{with} \quad Q = +3.2723 \text{ MeV}$$
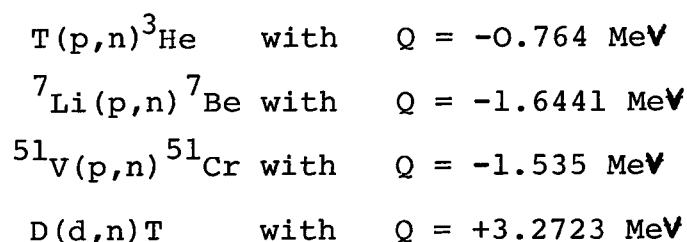
Many other target nuclei could be used to produce neutrons but the above generally prove to be the most convenient and efficient for proportional counter work.

This method does enable mono-energetic neutrons to be produced over a wide range of energies and with few associated gammas, so that rise-time discrimination is usually not necessary. However it requires the use of a variable energy accelerator and also a number of factors work together to cause a small neutron energy spread.

A third method involves the use of timing to produce quasi mono-energetic neutrons. Accelerated particles are bombarded into a target to produce neutrons with a range of energies. If the accelerator is pulsed then bursts of neutrons are produced. For each burst or pulse, the time is measured from when the accelerated particles hit the target to when the interactions occur in the counter. The distance between the target and the counter, combined with the measured time, enables the neutron energy to be defined. In this sense the neutrons entering the counter are "mono-energetic" as required for counter calibration.

The presence of gammas may cause some problems with this method, but the major difficulty is accurate timing of events in the counter. This necessitates the use of short timing constants in the amplification of pulses from the counter, which in turn may distort the observed ionisation spectrum (see Ritchie et al 1975). Both Verbinski (1974) and Werle (1969) have applied this technique, and further details may be found in these references.

Of the three available methods of producing mono-energetic neutrons for counter calibration, the first was rejected, as stated above. The second was chosen in preference to the third in order to avoid the severe timing difficulties and associated

inaccuracies, and also because the available accelerator had an energy range and resolution (~ 2 keV) more suitable for the second method.

The following sections discuss in detail the causes and magnitude of neutron energy spread for this method and then the choice of target material.

2.5 Neutron Energy Spread

The bombardment of target materials with accelerated particles will result in truly mono-energetic neutrons only if an ideal situation exists. This requires an infinitely thin target whose nuclei are completely at rest, an accelerated beam of truly mono-energetic particles, a point detector, and a scatter-free environment. In a non-optimal situation a slight spread in neutron energy may be observed as discussed below.

First, finite target thickness can cause neutron energy spread to be observed in the neutrons leaving the target at a given angle. Clearly the neutron energy (at a particular angle) depends on the energy of the incident particle, but in the case of finite target thickness, the energy of the bombarding particle is degraded as the particle traverses the target, resulting in neutrons with various energies at a particular angle. Further, the energy loss of the incident particle alters the cross-section of the reaction, resulting in a still greater neutron energy spread. Thus, the final neutron energy distribution at a particular angle depends on the incident particle's energy, its rate of energy loss in the target and the cross-section

of the reaction. However, if a "thin" target is used, the
problem is considerably simplified. This is a target in which
the energy loss by the incident particle in the target is such
that the reaction cross-section and the rate of energy loss of
the particle may be considered constant. Use of such a target
implies that the final neutron energy distribution at a partic-
ular angle depends only on the energy loss distribution of the
incident particle.

Secondly, the accelerated particle may not be truly mono-
energetic but may have a slight energy spread, which clearly
can cause a neutron energy spread. This effect is often referred
to as the "machine ripple". The magnitude of the neutron energy
spread is dependent upon the magnitude of the machine ripple;
the reaction used and the angle of observation also affect the
degree of dependence. For a particular light element reaction,
the effect of machine ripple on neutron energy spread is less
important at back angles than at zero degrees, where angles are
measured from the direction of the accelerated particle. For
example, consider the $T(p,n)^3He$ reaction and angles of 150 and
zero degrees. As the incident proton energy increases from
1.2 MeV to 3.0 MeV the change in neutron energy is 420 keV
for 150° and 1880 keV for 0°, so, assuming an approximately
linear relationship between neutron energy and proton energy,
it can be seen that the same absolute proton energy spread
will cause a greater neutron energy spread at 0° than at 150°.
This difference is even more marked for light element reactions
with positive Q values. For medium weight element reactions,
this angular dependence is greatly reduced. A more detailed
analysis of this effect is given in Marion and Fowler (1960).

This machine ripple usually increases as the energy of the accelerated particle increases and as the beam current drawn from the accelerator increases (see England (1974)). For most variable energy accelerators, the machine ripple is small; for example on the B.R.C.[1] Dynamitron it is in the order of 2 keV FWHM (full width half maximum) for 2 MeV protons at a current of approximately 1 micro-amp (Weaver 1975).

Thirdly, thermal motion of the target nuclei can obviously cause neutron energy spread, but this effect can be shown to be small (Marion and Fowler 1960). For example in the ^{7}Li(p,n)^{7}Be reaction at room temperature, it gives rise to a neutron energy spread of approximately 120 eV for proton energies near threshold, which is small in comparison to the machine energy ripple discussed above. This is the case for most reactions and so this effect can usually be neglected.

Fourthly, unless there is a point counter further neutron energy spread can be caused by geometric factors. A finite counter subtends a solid angle to a finite target. The finite target arises from the fact that an accelerated beam cannot physically be focussed to a point at the target. Thus neutrons detected in the counter may have been emitted from the target at different angles and, as the neutron energy is a function of angle, the counter will observe a spread in neutron energy. Moreover, depending on the angular differential cross-section, the neutron energy distribution detected by the counter may have a degree of asymmetry - except at 0° where the distribution is symmetric about its mean.

---

(1) Birmingham Radiation Centre

In light element reactions these geometric effects can be large since the neutron energy is highly dependent on angle and so a small variation in the angle of the neutrons causes a large variation in the neutron energy. However in medium weight target reactions eg. ^{51}V(p,n)^{51}Cr, the neutron energy spread is considerably reduced since the angular dependence is less. For example, contrast the angular dependence in the T(p,n)^{3}He and ^{51}V(p,n)^{51}Cr reactions: at an incident proton energy of 2.2 MeV the tritium reaction gives rise to a neutron energy of 1411 keV at 0° and 1134 keV at 40°, a difference of 277 keV, while the vanadium reaction gives rise to a neutron energy of 657 1eV at 0° and 646 keV at 40°, a change of only 11 keV. Thus in medium weight element reactions, large solid angles may be used without undue neutron energy spread from this cause.

Finally mono-energetic neutrons from the target can be further degraded by room returns and scatter of neutrons into the counter from the target assembly (i.e. the target backing and beam pipes). Here, neutrons from the target which would have originally missed the counter are scattered into it, resulting in neutrons at a different energy to those expected. This effect is very dependent on the nature of the room and the target assembly and thus is hard to quantify. However, Ryves (1973) made some Monte Carlo simulations of the extent of this effect in the lithium reaction with a typical target assembly. He found that there were fewer scattered neutrons bombarding the counter if it were placed at zero degrees, than if it were placed at other angles. Further, at zero degrees the majority of the scattered neutrons come from interactions

with the target backing, indicating that thin target backings
are desirable.

Therefore in a real situation, truly mono-energetic neutrons
cannot be produced for all the above reasons. In designing an
experiment, the extent of each of these effects for the reaction
to be used must be carefully assessed and the angle of the
counter and target-to-counter distance chosen accordingly.
Provided that the sum of these effects is less than the counter's
resolution at the observed neutron energy they will not limit
the accuracy attainable.

In the next section, the choice of target material is
discussed taking into account the above neutron energy spread,
as well as yield and other considerations.

2.6   The Choice of Target Materials

Since the counters to be calibrated will be used eventually
over an energy range from about 10 KeV to 2.8 MeV it is desirable
to calibrate them over the same energy range. Hence mono-
energetic neutrons from about 10 KeV to 2.8 MeV must be produced.
The available accelerator, the B.R.C. Dynamitron, is capable of
accelerating various particles (including protons and deuterons)
in the range 0.75 to 3.0 MeV. Therefore, in order to cover the
required energy range a number of different target materials
must be used, the choice of target material for a particular
neutron energy depending upon yield and energy spread consider-
ations as discussed below.

For each possible target material there is an optimal

neutron energy range, E_ℓ to E_u, over which it may be used

for the production of mono-energetic neutrons. The upper limit

of this range, E_u, is the energy above which the recoil nucleus

may be left in an excited state or a competing reaction may

take place. Such competing reactions result in two neutron

energies being observed above threshold energies of the two

reactions. For the four target materials considered (chosen

for their high yield), the competing reactions and upper limits

on the neutron energy range are given in table 2.1 below. For

reactions with a negative Q value there is also a lower neutron

energy limit, E_ℓ , below which neutrons leave the target only

in a cone about an angle of zero degrees and are not mono-

energetic. (In this context angles are measured from the

direction of the accelerated beam.) Within this cone there are

two possible neutron energies. Their energy difference decreases

as the laboratory angle increases and equals zero on the bound-

aries of the cone. This phenomenon arises from the transfor-

mation from the centre of mass coordinate system to the laboratory

system. In the centre of mass sytem there is clearly a unique

energy the neutron may take for a particular incident-particle

energy, regardless of angle. Thus, consider a neutron emitted

at velocity $V_n > 0$ and at an angle of zero degrees in the centre

of mass system. It will appear in the laboratory system at an

angle of zero degrees with velocity $V_n + V_c$ where V_c is the

velocity of the centre of mass in the laboratory system ($V_c > 0$).

However if this neutron had a negative velocity ($V_n < 0$ i.e.

emitted at 180 degrees) in the centre of mass system, then for

$|V_n| < V_c$ it will appear at an angle of zero degrees in the

laboratory system with a velocity $V_c + V_n = V_c - |V_n|$, while for $|V_n| > V_c$ its velocity in the laboratory system is $V_c + V_n = V_c - |V_n|$ which is negative, i.e. it is emitted at an angle of 180° in the laboratory.

Thus for $|V_n| < V_c$ it is possible to observe neutrons at zero degrees in the laboratory with two distinct energies, while if $|V_n| > V_c$ then mono-energetic neutrons are observed at zero degrees. This argument may be extended to other angles (see any standard text such as Marion and Fowler (1960) or Evans 1955) and hence it may be shown that for neutron energies below E_ℓ this "dual energy" may be observed in cone about zero degrees while mono-energetic neutrons are observed only at the edge of this cone. Also, as the energy increases, the cone half apex angle increases, until as neutron energy approaches E_ℓ, the apex angle approaches 90°. Once E_ℓ is reached, the cone defocuses and mono-energetic neutrons are observed at all angles in the laboratory system. Thus, if a target material with a negative Q value is to be used to produce mono-energetic neutrons below E_ℓ then the neutron energy at an angle of zero degrees must exceed E_ℓ and the counter must be placed at angles greater than zero degrees - but then there is an increased probability of observing scattered neutrons (See Ryves 1973). The value of E_ℓ for various target nuclei depends upon the centre of mass velocity in the laboratory system which is small for heavy target nuclei and large for light target nuclei. Table 2.1 gives the values of E_ℓ for the three target nuclei with negative Q values considered.

Table 2.1: Energy Ranges of Various Target Materials

Target Nuclei	Q Value (MeV)	Threshold Energy (MeV)	Lower Neutron Energy Limit, E_ℓ, (keV)	Competing Reaction	Threshold of Competing Reaction (MeV)	Upper Neutron Energy Limit, E_u, (keV)
Vanadium	-1.535	1.5656	2.36	$^{51}V(p,n)^{51}Cr$*	2.355	775
Lithium	-1.6441	1.8803	126	$^{7}Li(p,n)^{7}Be$*	2.378	626
Tritium	-0.764	1.014	288	$T(p,n)^{3}He$*	$>$10 Mev	9,000
Deuterium	+3.2732	—	1800 (at back angles)	$D(d,np)D$	4.45	7,710

* Nucleus left in excited state

Target materials with a positive Q value have a lower
limit on neutron energy which is governed by the Q value as
well as available machine energy. On the B.R.C. Dynamitron
the deuterium reaction will give mono-energetic neutrons from
3.4 MeV to 6.27 MeV at an angle of zero degrees, but if back
angles (angles greater than 90°) are employed, then mono-
energetic neutrons of energies down to 1.8 MeV may be produced.

So far, the energy range over which each possible target
material is suitable to produce mono-energetic neutrons has
been discussed. Next comes the choice of which target should
be used at which energies to cover the whole neutron energy
range from 10 keV to 2.8 MeV, as required for counter cali-
bration. Factors affecting this choice are, of course, the
energy range for each material as discussed above, ease of
target preparation and in particular yield considerations.

For low neutron energies above 10 keV and below 126 keV,
then the choice is between vanadium, lithium and tritium,
since deuterium is not feasible at this low neutron energy.
Both lithium and vanadium are relatively easy to prepare as
thin targets unlike tritium which is particularly difficult as
tritium readily diffuses through materials. Left with the
choice between lithium and vanadium, lithium proves the
easier target to prepare, but at neutron energies below 126 keV
displays the cone of dual energies discussed above - a problem
not encountered with vanadium at these energies. A further
argument in favour of vanadium is that the neutron energy
from this reaction is almost independent of angle, in sharp
contrast to the lithium reaction, enabling large solid angles

to be used without appreciable variation in neutron energy. This, coupled with the vanadium's high melting point, enables high beam currents to be used, so that the neutron yields of vanadium can be shown to be comparable to those obtained from the lithium reaction.*

For all these reasons, vanadium is the most suitable choice of target material to produce monoenergetic neutrons in the energy range 10 keV to 126 keV.

In the energy range above 126 keV, lithium produces mono-energetic neutrons at zero degrees and has a slightly greater yield than vanadium for the same energy spread. Combined with the easier preparation of lithium targets, these factors make lithium a more suitable choice for neutron energies greater than 126 keV. It is possible to overlap the neutron energies from the vanadium and lithium reactions in order to check the validity of the target thickness corrections. Lithium may be used to produce monoenergetic neutrons up to 626 keV, where the competing reaction sets in. The tritium could be used above 288 keV but sufficiently thin targets are difficult to obtain, and therefore lithium was used in the energy range 126 - 626 keV.

For neutron energies above 626 keV, tritium is a suitable source of monoenergetic neutrons because at these high energies target thickness is less of a problem. Again a region of overlap between the lithium and tritium observations

* In these experiments, lithium is to be used in the form of lithium carbonate to avoid the use of a cold trap, a Birmingham Radiation Centre requirement when either pure lithium or lithium fluoride is used. Other lithium compounds may cause a slight modification of these yield calculations.

may be a useful check. The upper energy limit for the tritium
reaction is theoretically governed by a competing reaction,
whose threshold is greater than 10 MeV. However, in this
case a further constraint is imposed by the available machine
potential. The Birmingham Radiation Centre Dynamitron is
able to accelerate protons to a maximum energy of 3 MeV, so
that the tritium reaction may only be used to produce mono-
energetic neutrons with energies below 2.2 MeV.

In order to obtain mono-energetic neutrons above 2200 keV,
the $D(d,n)^3He$ reaction must be used. Again there exists a
region of overlap between the upper limit of the tritium
reaction (2.2 MeV) and the lower limit of the deuterium reaction
(1.8 MeV). However, great care must be taken with the deuter-
ium reaction to prevent deuterium building up on the beam
collimators which could become a secondary source of neutrons.
This reaction more than adequately covers the upper limit of
the neutron energies desired for counter calibration.

To summarise, the choice of target material to produce
mono-energetic neutrons of various energies in the range of 10
to 2800 keV has been discussed and is given in Table 2.2. The
boundary energies between the targets are not rigid and so
a region of overlap exists, as is desirable in experimental
work.

This completes the discussion of the background underlying
the experimental work which is described in the following
chapter.

Table 2.2

Target Materials to be used to Produce

Mono-Energetic Neutrons in the

Energy Range 10 - 2800 keV

Target Material	Neutron Energy Range (keV)
Vanadium	10 - 126
Lithium	126 - 626
Tritium	626 - 2200
Deuterium	2200 - 2800 +

Chapter III   EXPERIMENTAL RESULTS OF COUNTER CALIBRATION

This chapter describes the work on the Birmingham Radiation Centre Dynamitron to calibrate the hydrogen proportional counters by the method chosen and discussed in the previous chapter. There, it was argued that four target materials should be used in turn to cover the entire neutron energy range desired. Unfortunately, it proved impossible to use more than two target materials due to pressure on accelerator time; in fact, lithium carbonate and titanium tritide targets were used in their respective energy ranges as given in the previous chapter. Originally, the vanadium reaction was to be used to produce neutrons of energies below 126 KeV and the deuterium reaction for neutron energies greater than 2.2 MeV, but the energy range covered in calibration procedure should prove adequate for the measurements in chapter V.

The first sections of chapter III are devoted to a description of the preparation of the two targets used, their assemblies and the estimation of target thickness. This is followed by the actual calibration procedure and results (ionisation measurements) in sections 3.3 and 3.4. The experimental response functions were derived from the mono-energetic neutrons' ionisation spectrum, obtained at the same time as the calibration results, and they are compared with the theoretical response functions in section 3.5. Finally resonance filter measurements are made as a check on the validity of the calibration results (as advocated in section 2.3) and they are discussed in section 3.6.

3.1   Target Preparation and Assemblies

This section contains a discussion first of the preparation of the lithium and tritium targets and secondly of the target assemblies used on the Dynamitron.

Target Preparation

The titanium tritide targets were obtained from the Radiochemical Centre at Amersham. These targets consisted of a copper backing material on to which a "thin" layer of titanium (i.e. one in which the energy loss of a 2 MeV proton is small - in this case, approximately 20 keV), had been evaporated. Tritium was then absorbed into the titanium layer, so forming a titanium tritide target.

The lithium target was made by vacuum evaporation of lithium carbonate on to either a nickel or stainless steel target backing. This lithium compound was chosen in preference to both lithium metal and lithium fluoride, despite their higher yields. A major reason for this decision was the Birmingham Radiation Centre regulation that a cold trap should be used in the vicinity of the target with these two materials; this could have increased the scattering of neutrons.* Further problems with lithium metal are that it oxidises easily and that target thickness has been reported to be unstable under proton bombardment (Marion and Fowler, 1960). Hence, lithium carbonate was used as the target material.

Before the evaporation process, the target backing was prepared in the following manner. First, the target backing was

---

* However, later experience with a cold trap and the tritium
  reaction revealed no undue increase in scattered neutrons.

polished with fine steel wire wool until the surface had a dull mirror finish. It was then rinsed successively in acid, water, acetone and distilled water and finally it was thoroughly dried in a heated oven. To enable target thickness to be measured after evaporation (see section 3.2) an alpha particle source, bismuth 212, was first deposited onto the target backing.

In the evaporation process itself, a molybdenum boat was used to hold the lithium carbonate. Prior to loading a boat with the lithium compound, it was cleaned and then baked out by passing current through it, whilst it was under vacuum in the evaporator. Air was then admitted to the chamber of the evaporator and the boat was filled with a standard amount of lithium carbonate. The target backing was placed 10 to 25 cm above the boat, depending upon the target thickness required. The chamber was re-evacuated and the boat temperature was raised until the lithium carbonate had melted. The temperature of the boat was then allowed to fall slightly and the evaporator was left pumping until the pressure had fallen to approximately 10^{-5} torr. At this stage the temperature of the boat was raised again causing the lithium carbonate to be evaporated. After approximately 3 minutes the current was switched off, the chamber let up to air, and the finished target was removed.

These targets were stored in a desiccator prior to use on the accelerator, normally for only a day or two. Where they were stored for longer periods, up to a week, or between runs exposed to air, no target deterioration was observed with regard to its thickness or adhesion to the backing surface.

Target Assemblies

Two target assemblies were constructed and used. One enabled the use of high beam currents, but gave rise to appreciable scattering, while the other considerably reduced the amount of scattering, but lower beam currents had to be employed to avoid loss of target material due to heat caused by the stopping of the incident particle in the target backing. In the following paragraphs the assemblies used with each target are described separately.

With the titanium tritide target only the low scatter target assembly was used. This target assembly (see fig. 3.1a) was able to withstand only 1 μA of 3 Mev defocused protons with no appreciable target deterioration. In this assembly the amount of material in the target region was kept to a minimum to reduce the possibility of a neutron that was emitted from the target at an angle that would avoid the counter being scattered into it by the target assembly. This possibility of scattered neutrons interfering with the measurements can be further reduced by replacing the viton O-ring vacuum seal with an indium or gold seal, or by soldering the target to its holder. To reduce the effects of scatter from the beam pipes, this holder was connected to the main beam pipes by a ½ metre long, stainless steel, drift tube with a wall thickness of 0.025 cm and a diameter of 2.54 cm (see fig. 3.1c). This low scatter assembly was used with the tritium target for both ionisation-energy measurements and response function measurements.

Both target assemblies were used with the lithium carbonate targets. The low scatter one was similar to that for the titanium tritide target, but here the lithium carbonate was evaporated directly on to the end cap of a short drift tube. Thus the target backing was the end cap itself, which was made of stainless steel machined to a thickness of approximately 0.025 cm and hard soldered to a 10 cm long, 2.5 cm diameter drift tube of wall thickness 0.025 cm, again made of stainless steel (see fig. 3.1b). The final thickness of the end cap was uncertain due to buckling, but it was thought to be approximately 0.018 cm. As with the tritium target assembly, the ½ metre long drift tube was again used to further reduce the possibility of scattered neutrons. This low-scatter target assembly was primarily used in response function measurements, as they are sensitive to scattered neutrons and could be distorted easily.

The high beam current assembly enabled a current of 60 μ A or more to be used with the lithium target. In this assembly, a heat pipe manufactured by Solek Ltd* was used to remove the heat energy deposited by the protons in the target backing. The heat pipe utilised the latent heat of evaporation to increase its thermal conductivity to several orders of magnitude greater than that of solid copper. The target holder comprised of a machined block of copper onto which a nickel target backing was hard soldered. The lithium carbonate was evaporated onto this backing. The reason for the nickel (rather than stainless steel) target backing was its high Q-value for the (p,n) reaction, -2.5 MeV (Maples et al, 1966), which would limit the production

---

* Solek Ltd, 16 Holybush Lane, Ratcliff.

of secondary neutrons. This target assembly was then clamped to the heat pipe, as the heat pipe's thermal conductivity was too great to permit soldering (see fig. 3.2). The beam handling performance of this assembly was governed, in fact, by the conductivity of the copper block.

Unfortunately, the scattering of neutrons by the target backing and secondly by the heat pipe allowed this assembly to be used only for ionisation measurements. For this purpose, a greater degree of scatter can be tolerated as one is interested only in the ionisation of the maximum energy recoil proton. Modifications of the target assembly aimed at reducing the neutron scatter encounter problems with the thermal conductivity of the target backing, which limits the maximum beam current.

A knowledge of the target thickness is required in the calculation of the mean neutron energy and therefore estimation of target thickness is the next step in the experimental procedure.

3.2 Target Thickness Estimation

Before an accurate estimation of the mean neutron energy can be made the mean target thickness must be known in order to calculate the mean proton energy. In this section the estimation of the thickness of lithium carbonate targets is discussed first and then that of tritium tritide targets. The lithium carbonate target thicknesses were estimated by two methods; one in which the measured yield curves* were compared with

---

* A yield curve is a plot of the number of neutrons per incident particle as a function of the particle energy.

calculated yield curves and the other by the measurement of the
energy degradation of an alpha particle traversing the target.
This latter method is discussed first.

As mentioned in the previous section 3.1, before lithium
carbonate was evaporated onto the target backing, an alpha
source Bismuth 212 was deposited onto the backing by electro-
static attraction of recoil nuclei from thorium 228 decay.
This alpha source produces alpha particles at two energies,
6.062 and 8.785 MeV. After the target was made, it was trans-
ferred through air to another vacuum chamber where it was
placed in front of a semi-conductor detector and the chamber
re-evacuated. The degraded energies of the alphas passing
through the target were measured. A bias amplifier was used to
expand the energy scale to enable a more accurate determination
of the alpha energy losses.

These alpha energies were compared with those from a
standard source prepared in the same manner but with no lithium
carbonate layer degrading the alpha energies. Thus the energy
loss for the two alpha groups could be found. The difference
between the two alpha energies from the standard source was used
to calibrate the system. Using the energy loss tables of
Williamson et al (1966) and Bragg's Law for energy loss in
compounds, the ratio of the energy loss per unit per path length
of alphas in lithium carbonate to that of protons at the lithium
threshold was calculated for   each alpha energy. Thus,
using these ratios and the observed energy losses it is possible
to calculate the thickness of the lithium carobnate layer in
terms of energy loss for protons of energy equal to that of the

lithium threshold which is 1880.4 keV. The accuracy of this method was between 10 and 15% depending upon the accuracy of the energy loss data and on the target thickness.

Secondly, the lithium carbonate target thickness was estimated from the relative neutron yield measurements made on the Birmingham Radiation Centre Dynamitron. Here, protons at various energies about the lithium threshold were used to bombard the target and the number of neutrons per unit charge was monitored to produce a yield curve. This was compared with a predicted yield curve whose derivation is described below (see figs. 3.3a and 3.3b).

A computer programme was written which assumed a particular mean target thickness, and calculated the effects on the relative yield curve when various assumptions were employed about the proton path length distribution and about the incident proton beam resolution. The programme assumed that no protons were lost traversing the target (as the probability of this is less than 10^{-6}) and that the incident proton beam can be represented by a gaussian distribution of proton energies about the mean incident energy at the front face of the target. (The full width half maximum of the gaussian was assumed to be 2 keV.) Further, no attempt was made to include straggling (i.e. discrete energy losses) of protons in the target and so a continuous slowing down approximation was used and the energy loss per unit path length was assumed constant. Under these assumptions, a particular energy from the gaussian representing the incident proton beam was selected and the proton energy distribution in the target was calculated from the assumed path length distribution;

hence its yield was calculated from the lithium differential cross-section. The total cross-section was obtained from Newson et al (1957) and the jacobian transforming solid angles from the centre of mass, where the cross-section is isotropic for proton energies less than 1.95 MeV, to the laboratory system was given by Palmer et al (1966). This calculated yield was then weighted by the probability of the incident proton energy in question from the gaussian distribution. This process was then repeated for the other energies of the original incident beam and each contribution was summed to give the expected neutron yield for the original gaussian distributuion. This procedure was repeated for the same path length distribution but for different mean incident proton energies to obtain a yield curve (i.e. the variance of the gaussian remained the same but the mean was altered).

As expected, the calculations showed a peak above the threshold energy in the relative yield curve, as did the experimental measurements. The energy difference ΔE, between the threshold energy and the energy value of the maximum yield was found to be highly correlated with target thickness. For targets less than 10 keV thick this energy difference was shown by the programme to be a good measure of the target thickness and was almost independent of the path length distribution assumed. As the target thickness increased beyond 10 keV, the energy difference, as expected, becomes more dependent on the path length distribution. For example, if the mean target thickness is 20 keV, and the path length distribution is a delta function (i.e. the proton energy distribution is rectangular) then ΔE is calculated to be 19 keV; on the other hand, if the path

length distribution is changed to a rectangular distribution starting at the origin (which is equivalent to a triangular proton energy distribution) ΔE is found to be 15 keV. In this example, the incident beam resolution was held constant. This extreme comparison indicates the validity of estimating the target thickness by ΔE. In general, it was found that for mean target thicknesses less than 20 keV, ΔE was a reasonable estimate of the target thickness, the accuracy of the estimate increasing as the path length distribution approached a delta function.

The major effect of variations in the incident proton energy resolution is on the predicted value of the threshold energy. The position of the threshold, found by extrapolation of the linear region of the calculated yield curve to zero yield, was found to be below the real threshold of 1880.4 keV if a finite proton energy resolution was assumed. The difference was found to be approximately equal to $^1/_3$ of the full width half maximum of the gaussian describing the proton energy distribution. This result was approximate as a continuous slowing down model was used instead of the more correct discrete one as used by Palmer et al (1966). The calculated yield curves for several different proton beam resolutions are shown in fig. 3.4. Normally the proton beam resolution is determined by the accelerator in use; this is 0.1% on the Birmingham Radiation Centre Dynamitron, which meant that the threshold would be underestimated by approximately 0.6 keV. This source of error is small in comparison to experimental error.

Table 3.1

Comparison of lithium carbonate target thicknesses

TARGET	1	2	3	4	5	6	7
Target thickness from alpha energy loss (keV)	22 ± 2	18 ± 2	18.5 ± 2	19.4 ± 2	7.6 ± 2	7.4 ± 1.5	4.5 ± .5
Target thickness from relative yield measurements (keV)	23 ± 1.5	20 ± 2	16 ± 1.5	18 ± 1.5	5.5 ± 2	7.1 ± 1	5 ± 1

In conclusion, from the calculations by the above computer model it can be seen that the energy difference between the experimental threshold energy and the position of the maximum yield will give a reasonable measure of target thickness. The accuracy of this method should, theoretically, be better for thin targets but biased for thick targets where this energy difference will tend to underestimate the target thickness. Experimental target thicknesses obtained by this method and by the previously described alpha particle method are compared for seven different targets in Table 3.1. The two methods were found to agree within experimental error.

The titanium tritide target thickness was estimated by employing a 2.5 atmosphere hydrogen filled counter to measure the neutron energy distribution from the target as well as the energy of the maximum recoil proton. Prior to this measurement the counter had been calibrated using the lithium carbonate targets. The titanium target was bombarded at a particular proton energy and then the estimated target thickness was adjusted to give a fit between the calculated and measured neutron energies. This procedure was repeated at a different proton energy. In order to obtain the thickness at a common proton energy, each estimated thickness was multiplied by the ratio, R:

$$R = \frac{\text{energy loss per unit path length at the threshold energy plus 50 keV}}{\text{energy loss per unit path length at the incident proton energy less 50 keV.}}$$

and the average of the two was found to be 109 ± 5 KeV. Further, a rough approximation of target thickness is given by twice the measured width (full width half maximum) of the unfolded neutron distribution. This was of the order of 96 keV, which is in

agreement with the previous estimate. This is a rather surpris-
ing estimate as the titanium layer was quoted to be 0.23 mg/cm^2
thick, corresponding to a 33 keV energy loss for 1.06 MeV protons.
This could possibly be explained by the diffusion of tritium
into the copper backing but it is thought more likely that the
titanium layer was considerably thicker than 0.23 mg/cm^2. During
the experimental measurements, the position of the peak on the
yield curve and its value were monitored to check whether tritium
was being lost from the target, but no appreciable loss was
observed.

So far the mean target thickness has been found for both
the lithium and tritium targets in terms of the energy loss of
a proton incident near the threshold energy. In order to find
the thickness at other proton energies, this value was multiplied
by $^1/_R$ for the tritium target and by:

$$^1/_{R'} = \frac{\text{energy loss per unit path length at the incident proton energy}}{\text{energy loss per unit path length at the threshold energy}}$$

for the lithium carbonate target. These energy losses per unit
path length were found from the energy loss tables of Janni
(1965) and/or Williamson et al (1966). This modified target
thickness was used to estimate the mean proton energy in order
to calculate the mean neutron energy.

For the lithium carbonate targets, the final uncertainty in
the neutron energy is in the order of 2 - 3 keV. This uncertainty
is due to errors in the estimation of the proton energy incident
on the target and the estimation of the target thickness, which
are approximately comparable. For the titanium tritide target
the largest source of error in the calculation of neutron energy

at low proton energies, is due to uncertainties in the target
thickness leading to an error in the neutron energy of 4 to 6 keV.
Above proton energies of 2.7 MeV, uncertainties in the proton
energy become more important and lead to further errors in the
neutron energy comparable to those due to target thickness. The
total error is of the order of 6-10 keV at these higher energies.

In the following section the experimental and analytical
procedure is discussed.

3.3   Experimental and Analytical Procedure

In these experiments to measure ionisation for counter
calibration and response function shape, the Birmingham Radiation
Centre 3 MeV Dynamitron was used. The machine is capable of
producing 750 keV to 3 MeV protons with beam currents up to 2 mA.
The experiments were performed in the low scatter cell, a room
10 m cubed with an iron grid floor dividing it in half instead
of the more normal concrete floor, in order to reduce room returns.
The upper half of this cell was used, with the beam pipe ending
approximately in the centre and 1 m from the grid floor. A
schemata of the layout is shown in fig. 3.5. First the experi-
mental procedure is described followed by the analytical proce-
dure.

In the measurements described in this work three different
proportional counter fillings, which covered three different
energy ranges, were used. The gas filling, operating voltage
and resolution of each counter is given in table 3.2.

Table 3.2

Counter Fillings

Gas Filling	Operating voltage	Resolution (FWHM of helium-3 peak)
2.5 atm hydrogen	2200 V	4.5 %
10 atm hydrogen	3600 V	6.5 %
2.27 atm hydrogen 8.07 atm argon	2500 V	10.5 %

Prior to any measurements with the recoil proton proportional counters the total gain of the detector system was first calibrated by the use of the helium-3 reaction with thermal neutrons. At the same time a precision pulser was used to establish the ADC back bias. Throughout a run, if gain changes were required then electronic, not gas, gain was altered and the pulser was used to estimate this gain change. This procedure, i.e. He^3 calibration, was repeated at the end of the day or run to check gas gain and back bias, and no two consecutive calibrations in one day differed by more than 0.5%, provided that there had been a warm-up period of several hours for the counter electronic. system. The electronic system used with these counters is given in detail by Bore 1973.

In the Dynamitron, to stabilise voltages along the accelerating tube the tube is coupled in several places to a resistor chain running from the top (3 MeV) terminal to the ground. The Dynamitron energy is measured using a digital voltmeter (DVM) to observe this current from the resistor chain passing through a standard resistor. Any change in the machine's calibration will therefore be observed as a change in the tabulated DVM reading for a fixed threshold or resonance energy.

In order to check the machine calibration prior to any experimental measurement a yield curve measurement was made. The threshold was found as described by extrapolation of the linear region on the yield curve just above threshold to give an energy intercept at zero counts. The relative yield curve and hence the threshold was measured by using a standard long counter at an angle 0° and 3.5 m from the target. If this

threshold value differed appreciably from the previous one,
or was the first in one day, then it was repeated until the
difference between successive threshold values was less than
1 keV. This was necessary since when the machine had been
switched off or started up at the beginning of the day, it
required some time for it to "warm-up". At the end of each
ionisation and/or response function measurement, and occasion-
ally during the measurement, further thresholds were measured.
The measured threshold was compared with the tabulated value for
the Dynamitron and the difference was used to correct the value
of the proton energy for the calculation of the neutron energy
in the ionisation and/or response function measurements.

In all measurements the counter was placed at zero degrees
at a distance of 30 cm or greater from the target so that
the neutron energy spread due to geometric factors was small
compared to the spread due to the counter's resolution. After
an ionisation spectrum from monoenergetic neutrons had been
collected it was analysed in the following manner. First the
ionisation value (channel number) of the maximum recoil proton
energy was estimated by inspection. This value was taken to be
half the height of the knee portion of the proton distribution
(see fig. 2.1). Secondly, the data were then smoothed "on-line"
by a travelling average technique which reduced the statistical
scatter by a factor of 5 but worsened the resolution by a
factor of 1.441. This smoothed data was differentiated "on-
line" and the magnitude of the result displayed. The mean
channel number (ionisation in arbitrary units) of the resulting
peak was taken to represent the maximum recoil proton's ioni-
sation. As a third and final check on this value a modified

version of SPEC4*was used. In this modified programme it was assumed that there was no neutron flux above a specified neutron energy. The smoothed data was unfolded and for the unfolding strict proportionality was assumed between E and I and the effective Q value used was 764 keV. This unfolding took place "on line" and the resultant neutron spectrum, a peak, was displayed. The mean of this peak was taken to represent the ionisation of the maximum energy recoil proton. It should be noted that the assumption of proportionality between E and I and an effective Q value of 764 keV can lead to a small error in the shape of the unfolded neutron spectrum, and hence in the mean of this peak. This error can be shown to be less than 1%.

By the above three methods, three estimates of the ionisation value of the maximum energy recoil proton have been found. Normally a weighted average of these values was taken. This average ionisation value (including the effect of ADC back bias) was normalised to a standard gain by the use of the helium-3 calibration.

The mean neutron energy which gave rise to the recoil proton distribution was calculated using kinematics. The proton energy incident on the front face of the target was first corrected for the deviation of the DVM reading of the threshold energy away from the tabulated value (see above). Then half the target thickness (see section 3.2) was subtracted from this corrected value of proton energy to give the mean proton energy in the target. This mean proton energy was finally used in the

---

* SPEC 4 is a computer programme to unfold neutron fluxes from proton recoil distributions; it was developed by Benjamin et al (1968a).

kinematic calculation to give the mean neutron energy. The
neutron energy distribution was assumed to be symmetric (see
previous chapter) and the mean neutron energy was then taken
to be the maximum energy of the recoil protons.

The analysis of the response function's shape is given in
section 3.5. In the next section the energy-ionisation measure-
ments are discussed.

3.4   Calibration Results

In this section the calibration results for the three
different counter fillings are given and discussed. The counter
fillings were given in table 3.2. First, the two hydrogen
fillings are considered together, followed by the argon-hydrogen
counter calibration results.

The results of the hydrogen filled counters are discussed
together as they are expected to be similar because the same gas
is used in both counters. However, the resolution (FWHM of the
764 keV helium-3 calibration peak) of the 10 Atm counter is
6.5%, 2% worse than the 2.5 Atm counter, which indicates that
the effects of electronegative impurities could be more important
in the high pressure counter.

The neutron energy range of the ionisation measurements
for the 2.5 Atm counter was 50 to 626 keV. These results were
obtained by using thin (of the order of 5 keV) lithium carbonate
targets on the high beam current (heat pipe) assembly, with the
exception of the points at 50 and 100 keV which were found using
the resonance filter method. The neutron energy range investi-
gated with the 10 Atm counter was 126 to 1600 keV and the results

were obtained using the heat pipe assembly with a thin lithium

carbonate target up to 770 keV. Points at 650 keV and above

770 keV were obtained by using the titanium tritide target

with the low scatter target assembly. The overlap region

between the two target materials was carefully examined to check

that there was no systematic error between the two measurements.

No such error was found.

Following the normal convention, the results were first

analysed assuming that ω was constant in the operational energy

regions of each counter. This assumption leads to an ionisation-

energy relationship of the form $I = KE + E_0$ (or $E = K'I + I_0$)

and a curve of this type was fitted to the results. However

as there are errors in the variables, a least squares estimator

would give biased and inconsistent estimates of the gradient

and intercept, even in large samples. Thus, an instrumental

variable estimator was used to fit the line (see Appendix I).

It should be noted that the errors in the ionisation values

were approximately 1%, whilst the errors in the mean neutron

energy were $\pm$ 2.5 keV for the lithium carbonate targets, and

$\pm$ 7 keV for the titanium tritide targets.

In figures 3.6 and 3.7 the results and fitted line are

plotted for the 2.5 Atm counter and the 10 Atm counter respect-

ively. With the 10 Atm counter, the points below 346 keV were

excluded from the estimation of the gradient and intercept as

they lay off a straight line through the remaining points by an

amount greater than the experimental error.

The 764 keV from the helium-3 reaction and its correspond-
ing ionisation value are also plotted for each counter. As
can be seen for both counters, E_o does not equal zero and the
effective ionisation value for the helium-3 reaction is not 764
keV. The instrumental variable estimator gave, for the 2.5 Atm
counter, $E_o = -7.7 \pm 0.5$ keV and the effective Q value of the
helium-3 reaction to be 779 ± 3 keV, whilst it gave $E_o = 15.7 \pm 2$
keV and the effective Q value of the helium-3 reaction to be
784 ± 4 keV for the 10 Atm counter.

To investigate these high estimated effective Q values the
helium-3 reaction was examined in greater detail, especially
the position of the triton and proton edges. These edges are
caused by the complete absorption by the counter's walls of
either the proton or triton energy, and hence can be given energy
values corresponding to those of the proton and triton. Normally
the proton and triton edges of this reaction are obscured by the
detection of both recoils from fast neutrons and electrons
knocked out of the counter's walls by gammas from the neutron
source. To overcome the problem of fast neutron interactions,
a source whose maximum energy is considerably less than the
triton's energy of 191.3 keV was needed and so the $^7Li(p,n)^7Be$
reaction with proton energies just above the threshold energy
were used. The neutrons were thermalised by surrounding the
counter with water, which also shielded the counter slightly
from gamma rays. The problem of gamma induced electrons was
further reduced by using a fresh lithium carbonate target so
that the gammas from the beryllium-7 decay were reduced.

This approach was tried with both counters but was only successful with the 2.5 Atm counter due to its lower gamma sensitivity. The ionisation spectrum of the helium-3 reaction in the 2.5 Atm counter is shown in figure 3.8. The ionisation value of the triton edge was plotted against its energy of 191.3 keV in figure 3.6, where the other ionisation measurements are shown. As can be seen this point lies off the calibration curve by an amount greater than the experimental error. This apparent increase in the triton energy accounts for the high effective Q value of 779 keV. These results could be explained by a 6% decrease in W, the average energy loss per ion pair for the 572.7 kev proton. It should be noted that, as we shall see, this is only one of several possible explanations.

This effective Q value is in disagreement with other workers such as Bore (1973), Verbinski et al (1974), and Kemshall (1973) but is in agreement with the value given by Carter (1974). The energy intercept of -7.7 keV for the 2.5 Atm counter agrees with the value found by Bore (1973) but Allen and Ferguson (1957) and Kemshall (1973) both found, over a more extended energy range, an intercept of zero within experimental error.

There are several effects which on their own or in combination with each other can explain these observed inconsistencies. The inconsistency in the ionisation produced by tritons and protons of similar energy and hence the effective Q value is best explained by a difference in W, the average energy loss per ion pair formed between the two particles. Using Fano's (1946) expression, the difference in W for the two particles is 9% compared with the 6 $\pm$ 2% observed. However the 9% figure

is probably in error due to charge exchange and/or pick-up
(see section 2.2).

As the range of the triton equals that of an equal energy
proton within 15%, the effects of electro-negative impurities
should be equal. Similarly, as both the range and number of
electrons produced by the triton and a similar energy proton are
approximately the same, the space-charge (local electric field
depression) effects cannot explain the discrepancy in relative
ionisation efficiencies.

As for the E_0 values, this can be explained by a non-
constant ω, although in the negative E_0 case it implies that
W rises as energy increases, while for positive E_0 W falls.
However the fact that the intercepts are different in each counter
implies that another effect, or other effects, are predominant
and the two main ones, electronegative impurities and space
charge effects, are discussed below.

Considering space-charge effects first; this effect occurs
when the electrons drifting towards the anode cause a reduction
in the local electric field, so that gas multiplication is
decreased. This causes an apparent decrease in ionisation and
results in the counter operation becoming non-linear (Hana et al
1949). Obviously this effect is greater for high energies than
low ones, causing an effect indistinguishable from an increase
in W as the energy rises. To quantify this effect, Benjamin
et al (1968b) define from resolution considerations a critical
value of 93 MeV for the product of gas multiplication and energy
deposited in the counter. When the product exceeds this value

more than

the resolution will have worsened by 2% as a result of space-

charge effects. On the other hand, Ichimori et al (1975),

from ionisation magnitude (ie pulse height) considerations,

suggest a critical energy-multiplication product value of 14 Mev

giving a critical energy of 200 keV for the 2.5 Atm counter.

However, examination of the linearity of the ionisation-energy

relationship (figure 3.6) where measurements were made with the

anode wire perpendicular to the neutron beam show that Ichimori's

value is probably too low and that for the 2.5 Atm counter it is

greater than 44 MeV. Using Benjamin et al's (1968b) data and

applying the criterion that the critical multiplication is

the value when the resolution begins to worsen due to space-

charge effects, instead of when the resolution has deteriorated

by 2%, then a critical energy-multiplication value of 48 ± 4 MeV

is obtained. In conclusion, for proportional counters a value

of the critical energy-multiplication product is in the order

of 50 MeV. Although this effect can explain apparently high

Q values it cannot explain the difference between the ionisation

values of the tritons and protons of similar energies.

Ionisation can also be affected by the presence of electro-

negative impurities. This effect is dependent on the electron

energy spectrum which is only weakly dependent on the initial

ion's velocity, its track length and position. This renders

quantification of this effect difficult, but the overall effect

is a general reduction in ionisation. As the effect of electro-

negative impurities is virtually independent of the initial ion

energy this cannot explain the apparent discrepancy in the W

values between the triton and a similar energy proton, as their

ranges and number of electrons produced are similar. However

this effect may explain the positive energy intercept observed with the 10 Atm counter and provide a possible explanation of the low ionisation values observed at 126 and 236 KeV (see figure 3.7).

Leaving the hydrogen filled counters, the argon-hydrogen filled counter is considered next. The ionisation-energy relationship for this counter was measured over the neutron energy range 346 to 2135 keV. These points were measured using the heat pipe assembly with a thin lithium carbonate target (5 keV) up to 700 keV, and a titanium tritide target on the low scatter assembly above this energy. Again, ω was assumed constant and a straight line was fitted using an instrumental variable estimator. This line and the energy-ionisation points, including the helium-3 point, are shown in figure 3.9. E_o was estimated to be 77 $\pm$ 4 keV and the helium-3 effective Q value to be 751.4 $\pm$ 5 keV.

The resolution of this counter is 10.5%, which is considerably worse than that of the hydrogen filled counters (4.5% for 2.5 Atm of hydrogen, and 6.5% for 10 Atm). Therefore, the effect of electronegative impurities are thought to be responsible for the high E_o value and low effective Q value. The counter's high gamma sensitivity prevented the helium-3 reaction from being studied in detail.

To summarise the ionisation-energy results for all three counters, it can be seen that the assumption of strict proportionality is invalid, so that the E-I relationship must be determined. However ω, the specific energy loss per ionisation,

has been shown to be constant within experimental error over each counter's energy range. The product of energy deposited and gas multiplication should be kept below 50 MeV so that space charge effects are kept to a minimum. Further, the operation of the 10 Atm hydrogen counter below 300 keV may be non-linear possibly due to the effects of electro-negative impurities. Also the high Q values of the helium-3 reaction in the hydrogen counter can be explained by a difference in the W values for tritons and protons of a similar energy.

In the next section the experimental response function shapes are compared with the calculated values, and the reasons for any discrepancies are discussed.

3.5 Response functions

In this section the shapes of the proton recoil distributions for the three counters are discussed concurrently and compared. With these spherical proton recoil counters, a major cause of distortion in the observed proton recoil distribution for mono-energetic neutrons is the truncation of proton tracks by the walls of the counter as discussed in section 2.1. Hence the range not the energy of the recoil protons will be the deciding factor in the shape of the recoil distribution. In order to compare the recoil proton distribution of one counter with that of another a dimensionless variable:

$$\frac{r}{a} = \frac{\text{range of a proton at the maximum recoil energy}}{\text{radius of the active volume of the counter}}$$

is introduced and the comparison made at the same range-over-radius value.

All recoil distributions were measured using the low scatter
assembly with either a thin lithium carbonate target or the
titanium tritide target. A representative sample of these
distributions is shown in figures 3.10 to 3.18. The full curve
shown with each is the calculated response function, appropriately
normalised. These latter curves were found by using the analyti-
cal expressions formulated by Snidow and Warren (1967). As can
be seen, the slope of the observed recoil distribution is greater
than that of the calculated distribution. A possible reason
for this might have been the production of low energy neutrons
from p-n reactions with the target-backing and beam-pipe materials.
To check this the relative neutron yields from thick targets of
the above materials were measured and compared with those from
a thin lithium carbonate target over the bombarding proton's
energy range. This indicated that the maximum number of neutrons
produced by these p-n reactions in the target backing and beam-
pipe materials was less than 1% of the number of neutrons produced
by a thin lithium target. Hence this factor may be eliminated
as a possible cause of distortion in the recoil proton distribu-
tions.

For calculated response functions with range-over-radius
values of less than unity, the predicted recoil proton distri-
butions are trapezoidal in shape. Following Benjamin et al
(1964 b), this characteristic can be quantified by calculating
or measuring the ratio of counts at half the maximum recoil
energy (i.e. half the neutron energy) to the counts at the maxi-
mum energy. This ratio defines the shape of the response
function or recoil distribution and the ratio is known as the
correction factor. For response functions with a range-over-

radius value greater than unity the response functions gradually become more and more curved.

In the measured recoil proton distributions with $r/_a$ less than unity, the trapezoidal shape is distorted at low proton energies due to gamma-perturbation, and further distortion occurs at slightly higher energies because of neutrons scattered into the counter from the target assembly and surroundings. However, a linear region is observed, as predicted, at higher energies and below the maximum recoil energy. Returning to the latter cause of distortion (scattered neutrons), Ryves (1973) has shown that for a counter at zero degrees the majority of the scattered neutrons come from the target backing. Clearly, most of these neutrons originate from the target at 90° and so must be scattered through 90° to enter the counter. The energy of these scattered neutrons may then be calculated and used as an approximate indication of the upper energy limit of this effect. The extent of distortion due to scattered neutrons depend on the incident proton energy and hence on the differential cross-section; the less forward peaked this is, the greater the distortion. In figures 3.10 to 3.18, the energy of the scattered neutrons is marked by an arrow and clearly this corresponds remarkably well to the boundary between the regions of distortion and no distortion, as hypothesised.

The correction factor, the ratio of counts at half the maximum recoil energy to counts at the maximum, can be estimated from the linear region of the data, between the distortion due to scattered neutrons and the maximum recoil energy. A line was fitted using least squares, after adjusting the data to take

account of A.D.C. backbias and additional backbias due to E_o.
The position of the maximum recoil was found by the method
described in section 3.4. These calculations were performed
"on-line", making rapid determination of the correction factor
possible.

For those recoil distributions with range-over-radius values
greater than unity, a straight line may be fitted to the data in
the vicinity of the maximum recoil energy and a correction factor
calculated in an analagous way, for example see Benjamin et al
(1964 b) and Kemshall (1973). However, as the recoil proton
distribution becomes more and more curved, this procedure will
lead to larger and larger errors in the estimated correction
factor, and so was not pursued for range-over-radius values
greater than 1.2.

A plot of the correction factors for the three counters
against range-over-radius is shown in figure 3.19. The error
bars on the experimental correction factors show the upper bounds
of the variances. It can be seen that the correction factors
for different gas fillings are not significantly different.
This indicates that the shape of the response function is
independent of (or very weakly dependent on) the differences in
the gas multiplication from one counter to the next, in contrast
to the results obtained by Bore (1973).

Also shown in figure 3.19 are the corresponding values
calculated from the analytical expressions of Snidow and Warren
(1967), the experimental curve of Broomfield et al (1970), and
thirdly a curve simulated by Broomfield et al, using a modified

version of the Monte Carlo code used before the advent of the Snidow-Warren analytical expressions. The experimental points presented lie above the analytical curve of Snidow and Warren, and below the experimental curve of Broomfield et al, but lie near or on the third simulated curve.

Broomfield's experimental curve was found by including all the observed points between the region of gamma-perturbation and maximum recoil energy, and so includes points that are biased upwards by scattered neutrons, (as mentioned above). This would lead to an over-estimation of the correction factors - which indeed seems to be the case in comparison to the points measured during the course of this work.

The third curve was calculated by using a Monte-Carlo code to simulate the distortion in the resonse function due to truncation of the proton track lengths by the walls of the counter. The original assumption of a uniform electric field throughout the counter was modified to take account of the variation in gas multiplication at the ends of the anode. The shape of the electric field in this region was measured by Benjamin et al (1964 a). They observed the variation in pulse height along the anode wire for alpha-particles of a given energy, and found that the pulse height fell to zero at the ends of the anode wire. Thus the electric field and hence the gas multiplication also fall to zero here, and so recoil proton tracks which originate in, and/or pass through this region will receive less gas multiplication than those entirely outside the region. This implies that the measured ionisation from one of these tracks will be less than that of tracks of similar energy outside this

region. Since this region of electric field distortion comprises

approximately 10% of the counter's active volume, the effect

is to significantly increase the number of low energy proton

recoils measured, thus increasing the distortion of the response

function.

We now consider response functions with range-over-radius

($^r/_a$) values greater than unity. For these, the Snidow-Warren

expressions indicate that the correction factor increases

rapidly with $^r/_a$ and so a measured response function would be

sensitive to neutron energy spread. The effect of this is

illustrated in figure 3.20 for a range-over-radius value of

1.35; the counter's response is calculated both for the case

of mono-energetic neutrons at 800 keV and for the case of a

spread of incident neutron energies, assumed to be gaussian with

FWHM of 46 kev and mean 800 keV. It can be seen that the

effect of the gaussian neutron energy spread is to reduce the

slope of the recoil proton spectrum and hence the correction

factor.

Broomfield et al (1970) found that for $^r/_a$ values greater

than 1.5, the observed recoil spectra for a 10 atmosphere hydro-

gen counter could be explained by the Snidow-Warren expressions

only if the range values used in these expressions were increased

by 5-8%. (They previously eliminated electric field distortion

as a cause of this discrepancy at these high $^r/_a$ values.)

However, comparison of compilations of range-energy data indicates

that the ranges are well known (within 2%) over the relevant

energy range (see, for example, Parker et al (1963), Williamson

et al (1966) and Janni (1966)).

A possible explanation of this discrepancy is that the calculated response function assumed a mono-energetic neutron source, whereas Broomfield's data will be influenced especially at low recoil proton energies by non-mono-energetic neutrons due to room returns and neutrons scattered through 90°. This was a factor they neglected to take account of when estimating correction factors for low r/a values, and again appears to be overlooked here. Thus, the effects of non-mono-energetic neutrons could account for the discrepancy between the experimental and calculated curves, and there would be no need to increase the range values to make the two coincide.

In contrast, for a one atmosphere hydrogen counter, Broomfield et al found that the range would have to be decreased by 1% in order to bring the calculated response function in line with their observations. This could possibly be due to a large neutron energy spread about the mean.

Figures 3.21 and 3.22 show response functions calculated from the Snidow-Warren expressions, and the effect of arbitrarily increasing the range by 10%. In figure 3.21, the $T(p,n)^3He$ reaction was assumed to produce 1600 kev neutrons incident on a 2.5 atmosphere hydrogen counter at zero degrees, resulting in $r/a = 4.1$. The upper limit of the region where neutrons scattered though 90° might be expected to fall is indicated by an arrow. Figure 3.22 shows the response function of a 10 atmosphere counter assumed to be bombarded by 2.6 Mev neutrons from the $D(d,n)^3He$ reaction, resulting in $r/a = 2.3$. Again an arrow indicates the upper limit of scattered neutrons. From these calculations it can be clearly seen that any attempt to fit analytical response

functions to measured ones must take into account the neutron energy distribution due to the effects of neutrons scattered through 90°, room returns, target thickness and geometric factors.

In conclusion, it has been shown that the analysis of recoil spectra must take account not only of neutron energy distribution but also of electric field distortion. For range-over-radius values less than unity, the dominant effect is the electric field distortion, but the influence of neutrons scattered through 90° is also important. The latter problem can be overcome by restricting the analysis to unaffected data points. The former explains the deviation of observed data from the Snidow-Warren predictions. For range-over-radius values greater than unity, the importance of the electric field distortion is greatly diminished, and neutron energy spread becomes the dominant factor. This neutron energy spread must be estimated before the analysis can proceed.

Furthermore, these measurements have shown no variation in the correction factors for counters containing different gases, in contrast to Bore's results (1973).

The following section describes resonance filter measurements which were made in order to check the validity of the energy-ionisation relationships found in section 3.4.

Use is made of the correction factors found in this section.

3.6 Resonance Filter Measurements

In this section the resonance filter method for counter calibration (see section 2.3) is used to check the validity of the E_o and "effective" Q-values found in section 3.4. The response correction factors found in section 3.5 are used in all neutron flux estimations. The measured neutron fluxes are compared with those predicted from the materials' resonances and anti-resonances, and the agreement or lack of agreement is discussed.

In these measurements the Nuffield Cyclotron at Birmingham University was used to produce neutrons. Here, thick lithium and cobalt targets were bombarded with 10 MeV protons which yield a continuous range of neutron energies, peaking at approximately 1 MeV and Maxwellian in shape (see Jones (1970) and Khadduri (1973) for further details of the neutron source spectra). Resonance filter material approximately 10 cm thick was placed between the counter and target. The anode wire of the counter was again perpendicular to the incident proton beam. It should be noted that in some experiments, 5 cm of lead was placed between the target and filter material to reduce the effect of gamma interactions in the counter. Before and after each neutron flux measurement, the counter's total gain was calibrated using the helium-3 reaction, and the ADC backbias and any further changes in electronic gain were found by using a precision pulser.

In order to unfold the experimental recoil data to obtain
a neutron flux, the neutron flux above the upper energy limit of
the counter must be known. These input neutron spectra required
for the unfolding routine[1] were derived by employing the multi-
group, one-dimensional, discrete ordinate transport code, ANISN
(Engle, 1967). The spectra calculated by this programme are
shown in figure 3.23. The absolute height of these spectra
is likely to be in error due to simplifying assumptions made;
in particular, the neutron source is assumed to be isotropic
and also approximations were made to represent the experimental
geometry in a form suitable for the programme. However, the
general shape of the spectra (i.e. the positions of maxima and
minima) should approximate the true spectra well enough to enable
unfolding to be carried out. Any errors induced in the unfolded
spectra should be small and confined to the upper energy groups.

The lower ends of the spectra found by the ANISN programme
also serve as theoretical spectra with which to compare the
unfolded experimental spectra. In the rest of this section, each
counter is discussed in turn.

Firstly the 2.5 atmosphere hydrogen filled counter is
discussed. The resonance materials used were lithium carbonate,
lithium fluoride and silicon carbide, and the neutrons were
produced by energetic protons bombarding a cobalt target. The
unfolded neutron spectra for these filters are shown in figure
3.24. The two spectra given for each material are the result
of converting the ionisation spectrum to a recoil proton spectrum
by two methods. The first assumed strict proportionality
between energy and ionisation with the helium-3 calibration

---

(1)   The unfolding code used was SPEC4 (see Appendix II).

energy equal to the Q-value of the reaction (764 keV); the second used the value of the helium-3 calibration energy and the energy-intercept E_O given in section 3.4. As can be seen, the first method results in an estimate of the magnitude of the neutron flux which is approximately 10% higher over the whole energy range than that of the second method. Furthermore, the first method leads to incorrect location of the troughs in the neutron spectra at approximately 50 and 100 keV due to resonances in fluorine, and at 440 1eV due to an oxygen-16 resonance.

The second method improves the fit between the measured and theoretical spectra, although the position of the minimum caused by the 440 keV oxygen-16 resonance still seems low. However, around 440 keV both the true neutron flux and the response function shape are highly dependent on energy, leading to possible errors in the unfolding process, as mentioned above in section 2.1. Similarly, the position of the minimum in the unfolded neutron spectrum due to a silicon resonance (at 195 keV) is improved by using the second method. However, the position of the lithium resonance at 258 keV is located correctly by both methods.

Summarising these results for the 2.5 atmosphere hydrogen filled counter, the position of the minima caused by resonances in the filter material below 300 keV are correct within experimental error when the parameters found in section 3.4 are used. However, the oxygen resonance at 440 keV still appears too low.

Secondly, the results for the 10 atmosphere hydrogen counter are discussed. The filter materials used were lithium carbonate and silicon carbide. The neutrons were produced by the bombardment of a thick lithium target by energetic protons. The unfolded spectra for these two filter materials are shown in figure 3.25. Again for each filter material there are two spectra, corresponding to whether the analysis used the strict proportionality assumption or the measured parameters given in section 3.4.

For both methods, the non-linearity of the energy-ionisation curve for the 10 atmosphere counter (see section 3.4) causes the troughs due to the lithium resonance at 258 keV and the silicon resonance at 195 keV to be incorrectly located. For the lithium carbonate filter the second method correctly locates the oxygen resonance at 440 keV whereas the first underestimates its location. However, the oxygen resonance at 1 MeV is poorly reproduced, both in shape and location, by both methods. For the silicon carbide filter, the resolution of the counter does not permit the silicon resonances between 500 and 600 keV to be fully resolved. Also the expected minima due to resonances in the region 800 to 1,000 keV are again poorly reproduced by both methods.

Finally, both methods produce similar estimates of the magnitude of the neutron flux. All in all, the second method correctly reproduces resonance detail in the mid-energy range of the counter, whilst both methods perform poorly at low and high energies.

Thirdly, the argon-hydrogen counter is discussed. Again just the lithium carbonate and silicon carbide filters were

used with this counter. 10 MeV protons were used to bombard a thick lithium target to produce neutrons. The unfolded spectra are shown in figure 3.26 and again there are two spectra for each filter material, one where strict proportionality is assumed and the other where the parameter values of section 3.4 are used.

With the lithium carbonate filter, one expects minima in the measured neutron flux at approximately 1.0, 1.31 and 1.66 MeV, all as a result of oxygen-16 resonances. Other oxygen and lithium resonances produce minima outside this counter's range. The first method of analysis (assuming strict proportionality) correctly locates the dip at 1.0 MeV within experimental error, but does not reproduce either of the other two dips. However, the second method correctly locates the minima at 1.0 and 1.66 MeV within experimental error.

For the silicon carbide filter, the predicted minima in the neutron flux are closely spaced and are poorly reproduced in the unfolded neutron spectra because of the argon-hydrogen counter's poor resolution. However, the more pronounced dip in the flux at 1.0 MeV is located more correctly by the second method than the first. For both the filters, the second method estimates the neutron flux to be approximately 10% higher than the first. Once again, the second method which uses the esti-mated parameters in preference to the assumption of strict proportionality predicts resonance structure more accurately.

To conclude, the above results using the resonance filter method illustrate the sensitivity of the magnitude and shape of the unfolded neutron flux to changes in the calibration parameters. Although the ADC backbias can be accurately determined, changes in the value of the energy intercept E_o, have significant effects on the total backbias and hence on the unfolded neutron flux. These effects are particularly important in the region of overlap between two counters and may lead to discrepancies in the unfolded spectra from each counter. Unfortunately a comparison of the magnitude of the flux in the region of overlap was not possible from these resonance filter measurements as they were not independently normalised.

This completes the treatment of counter calibration and the following chapter moves on to discuss the determination of neutron yields by the associated particle technique.

CHAPTER IV   THE ABSOLUTE NEUTRON YIELD

Introduction

In an ideal integral "bench mark" type of experiment to
compare measured and theoretical neutron spectra, several import-
ant criteria exist. They are that the neutron yield must be
determined accurately (better than a few percent), the geometry
of the assembly must be simple, i.e. only one type of material
present and any perturbation of the assembly must be small.
If these criteria are met it enables the measured neutron flux
to be directly compared with the calculated flux without the
need for arbitrary normalisation.

To simulate a fusion reaction the $T(d,n)^4He$ reaction is
used as a neutron source whose absolute neutron yield can be
measured by the associated particle technique. This technique
consists of measuring the number of alpha particles incident on a
detector placed at an angle $\emptyset_a$ to the incident deuteron direction
and subtending a solid angle $\Delta\Omega_a$ at the titanium tritide target.
The errors associated with this method are discussed in this
chapter. Particular emphasis is placed on the experimental
conditions expected where the third harmonic deuteron beam of
the Nuffield Cyclotron was to be degraded from approximately
2.2 MeV to approximately 150 keV and the alpha detector was at
an average angle of $\emptyset_a = 174^O$ from the direction of the incident
deuteron beam. Further details of the assembly are given in the
following chapter.

4.1 Theory of Neutron Yield from Associated Particles

The theoretical calculation of this section essentially follows that laid down by Benveniste and Zenger (1954). The total neutron yield from the $T(d,n)^4He$ reaction is shown to be the number of alphas observed multiplied by a conversion factor, CF, where

$$CF = \frac{4\pi}{\Delta\Omega_a} \cdot R(E_d, \emptyset_a) \qquad (4.1)$$

where $4\pi/\Delta\Omega_a$ is simply the geometric factor and $R(E_d, \emptyset_a)$ is called the anisotropic correction factor which is dependent upon the incident deuteron energy, E_d, and $\emptyset_a$, the angle of the alpha counter. This factor $R(E_d, \emptyset_a)$ can be derived by the following arguments.

Consider a parallel beam of N_d deuterons per second per unit area incident with energy E_d on a titanium tritide target containing N_t tritium atoms per unit volume. Upon entering the target a deuteron is continuously slowed down so that it has an energy range of 0 to E_d, the incident energy, in the target (providing the target is thick).

Consider a thin lamina in the target at a depth of x, of thickness dx and of unit area and suppose the deuteron has an energy E in this lamina. Thus, the number of neutrons per second per unit solid angle, dN, produced by reactions in this lamina is simply

$$dN = N_d N_t(x) \frac{d\sigma(E)}{d\omega} dx. \qquad (4.2)$$

$$= N_d \, N_t \, (x) \, \frac{d \, \sigma(E)}{d \, \omega} \quad . \quad \frac{1}{\left(\frac{dE}{dx} \right)} \quad . \quad dE \qquad (4.3)$$

where the assumption has been made that the number of incident deuterons does not change with the depth in the target. Here (dE/dx) is the rate of energy loss in the target material and $d \, \sigma(E)/d\omega$ is the angular differential cross-section.

In the following, the subscripts a and n refer to the alpha and neutron respectively, whilst primed letters refer to the centre of mass system and unprimed to the laboratory system.

In the centre of mass system let $N_n' \, (\theta_n', E) \, dE$ be the number of neutrons per second per solid angle produced at an angle of θ_n' as a result of deuterons of energies between E and E + dE, and similarly let $N_a' \, (\phi_a', E) \, dE$ be the number of alphas.

Hence using this notation and conserving the number of alphas between the centre of mass and laboratory systems, one obtains:

$$N_a \, (\phi_a, E) \, dE \quad d\omega_a = N_a' \, (\phi_a', E) \, dE \quad d\omega_a' \qquad (4.4)$$

and similarly

$$N_n \, (\theta_n, E) \, dE \quad d\omega_n = N_n' \, (\theta_n', E) \, dE \quad d\omega_n' \qquad (4.5)$$

where $d\omega'$ and $d\omega$ are the differential solid angles in the centre of mass and laboratory systems respectively.

For an alpha detector subtending a solid angle of $\Delta\Omega_a$ we have, therefore, that the number of alphas observed due to deuterons of energies between E and E + dE is:

$$\Delta\Omega_a \, N_a(\emptyset_a', \, E)dE \;=\; N_a' \, (\emptyset_a', \, E)dE \, \left(\frac{d\omega}{d\omega}\right)_a' \Delta\Omega_a \qquad (4.6)$$

and similarly for the number of neutrons:

$$\Delta\Omega_n \, N_n(\Theta_n', \, E)dE \;=\; N_n' \, (\Theta_n', \, E)dE \, \left(\frac{d\omega}{d\omega}\right)_n' \Delta\Omega_n \qquad (4.7)$$

Noting that the reaction is isotropic in the centre of mass system for small incident deuteron energies and employing the assumption that the incident deuterons are not scattered by the target nuclei, the following is obtained from expressions (4.3), (4.4) and (4.5)

$$N_n' \, (\Theta_n', \, E)dE = N_a' \, (\emptyset_a', \, E)dE = \frac{d\sigma'(E)}{d\omega'} \; \frac{dE}{\left(\frac{dE}{dx}\right)} \; N_t(x) \, N_d \qquad (4.8)$$

So combining expressions (4.6), (4.7) and (4.8) and integrating over all deuteron energies it is possible to obtain a conversion factor which is simply, from the previous definition, the ratio of the required neutron yield to the number of observed alpha particles:

$$CF \;=\; \frac{\Delta\Omega_n \displaystyle\int_o^{E_d} N_n \, (\Theta_n', \, E) \; dE}{\Delta\Omega_a \displaystyle\int_o^{E_d} N_a \, (\emptyset_a', \, E) \; dE}$$

$$= \frac{N_d \displaystyle\int_0^{E_d} N_t(x) \, \frac{d\sigma'(E)}{d\omega'} \left(\frac{1}{\frac{dE}{dx}}\right) \displaystyle\int_{\Delta\Omega_n} \left(\frac{d\omega'}{d\omega}\right)_n d\omega_n \, dE}{N_d \Delta\Omega_a \displaystyle\int_0^{E_d} N_t(x) \, \frac{d\sigma'(E)}{d\omega'} \cdot \frac{1}{\left(\frac{dE}{dx}\right)} \left(\frac{d\omega'}{d\omega}\right)_a dE} \qquad (4.9)$$

This simplifies to the following, if the total neutron yield is required (remembering that the reaction is isotropic in the centre of mass system for low deuteron energies, see Benveniste et al, 1960):

$$CF = \frac{4\pi}{\Delta\Omega_a} \cdot \frac{\displaystyle\int_0^{E_d} N_t(x) \, \frac{\sigma'(E)}{4\pi}\left(\frac{1}{\frac{dE}{dx}}\right) \cdot dE}{\displaystyle\int_0^{E_d} N_t(x) \, \frac{\sigma'(E)}{4\pi} \frac{1}{\left(\frac{dE}{dx}\right)} \left(\frac{d\omega'}{d\omega}\right)_a dE} \qquad (4.10)$$

Thus from expressions (4.10) and (4.1) and assuming the tritium concentration $N_t(x)$, is constant throughout the target, then:

$$R(E_d, \varnothing_a) = \frac{\displaystyle\int_0^{E_d} \sigma'(E) \left(\frac{1}{\frac{dE}{dx}}\right) dE}{\displaystyle\int_0^{E_d} \sigma'(E) \left(\frac{1}{\frac{dE}{dx}}\right)\left(\frac{d\omega'}{d\omega}\right)_a dE} \qquad (4.11)$$

The factor $\left(\dfrac{d\omega'}{d\omega}\right)_a$ is the rate of change of the centre of mass solid angle to the laboratory solid angle and is given by (see Fowler and Brolley 1956):

$$\left(\frac{d\omega'}{d\omega}\right)_a = \frac{E_a}{E_t (AB)^{\frac{1}{2}} (B/A - \sin^2\varnothing_a)^{\frac{1}{2}}} \qquad (4.12)$$

where:-

$$A = \frac{m_d \; m_a}{(m_n + m_a)^2} \cdot (1 - Q/E_t)$$ (4.13)

$$B = \frac{m_t \; m_n}{(m_n + m_a)^2} \left(\frac{m_a + m_n - m_d}{m_t} + \frac{m_d}{m_t} \; \frac{Q}{E_t} \right)$$ (4.14)

$$E_a = E_t A \left(\cos \phi_a + (B/A - \sin^2 \phi_a)^{\frac{1}{2}} \right)^2$$ (4.15)

and where m denotes the mass of the particle and subscripts d
and t refer to deuteron and tritium respectively.

Q is the reaction "Q" value and E_t = E + Q where E is the
deuteron energy in an interval.

To summarise, this section has developed an expression for
the anisotropic correction factor, (4.11). This expression can
be evaluated in experimental work in order to calculate the
total neutron yield. Since both $\sigma'(E)$, the centre of mass cross
section for the $T(d,n)^4$He reaction, and $^{dE}/_{dx}$, the rate of
energy loss, vary with energy the integrations required in (4.11)
for $R(E_d, \phi_a)$ were performed by a numerical summation method
on a computer. In the following section factors affecting
$R(E_d, \phi_a)$ the anisotropic correction factor are discussed.

4.2 Factors Affecting the Value of the Anistropic Correction Factor

Although the anisotropic correction factor may be computed
to a high degree of accuracy there exist several factors in the
input data which introduce uncertainty in the value computed.
These factors are discussed below.

Basic to the derivation of the anisotropic correction factor $R(E_d, \emptyset_a)$ (hereafter abbreviated to R) is the assumption that the reaction, $T(d,n)^4He$, is isotropic in the centre of mass co-ordinate system. However this is not so for deuteron energies greater than 200 keV (Benveniste et al 1960). This anisotropy obviously increases as the deuteron energy is increased. The numerator of the expression for the anisotropic correction factor is unaffected by anisotropy, as it represents the total neutron yield. On the other hand, as the denominator is angular dependent it will be affected. Benveniste et al (1960) have calculated that for 500 keV deuterons the observed anisotropy would affect the denominator by about 1% as the yield of alphas in the 300 - 500 1 eV range only accounts for one seventh of the total alpha yield. Also non-uniformity in the tritium loading of the target, as reported by Gunnerson et al (1960), and Perkins (1966) will decrease the effect of anisotropy.

In the denominator of expression (4.11) for R the term $(d\omega'/d\omega)_a$ is dependent on the deuteron-alpha detector angle $\emptyset_a$. The Rutherford scattering of the deuterons as they are slowed up in the target will clearly affect this term. Thus multiple scattering leads to a distribution of $\emptyset_a$'s about the alpha detector observation angle. Estimation of this effect leads to a correction of R of less than 0.1% for detectors at 90°, less than 0.5% for detectors at 135° and in the order of 1% for detectors at 174°.

Thirdly, errors in the cross section for the $T(d,n)^4He$ reaction and in the specific energy loss are in the order of 6 - 10%. Examination of expression (4.11) for R shows that just a

change in the magnitude of these will obviously have no effect on R, the anisotropic correction factor, as both the cross section and specific energy loss appear in the numerator as well as the denominator. However, if the energy shape of these quantities is altered (rather than just the magnitude) then R will be affected. Benveniste et al (1960) showed that a 50% change in the specific energy loss, dE/dx, in the sensitive region about the $T(d,n)^4He$ reaction's resonance gave only a 2% change in R. The specific energy loss, dE/dx, is also dependent upon the loading factor, which is the ratio of the number of tritium atoms to titanium atoms. The loading factor is normally poorly known, but fortunately it can be shown that a change in the loading factor from one to zero will only change dE/dx by 15% and hence give rise to a small change in R - less than 0.3%.

Fourthly, changes or uncertainty in the incident deuteron energy can give rise to uncertainty in R. The dependence of R upon E is illustrated in figure 4.1 for various angles. Clearly, the possible error in R increases as the observation angle is increased, but for an angle of 174° R changes only by approximately 5% as the incident energy changes from 100 to 200 keV. Further, if the probability distribution of the incident deuteron energy is known to be given by $P(E_d)$, then the average anisotropic correction factor may be found as:

$$\bar{R}_E = \int_{E_I} P(E_d) \ R(E_d, \phi_a) \ dE_d \qquad (4.16)$$

where E_I is the range of incident deuteron energies. For a symmetric deuteron energy distribution, $\bar{R}_E$ can be closely approximated by using the average deuteron energy in the formula for R.

For example, at an observation angle of 174° if the incident deuteron beam has a gaussian shape with 50 keV full width half maximum and a mean of 150 keV, then the expected value of R changes by 0.1% when compared with a monoenergetic incident deuteron beam at 150 keV.

Fifthly, uncertainties exist in the angle of observation due to poor definition of the alpha counter angle, the beam position and its radial density as well as the effects of the deuterons undergoing Rutherford scattering in the target. As illustrated in figure 4.2, R varies smoothly with the observation angle and a change of $\emptyset_a$ from 160° to 180° results in an increase in R of approximately 1.2% for a deuteron energy of 150 keV. Again, if the angular probability distribution is known and is $P^*(\emptyset_a)$, then an average anisotropic correction factor is given by:

$$\overline{R}_\emptyset = \int_\emptyset P^*(\emptyset_a) \cdot R(E_d, \emptyset_a) \, d\emptyset_a \qquad (4.17)$$

where $\emptyset$ is the range of the observed alpha angles. Again, for reasonable $P^*(\emptyset)_a$ distributions, a suitable estimate of $\overline{R}_\emptyset$ was found to be given by using the average $\emptyset_a$ value in the expression for R. It should be noted that generally errors in the angle of observation due to uncertainty in the definition of the mean alpha counter angle and beam position are small in comparison to those caused by Rutherford scattering in the target.

In most experimental situations uncertainties in both the incident deuteron energy and the observation angle occur simultaneously. Clearly the two probability distributions $P(E_d)$ and $P^*(\emptyset_a)$ are independent, so that the average anisotropic correction

factor due to both these effects is given by:

$$\bar{R}_{E\emptyset} = \int\limits_{E_I} \int\limits_{\emptyset} R(E_d, \emptyset_a) \; P(E_d) \; P^*(\emptyset_a) \; d\emptyset_a \; dE_d \qquad (4.18)$$

Finally, a non-uniform tritium distribution in the target will cause errors in the anisotropic correction factor. Non-uniformity arises due to several factors, such as outgassing from the surface causing a dead layer approximately 10 keV thick for 150 keV incident deuterons (Gunnersen et al, 1960). Also non-uniformity may be caused by the tritium being displaced by the deuterons (an effect lessened by the use of fresh targets), and by the diffusion of tritium into the copper backing.

To examine the surface concentration of tritium, auto-radiographs were taken of several titanium tritide targets and the results are shown in figure 4.3. Here the beta particles from the radioactive decay of tritium are detected in the film. Two of the targets examined had not been used on an accelerator and therefore had a relatively uniform surface concentration of tritium. The others had been used on various accelerators and they had surface blemishes which corresponded to the areas low in tritium as shown by the autoradiographs. However, this only examines the surface of the target due to the beta particles' low energy and hence very limited range. No measurements of the tritium concentration deep in the target were made although this method may be extended by chemically etching away a small layer of titanium tritide, taking a fresh auto-radiograph, and then repeating the process until the copper backing is exposed.

Alternatively, the tritium concentration may be measured as a function of depth, x, in the target. This has been done by Gunnersen et al, 1960 and by Perkins, 1966. If the tritium distribution is known then using expressions (4.10) and (4.1) the anisotropic correction factor for a non-uniform tritium distribution becomes:

$$R_t(E_d, \phi_a) = \frac{\int_0^{E_d} \left[\frac{N_t(x) . \sigma'(E) . dE}{\left(\frac{dE}{dx}\right)} \right]}{\int_0^{E_d} \frac{N_t(x) . \sigma'(E)}{\left(\frac{dE}{dx}\right)} . \left(\frac{d\omega'}{d\omega}\right)_a . dE} \qquad (4.19)$$

where $N_t(x)$ is the number of tritium atoms at depth x in the target, and x may be simply found by summation of $dE . \left(\frac{dE}{dx}\right)^{-1}$ when performing the integration numerically. If the tritium distribution measured by Perkins is compared with a uniform tritium loading then R is reduced by about 2% for 150 keV deuterons at 174°.

In conclusion, bearing in mind the experimental conditions where a degraded deuteron beam is to be used, then the greatest uncertainty in the anisotropic correction factor is caused by either the unknown tritium distribution or the errors associated with the final energy of a degraded deuteron beam. This implies that the degrader foil thickness must be accurately known and that the foil must be made of a material whose range-energy relationship is well known. Thus suitable materials for the degrader foil are aluminium, silver and gold.

In the next section, the geometric factor $\dfrac{4\pi}{\Delta\Omega_a}$ is discussed.

4.3 Calculation of the Geometric Factor

To compute the geometric factor the solid angle subtended by the alpha detector at the target, $\Delta\Omega_a$, is required. Factors affecting the estimation of $\Delta\Omega_a$ are discussed in this section.

Consider first the case of a point source and a simple counter geometry. It follows from the definition of the solid angle $\Omega = A/D^2$, where A is the area of the counter and D is its distance from the target, that:

$$\Delta\Omega_a = \frac{1}{D^2} \int_\emptyset 2\pi D^2 \; Sin \; \emptyset_a \; d\emptyset_a \qquad (4.20)$$

$$= \int_\emptyset 2\pi \; Sin \; \emptyset_a \; d\emptyset_a \qquad (4.21)$$

Here $\emptyset_a$ is the angle subtended by the detector at the target and $\emptyset$ is the range of $\emptyset_a$.

However this simple case is difficult to achieve in practice as one cannot focus the deuteron beam with a high degree of precision. The experimental situation (described in detail in chapter 5) is further complicated by the use of a foil to degrade the deuteron energy. Deuterons traversing this foil suffer nuclear collisions resulting in a considerable angular spread (about 20°) about the original deuteron beam direction. Thus in order to maximise the number of deuterons reaching the target the point source condition was relaxed so

that a finite source situation is encountered. A further
problem arose as a result of the unusual construction of the
alpha detector, designed to reduce perturbation to the measured
system (see section 5.2). In order to define the solid angle,
$\Delta\Omega_a$, the collimator of the detector consisted of a series of
holes in a ring perpendicular to the original deuteron beam.
Clearly, this further complicated the computation of the solid
angle required for the calculation of the geometric factor $(4\pi/\Delta\Omega_a)$.

Thus as there no longer exists a simple analytical expres-
sion for calculating the solid angle, a computer programme
derived from Williams (1966) was written to enable the solid
angle to be found. The programme simulates the isotropic
emission of particles uniformly situated on a disc representing
the tritium target; random numbers are used to give the point
of origin on the tritium target and the direction cosine. It
is then ascertained whether the particle passes through the
apertures defining the active area of the alpha detector. To
increase computing efficiency the particles were restricted
to the maximum solid angle of interest, defined by a circle
with radius equal to the sum of the source radius[1] and maxi-
mum detector radius at a distance equal to that between the
source and detector.

In this calculation of the solid angle, the emission of
alphas from the tritium target surface has been assumed to be
uniform i.e. independent of position on the target. Clearly,
the accuracy of this Monte Carlo calculation will suffer if

---

(1) The source radius on the tritium target was determined by
    the collimators which defined the degraded deuteron beam.

the emission density of the alphas is non-uniform and/or unknown. This emission intensity is dependent upon both the radial tritium distribution and the radial deuteron intensity on the target. The former effect has been discussed in the previous section. The latter effect, radial deuteron intensity, was studied by placing a plastic foil in the target position and observing the radiation damage caused by the degraded deuteron beam. This indicated that the radial deuteron beam intensity was uniform. Thus the assumption of uniform alpha emission from the tritium target is reasonable in this programme. However, if the above radial tritium and deuteron distributions were non-uniform and were known, they could be incorporated into the programme quite simply as a weighting to each particle.

The programme can be shown to calculate solid angles with an accuracy better than 1% for 10,000 particles tracked. To obtain this degree of accuracy in practice, however, it is necessary that the errors on all pertinent dimensions be less than 1%. In the configuration used with the lithium sphere the solid angle was only weakly dependent upon the tritium and deuteron distributions. However the difficulties in measuring certain dimensions associated with the counter geometry lead to an uncertainty in the estimate of the solid angle of approximately 7%.

An additional advantage of this programme is that it can be used to obtain the angular distribution of alphas which passed through the apertures defining the alpha detector's active surface; this is required in the calculation of the anisotropic correction factor. In the following section the effects of

competing neutron reactions are discussed and estimated where possible.

4.4   Competing Reactions

The previous sections have discussed the conversion factor to be used in the calculation of the neutron yield from the $T(d,n)^4He$ reaction. In fact, the neutron yield is calculated as the product of the conversion factor and the alpha count rate, as observed by the alpha detector.

However, competing reactions cause two major problems here. First, the total neutron yield may exceed that calculated above due to other reactions which also produce neutrons. Secondly, the calculated neutron yield may be over-estimated due to competing reactions which apparently increase the number of detected alphas.

The neutron producing reactions are discussed first. Here neutrons may be produced by either (d,n) reactions in the degrader foil and collimators, or by deuteron build-up on the collimators and target. The (d,n) reactions in the foil and collimators produce an insignificant number of neutrons because the high coulomb barrier results in the cross sections of these (d,n) reactions being small in comparison to that of the tritium reaction. Therefore these neutron producing reactions may be neglected and the most likely cause of a significant number of competing neutrons is the deuteron build-up.

Deuteron build-up is the commonly assigned term to the process where deuterium accumulates on the target and the

collimators defining the deuteron beam, and so becomes a secondary source of neutrons via the $D(d,n)^3He$ reaction. With regard to the collimators, this effect may be minimised by two actions. One is to conduct the experiment with the collimators hot, enabling the deuterium to diffuse away from the surface readily. Secondly, the collimators should be a material with a high diffusion coefficient, again encouraging the rapid diffusion of deuterium away from the surfaces.

Moreover, at low energies (less than 200 keV) the cross section of the $D(d,n)^3He$ reaction is approximately 100 times less than the cross section of the $T(d,n)^4He$ reaction. Thus using low deuteron energies will assist in minimising the effects of deuteron build-up on both the collimators and the target.

The deuteron build-up in the target may be monitored indirectly by observing protons from the $D(d,p)T$ reaction in the target. The alpha detector observes both these protons and the alphas from the $T(d,n)^4He$ reaction, but they may be distinguished by a detector with good resolution as their energies are significantly different. For example, at a deuteron energy of 150 KeV the alphas have an energy of 2.80 MeV while the protons have an energy of 2.62 MeV both at an angle of 180°. The number of protons can then be used to estimate the number of competing neutrons from deuteron build-up in the target via the relationships given by Ruby et al, 1963. Alternatively, a crude estimate of this may be obtained by multiplying the conversion factor for the $T(d,n)^4He$ reaction by the number of protons. Therefore it can be seen that the deuterium build-up in the target may be

readily monitored. However, the deuterium build-up on the collimators cannot be so readily monitored.

Now consider the second type of competing reaction where the number of alphas appears to be increased. For example, the $^{16}O(d,p)^{17}O$, $^3He(d,p)^4He$ and $D(d,p)T$ reactions produce protons of a similar energy to that of the alphas from the $T(d,n)^4He$ reaction. Thus these protons may be mistaken for alphas so increasing the apparent number of associated particles; hence the calculated neutron yield will be over-estimated. The cross section of the oxygen reaction is small and its effect on the neutron yield has been shown to be less than 0.02% by Robertson et al, 1966.

However the helium-3 and the $D(d,p)T$ reactions have a more significant effect. If the alpha detector has good resolution, the protons may be distinguished from the alphas (see Robertson et al) and hence the true neutron yield calculated. On the other hand, for a detector of poor resolution several workers have examined the effects of including the protons with the alphas. In a fresh tritium target the concentration of helium-3 is low but increases with time due to the radioactive decay of the tritium. A simple calculation shows that in a one year old target approximately 8% of the tritium has decayed to helium-3. Robertson et al, 1966, showed that for such a target at an incident deuteron energy of 400 keV, this helium-3 reaction could result in a 6% error in the neutron yield if the protons were included; whilst for a fresh target at an incident deuteron energy of 200 keV, the error is in the order of ½%. However, Fewell, 1967, disagreed with these calcualtions on the grounds that the reactions were assumed to take place at maximum

accelerator potential and that all the helium-3 was assumed to remain in the target. Thus Fewell estimated the error to be less than 0.3% for deuterons with energies less than 200 keV. However, he assumed a uniform tritium concentration in the target, but this is not supported by the experimental work of Gunnersen et al, 1960, or Perkins 1966 and so accounting for this would tend to increase his figure of 0.3%.

In conclusion, for competing neutron reactions the major contribution is from the $D(d,n)^3He$ reaction caused by deuteron bombardment of deuterium captured in the target and collimators. The effect of this reaction can be minimised by the use of low energy deuterons. The magnitude of the $D(d,n)^3He$ reaction in the target can be quantified by observing the protons from the $D(d,p)T$ reactions. The magnitude of the neutron yield from the collimators acting as secondary neutron sources is difficult to estimate but may be minimised by running the collimators hot. The effect of the second type of competing reaction where the number of alpha-particles is apparently increased may be considerably reduced by the use of fresh targets and of a good resolution alpha detector, to give an error of much less than ½% for incident deuterons of 200 keV.

In the next section the factors relating to the stability and estimation of the deuteron energy incident on the degrader foil are discussed.

4.5   Estimation of Deuteron Energy

In this section the reasons for estimation of the deuteron beam energy are discussed. In the experiment described in chapter 5, the deuteron beam from the cyclotron is degraded to approximately 150 KeV. However the Nuffield cyclotron accelerates particles to 10 MeV per nucleon so that deuterons are accelerated to 20 MeV. To degrade deuterons from this energy to 150 Kev accurately would be extremely difficult.

Fortunately, the cyclotron can be operated in the third harmonic mode enabling deuterons of about 2.2 MeV to be extracted instead of the normal 20 MeV. This is accomplished in a fixed frequency machine such as the Nuffield cyclotron by reducing the magnetic field to a third of its normal value. In this case the time for an orbit increases by a factor of three so that the deuteron spends $1\frac{1}{2}$ cycles of the cyclotron frequency inside the dee instead of the normal $\frac{1}{2}$ cycle.

However, the operation of the cyclotron in this mode has some undesirable side effects: the reduction of the magnetic field results in some loss in the vertical and radial focussing properties as well as a reduction in the number of orbits before extraction. These effects cause a decrease in phase stability, resulting in a greater energy spread in the extracted beam. Also, as the orbits are larger and less well defined than normal, extraction after a set number of orbits is difficult to achieve. The combination of these effects gives rise to an increase in the extracted beam energy spread and instability in the mean energy extracted.

Machine studies by Siekierkowski, 1975, using third harmonic deuterons indicate that over a 5 hour period there is approximately 100 keV variation in the beam energy. Also, from day to day the initial beam energy showed an even greater variation - in the order of 200 keV. In these machine studies, low beam intensities (a target current of a few nano amps) were used. This could have been a major factor in the instability of the beam energy as several sets of machine conditions may be found from which the required beam intensity may be extracted. On the other hand if high beam currents are desired then the mean energy may be much better defined as only one set of machine conditions may satisfy the high beam current required. From Siekierkowski's work it is clear that the final degraded deuteron energy must be determined and controlled.

In this work thin foil was used to degrade the deuteron energy to approximately 150 keV. To enable the final energy of the deuteron to be controlled the angle of the foil with respect to the direction of the incident beam was altered remotely. This changes the apparent thickness of the foil, thus changing the emerging deuteron's mean energy. The apparatus used in the control of the foil angle is described in chapter 5. The mean energy of deuterons leaving the foil was calculated from the range-energy tables of Williamson et al 1966. Simple calculations show that the foil thickness must be known to 1% to enable estimation of the energy of the emerging deuteron beam to an accuracy of 10 keV about 150 keV. For this reason aluminium was chosen for the foil material as its range-energy relationship is well known; further aluminium foil of high purity is easily obtainable in uniform thicknesses. Further calculations show that the angle

of the foil must be known to $\pm 0.25°$ and the incident energy

to $\pm$ 2.5 keV for a final emerging deuteron energy of 150 keV

$\pm$ 15 keV.

However, these calculations give no measure of the emerging

deuteron beam energy distribution. For small energy losses, Bohr

(1915) showed that the energy loss distribution is gaussian.

However, for greater energy losses Tschalär, 1964, has shown the

distribution to be symmetric and gaussian in form for energy losses

less than 50%. As the energy loss increases to greater than

50% the distribution becomes asymmetric. Landau, 1944, showed

that for large energy losses, as is the case here, the distribu-

tion is asymmetric with a low energy tail. However no attempt

was made to calculate the final deuteron energy distribution as

in this energy region (less than 2 MeV) charge pick-up and inner

shell corrections to the stopping power are important. (Note

that non-uniformity of the foil will broaden the final emerging

deuteron energy distribution but this effect is thought to be

small in comparison to the energy straggling.)

Provided that the final deuteron energy, as computed

from range-energy tables, is the true mean then the effect on

the anisotropic correction factor of this low energy tail will

be small. This was shown by assuming an asymmetrical distribution

whose effect was to lower the anisotropic conversion factor by

approximately 0.3%. The distribution had a mean deuteron energy

of 150 keV and the alpha detector was at an angle of 174°.

In conclusion, the incident deuterons mean energy and foil

angle must be known to $\pm$ 2.5 keV and $\pm$ 0.25° respectively if the

random error in the anisotropic correction factor due to these uncertainties is to be limited to $\pm$ 1%. In order to achieve this accuracy in practice the incident beam energy must be continuously monitored and the foil angle changed accordingly in order to maintain the calculated emerging deuteron energy at the desired value.

In the following section the overall accuracy of the conversion factor as defined by equation 4.1 is estimated.

4.6   Estimation of Total Error in the Conversion Factor

In this section the total error in the conversion factor of the associated particle technique is estimated. This factor is the product of the geometric and anisotropic correction factors which are defined in the first part of this chapter. In this estimation of the error the experimental configuration described in the next chapter is used. Summarising this config- uration, the third harmonic deuteron beam from the Nuffield cyclotron is degraded to approximately 150 keV and the alpha particles produced by the $T(d,n)^4He$ reaction, are detected by a silicon surface barrier detector at an angle of 174°. In order to find the uncertainty in the conversion factor due to inprecise knowledge of the degraded deuteron beam energy, the errors on the foil thickness and the initial energy of the third harmonic deuteron beam must be known. The former error was measured to be $\pm$ 1% and for the purposes of these calculations, the latter error was assumed to be $\pm$ 10 keV.

TABLE 4.1   Error in Conversion Factor

Cause of error	Resulting error in conversion factor
Scattering of deuterons in the target	$\pm$ 1%
Error in cross section and dE/dx data	$\pm$ 0.5%
Error in alpha detector angle	$\pm$ 0.1%
Finite deuteron energy distribution	$\pm$ 0.3%
Competing reactions (excluding deuterium build-up)	$\pm$ 1%
Error due to uncertainty in emerging deuteron energy	$\pm$ 3.5%
Error due to uncertainties in the solid angle calculation	$\pm$ 7%
Error due to non-uniform tritium loading	$\pm$ 1%
TOTAL ERROR	8%

In the calculation of the geometric factor the programme described in section 4.3 was used. The input parameters for this programme were related to the experimental configuration outlined in the next chapter. This showed that, as expected, one of the most important dimensions was the distance between the alpha source (the tritium target) and the defining apertures of the alpha detector. A 3% change in this resulted approximately in a 6% change in the solid angle. The radius of the deuteron beam on the target was a less critical dimension; a change from a point source to a 2 cm diameter source gave a 1% change in the solid angle. The overall error in the solid angle due to uncertainties in the pertinent dimensions was estimated to be in the order of 7%.

The various errors associated with the calculation of the anisotropic correction factor are given in table 4.1 for the experimental conditions stated above (150 keV deuteron energy and 174° angle), and the assumptions made in section 4.2.

As can be seen, the error in the mean deuteron energy and the solid angle are the dominant sources of error in the conversion factor. This excludes the uncertainty due to extra neutrons caused by deuterium build-up, as this proved difficult to calculate. However, if the solid angle was known accurately then the total error in the conversion factor from all remaining sources would be in the order of 4%.

In integral measurements it is desirable to measure neutron fluxes to within 4% and thus the absolute neutron yield in the assembly must be known to better than this. So the accuracy in the conversion factor implied here ($\pm$ 8%) shows the need for

external calibration of the conversion factor if cross section
data adjustment is desired on the basis of these neutron flux
measurements.

Whatever external calibration method is chosen the experi-
mental conditions and layout used on the cyclotron must be
reproduced as closely as possible; this requires matching the
energy of the primary beam, the foil thickness, the counter to
target geometry, and naturally, the target and holder themselves.
Further, the calibration method must be able to measure neutron
yields to within a few percent. If the calibration is carried
out at several primary incident beam energies the conversion
factors so measured may be checked against those calculated as
in sections 4.1 and 4.3. Furthermore, these measurements will
also indicate the extent of deuterium build-up.

Fortunately, within the Physics Department of the University
of Birmingham, there exists a continuous flow bath facility for
the absolute measurement of neutron sources. This facility has
been developed by Scott (1969), Atta (1972) and Scott and Campbell,
1975, and now provides a very rapid method for the absolute meas-
urement of neutron fluxes to within 2%. In this bath, the original
manganese solution has been replaced with vanadium sulphate as
the vanadium's half-life is considerably shorter than that of the
manganese, enabling many more measurements to be made during a
day. Measurements using the vanadium bath are presented in the
following chapter.

In conclusion, the errors associated with the anisotropic
correction factor and, to a greater extent, the geometric factor
lead to the need to calibrate the neutron yield from the titanium

tritide target. This neutron yield may be measured using the vanadium bath facility to within 2% enabling the yield calculations to be checked. This combined approach should finally result in acceptable estimates of the neutron yield.

This chapter completes the more theoretical aspects of the neutron yield determination. The following chapter turns to the experimental details and results. In particular, the lithium fluoride assembly and neutron flux measurements in the assembly are discussed.

CHAPTER V   LITHIUM FLUORIDE ASSEMBLY AND MEASUREMENTS

In the first part of this chapter the lithium fluoride assembly and the drift tubes associated with it are described. Then the measured neutron flux is compared with the neutron flux calculated by a one-dimensional transport code, ANISN.   Although the flux shapes show good agreement the absolute values differ. The reason for the discrepancy was found using a vanadium bath to measure the neutron yield absolutely and independently of the alpha detector.   This is described in the final section of the chapter.

5.1   The Lithium Fluoride Assembly

First it is useful to restate a few of the criteria for an integral "bench-mark" type of experiment.   They are that there should be only one type of material present so that the neutronic properties may be easily and accurately represented, and that any containment vessel employed should not perturb the system.   Further, the neutron source strength and energy spectrum should be known.   These enable one to assess any ambiguities between the experimental and calculated neutron fluxes.

The problems involved in the calculation of neutron fluxes are further eased where the material is arranged or contained in a spherical geometry and an isotropic neutron source is used.   As the neutrons from the $T(d,n)^4He$ reaction are emitted isotropically in the centre of mass system for incident deuterons of energies less than 200 keV it was decided to use a spherical geometric arrangement and degrade the deuteron energies to 200 keV or less.   At this energy, the yield per unit

solid angle is only 14% greater at 0° than at 180° - a factor

ignored in the transport code used (see section 5.4).

Having chosen the geometric arrangement and neutron source,

the material in which the neutron flux is to be measured may now

be decided.   Lithium fluoride was used in preference to lithium

or any other lithium compounds as it is chemically stable and not

hydroscopic, unlike most lithium compounds and lithium itself.

Furthermore, it was relatively cheap and readily available in

fairly large quantities.   Also the neutron cross-sections of

fluorine are fairly well known and, further, lithium fluoride

has been proposed as a possible constituent for the breeder

blanket of a fusion reactor.   As the lithium fluoride was only

available in powder form, some kind of hollow spherical

containment vessel had to be provided.

In order to decide the size of the system the mean-free

path for a 14 MeV neutron in lithium fluoride was first

calculated.   Simple experiments showed that the density of the

lithium fluoride could vary from 0.7 gm cm^{-3} to 1 gm cm^{-3}

depending upon how it was packed into the container, and this

gave the range of mean-free paths to be from 12.6 to 18 cm.   As

in any integral experiment, the size of the assembly must be such

that a neutron, on the average, should undergo several collisions

before being absorbed or escaping from the assembly.   This led

to the requirement that the hollow sphere have an internal

diameter of at least 1 m;   for financial and practical reasons

an internal diameter of 1.25 m was chosen.

Ideally the walls of the hollow container must be

infinitely thin, so that they will not perturb the neutron flux

by acting as a neutron reflector.   However, as this is clearly

impossible some compromise must be achieved. For financial and practicable reasons (such as the ease of future modification of ports), glass reinforced plastic (G.R.P.) was chosen as the construction material. The walls were made 6 mm thick which was more than adequate to hold the tonne of lithium fluoride; being G.R.P. the number density is low and hence there should be no undue perturbation of the neutron flux due to scattering from this wall.

Due to the limited width of the door into the irradiation cell at the Nuffield Cyclotron the hollow sphere had to be made in at least 2 pieces. However to ease the problems in construction the spherical shell[1] was made in four identical quarters and then assembled in situ. So that the sphere could be filled and emptied and measurements made, all the quarters except for one had a 10 cm port centrally. The odd port had a line of five ports as can be seen in figure 5.1. They were positioned so that from the centre of the sphere one port subtended an angle of $0°$, two were at $±45°$ and two were at $±80°$. All the quarters had a 5 cm flange along their edges to facilitate assembly. Prior to bolting the quarters together, a layer of 4 mm thick self-adhesive closed-cell neoprene was applied to one surface of each joint. This neoprene acted as a seal preventing the lithium fluoride leaking out.

The sphere was positioned so that there was a port top and bottom to facilitate filling and emptying. The remaining six ports lay in a horizontal plane. Two of the measurement

---

(1)   The G.R.P. shell was manufactured by Hickman and Lang Mouldings Limited, Rockery Street, Wednesfield, Staffordshire.

ports were blanked off.

In figure 5.1 one half of the hollow sphere is shown. Also shown in this photograph are the two stainless steel measurement tubes and the stainless steel neutron source tube. The measurement tubes are blind tubes of approximately the sphere radius in length, 5 cm in diameter, with a wall thickness of 0.025 cm. The wall thickness of the neutron source tube is again 0.025 cm but its length is a little greater than the diameter of the sphere and it is 7.6 cm in diameter. Into the ports of the sphere "plugs" were placed with holes the diameter of the tubes, to support the tubes and hold them in place. Once again closed-cell neoprene was used as a seal between the plug and sphere, also O-rings were used to seal the joint between the plug and tube.

As the neutron source tube was open at each end, measurements could be made at angles of 45°, 135°, 80° and 100° with just two measurement tubes by simply rotating the sphere through 180°, the measurement angles being with respect to the direction of the deuteron beam. Figure 5.2 is a horizontal cross-section of the sphere through its centre showing schematically the tube positions. The assembled sphere now in the irradiation cell was placed on its stand which performed the dual task of supporting the sphere and positioning it so that the neutron source tube in the sphere was at the correct height for the deuteron drift tube.

Once on its stand the sphere was loaded with 730 Kg of lithium fluoride. When the level of the lithium fluoride was approaching the top care was taken to prevent voids forming in the filling near the inner face of the sphere. From this

loading the average density of the lithium fluoride was
calculated to be 0.718 ± 0.005 gm cm^{-3} [1].

A sample of the lithium fluoride was analysed as a check
on the level of impurities present.   This was done by the
Centre for Materials Science at the University of Birmingham,
who also measured the abundances of the two lithium isotopes.
The mass-spectrometer results on the levels of impurity are given
in table 5.1 and the ratio of the quantities of the lithium
isotopes present was found to be the natural ratio within
experimental error.   From table 5.1 the upper bound on the
level of impurities is 1030 parts per million (0.1%) with iron
at 540 parts per million being the largest contaminant.

---

[1]   More recent measurements by Evans and Perkins on the same
lithium fluoride assembly have indicated that the density of the
lithium fluoride was non-uniform.   This factor was not appreciated
previously and the effects of it could be significant.

TABLE 5.1:   MASS SPECTROGRAPHIC ANALYSIS OF LITHIUM FLUORIDE

SAMPLE

Element	Impurity concentration (ppm atomic)	Element	Impurity concentration (ppm atomic)
U	<0.1	Ru	<0.5
Th	<0.1	Mo	<0.6
Bi	<0.1	Nb	<0.1
Pb	70	Zr	≤0.3
Tl	<0.2	Y	<0.1
Hg	<0.5	Sr	≤0.2
Au	<0.1	Rb	<0.2
Pt	<0.4	Br	<0.3
Ir	<0.2	Se	<0.3
Os	<0.4	As	≤0.1
Re	<0.2	Ge	<0.4
W	<0.5	Ga	<0.4
Ta	<0.1	Zn	3
Hf	<0.4	Cu	2
Lu	<0.1	Ni	2
Yb	<0.5	Co	1
Tm	<0.1	Fe	540
Er	<0.4	Mn	5
Ho	<0.1	Cr	2
Dy	<0.5	V	<0.1
Tb	<0.1	Ti	2
Gd	<0.6	Sc	<0.1
Eu	<0.3	Ca	15
Sm	<0.5	K	1
Nd	<0.5	Cl	6
Pr	<0.1	S	45
Ce	<0.1	P	1
La	<0.1	Si	160
Ba	≤0.2	Al	150
Cs	<0.1	Mg	4
I	<0.1	Na	5
Te	<0.4	F	Matrix

Element	Impurity concentration (ppm atomic)	Element	Impurity concentration (ppm atomic)
Sb	<0.3	O	
Sn	⩽0.4	N	
In	<0.2	C	
Cd	<0.5	B	⩽0.6
Ag	<0.3	Be	⩽1
Pd	<0.5	Li	Matrix
Rh	⩽0.5		

5.2   Drift Tube, Counter and Target Assemblies

Two target assemblies were constructed; one for use with the vanadium bath facility at the Birmingham Radiation Centre and the other for use with the lithium fluoride sphere on the Nuffield Cyclotron. The conversion factor (i.e. ratio of total neutron yield to detected alpha count rate) was measured using the vanadium bath facility with deuterons from the Dynamitron. In order to make these measurements applicable to the lithium fluoride assembly, both experiments employed the same distances between the foil, collimators and target, and between the alpha-detector and target (see section 4.6).

The differing requirements for the two target assemblies are now outlined. The first requirement is that the vanadium bath target assembly should fit inside the neutron source tube of the vanadium bath. This restricted the greatest diameter of this assembly to be less than 4.5 cm. On the lithium fluoride assembly this requirement is less exacting as the neutron source tube's diameter is 7.5 cm. The second requirement is that the lithium fluoride target assembly required provision for changing the degrader foil angle (with respect to the incident deuteron beam) so that the emerging deuteron energy could be controlled. The third requirement is the need to monitor the energy of the third harmonic deuteron beam from the Nuffield Cyclotron before it is degraded for reasons discussed in section 4.5. These latter two requirements are not necessary for the vanadium bath assembly as the energy of the deuterons from the Dynamitron can be measured to ±3 keV, and their energy may be smoothly varied from 750 keV to 3.0 MeV. This property of the Dynamitron

enables the conversion factor to be measured as a function of energy.

The vanadium bath target assembly is shown schematically in figure 5.3 and a photograph of the alpha detector and its assembly, the target and its holder, is given in figure 5.4. From figure 5.4 it can be seen that an alpha detector[1] of unusual shape is employed. The detector is a silicon surface barrier type with a resistivity of approximately *100* ohm m. ~~to increase its resistance to radiation damage caused by neutrons~~. Its special shape (an anulus) enables the deuteron beam to pass through it so that a very compact alpha detection system can be constructed. Thus the first requirement is met, and also the flux perturbation in the lithium fluoride sphere is minimised. The detector is housed in a PTFE sleeve as shown in figure 5.4. The two metal discs shown in figure 5.4 act as electrical contacts for the alpha detector; the one nearest the accelerator was earthed and acted as a collimator for the degraded deuteron beam, whilst the other, nearer the target, is the collector electrode, and also provides the defining apertures for the alphas from the target. These two discs sandwich the detector in the PTFE sleeve.

Thus, inside the main drift tube of the vanadium bath the degrader foil, its holder and the collimators are fitted and then the alpha detector assembly. Both the degrader foil assembly and alpha detector assembly are tight sliding fits in this drift

---

(1)   My thanks to Mrs. A. Chackett of the Nuclear Structure Group for manufacturing this counter.

tube, enabling them to be positioned accurately. The drift
tube is 3.1 cm in diameter, 0.75 m long with a 2 in. Dependex flange
one end and at the other end a flange (containing vacuum lead
throughs for electrical connections to the alpha detector) to
which the target holder may be bolted. Both the above assemblies
are placed a few centimeters from the latter flange which
provided a good reference point, so that the distance between the
foil and target and the distance between the counter and target
could be easily measured and then reproduced.

Secondly, the lithium fluoride target assembly (see
figure 5.5) employed the same main drift tube, alpha detector
assembly, target holder and target as the vanadium bath assembly.
However, on to the 2 in. Dependex flange of the main drift tube
a scattering chamber is attached, in order to measure the
initial deuteron beam energy. In this chamber a few of the
deuterons in the beam are scattered by a tungsten wire (0.02 cm
in diameter) into a silicon surface barrier detector. Tungsten
was chosen in order to minimise the correction for the recoil
energy.

The second difference between the lithium fluoride and
vanadium bath assemblies was that in the lithium fluoride
assembly two further sections were added between the flange
containing the vacuum lead throughs on the main drift tube and
target assembly. The section nearer the accelerator contained
the rotating foil and collimators, and the other section housed
the alpha detector in the same geometric arrangement as the
vanadium bath assembly.

The foil was rotated by a shaft which passed through the
chamber wall (see figure 5.5) and was sealed by two well greased

O-rings. This shaft was driven by a toothed rubber belt which was itself driven by a stepping motor through a gear box. The motor gave 48 steps per revolution and the gear box gave 100:3 reduction, so that it took 1,600 steps of the motor for a complete 360° rotation of the foil. The stepping motor was controlled by an integrated circuit[1] to which logic signals could be fed controlling the direction of rotation and whether or not the motor rotated. The logic signals for this integrated circuit were generated by a purpose built four decade reversible scalar. A switch on the scalar controlled both the direction of rotation as well as the direction of counting. The scalar was also provided with a push button giving either a single pulse or, if held for long enough a series of pulses, to step the motor around (one pulse per step). These pulses were used to either increase or decrease the scalar reading, depending on which direction the motor was rotating.

Thus the scalar provided both a control unit for the stepping motor and a digital readout of the position of the foil. Once a reference angle was defined the angular position of the foil was known to ± 0.225° and could be altered remotely. However, back-lash in the gearbox necessitated the foil always being brought to rest in the same direction, otherwise an error of approximately 3° could result.

The collimators in the foil section were used to define a geometric area 1.3 cm in diameter on the tritium target. The

---

(1)   The motor and integrated circuit were supplied by McLennan Engineering Limited, Kings Road, Crowthorne, Berkshire.

collimators were made from molybdenum, a refractory metal, so that they could be run hot without fear of melting. The rationale behind running the collimators hot was that any deuterium on the surface would then readily diffuse from the surface into the bulk of the material or vacuum chamber so limiting the deuterium build-up effect.

However, running the collimators hot caused problems, as some of the heat was conducted to, or absorbed by, the alpha detector, so increasing its leakage current to an unacceptable level after only a few hours of beam. This increase in leakage current caused a deterioration in the counter resolution and a decrease in pulse height for a given energy event. This problem was overcome by directing a cooled air blast over the drift tube in the vicinity of the alpha detector.

These collimators and degrader foil limited the current transmitted to the target to approximately 15 nA for 6 µA incident on the collimators and foil of the lithium fluoride assembly. This transmission ratio was improved slightly on the vanadium bath assembly due to the Dynamitron's better focussing properties.

5.3   Experimental Procedure

Prior to a neutron flux measurement in the lithium fluoride assembly the thickness of the aluminium degrader foil was measured.   This thickness is required so that the emerging deuteron energy may be estimated.   The foil thickness was found by accurately weighing a measured area and by measuring the energy loss of alpha particles traversing the foil and transforming this energy loss to foil thickness by using the range-energy tables of Williamson et al, 1966.   This enabled average foil thicknesses to be measured to an accuracy of ± 1.5%.

The foil was then clamped to its holder and bolted to the rotating shaft (see figure 5.5).   Next the angular position of the foil was adjusted so that it was perpendicular to the direction of the third harmonic deuteron beam.   This angular position was obtained by measuring the depth of either side of the foil holder from a surface at 90° to the incident beam.   By careful measurement the zero degree angular position of the foil holder was found within one motor step (corresponding to angular uncertainty of $\pm 0.225^{\circ}$) and the reversible scalar was set to zero.   If during this setting up procedure or during the flux measurement the direction of the stepping motor was reversed then the back-lash in the gearbox was taken up.   Periodically, during a series of runs the foil was inspected for damage, buckling or carbon deposits and was replaced if the condition warranted it.

The target system alignment before spectrum measurements proved troublesome, as the degrader foil rendered direct methods of observation of the deuteron beam by scintillator material or other methods difficult.   Thus the target was aligned by the more tedious method where the drift tube was moved until the

currents in the steering coils and on the collimators were minimised for a given target current. For ease of alignment, this took place with the target assembly outside the lithium fluoride sphere. Once the target was aligned, the sphere was positioned so that the tritium target was at the centre of the sphere (within ± 0.3 cm). The currents in the steering coils and on the collimators before the positioning of the sphere were noted and then compared to the currents for maximum target current afterwards to check that the target had not accidentally been knocked out of alignment. If the target assembly was misaligned then this procedure (minimising steering and collimator currents for a given target current) was repeated. See figure 5.6 where the drift tube is shown before entering the sphere.

The power and high voltage supplies for the detectors were allowed to warm-up for approximately 12 hours before use. This reduced gain changes as a result of temperature changes and enabled a check to be made for spurious pulses caused by high voltage breakdown on the insulator surfaces in the proportional counter.

Prior to a spectrum measurement the total gain of the proportional counter was measured using the He-3 calibration method. The surface barrier detectors were calibrated using bismuth 212 sources. Further, a precision pulser was used to establish the A.D.C. back bias and electronic gain changes, if made, for all the detectors.

Once this stage was reached the position for the flux measurement was chosen and the counter, along with appropriate lithium fluoride filler blocks were placed in the measurement tube. These blocks were used to position the counter in the

tube and to fill any voids around it. The remaining tubes were also filled with filler blocks to reduce the perturbation of the system.

Just before a flux measurement the third harmonic deuteron beam energy was estimated and the angular position of the foil changed in order to ensure that the mean degraded deuteron energy was 200 keV. The alpha and proportional counters were then started simultaneously and the time noted. Periodically during a run the deuteron energy was measured and the foil angle changed if required to maintain the degraded deuterons at the energy of 200 keV. So that changes in the deuteron energies were minimised during a run, the operators were asked to keep a constant target current by changing the machine parameters and as a last resort changing the current in the analyser magnet. The count rates in the alpha and neutron detectors were in the region of 2 KHz to 3 KHz. At the end of a run the dead time corrections were calculated for both counter systems; the correction factors were combined and used to adjust the neutron yield accordingly. Also, at the end of a run, a helium-3 and pulser calibration on the proportional counter was made, to ensure the A.D.C. back-bias and total gain had not changed by more than 1%. If a flux measurement was likely to exceed eight hours then a helium-3 and pulser calibration was carried out after approximately four hours.

The neutron yield was calculated from the number of associated alpha particles. An 'on-line' computer programme was written enabling a rapid determination of this number.

5.4 Computational Method

The distribution in space and energy of neutrons in the sphere may in principle be predicted by the neutron transport equation (often called the Boltzmann equation). However, the analytical solution proves intractable in most cases due to first the cross-section data required being often a complicated function of energy, and secondly the geometry of the materials being complex.

The transport equation (5.1) uses the fact that the rate of change of the number of particles in a system may be expressed as the difference between the production rate and the loss rate for an infinitesimal volume in space for neutrons at a particular velocity. The transport equation giving the angular neutron flux may be written as:

$$\frac{1}{V} \frac{\partial \Phi(r,\Omega,E,t)}{\partial t} + \Omega . \nabla \Phi(r,\Omega,E,t) + \Sigma_T(r,E).\Phi(r,\Omega,E,t)$$

$$= \iint_{E'\Omega} \Sigma_T(r,E^1) . f(r;\Omega^1,E^1 \rightarrow \Omega,E).\Phi(r,\Omega^1,E^1,t)d\Omega^1 dE^1$$

$$+ S(r,\Omega,E,t) \tag{5.1}$$

where symbols have their conventional meanings. A detailed and careful derivation of the linear transport equation (5.1) is given in Bell and Glasstone, 1970.

Considering a steady-state situation in a sphere whose material properties vary only as a function of the distance from the centre then Bell and Glasstone showed that the transport equation (5.1) may be rewritten as

$$\frac{\mu}{r^2} \frac{\partial[r^2 \Phi(r,\mu,E)]}{\partial r} + \frac{1}{r} \frac{\partial[(1-\mu^2)\Phi(r,\mu,E)]}{\partial \mu} + \Sigma_T(r,E).\Phi(r,\mu,E)$$

$$= \int_{E'} \int_{-1}^{+1} \Sigma_T(r,\mu^1,E^1).f(r;\mu^1,E^1 \rightarrow \mu,E).\Phi(r,\mu^1,E^1)d\mu^1 dE^1 + S(r,\mu,E)$$

$$\tag{5.2}$$

where μ is the directional cosine.

In this equation, time and some spatial variables have been eliminated.

However, equation (5.2) is still complicated and so the energy dependence is removed by dividing the energy interval of interest (0.01 eV to 15 MeV) into a finite number of intervals (or groups). In each group the cross section is assumed to be constant, i.e. an average over energy and therefore independent of energy. This is called the multi-group approximation. Integration of the transport equation (5.2) over a finite energy range, say $E_g < E < E_{g-1}$ leads to a complication as can be seen by considering the following. The angular neutron flux in the group g, may be defined as;

$$\Phi_g(r,\mu) = \int_{E_g}^{E_{g-1}} \Phi(r,\mu,E^1) dE^1 \tag{5.3}$$

Thus the term $\Sigma_T(r,E).\Phi(r,\mu,E)$ in equation (5.2) becomes $\Sigma_{Tg}(r,\mu)\Phi(r,\mu)$ where

$$\Sigma_{Tg}(r,\mu) = \frac{\int_{E_g}^{E_{g-1}} \Sigma_T(r,E)\Phi(r,\mu,E) dE}{\Phi_g(r,\mu)} \tag{5.4}$$

As can be seen, the group macroscopic cross section has now gained a dependence on μ but this complication may often be avoided either by assuming a form for the angular dependence of the neutron flux or by assuming that within an energy group the dependence of Φ on E is separable from r and μ.

One method of solving the resulting transport equation (5.2) is to represent the angular neutron flux as a sum of Legendre polynomials; and then apply the multigroup approximation: a method known as the Pn method. This method is described fully in Bell and Glasstone. However, for this work the transport equation was solved by a different method, known as the discrete ordinate, or discrete Sn, method. In this, the

transport equation is solved in a discrete set of directions only; angular integrals are then approximated by sums, and angular derivatives by differences. Next, the multigroup approximation is used and a discrete mesh is imposed on the spatial co-ordinate. However, there now exist problems arising from (1) the choice of the meshes, (2) approximations of the integrals over μ and (3) approximation of the differentials with respect to μ. Also the solution obtained by this method is dependent upon the choice of meshes and the approximations chosen. The virtue of it is, however, that the accuracy may be improved by increasing the number of directions and decreasing the spatial mesh size - the only limitation being the computer size and speed. An excellent review of the discrete ordinate method is given by Lathrop, 1972.

There already exist several computer codes (see Lathrop, 1972) which solve the linear neutron transport equation by the discrete ordinate method. From the codes available, ANISN (a one-dimensional transport code with anisotropic scattering) was chosen as it is readily available, is flexibly dimensioned and the scattering data may be represented by a high order Legendre polynomial expansion enabling accurate approximations to be made. This latter capability is useful as elastic scattering from light elements, such as lithium, is anisotropic in the laboratory system - the degree of anisotropy increasing at high energies. This code can output the angular flux at a spatial mesh-point or, by integration of the flux over 4π steradians, the total scalar flux which in this case is the quantity of interest. The code is described fully by Engle, 1967 and Price, 1974.

The multigroup constants for use in ANISN were condensed from the American ENDF/B-III nuclear data library. This library contains basic differential data for elastic, inelastic, capture, fission and other reaction cross-sections for many nuclei and a description of this library is given by Honeck, 1967. To process ENDF/B-III data into multigroup format the code SUPERTOG-III (Wright et al, 1969) was used. In SUPERTOG-III the multigroup cross-section constants are obtained by weighting the cross-sections by a function P(E) and integrating over a group as shown in the equation below:

$$\sigma_g = \frac{\int_{E_g}^{E_{g-1}} \sigma(E)\ P(E)\,dE}{\int_{E_g}^{E_{g-1}} P(E)\,dE} \tag{5.5}$$

Here the angular dependence of the neutron flux has been assumed separable from the energy dependence. The weighting used in this case was 1/E below 0.067 MeV which was smoothly joined to a fission spectrum above this energy. Further, where resonance data is included, the infinite dilution approximation is used. The choice of the appropriate weighting function is a central problem and a source of uncertainty.

This code SUPERTOG-III produces a library of multigroup constants in 100 energy groups (GAM-III format) ranging from thermal energies to 14.9 MeV with P-8 expansions of the scattering kernels. These constants are then used by ANISN to predict the total neutron flux.

With this code there are several sources of inaccuracies in the prediction of the neutron flux. First an error may be caused by an inappropriate choice of mesh sizes - this can be

easily checked by simply changing the mesh sizes. Further
sources of inaccuracy are errors in the multigroup constants
arising from poor choice of weighting in equation (5.5) and
errors in the differential data. Another source of error in the
predicted neutron flux may arise from approximations made about
the geometry of the assembly, in order that the code ANISN may be
used. An example of this in the lithium fluoride assembly is
the representation of the neutron source (the tritium target) as
a sphere, whereas in fact it is a disc. Further approximations
are introduced by ignoring voids caused by the drift tube and
also ignoring perturbations caused by the presence of the counter
and its associated electronics.

The predicted neutron fluxes presented in the following
section will be further in error as the neutron source is
assumed to be isotropic in the laboratory system and as neutrons
are assumed to be emitted with the average energy of the top
energy group. In reality, the neutron energy from a tritium
target is a complicated function of deuteron energy, stopping
power, and the angle of observation (see Benveniste and Zenger,
1954). For example, at zero degrees with respect to the
incident deuteron of 300 keV the neutron energy may vary from
14.1 MeV to 15.8 MeV depending on the stopping power. The
error due to these assumptions is obviously greatest in the high
energy regions and is probably small in the energy region of the
neutron flux measurements made by these counters. Finally, a
part of the discrepancy between the predicted and observed fluxes
may be due to the assumption that the lithium fluoride density
was uniform. Measurements made later by Evans and Perkins 1976 have
shown that this assumption is invalid.

5.5   Lithium Fluoride Measurements

The energy variation of the third harmonic deuteron beam
from the Nuffield Cyclotron is discussed here.   The energy of
this deuteron beam before it was degraded was measured by
scattering a small fraction of the beam into a surface barrier
detector.   The energy calibration of this detector was made by
using the two alpha energies (8.785 MeV and 6.062 MeV) from a
bismuth 212 source and assuming first that ω was constant for
deuterons and alphas over the energy range of interest, secondly
that there was no difference in the W values for a deuteron and
an alpha of the same energy, and thirdly that the window or dead
layer of the counter was small.   This calibration procedure led
to a random error of ± 10 KeV between measurements and possibly
a systematic error for all the measurements due to the above
assumptions.

The primary deuteron beam was scattered into the surface
barrier detector by a tungsten wire and the calculated and
experimental scattered deuteron spectra are compared in figure
5.7.   The trapezoidal shape of these scattered spectra is a
result of the wire diameter (0.02 cm) being large in comparison
to the range of a 2.5 MeV deuteron in tungsten.   The calculated
scattered deuteron spectrum was derived by calculating all the
possible path lengths through the wire to the detector and
weighting each possible path length with the probability of that
nuclear scattering occurring.   It was assumed that there was a
uniform flux of deuterons incident on the wire, and that the
simple Rutherford cross-section was applicable.   The path
length probability distribution was transformed into the energy
distribution of the scattered deuterons by using the range-energy

data tabulated by Williamson et al, 1966. From this calculation it was decided to use the mid-point of the knee of the observed trapezoidal spectrum as a measure of the maximum energy of the scattered deuteron. This energy was then corrected for the energy loss to the recoil tungsten nuclei to give the energy of the third harmonic beam.

During a flux measurement the deuteron energy was measured at approximately fifteen minute intervals, and the means of these measurements are shown graphically in figure 5.8. Also shown are the extremes of the deuteron energy variation during a flux measurement (run). As can be seen the means varied from 2.35 to 2.18 MeV. The average deviation about the mean deuteron energy during a run was ± 20 keV, the worst being ± 51 keV and the best being ± 9 keV. In figure 5.9 the deuteron energy as a function of time is given for three runs: one with the greatest energy deviation and two normal runs. The deviations observed here are smaller than those observed by Siekierkowski, 1975, probably due to the fact that in our measurements larger beam currents were required than those used by Siekierkowski. Hence there were fewer stable machine conditions which gave rise to the required beam current.

Experimental neutron fluxes were measured in the lithium fluoride sphere at distances of 27 cm and 37 cm from the centre. Measurements were made at an angle of 0° with respect to the incident deuteron direction and each of the three counters calibrated in chapter III was used in turn. Their energy ranges are discussed in the following chapter but the upper energy limit of the hydrogen—argon counter was limited to approximately 2.5 MeV. (2.466 MeV was actually used, as this corresponded

to a multigroup energy boundary).   The lower energy limit of the
measurements presented here is governed partly by the effect of
gamma rays on the 2.5 Atm. counter, resulting in an increase in
the measured neutron flux below approximately 65 keV;   also the
energy-ionisation relationship is not known below 50 keV.   The
results from the counter measurements are presented in figures
5.10 and 5.11, where the calculated fluxes are also shown for
comparison.

Upon unfolding it was clear that the neutron fluxes which
each counter predicted in the overlapping regions were in greater
disagreement than expected.   This disagreement is thought to be
due to deuterium building up on the collimator surfaces which
then acted as secondary neutron sources;   we noted earlier that
the collimators could not be allowed to heat up as planned
because of the effect on the semiconductor detector.   This
secondary source would not be constant over time so that the
product of the conversion factor and the number of alpha
particles could not hope to give the correct source strength.
Thus this incorrect prediction would obviously lead to errors in
the overlapping region between different counters.   The extent
of the deuterium build-up is estimated in the following section
where the absolute conversion factor is also measured.

In order to compare the shape of the measured neutron
spectra with the calculated (or theoretical) spectra the
estimated spectra were normalised to the calculated ones.   The
neutron spectrum predicted from the recoil data of the hydrogen-
argon counter was normalised to the theoretical spectrum by
equating areas in the energy region 1.0 to 1.5 MeV.   Similarly,
the energy region 0.8 to 1.0 MeV was used to normalise the 10

atmosphere hydrogen counter, and 303 to 365 keV for the 2.5 atmosphere hydrogen counter. This latter energy region was chosen here as both the flux and response function shapes were not changing rapidly.

As can be seen from figures 5.10 and 5.11, the resonance dips due to the fluorine resonances at 100 and 775 keV and the lithium resonance at 250 keV are correctly located. However, the resonance structure in the unfolded flux due to the fluorine resonance at 1.27 MeV appears to be a group too low, indicating an error in the estimated parameters found from the measured energy-ionisation relationship of the hydrogen-argon counter. The error in the predicted flux position is outside that expected from the errors on the parameters. However, this error could have resulted from a systematic error in the calculation of the mean neutron energy used to find the energy-ionisation relationship (see chapters II and III), but this is thought to be unlikely as in the region of overlap between data obtained from the use of the $^7Li(p,n)^7Be$ and $T(p,n)^3He$ reactions there was no indication of such a shift. Another possibility was that this energy-ionisation relationship might change with time, due to electronegative gas being released from the internal surfaces of the counter, but the resolution of the counter (a good measure of impurity levels) remained unchanged during this period.

The unfolded flux above 1.65 MeV and below 90 keV was less than the theoretical flux (the discrepancy being greater for measurements made at 37 cm). This decrease in flux above 1.65 MeV is hardly surprising if there is a significant number of neutrons from the secondary source. However, the

discrepancy between the two fluxes below 90 KeV is more surprising as one would expect secondary neutrons to increase the neutron flux in the low energy groups as their source energy is less. Further the unfolded flux in the energy range 400 to 700 keV appears to be high. It should be noted that the error in the measured neutron flux due to an incorrect input of neutron flux above E_{MAX} into the unfolding programme is small for all groups except those in the vicinity of E_{MAX}.

Measurements were also made in order to estimate the degree of anisotropy, the effects of voids around the counter and so on, but they proved unreliable due to the effect of the secondary neutron source which varied with time. This strength of the secondary neutron source is examined in the following section.

5.6   Vanadium Bath Measurements

Due to the uncertainties discussed in chapter IV in the
estimation of the analytical conversion factor (the ratio of the
total neutron yield to detected alpha particles), the vanadium
bath was used in an attempt to obtain an absolute conversion
factor.   However, owing to the discrepancies found in the flux
measurements described in the previous section its chief use was
to quantify the strength of the secondary neutron source.   First
the principles of the vanadium bath technique for determining
neutron yields are outlined.

The bath is a development of the continuous flow
manganese baths which are used for the absolute measurement of
neutron yields from either radio-isotopes or accelerator sources
(see Scott, 1969).   In this bath the original solution of
manganese sulphate was replaced by an acidic solution of
vanadyl sulphate because its half-life, 3.77 minutes, was shorter
than that of manganese, 2.58 hours.   This enabled more rapid
determination of the neutron yields as the time for the bath to
reach its peak activity or for the activity to decay is
considerably reduced.

The vanadium bath system is shown schematically in
figure 5.12.   The bath is a hollow G.R.P. sphere 86 cm in
diameter with a well shielded counting chamber about 8 m from the
sphere.   The neutron source is at the centre of the sphere.
Neutrons from this source are absorbed by the vanadium to form
vanadium-52 which later decays by β-emission, also emitting a
gamma ray.   The activity in the bath can be continually sampled
by passing some of the solution through the counting chamber
containing a sodium iodide detector (7.5 cm in diameter) where

the activity of the sample is measured.   The sample is then

returned to the bath.

So, assuming that the mixing is instantaneous in the

bath so that the sample pumped to the counting chamber represents

the average activity in the bath, the equation governing the

growth of activity in a continuously cycled system is:

$$\frac{dA(t)}{dt} = -\lambda.A(t) - \frac{c}{pV}.A(t) + \frac{c}{pV}e^{-\lambda p}.A(t-p)+f.S(t)$$

$$(5.6)$$

where: A(t)   is the total activity in the vanadium bath

V   is the volume of the bath

c   is the volume of the counting chamber and associated

pipe work

p   is the time taken to pump the active solution around

the counting loop

S(t)   is the neutron source strength

f   is the fraction of neutrons absorbed by the vanadium

and λ is the vanadium-52 decay constant.

The derivation of this equation also assumes that there is no

mixing in the counting chamber or in the pipework leading to it.

However, where the mixing time in the bath is non zero,

or not negligibly small when compared to $1/\lambda$, then the sample

pumped through the counting chamber will differ from the average

bath activity.   Thus, assuming that the sample activity

represents the average activity at a time, t-L, where L is the

mixing lag then equation (5.6) may be rewritten as:

$$\frac{dA(t)}{dt} = -\lambda.A(t) - \frac{c}{pV}.A(t-L) + \frac{c}{pV}.A(t-p-L).e^{-\lambda p} + f.S(t)$$

$$(5.7)$$

This equation may be solved numerically to find S(t) as described by Scott and Atta (1973).

At the present the vanadium bath facility is attached to the Birmingham Radiation Centre Dynamitron, and so it was planned to make use of the Dynamitron's well known and stable beam energy. The drift tube and alpha counter assembly for the vanadium bath experiment were described in section 5.2 and every care was taken to mock-up the cyclotron assembly as accurately as possible. Prior to conversion factor measurements, the vanadium bath was checked by using a standard source to find the calibration factor (the ratio of the number of gamma rays detected by the sodium iodide detector to the number of source neutrons). This was found to agree to within 1% with previous estimates. This factor may change if there is an airlock in the counter chamber, a leakage of vanadyl sulphate from the bath or a change in pumping speed, p, or mixing lag, L.

The conversion factor was measured for several incident deuteron energies and the results are shown in figure 5.13. The two separate curves correspond to the alpha detector being located at different distances from the target, the upper curve corresponding to the distance used on the lithium fluoride sphere flux measurements. At an energy of 2.35 MeV, the ratio of the conversion factors from the two curves was found to be 3.26, which equals the ratio of the solid angles (3.37) subtended to the target within the expected error. Where more than one measurement was made at a particular energy, the results were averaged. The values for the conversion factor take no account of the leakage of neutrons from the sphere or of oxygen and sulpher losses, all of which are energy dependent.

For a neutron source energy of 14 MeV, leakage is approximately 7% and other losses about 16%. However, for the range of neutron energies expected from the tritium target, the variation of these losses is considered to be small. From figure 5.13 it can be seen that as the deuteron energy decreases the conversion factor rises, a result contrary to that expected from the theoretical calculations in chapter IV (see figure 4.1).

The analytical conversion factors calculated by the methods given in chapter IV may be compared with those measured using the vanadium bath. Consider an incident deuteron energy of 2.35 MeV. As the aluminium foil is 33.7 μm thick, the degraded deuteron energy is 322 keV from the range-energy tables of Williamson et al, 1966. The anisotropic correction factor was calculated to be 1.28 and the solid angle the alpha detector subtented at the target was $(1.55 \pm 0.1) \, 10^{-2}$ steradians for the detector arrangement corresponding to the upper curve. This gave an analytical conversion factor of 1038 compared with a measured value of 2423. That is, apparently only 43% of the neutrons came from the $T(d,n)^4He$ reaction (provided that there is no large systematic error in the analytical conversion factor). This fraction falls to 15% as the deuteron energy from the machine falls to 2.25 MeV.

As discussed in chapter IV the error in the analytical correction factor was estimated to be ~4%. As mentioned, one of the largest unknowns in this estimation was the energy distribution of the degraded deuteron beam. This distribution is a function of energy straggling due to discrete energy losses whilst slowing down in the foil and of non-uniformity in the thickness of the foil. The first is difficult to quantify

because of charge exchange effects and inner shell corrections.
The second may be easily quantified if straggling is ignored.
For example, the degraded deuteron energy distributions for
deuterons of energies 2.35, 2.30 and 2.275 MeV incident on a
non-uniform foil of mean thickness 33.7 μm were calculated
neglecting energy straggling due to discrete losses.   The
results are shown in figure 5.14.   The path length probability
distribution for deuterons traversing the foil was assumed to be
triangular with a FWHM of 3 μm.   This 10% variation in foil
thickness was considered likely (see Sofield et al, 1976) bearing
in mind that the foil was rolled to this thickness.   As can be
seen, the distributions are asymmetric with a low energy tail.
The mean energies of these distributions (with the exception of
the 2.35 MeV case) were greater than the means calculated
assuming a uniform foil of thickness 33.7 μm.   The difference
in the means was greater for incident deuterons of lower energies.

It is thought that energy straggling will cause a
variation in the degraded energy of a magnitude similar to that
caused by a non-uniform foil (see also section 4.5). Thus, the final
degraded deuteron energy distribution could be even more skewed
as a result of energy straggling.

However, the effect of this skewed deuteron energy
distribution on the analytical conversion factor can be shown to
be small, if the mean of the distribution is known.   On the
other hand, if the mean used in the calculation of the conversion
factor is in error (due to straggling, a non-uniform foil or
inaccurate range-energy data), then there will be a resulting
error in the conversion factor.   For example, the conversion
factor decreases by 10% if the calculations are made using a
mean of 50 keV instead of 300 keV.   Thus, even a skewed degraded

deuteron energy distribution and errors in its mean will not give rise to large errors in the calculation of the analytical conversion factor.

Therefore, errors in the analytical conversion factor cannot explain the discrepancy between the measured and analytical conversion factors. As the analytical conversion factor and alpha count rate estimate the yield only from the tritium reaction, while the measured conversion factor is derived from the total neutron yield, there must be a secondary (or in this case primary) source of neutrons present to account for the discrepancy. These neutrons were thought to come from deuterium building up in the foil and collimators before the alpha detector assembly. Other secondary neutron sources such as $^{27}Al(d,n)^{28}Si$ are thought to be unlikely as their coulomb barriers are considerably higher, and hence their cross-sectionsare greatly reduced. Thus the upward trend in the experimental conversion curve as the incident deuteron energy decreases (see figure 5.13) is simply explained by a constant secondary neutron source and a decreasing alpha count rate. Any further work must reduce this secondary neutron source to a small percentage of the neutron yield from the $T(d,n)^{4}He$ reaction.

CHAPTER VI   COUNTER GASES AND FILLING TECHNIQUES

In this chapter the desired characteristics for counter gases are outlined and then the possible gas fillings are discussed. This is followed by a discussion of the factors affecting the energy range of a counter. Finally the counter filling rig and filling procedure is described. It should be noted that the counters used in the calibration and neutron flux measurements already described were filled using the rig outlined here.

6.1   Counter Gases

In this section the desired properties of a gas or gas mixture used in a recoil proton proportional counter are given. Then the advantages and disadvantages of suitable gases, hydrogen, methane or a binary gas mixture of an inert gas e.g. argon and hydrogen are discussed.

For any gas used in these counters it is desirable both that W, the average energy loss per ion pair is known and that ω, the specific energy loss per ion pair is constant over the energy range of interest. This enables the ionisation spectrum to be easily transformed to the recoil proton spectrum using the relationships given in section 2.1. All gases or mixtures used must contain hydrogen, and a high hydrogen content is preferred, as the efficiency of the counter is proportional to the number of hydrogen atoms contained in it. As electrons are to be collected the use of electronegative gases (gases with high electron affinities) in the counter is obviously not possible and, indeed even small traces of these gases are undesirable.

Finally, it is desirable that the gas or gas mixture chosen should have a high proton stopping power and a low electron stopping power but unfortunately these quantities are related positively.

The stopping powers and the pressure of the gases used in a counter govern that particular counter's energy range. Clearly the greater the stopping power for protons, the greater the upper energy limit of the counter, as higher energy recoil protons are stopped in the counter's active volume. The lower energy limit of the counter is governed by the maximum energy an electron can deposit in the counter and the use of high Z gases (or high Z materials in the walls of the counter) should be avoided. However, in order to measure a neutron spectrum over a particular energy region, some of these requirements may have to be relaxed.

The most obvious gas to use is hydrogen. Its advantages are that it is very easily purified by using a palladium barrier and its stopping power for electrons is low. The behaviour of W, the average energy loss per ion pair, has been discussed for protons in hydrogen in greater detail in chapter 2, but due to the lack of direct experimental measurements, W and ω have often been assumed constant. A disadvantage of hydrogen is that the electron drift velocities at the pressures used in these counters are small. Hence, the pulse rise time for a long ionisation track can be as long as 10 μs, necessitating the use of long amplifier time constants in order that the pulse height from the amplifier be independent of the pulse rise time. A further disadvantage is the low stopping power of hydrogen for protons, thus limiting the upper energy of a counter employing just hydrogen as its filling.

Methane has also been used as a gas filling. Its advantages are that its stopping power for protons is high, the hydrogen content (four atoms per molecule) is high and the electron drift velocities at the operating pressures are greater than those for hydrogen. However, methane suffers from several disadvantages. Firstly it is hard to purify to the degree necessary when high pressures (8 to 10 atmospheres) are required (see Kemshall 1973 or Bore 1973). Secondly, from energy ionisation relationships for this gas, ω has been shown to vary below the region of 200 keV. Finally, there exists the problem of heavy atom recoils which distort the ionisation spectrum and hence the final neutron spectrum. Unless account is taken of this effect (See Kemshall 1973 and Gold and Bennett 1968), it will lead to an over-estimation of the neutron fluxes especially at low energies. The magnitude of this effect is hard to quantify since it depends on the cross section for the recoil reaction and the neutron flux, as well as W and ω for the heavy recoil. It should be noted that W and ω are expected to be energy dependent as charge exchange effects and energy dissipated in elastic nuclear collisions are important for heavy recoil nuclei below 1 MeV.

Finally gas mixtures of hydrogen or methane with an inert gas such as argon may be used. Such gas mixtures have been used by Werle, 1972, who used various mixtures including methane and krypton, and Bore, 1973, who used an argon : hydrogen mixture. An advantage of using an inert gas is that it increases the stopping power of the gas mixture, so increasing the upper energy limit of the counter. A further advantage is that the electron drift velocities may be increased by a suitable choice

of inert gas, such as argon. However, the W and ω values are
not well known for protons in gas mixtures. Other disadvantages
of using inert gas mixtures are that the sensitivity of the counter
to gamma rays is increased, purification of the gas becomes a
problem and it is difficult to know for certain that the two
gases mix evenly prior to transfer to the counter. This leads
to uncertainty in the number of hydrogen atoms in the counter,
and so to uncertainty in the unfolded neutron flux. The question
of heavy recoil nuclei arises again here, but may not cause a
problem in this case because of the heavy atomic weight of the
inert gas. This can be seen by considering a neutron of energy
E_n. Then by energy and momentum conservation the maximum
energy, E_{RMAX}, of a heavy recoil is given by:-

$$E_{RMAX} = \beta \, E_n \tag{6.1}$$

$$\text{where} \qquad \beta = \frac{4A}{(A+1)^2} \tag{6.2}$$

and A is the mass number of the recoil nuclei. For example, β
for carbon recoils in methane equals 0.284 and for argon recoils
β equals 0.095. Clearly if β is sufficiently small, recoil
nuclei are no longer a problem.

In conclusion, hydrogen and a gas mixture of hydrogen and
argon were chosen to cover the energy range of interest. Methane
was not chosen because of the purification problems, non-linearity
in the energy-ionisation relationship and the problem of heavy
recoil nuclei.

6.2   Counter Energy Range

In this section the energy ranges and factors affecting these ranges are discussed for the counters used in the measurements already presented. Each counter has an energy range E_γ to E_{MAX} to which the counter is restricted unless special techniques are used. The lower energy limit, E_γ, is governed by the maximum energy knock-on electrons can deposit in the counter. This lower limit can be extended either by using rise-time discrimination (See Bennett 1967a and Taylor 1969) to distinguish between gamma and neutron induced events, or by reducing the stopping power of the gas filling. However, both these methods have their disadvantages: the first vastly increases the complexity of the experiment, whilst the latter method reduces the upper energy limit, E_{MAX}, of the counter.

The upper energy limit of each counter is governed by the degree of response function distortion and the unfolding technique. In this work a modified version of the computer code, SPEC 4, (Benjamin et al 1968a) was used to estimate the neutron flux from the proton recoil data. This unfolding technique was originally liable to oscillate when the correction factor (a parameter describing the distortion in the response function due to wall and end effects) became greater than 1.6. This corresponds to a value of the range over radius (r/a) parameter of 0.7. However, these oscillations were much reduced by Benjamin et al, 1968a by using the differential of the response function (instead of the response function itself) to carry out the unscambling process. Unfortunately, differentiation is a "noisy" process and as the correction factor increases very rapidly for r/a $>$ 2.0, the unfolding technique is limited to a region where the

correction factor is less than 2.0 for recoil data with poor
statistics and less than 2.5 where the recoil data statistical
accuracy is exceptionally good and also the neutron flux at
E_{MAX} is fairly flat. The unfolding code is discussed more
fully in appendix II.

As every counter has a limited energy range it was decided
to use three counters with different gas fillings to measure
the neutron flux in the lithium fluoride assembly from 20 KeV
to 2.5 MeV. The counter fillings were (1) 2.5 atmospheres of
hydrogen, (2) 10 atmospheres of hydrogen and (3) a hydrogen-
argon mixture containing approximately 2.25 atmospheres of
hydrogen and 8 atmospheres of argon. The use of more than one
counter reduces the need for rise time discrimination between
gamma and neutron induced events in the counter, as the counters
cover different but overlapping energy ranges. In table 6.1
the energy ranges of these counters are given. It should be noted
that the E_γ given here apply to the lithium fluoride assembly,
and will be different in other situations, where the neutron to
gamma ratio is different. Also E_{MAX} is given for several correc-
tion factors; if the statistical accuracy of the ionisation spec-
trum is poor, then the lower correction factors and E_{MAX} values
are applicable. In general E_{MAX} was chosen from the range in
table 6.1 so that the chosen value corresponded to a multigroup
boundary. This made the comparison of experimental and theoretical
spectra easier.

TABLE 6.1: ENERGY RANGES OF COUNTERS USED

Counter filling	E_γ (keV)	E_{MAX} (keV)	
		for correction factor of 2.0	for correction factor of 2.5
2.5 ATM Hydrogen	60	510	580
10 ATM Hydrogen	300[1]	1150	1310
2.27 ATM Hydrogen 8.03 ATM Argon	900	2510	2800

[1]   In the 10 ATM Hydrogen counter the lower energy limit, E_γ, is governed by non-linearity in the energy-ionisation relationship as found in section 3.4.

6.3   Counter Filling Rig

The rig used to fill counters in this work is similar to that described by Bore, 1973, but modifications have been made in order to improve the knowledge of the partial pressures of a binary gas mixture and to improve the purification of gases.

A schematic diagram of the filling rig is shown in figure 6.1. On the rig the original 1" oil diffusion pump was replaced with a 2" diffusion pump to improve the pumping speed. Further, the fore line trap using molecular sieve material type 3A[1] was supplemented by an activated alumina trap, as this type of trap is more effective for trapping vapour from the rotary pump oil. These traps were used to prevent contamination of the high vacuum system during roughing out. With the liquid nitrogen cold trap operating above the diffusion pump, and the rig at ambient temperatures, the complete system could be evacuated to 10^{-5} torr. Prior to their final assembly the individual components of the system were first cleaned by immersion in an acid bath, washed clean of acid by water and then ultrasonically cleaned. Finally they were rinsed successively with distilled water and acetone. (Solvents containing electronegative elements were avoided to prevent possible contamination of the system.) After the final rinse the components were baked in an oven at temperatures exceeding $100^{\circ}C$ to thoroughly dry them. After removal from the oven, they were assembled and pumped down as quickly as possible.

On the filling rig, different sections were connected using small bore copper pipes and brass junction boxes. Ordinary

---

(1) Supplied by BDH Chemicals Ltd, Poole, England (manufactured by Union Carbide)

nitrile rubber 'O' ring seals and diaphragms were used in the
½" and ¼" valves in the low vacuum section. However, in the
high pressure and high vacuum sections (see figure 6.1) the
nitrile 'O' ring seals and valve diaphragms were replaced with
viton in order to bake out the system at temperatures of $150^{\circ}C$.
Further, solid nuts were employed in the pressure section to
prevent leaks, by expansion of joints when the system was under
pressure.

To improve the knowledge of the partial pressures of a
binary gas mixture an 8" Burgeon standard test gauge (range
-15 to 200 psig) was employed in addition to the original 6"
Burgeon test gauge. The 8" gauge was used to calibrate the
6" test gauge, whose readings were found to be consistently
3 psi too high over the range from zero to 180 psig. With these
two gauges and a knowledge of the volumes involved, a counter
can be filled with a binary gas mixture to a wide range of
partial pressures; the partial pressures were measured to an
accuracy of $\pm$ 2%. This accuracy assumes that after opening the
valve separating the two gases and leaving the gases to mix for
approximately one hour, the gases mix perfectly i.e. any small
volume element contains the two gas molecules in the ratio of
the partial pressures.

A palladium barrier diffusion unit[1] was used to purify
hydrogen. Here only hydrogen - being a small atom - is able
to diffuse through the palladium silver alloy, which is electri-
cally heated to $300^{\circ}C$ to increase the diffusion rate. This
diffusion rate can be controlled by varying the temperature of

---

(1) Al Diffusion Unit manufactured by Johnson Matthey Ltd,
    81 Hatton Gardens, London EC1

the alloy and the pressure difference between the pure and impure sides. Bore, 1973, has shown that hydrogen purity obtainable from this device is adequate for the hydrogen counter fillings used, and so the only modification to the hydrogen purification process was to replace the purging gas, commercial nitrogen, on the impure side of the diffusion barrier, with oxygen free nitrogen.

Due to the difficulties in purifying methane (see Kemshall, 1973 or Bore, 1973) it was decided to try and improve the gas purification technique. Unfortunately due to the molecular size of methane or argon the above diffusion method cannot be used, so that a completely different technique must be employed. It was decided to retain the use of the molecular sieve material as a purification agent because it has a very high affinity for water vapour, which is an expected contaminant always present as residual gas molecules in the vacuum system. However at room temperatures the molecular sieve material only has a small affinity for oxygen, another expected contaminant.

In order to try to remove oxygen from the filling gas a second purification agent is required. Gibbs et al, 1956, showed that copper turnings were an excellent oxygen getter, and so this material was chosen. In order to reduce the temperature requirement of $600^{\circ}C$ for copper, a BASF catalyst was chosen. The catalyst comprises of copper oxide on a diatomic earth. To use this catalyst the copper oxide must be first reduced to copper by passing hydrogen through it at approximately $100^{\circ}C$, when the following chemical reaction takes place:

$$CuO + H_2 \rightarrow Cu + H_2O$$

and the water vapour is removed by the gas stream.

Once reduced the catalyst may be used to remove oxygen from a gas. In this case the following chemical reaction occurs:

$$2Cu \; + \; O_2 \rightarrow 2CuO$$
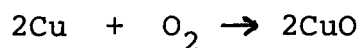
and the oxygen is chemically bound with the copper.

On the filling rig the gas purification is carried out in the horizontal storage section. The purifiers are contained in tubes connected to this section by valves. Prior to use the catalyst is heated with hydrogen for several days to ensure complete reduction of the copper oxide. Next, in order to release trapped gases both the catalyst and molecular sieve material are baked out at approximately $160^{\circ}C$ under vacuum until there is no appreciable outgassing from the purifier sections. To purify a gas the gas is kept in contact with both the catalyst, heated to $80^{\circ}C$, and the molecular sieve material at room temperature for approximately a day prior to filling a counter.

Helium-3, used for counter calibration, was stored in a stainless steel cylinder.[1] Before filling the cylinder with helium-3 it was partially filled with a mixture of molecular sieve and reduced BASF catalyst and baked out under vacuum for several days. This mixture ensured that the helium-3 once in the cylinder will be continuously purified of water vapour and oxygen. In this case oxygen would be removed very slowly and continuously as the catalyst is active at room temperature.

(1) Supplied by Hone Instruments

To summarise, hydrogen is purified by diffusion through palladium. For gases other than hydrogen, the electronegative impurities, i.e. water vapour and oxygen, are removed by a molecular sieve material and a BASF catalyst respectively. These two substances are expected to be present as both residual gas molecules in the filling rig and as contamination in the gases used to fill the counter. The effect of electronegative impurities is hard to quantify, but generally causes a worsening of resolution and a non-linearity in ω , the specific energy loss per ion pair, at low recoil proton energies.

6.4   Counter Filling Procedure

Before any counter fillings were made the rig (described in the previous section) and counter were first evacuated. Normally pure gas (hydrogen or argon-hydrogen mixture) was stored under pressure in the pressure sections of the rig between fillings of the counter to prevent contamination of the rig by electronegative impurities from the atmosphere leaking into the system. Once evacuated, the system and counter shell were baked out at approximately $150^{\circ}C$ until the pressure fell below 10^{-4} torr and there was no substantial outgassing or leakage. Once this stage was reached the rig and counter were left for at least a week before a counter filling was attempted to ensure outgassing was complete.

As the procedures are different for the counter fillings containing a gas mixture and those containing just hydrogen they are described separately. In both cases the rig is assumed to be at the above stage. The letters by the valves in figures 6.1 to 6.3 are used to describe the valves in the following

text. Where a section of the system is isolated, than all valves leading to that section are closed.

First the hydrogen counter's filling procedure is outlined referring to figure 6.2. Here, the hydrogen was purified by the palladium barrier diffusion unit. Approximately 24 hours prior to a gas filling the impure side of the palladium barrier was purged of air by oxygen-free nitrogen for 10 minutes, and then the temperature of the barrier was raised to 300°C. This nitrogen flow was continued until just before the counter was filled. The purpose of this procedure was not only to remove air from the impure side of the palladium, but also to remove oxygen from the pure side. At 300°C hydrogen remaining from previous fillings readily diffuses out of the palladium, and combines with the oxygen to form water vapour, which may then be pumped away.

Several hours before the counter was to be filled the heating tapes were switched off and the filling rig was allowed to cool to ambient temperatures. Once the rig was at ambient temperature, the palladium barrier was isolated from the rest of the rig and the nitrogen flow replaced by impure hydrogen at approximately 200 psig. After a few minutes the diffusion pump and cold trap were isolated and then the palladium barrier section was opened to the rest of the system, filling it with pure hydrogen. The palladium barrier section was again isolated and the rest of the system re-evacuated. This practice flushed out the system and coated all surfaces with pure hydrogen, so hopefully reducing the number of residual oxygen and water vapour molecules. Again the pressure in the palladium barrier section

was allowed to build up for approximately 3 minutes, whereupon
the 6" test gauge section was isolated from the rest of the
system and the valve, A, between the palladium barrier and this
section was opened, allowing pure hydrogen into the section.
This was judged so that as soon as this valve was opened the
pressure in the 6" gauge section rose above atmospheric pressure
minimising the possibility of an in-leakage of air.

Once the pressure in these two sections had risen to
approximately 50 psig, the horizontal storage and 8" gauge
section was isolated and the valve, B, between this section and
6" gauge section was opened. Again it was judged so that the
pressure in the three sections was above atmospheric pressure.

When the hydrogen pressure in these sections approached
the pressure to which the counter was to be filled the counter
and helium-3 sections were isolated. Next, helium-3 was released
from its storage cylinder, filling the counter to the desired
pressure (0.2 torr for the 2.5 atmosphere counter and 0.1 torr
for the 10 atmosphere counter). Once this was completed, the
valve, C, between these two sections was closed and the valve, D,
between the counter section and 8" gauge section was opened allow-
ing hydrogen into the counter. The hydrogen pressure was allowed
to rise to the desired value, whereupon the palladium barrier
was isolated from the rest of the system. The counter was then
sealed and the temperature of the counter shell and gas pressure
were noted. The system was left for a few minutes and these above
measurements re-taken to check for consistency. The counter was
then ready for testing.

The rig when operated in the above manner was consistently able to produce hydrogen fillings of good resolution (3.5% to 5% for the 2.5 atmosphere filling and 6% to 7% for the 10 atmosphere filling).

The filling procedure for the binary gas mixture was as follows. Before baking out the system in preparation for an argon-hydrogen counter filling, the BASF catalyst was reduced by heating it with hydrogen to approximately $150^{\circ}C$. The catalyst purifier was then evacuated and along with the rest of the system, including the molecular sieve purifier, baked out until there was no further outgassing. Once the rig was ready for a counter filling the heating tapes were switched off and the rig allowed to cool to ambient temperatures. 24 hours before a counter filling, the palladium barrier was prepared in the manner described above. At the same time, argon was bled into the horizontal storage section and purifiers to the required gas pressure. During this process, these sections and the 6" gauge and argon sections were isolated from the rest of the system. On completion the valves B (between the horizontal storage and 6" gauge sections) and E (between the 6" gauge and argon sections) were closed and the 6" gauge section re-evacuated. Heating tapes were then switched on for all sections except the argon, horizontal gauge and molecular sieve purifier sections.

The catalyst purifier section was raised to approximately $90^{\circ}C$ and the argon left to circulate through the catalyst and molecular sieve material (at room temperature) by natural convection for 16 hours. Finally, 8 hours before the counter was filled the molecular sieve purifier section was cooled. (The effects of cooling the molecular sieve material and heating the purifier to temperatures other than $90^{\circ}C$ are discussed later.)

Approximately half an hour before mixing hydrogen and argon the purifiers were isolated from the horizontal storage section and the gas allowed to reach ambient temperatures, whereupon its pressure was noted. During this period hydrogen was being emitted to the 6" gauge section, the process being similar to that outlined in the hydrogen counter filling procedure. When the hydrogen was at the required pressure the 6" gauge section was isolated from the palladium barrier section and the valve, B, (between the horizontal and 6" gauge sections) was opened, allowing the hydrogen and argon to mix. This mixture was left for approximately ¾ hour to ensure even mixing of hydrogen and argon.

At the end of this period the helium-3 was admitted to the counter and then finally the gas mixture was bled into the counter. The pressure and temperature of both hydrogen and argon prior to mixing and before and after filling the counter were noted, in order to calculate the partial pressures of the gas mixture.

The resolution of the argon-hydrogen counters was poor at 10% - 13% (full width half maximum of helium-3 peak) compared with the resolution of the 10 atmosphere hydrogen fillings, which was 6% - 7%. Various combinations of molecular sieve temperature and catalyst temperature were investigated in order to improve the counter's resolution. It was found that varying the molecular sieve purifier's temperature from room temperature to a "dry ice" temperature had little effect on the filled counter's resolution. This probably indicates that water vapour is not a significant contaminant. However, raising the temperature of the catalyst to increase the oxygen removal rate only

caused a decrease in the counter's resolution. This result could be caused by electronegative impurities being released from the catalyst due to the higher temperature (30°C less than the baking out temperature).

It was concluded that the resolution of the argon-hydrogen counter could not be significantly improved by simple manipulation of these temperature parameters. A more efficient gas purification system is required - possibly a dynamic purifying process with a small flow rate to ensure that the impurities are removed. In such a system the water vapour and pump oils could be removed by a trap of molecular sieve and activated alumina cooled to liquid nitrogen temperatures. The oxygen could be removed in a better designed reaction vessel by the same BASF catalyst or some other getter such as barium-titanium, employed by Miyajima et al 1976, to purify xeon which they later used in a liquid xeon proportional counter. Furthermore, the filling rig could be improved by the use of stainless steel tubes and junction boxes as well as decreasing the distance from the counter to the cold trap, in order to improve the pumping speed and thus reduce the ultimate pressure attainable and therefore decrease the number of residual gas molecules present in the counter.

Alternatively a UHV system as described by Goodings et al, 1971, could be constructed but despite the large increase in cost they experienced little improvement in counter resolution.

CHAPTER VII: CONCLUSIONS AND RECOMMENDATIONS FOR FUTURE WORK

The original objects of this work were to fill and calibrate a set of recoil proton proportional counters, to investigate any anomalies in the calibration characteristics, and to use the calibrated counters to measure the slowing down spectra in lithium fluoride for a simulated fusion neutron source. The measured spectra were then to be compared with the theoretical spectra in order to reveal discrepancies in the cross-section data used.   As this work naturally falls into two parts, first the calibration of the counters and secondly the flux measurement, they are discussed separately.

In the calibration of the counters it was shown theoretically that the assumption of constant W, the average energy loss per ion pair, was invalid especially at low ion energies (less than 50 1eV).   Later experimental measurements revealed that this was indeed so over the counter's energy range. These measurements also showed that the exact form of W(E) for the two hydrogen fillings were markedly different, indicating that electro-negative impurities were playing an important role.   The assumption of constant ω, the specific energy loss per ion pair, was shown to be correct for the 2.5 atmosphere hydrogen counter between 50 1eV and 620 1.eV and so the energy, E, and ionisation, I, could be related by the simple expression $E = \omega I + E_o$. However, for the 10 atmosphere counter ω was found to vary below 300 keV, so that the above simple relationship between energy and ionisation did not hold below 300 keV.   This factor limited the counter's energy range,   which could be increased only by making changes to the unfolding programmes to allow ω to vary.

However, to do this the E-I relationship needs to be measured more accurately below 300 keV, and so this idea was not pursued further.

With the hydrogen-argon counter, ω was found to be constant, so that the relationship $E = \omega I + E_o$ could be used. However, later examination of resonance dips in the unfolded neutron spectra indicated an inconsistency using the measured parameters E_o and Q_{eff} for the ^{3}He(n,p)T peak.

It should be noted that with all the three counters examined, the apparent energy, Q_{eff}, deposited in the counter by the calibration reaction ^{3}He(n,p)T was not 764 keV, the Q-value of the reaction. With the hydrogen counters Q_{eff} was found to be approximately 780 keV, the discrepancy being due to the difference in the W values for the triton and proton. With the hydrogen-argon counter, Q_{eff} was found to be less than 764 keV, principally due to electron capture by electronegative impurities.

In comparison, the response function measurements were closer to those predicted theoretically. For example, the different counter fillings had no appreciable effect on the response function shapes as long as comparisons were made at the same proton range over radius (r/a) value less than unity. The response function shapes have been shown to be sensitive to scattered neutrons and so great care must be taken not to include the effect of these. After eliminating these effects, the response of the counter can be entirely predicted by knowing the counter's finite size and electric field distortion at the ends of the anode wire. The response function shape for r/a values greater than unity were shown to become increasingly more sensitive to the energy spread of the neutron source, rendering the response function shape difficult to analyse. The increase

in proton ranges required by Broomfield et al, 1970 to force a
fit between the analytical and experimental response functions
may be attributed to this sensitivity to the neutron energy
distribution.   Thus, if the code SPEC4 is still to be used to
unfold neutron spectra, it should be modified to eliminate the
effects of the proton range correction factor.

The following conclusions may be drawn about counter
calibration.   The assumption of constant W over the energy range
of the counters is invalid and its behaviour is found to be
dependent upon the counter filling, indicating a higher
sensitivity than expected to electronegative impurities.   This
readily explains the wide variety of observed W values, and
positions of the resonance dips in unfolded neutron spectra as
reported by previous workers.   Further, non-constant W(E) and
the fact that Q_{eff} is different for different gas fillings imply
that the energy-ionisation relationship must be measured for each
counter prior to flux measurements.   The best available method
for counter calibration is to produce mono-energetic neutrons by
accelerating particles onto certain target nuclei.   The speed
and accuracy of this method may be improved by use of the heat
pipe assembly described in chapter III.

Two areas for further research immediately arise from
the previous discussion.   First, the sensitivity of counter
calibration to electronegative impurities should be investigated
in greater detail.   In this connection, it could prove
instructive to extend the work of Kemshall, 1973.   He added
known quantities of oxygen - an electronegative impurity - to a
counter and measured the deterioration in the resolution of the
He-3 peak.   Measuring the energy-ionisation relationship at the

same time would give valuable insight into the effect which electronegative impurities have on this relationship, and enable greater confidence to be placed in these counters.

Secondly, in order to make meaningful comparisons between experimental and analytical response functions for r/a values greater than unity, the neutron energy distribution should be taken into account. Thus, there is a need to calculate and measure the neutron energy distribution incident on the counter, including scattered neutrons.

Turning to consider the neutron flux measurements in the lithium fluoride assembly, it can be seen from the results given in chapter V that there is some disagreement between the absolute values of the measured and calculated neutron spectra. The discrepancy, which was too great to be attributed to the calculational method (ANISN), was attributed to a secondary neutron source possibly caused by deuterium build-up in the collimators and foil. However, on normalising the measured flux to the calculated one, shape discrepancies were found in the region of 1.3 MeV and 400 keV to 600 keV where the measured flux was higher than the calculated flux, and also below 80 keV where the measured flux was considerably lower. These discrepancies, especially the latter, cannot be attributed solely to the influence of the secondary neutron source and so further investigation is required. At low energies (less than 80 keV) the energy-ionisation relationship of the 2.5 Atm counter must be first measured. This is because below 50 keV, ω, the specific energy loss per ion pair, is expected to become increasingly non-constant due to both changes in the cross-sections of the collision processes involved and the

effects of electronegative impurities. The latter effect is probably dominant above 15 keV for this counter. The discrepancy in the resonance dip at 1.3 MeV can only be resolved by remeasurement of the energy-ionisation relationship for the argon-hydrogen counter.

In the calculational method itself, some approximations are made, especially with the source term. Some of the assumptions are that the neutron source is a uniform sphere, it is isotropic and its energy is represented by a single neutron in the energy group 13.5 MeV to 14.9 MeV. The first assumption concerning the geometry of the source is only poor for distances close to the source. The other two assumptions are obviously more important. In any experiment where the neutron source is tritium bombarded with deuterons, these assumptions are obviously invalid, the degree of approximation becoming larger as the deuteron energy increases. This is first because the reaction, although isotropic in the centre of mass system for bombarding energies of less than 200 keV, is anisotropic in the laboratory frame: the degree of anistropy is clearly dependent on the energy of the incident particle. Secondly, the tritium atoms react with deuterons which are being slowed down in the target, and so give rise to a range of neutron energies. This neutron energy spread extends for approximately an MeV about 15 MeV at zero degrees. In the particular case here, where the energy of the deuterons is degraded before entering the target, there is appreciable energy spread in the degraded deuteron energies due to foil irregularities and energy straggling, and so both the neutron energy spread and the degree of anisotropy are increased.

Clearly, the calculational method could be improved by better representation of the source spectrum. This necessitates the generation of more multigroup constants, as the present library only extends to 14.9 MeV. It might also prove necessary to decrease the group width in this region if an even better representation of the source spectrum is found to be necessary. Also since ANISN cannot deal with an anistropic neutron source, if this code is to be used in the future the degree of experimental source anisotropy must be minimised. In the present experimental set-up the neutron yield per steradian at zero degrees with respect to the incident deuteron beam is 10% to 15% greater than that at 180°. This figure could be improved by lowering the deuteron energy, possibly by increasing the foil thickness. Unfortunately, this will decrease the total neutron yield, and in some cases could result in only a small change in the degree of anisotropy. In experiments where a mono-energetic deuteron beam is used, the deuteron energy should clearly be as low as possible, provided that the neutron yield is still adequate.

These problems associated with the assumption of an isotropic source in ANISN, may be overcome by using a two-dimensional Sn transport code or a Monte Carlo approach to determine the calculated fluxes. Both a one and two dimensional transport code could be improved by generation of new multigroup constants, extending the energy range above 14.9 MeV. A further improvement in the multigroup constants could be obtained by choosing a weighting function more appropriate to fusion work, since the one used for this work related to fission reactors. However, errors due to this are likely to be small as a fine

multigroup structure was used.

Returning to the problem of the secondary neutron source, future neutron flux measurements using the cyclotron and degrader foil must first identify this source. If it can be established that deuterium build-up is indeed responsible, then a reduction in this source could be obtained by reducing the degree of collimation and also decreasing the distance between the foil and target, so improving the transmission ratio (i.e. the ratio of the target current to the total foil and collimator current). However, it is unlikely that the transmission ratio could ever be increased to unity, so that some of the beam would still be stopped on the collimators or in the foil, giving rise to secondary neutrons again. There are several solutions to this, one being simply to move the collimators well away from the measurement area, but the target current would then be so small as to render spectra measurements too time consuming. Another solution would be to use a different collimator material in which the deuterium diffusion properties are radically different. The material could either have the property that the deuterium was totally bound at the end of its range, or that the deuterium readily diffused away, considerably reducing the possibility of a $D(d,n)^3He$ reaction.

A further improvement in the transmission ratio may be achieved by allowing the deuteron energy emerging from the degrader foil to increase. However, this would further invalidate the calculational code ANISN, due to the source anisotropy which it cannot represent.

The only long term solution may be to move the lithium fluoride assembly to another accelerator which could produce

mono-energetic deuterons of less than 200 keV.   The Dynamitron
might just satisfy this requirement, as the recent installation
of solid state rectifiers now allows particles of energy 750 keV
to be extracted.   Thus using mass three deuterons (D_3^+) this
results in an average energy of 250 keV per deuteron nuclei when
this molecule breaks up in the target.   However, the possibility
of time dependent studies would be lost, as the Dynamitron,
unlike the Cyclotron, has no nanosecond pulsing facility (see
Rippon, 1973 or White, 1975).

It should be noted that in the discussion above deuterium
build-up in the target has been neglected as it is thought to
contribute less than 1% of the neutrons if fresh targets are
used.

In conclusion, future work must first eradicate the
secondary neutron source and improve or reduce the
approximations in the calculational method.   If the use of a
degrader foil is continued then the effects on the neutron source
spectrum of the large energy spread in the deuterons incident
on the tritium target should be calculated or measured.

Further, a sensitivity profile could be useful to
identify the neutron energy regions of greatest interest (see
Oblow, 1973 and Oblow, 1974).   These make use of known
uncertainties in the cross-section data to find the most
profitable regions for the measurement of neutron fluxes.   This
technique may be extended to compare the sensitivity profile for
the sphere with that for a conceptual Tokamak reactor blanket
(see Beynon et al, 1976).   It may then be possible to modify
both the material geometry and the materials present in the
sphere (for example, by surrounding it with a steel reflector)

so that the profiles coincide.   This is desirable since one of
the original aims of the thesis was to test the cross-sectional
data of greatest importance in the development of fusion
reactors.

<u>REFERENCES</u>

Alfieri K.A., Block R.C. and Turinsky P.J.   Nucl.Sci.Eng. <u>51</u>
(1973) 25.

Allen W.D. and Ferguson A.T.G.   Proc.Phys.Soc. (London) <u>70A</u>
(1957) 639.

Bainbridge G.R.   "Aspects of Energy Conversion" (eds. Blair I.M.,
Jones B.D., Van Horn A.J.) Pergamon Press (1976).

Bell G.I. and Glasstone S.   "Nuclear Reactor Theory".   Van
Nostrand Reinhold Co. New York (1970).

Benjamin P.A.(a), Kemshall C.D. and Redfearn J.   A.W.R.E.
NR1/64 (1964).

Benjamin P.W.(b), Kemshall C.D. and Redfearn J.   A.W.R.E.
NR2/64 (1964).

Benjamin P.W.(a), Kemshall C.D. and Brickstock J.   A.W.R.E.
O9/68 (1968).

Benjamin P.W.(b), Kemshall C.D. and Redfearn J.   Nucl.Ins.
Meth. <u>59</u> (1968) 77.

Bennett E.F.(a).   Nucl.Sci.Eng. <u>27</u> (1967) 16.

Bennett E.F.(b).   Nucl.Sci.Eng. <u>27</u> (1967) 28.

Bennett E.F. and Yule T.J.   Nucl.Inst.Meth. <u>98</u> (1972) 393.

Benveniste J. and Zenger J.   University of California Radiation
Laboratory U.C.L.R.-4266 (Internal) (1954).

Benveniste J., Mitchell A.C., Schrader C.P. and Zenger J.H.
Nucl.Inst.Meth. <u>7</u> (1960) 306.

Beynon T.D., Curtis R.H. and Lambert C.   To be published (1976).

Bohr N.   Phil.Mag.<u>30</u> (1915) 581.

Bohr N.   Math.Fys.Medd. <u>18</u> (1940-48) No.8.

Bore A.   Ph.D. Thesis.   University of Birmingham (1973).

Boring J.W., Strohl G.E. and Woods F.R.   Phy.Rev. 140 (1965) A1065.

Broomfield A.M., Patterson W.J. and Sanders J.E.   I.A.E.A. Specialist's Meeting, Fast Reactor Spectrum Measurements and their Interpretation.   Chicago (1970).

Burcham W.E.   "Nuclear Physics"   Longmans Green (1963).

Carruthers R., Davenport P.A. and Mitchell J.T.D.   U.K.A.E.A. Report No. CLM-R85 (1967).

Carter M.D.   Private communication (1974).

Carter M.D.   Private communication (1976).

Dale W.B.   "Aspects of Energy Conversion" (eds. Blair I.M., Jones B.D. and Van Horn A.J.)   Pergamon Press (1976).

Dennis J.A.   Rad.Effects 8 (1971) 87.

Dennis J.A.   Phys.Med.Biol. 18 (1973) 379.

England J.B.A.   "Techniques in Nuclear Structure Physics" Part I.   MacMillan (1974).

Evans N. and Perkins J.   Private communication (1976).

Engle W.W. Jr.   U.S.A.E.C. Report K-1693 (1967).

Evans R.D. "The Atomic Nucleus" McGraw-Hill (1955).

Fano U.   Phy.Rev. 70 (1946) 44.

Fewell T.R.   Nucl.Instr.Meth. 61 (1968) 61.

Fowler J.L. and Brolley J.E. Jr.   Rev.Mod.Phy. 28 (1956) 103.

Garber D.I.   BNL 400, 3rd Ed., V.1, January 1970.

Gibbs D.S., Svec A.J. and Harrington R.E.   Ind.and Eng.Chem. 48(i) (1956) 289.

Gold R. and Bennett E.F.   Nucl.Inst.Meth. 63 (1968) 285.

Goodings A., Jaques T.A.S., Allen F.A., Mauger R.A. and McMinn K.W.   Vacuum 21 (1971) 515.

Gunnerson E.M. and James G.   Nucl.Inst.Meth. 8 (1960) 173.

Haines E.L. and Whitehead A.B.   Rev.Sci.Inst. 37 (1966) 190.

Hanna G.C., Kirkwood D.H.W. and Pontecorvo B.   Phy.Rev. 75 (1945) 985.

Hatton D.   Ph.D. Thesis, University of Birmingham (1970).

Honeck H.C.   BNL 50066 (T-467) ENDF-102 (July 1967).

Hopkins J.C., Drake D.M. and Condé H.   Nucl.Phys. A107 (1968) 139.

Ichimori T., Obu M. and Shirakata K.   Nucl.Inst.Meth. 127 (1975) 571.

Janni J.F.   Tech.Report No. AFWL-TR-65-150 (1965).   (Air Force Weapons Laboratory).

Johnston J.   "Econometric Methods" McGraw-Hill (1963).

Jones R.T.   Ph.D. Thesis, University of Birmingham (1970).

Jowett J.   M.Sc. Thesis, University of Birmingham (1975).

Kemshall C.D.   A.W.R.E. Report No. 031/73.

Khadduri I.Y.   Ph.D. Thesis, University of Birmingham (1973).

Landau L.   Journal of Physics U.S.S.R. 8 (1944) 201.

Larson H.V.   Phys.Rev. 112 (1958) 1927.

Lathrop K.D.   Reactor Technology 15 (1972) 107.

Lawson D.J.   Proc.Phys.Soc.(London) B70 (1957) 6.

Lindhard J., Nielsen V., Scharff M. and Thornsen P.V.   Math. Fys.Medd. 33 (1963) No.10.

Lowry R.A. and Miller G.H.   Phys.Rev. 109 (1958) 826.

Maples C., Goth G.W. and Cery J.   Nucl.Data A2 (1966) 429.

Marion J.B. and Fowler J.L.   "Fast Neutron Physics" part I, Interscience Publishers Inc. New York (1960).

Meadows P.H., Meadows, Randers J. and Behrens W.W.   III "The Limits to Growth" Pan Book Ltd. (1972).

Miyajima M., Masuda K., Hitachi., Doke T., Takahashi N., Konno S., Hamada T., Kubota S., Nakamoto A., and Shibamura E.   Nucl.Inst.Meths. 134 (1976) 403.

Newson H.W., Williamson R.M., Jones K.W., Gibbons J.H. and Marshak H.   Phy.Rev. 108 (1957) 1294.

Oblow E.M.   ORNL-TM-4110 (1973).

Oblow E.M.   ORNL-TM-4437 (1974).

Parker J.B., White P.H. and Webster R.J.   Nucl.Inst.Meth. 23 (1963) 61.

Palmer D.W., Mourad W.G., Donhowe J.M., Nielsen K.E. and Nickles R.J.   Nucl.Phys. 75 (1966) 575.

Perkin C.   Proc. 4th Conference on Accelerator Targets for the Production of Neutrons EUR 2641c (1966).

Perkins J.   M.Sc. Thesis, University of Birmingham (1975).

Phipps J.A., Boring J.W. and Lowry R.A.   Phys.Rev. 135 (1964). A36.

Powell J.E. and Rogers J.W.   Nucl.Inst.Meth. 87 (1970) 29.

Price W.G. Jr.   MATT. 1035 April 1974.

Ribe F.L.   Rev. of Mod.Phys. 47 (1975) 7.

Rilchie A.I.M. and Rose A.   Nucl.Inst.Meth. 127 (1975) 237.

Roberts P.   Ph.D. Thesis, University of Birmingham (1973).

Robertson J.C. and Zieba K.J.   Nucl.Inst.Meth. 45 (1966) 179.

Rogers J.W.   Nucl.Inst.Meth. 80 (1970) 313.

Ruby L. and Crawford R.B.   Nucl.Inst.Meth. 24 (1963) 413.

Ryves T.B.   J. of Nucl.Eng. 27 (1973) 365.

Scott M.C.   Ph.D. Thesis, University of Birmingham (1969).

Scott M.C. and Atta M.A.   Nucl.Inst.Meth. 106 (1973) 465.

Scott M.C. and Campbell J.   Birmingham Radiation Centre Report BRC 7505 (1975).

Shalev S. and Cuttler J.M.   Nucl.Sci.Eng. 51 (1973) 52.

Siekierkowski E.Z.   M.Sc. Thesis, University of Birmingham (1975).

Snidow N.L. and Warren H.D.   Nucl.Inst.Meth. 51 (1967) 109.

Sofield C.J., Cookson J.A., Freeman J.M. and Parthasaradhi K.
   Nucl.Inst.Meth. 138 (1976) 411.

Steiner D.   Nucl.Sci.Eng. 58 (1975) 107.

Stewart L.S. and Young P.G.   Trans.Am.Nucl.Soc. 23 (1976) 22.

Stier P.M., Barnett C.F. and Evans G.E.   Phys.Rev. 96 (1954)
   973.

Taylor J.R.   A.E.E.W.-R651 (1969).

Tschalar C.   Nucl.Inst.Meth. 64 (1968) 237.

Verbinski V.V. and Giovannina R.   Nucl.Inst.Meth. 114 (1974)
   205.

Weaver D.R.   Private communication (1975).

Werle H.   Nucl.Inst.Meth. 99 (1972) 295.

Werle H., Fieg G., Seufert H. and Stegemann D.   Nucl.Inst.Meth.
   72 (1969) 111.

Wilkinson D.H.   "Ionization Chambers and Counters" Cambridge
   University Press London (1950).

Williams I.R.   Nucl.Inst.Meth. 44 (1966) 160.

Williamson C.F., Boulot J.P. and Picard J.   CEA-R 3042 (1966).

Wright R.Q., Greene N.M., Lucius J.L. and Craven C.W. Jr.
   ORNL-TM-2673 (Sept. 1969).
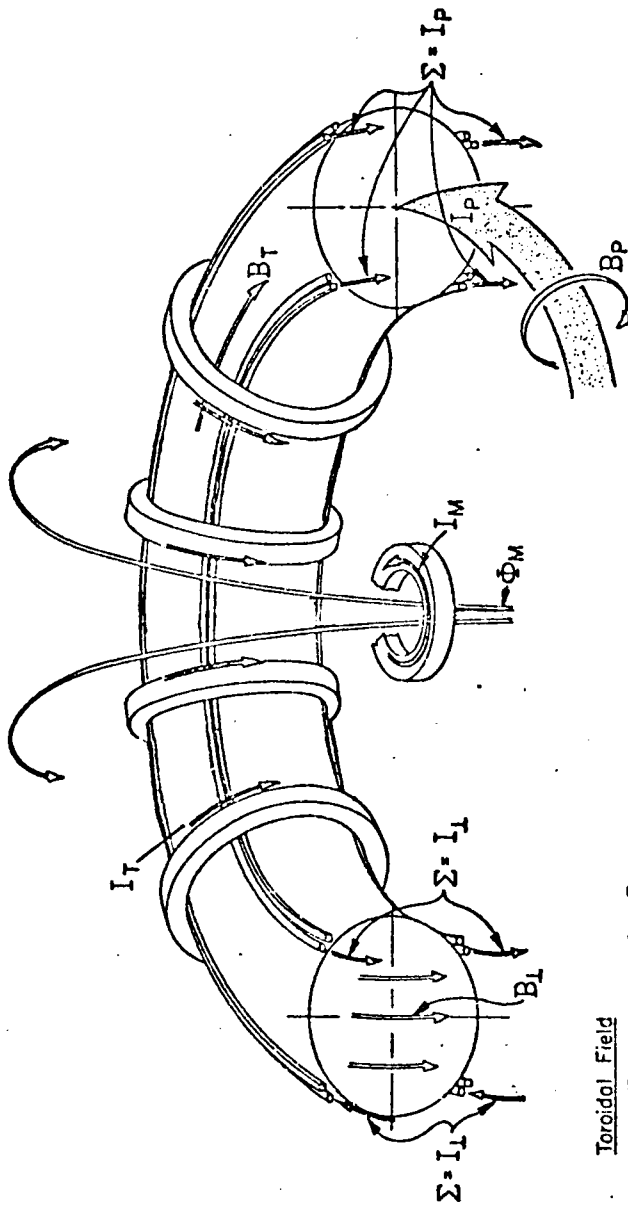
Toroidal Field
 B_T Generated by I_T

Poloidal Field
 B_P Generated by plasma current I_P = sum of external currents

Transverse Field
 $B_\perp$ Generated by external current I_L

Magnetizing Flux
 Φ_M Generated by the magnetizing current I_M

Figure 1.1: Principles of Tokamak confinement
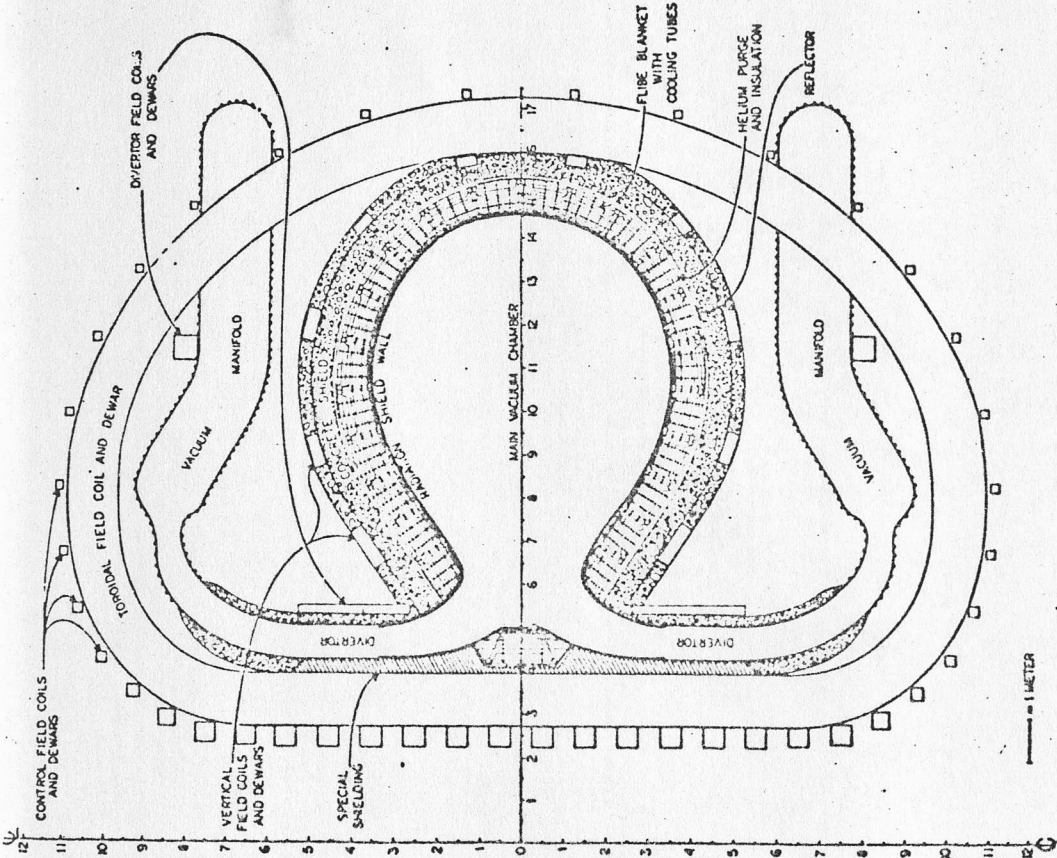
Figure 1.2a: Cross-section of a conceptual Tokamak reactor (Steiner, 1975)
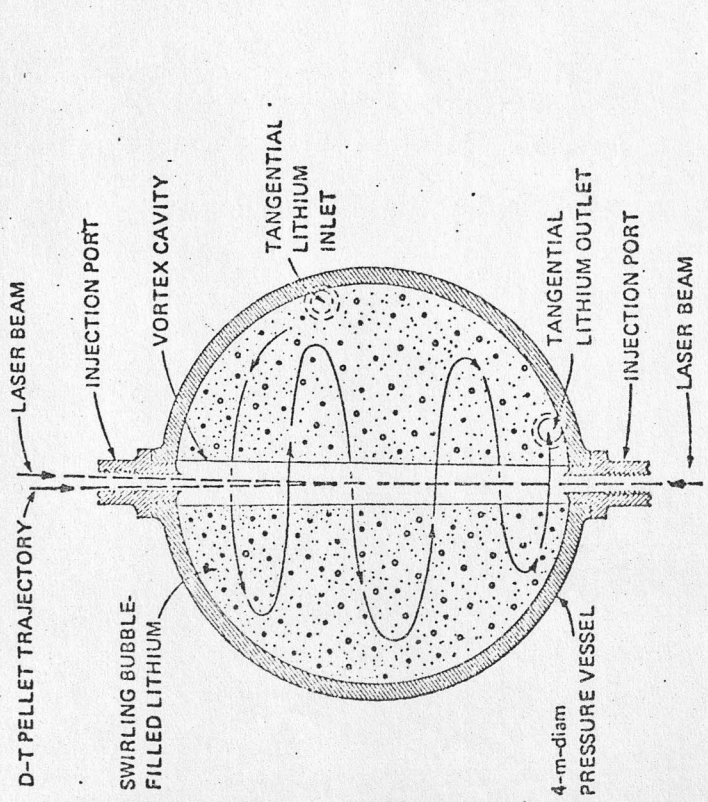
Figure 1.2b: Cross-section of swirling-lithium vortex laser pellet reaction (Steiner 1975)
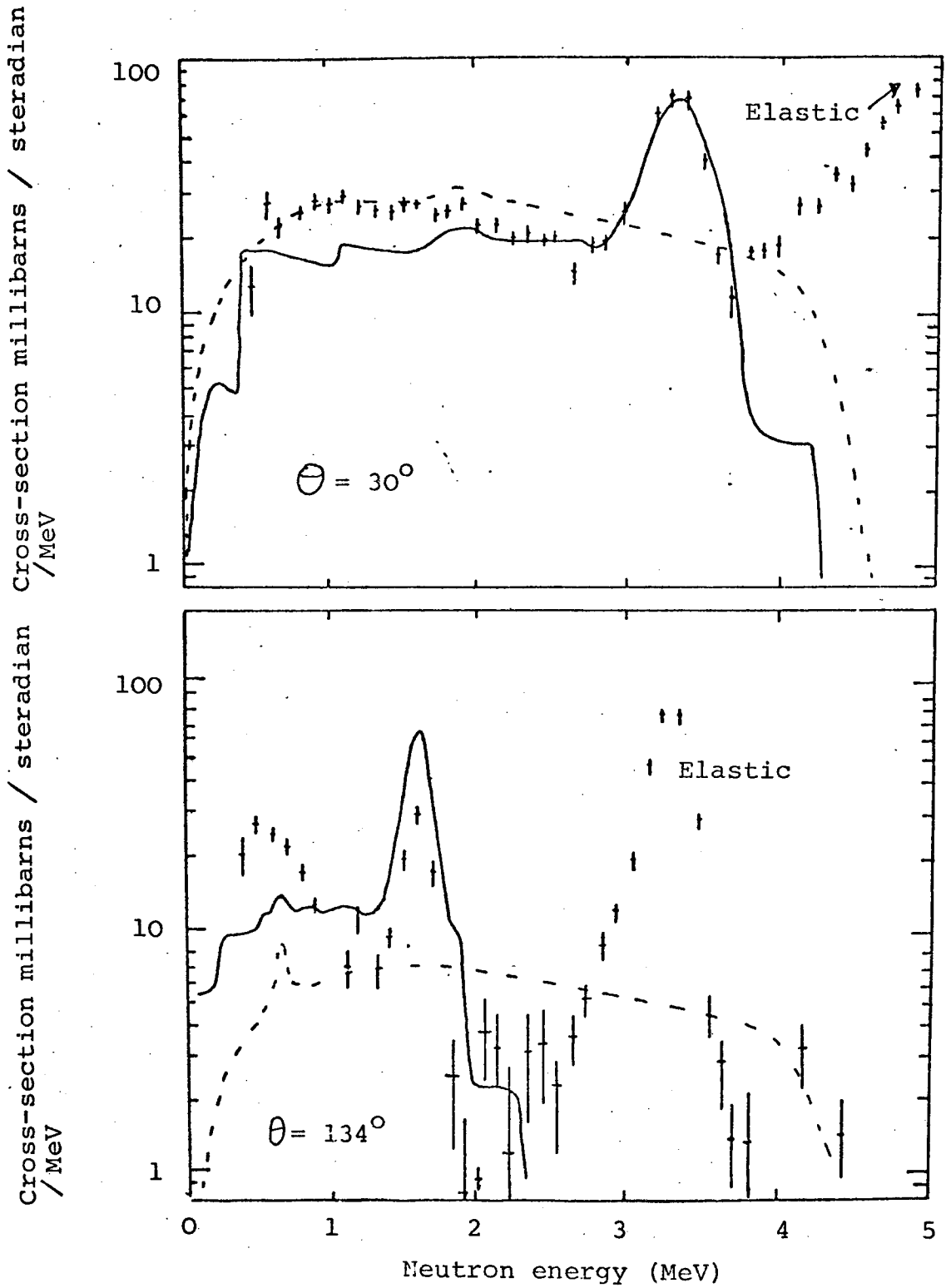
Figure 1.3: Laboratory energy spectra of the neutrons scattered by 5.74 MeV neutrons from ^{6}Li
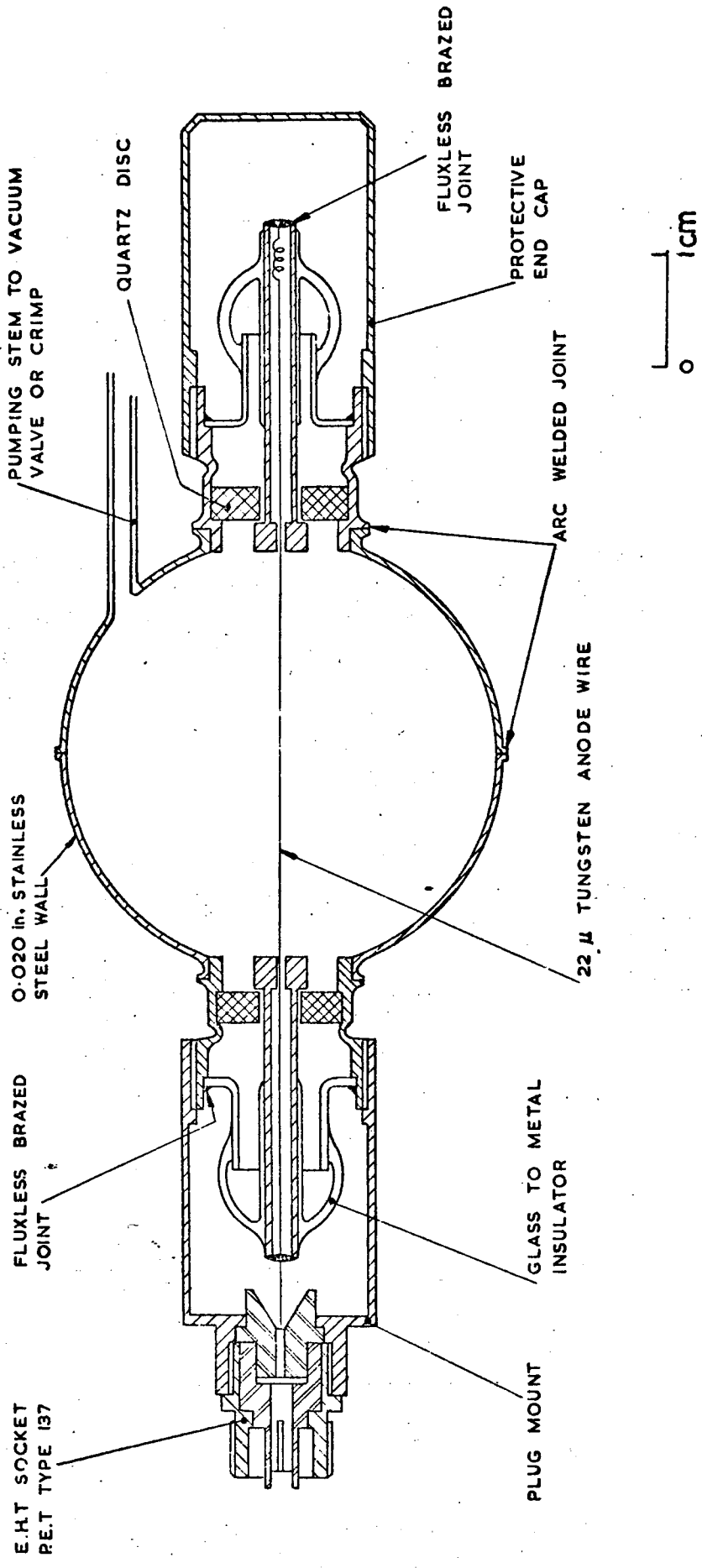
Figure 1.4: Cross-section of a spherical proportional counter, Type SP2

FLUXLESS BRAZED JOINT

PROTECTIVE END CAP

QUARTZ DISC

PUMPING STEM TO VACUUM VALVE OR CRIMP

ARC WELDED JOINT

22 μ TUNGSTEN ANODE WIRE

0.020 in. STAINLESS STEEL WALL

FLUXLESS BRAZED JOINT

GLASS TO METAL INSULATOR

E.H.T SOCKET RE.T TYPE 137

PLUG MOUNT

1cm

0
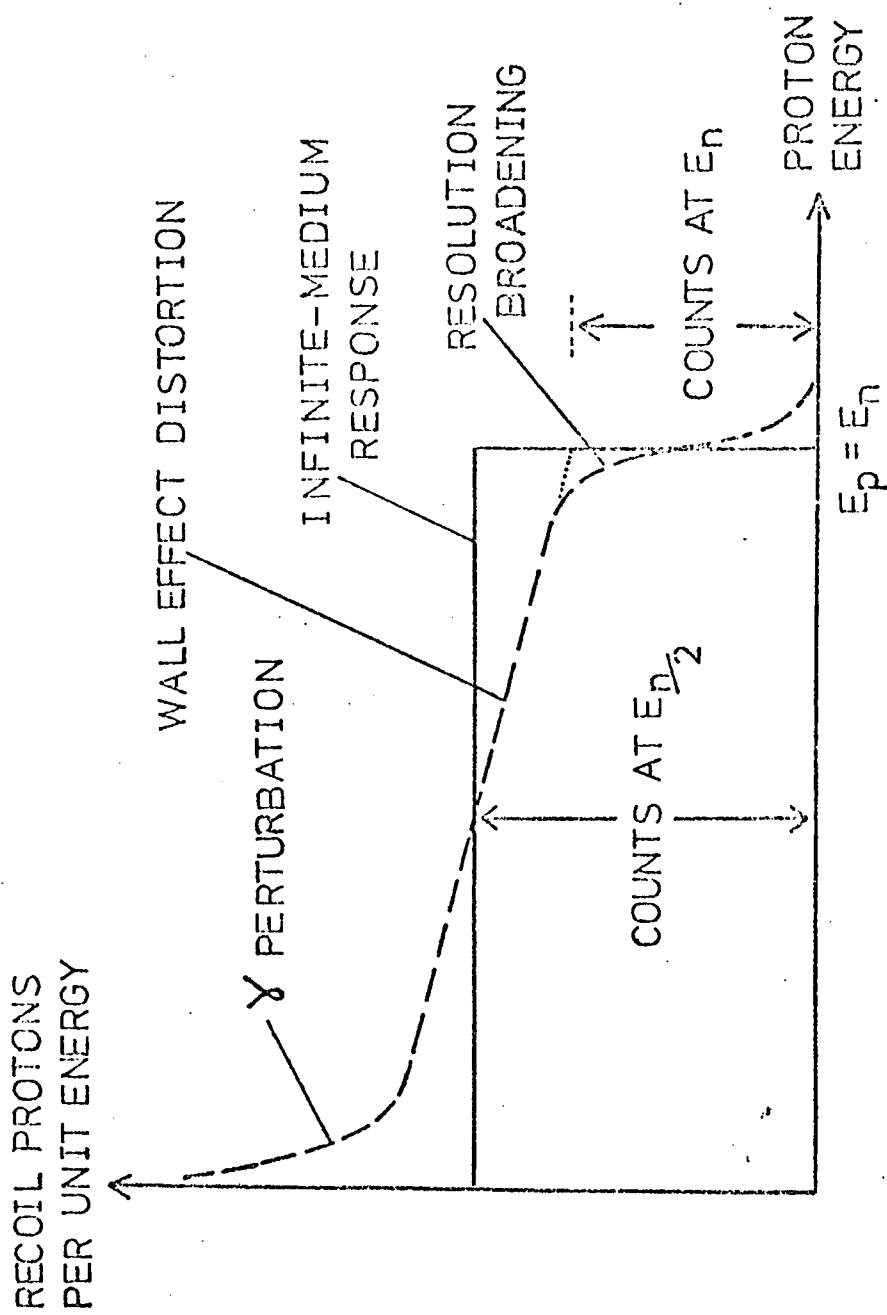
Figure 2.1: Proton recoil spectrum to monoenergetic neutrons

Li₂ Co₃ evaporated directly on to the end cap

End cap

Wall thickness 0.0254 cm

Viton 'O'-ring

Tritium target

Clamping ring
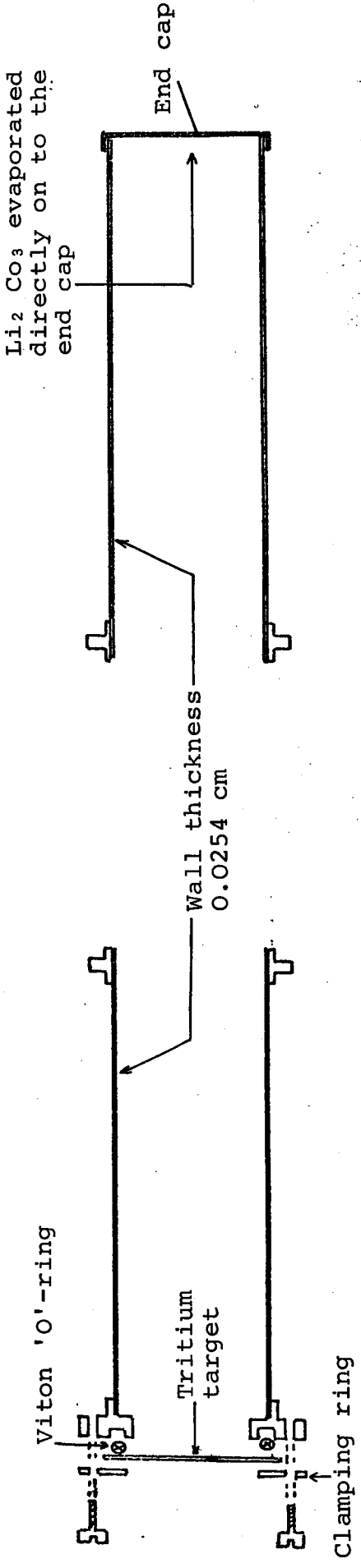
Figure 3.1a: Cross section of the tritium target holder (Full scale)

Figure 3.1b: Cross section of the lithium carbonate target holder (Full scale)

½ m drift tube

Clamping nut

'O'-ring
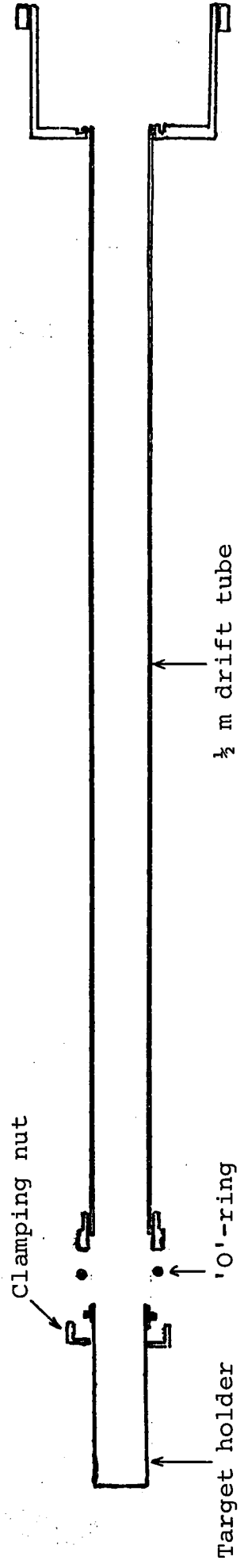
Target holder

Figure 3.1c: Cross section of the low scatter target assembly (approx. 2/5 full scale)

Cooling fin for the
heat pipe

Heat pipe

Drift tube

Target assembly clamped
to the heat pipe
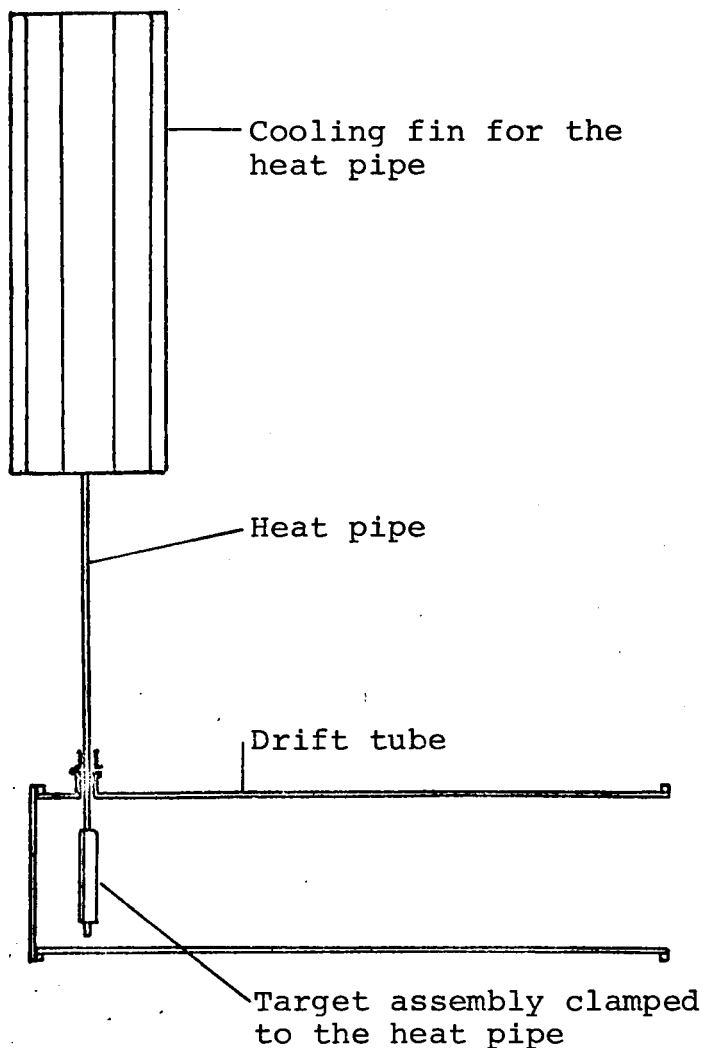
Cross-section of heat pipe target assembly
(1/5 full-size)

Li_2CO_3 evaporated onto
this surface
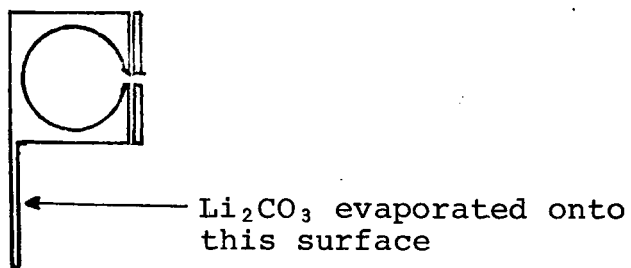
Cross-section of the target holder
(full-size)

Figure 3.2: Heat pipe target assembly

Figure 3.3b: Yield curve for a 11 keV thick target

Figure 3.3a: Yield curve for a 5 keV thick target

Curve	FWHM of Incident Proton Energy Distriution (keV)
A	8
B	4
C	2
D	0.1

Neutrons per unit charge (arbitrary units)

Incident Proton Energy (keV)
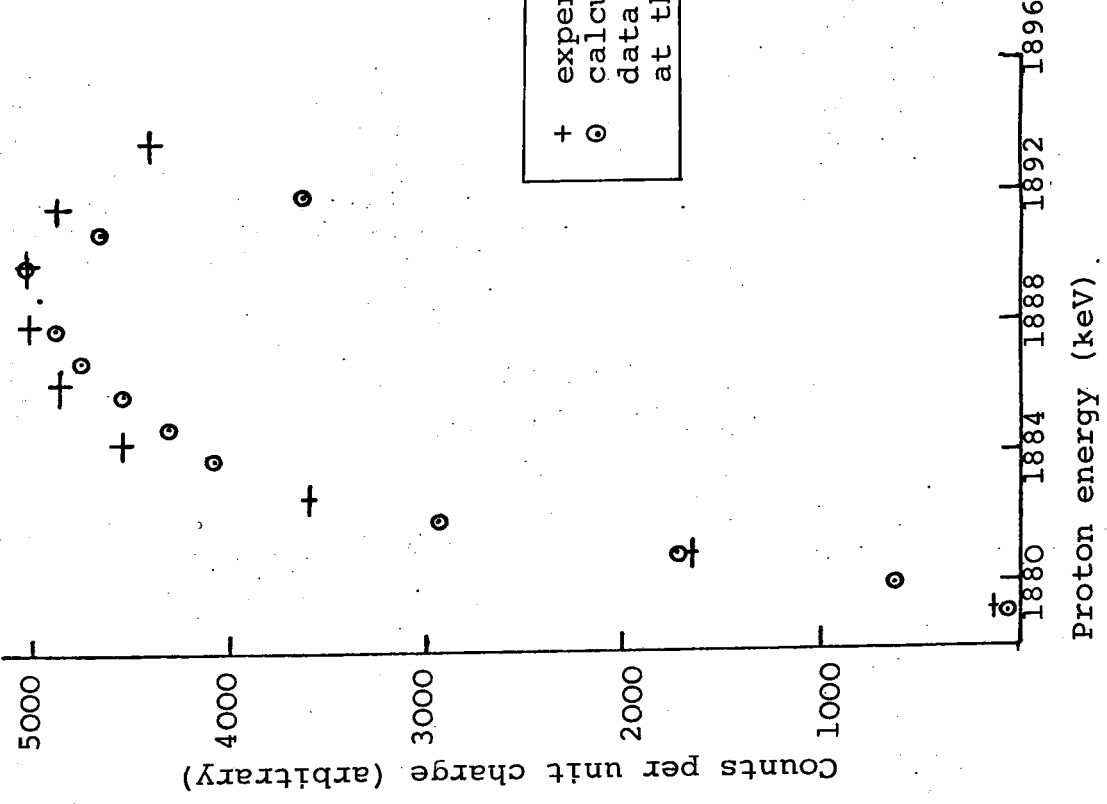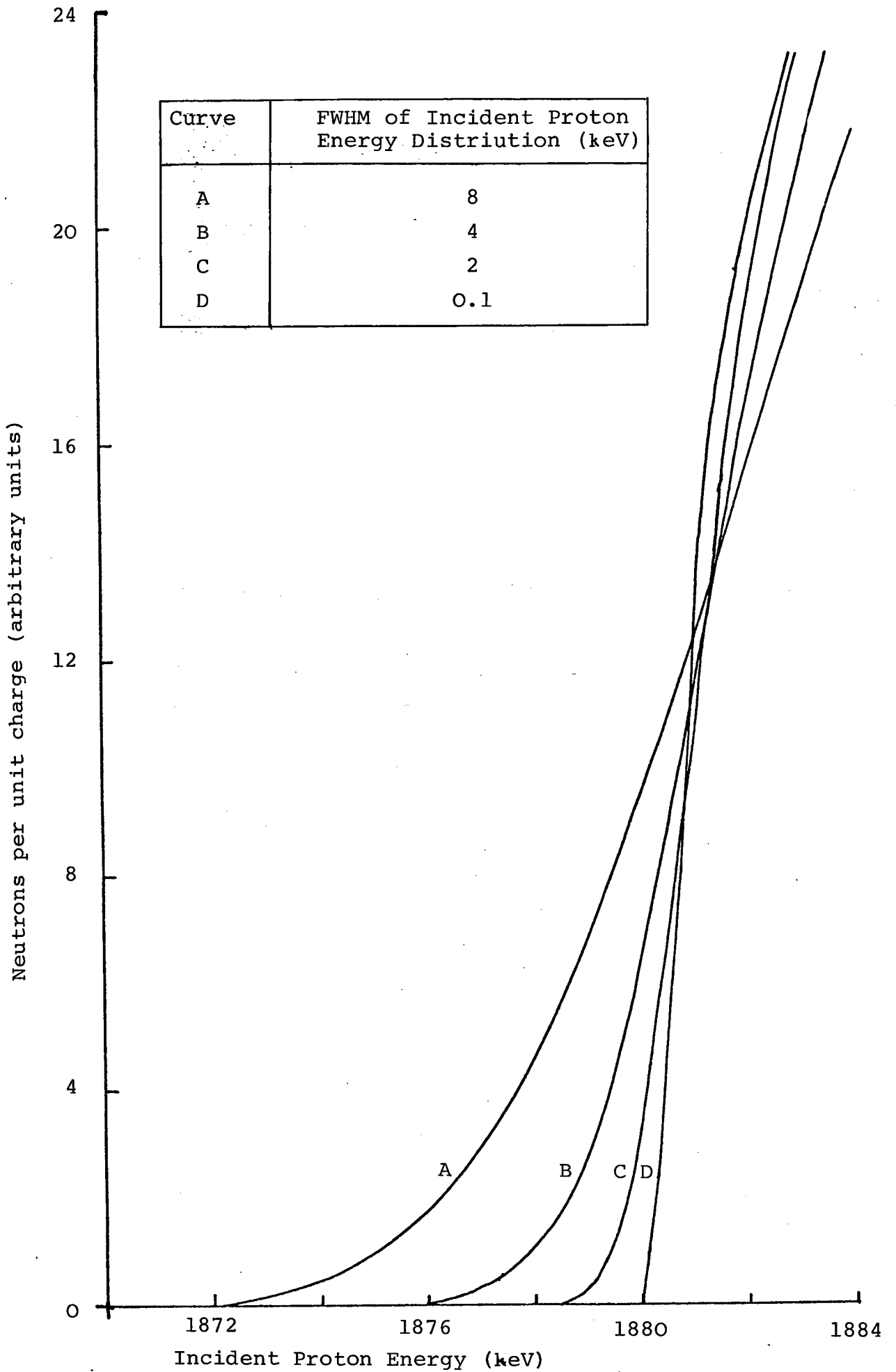
Figure 3.4: Yield Curves for Several Incident Proton Energy Distributions
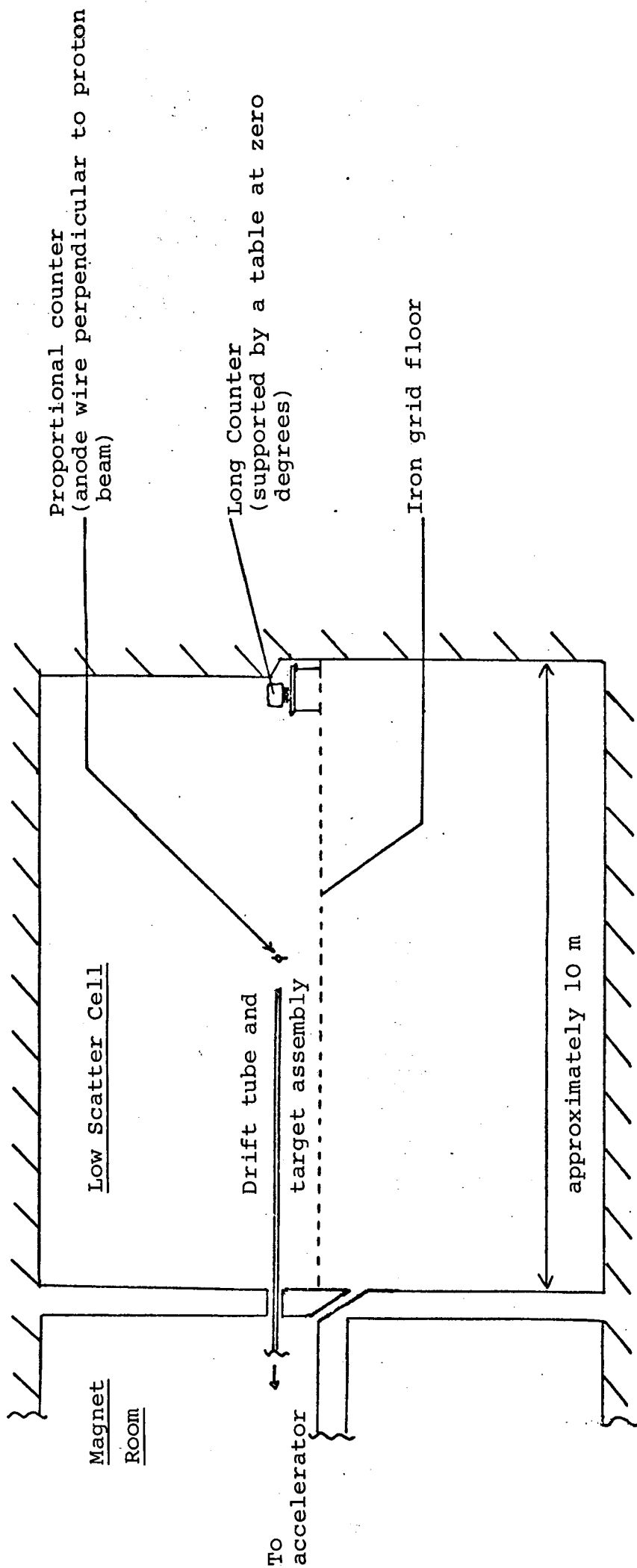
Figure 3.5: Schematic diagram of the experimental arrangement for the calibration measurements

The figure shows Ionisation (arbitrary units) on the vertical axis (0 to 250) plotted against Proton energy (keV) on the horizontal axis (0 to 800).

Legend:
- † Dynamitron measurements
- ✗ Filter measurements
- ⊡ He-3 764 keV calibration
- — Fitted curve in the form of $I = 0.296E + 2.3$
- ⊙ Triton edge, 191.3 keV
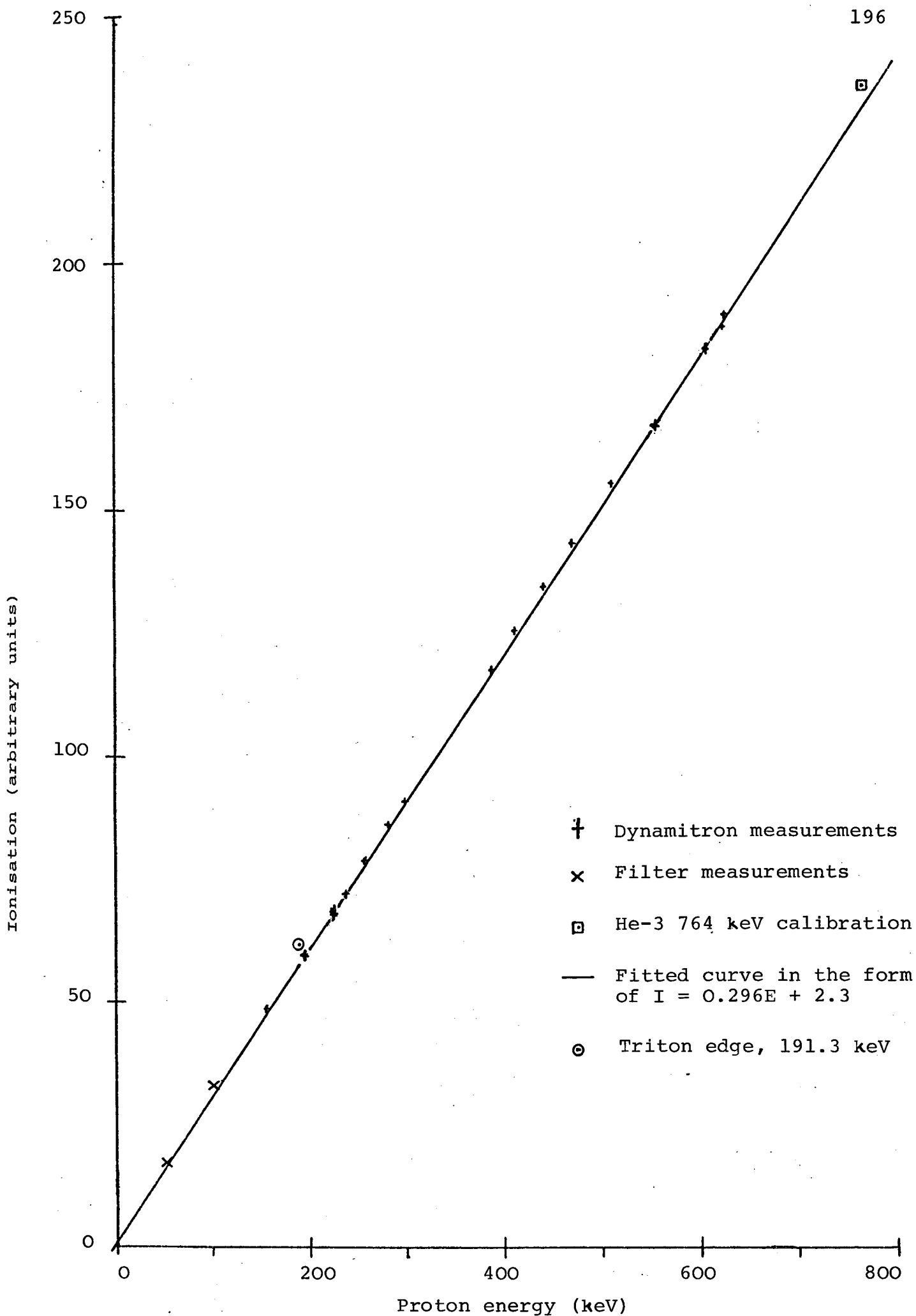
Table 3.6:   Energy Ionisation Relationships for the 2.5 Atm
            Hydrogen Counter
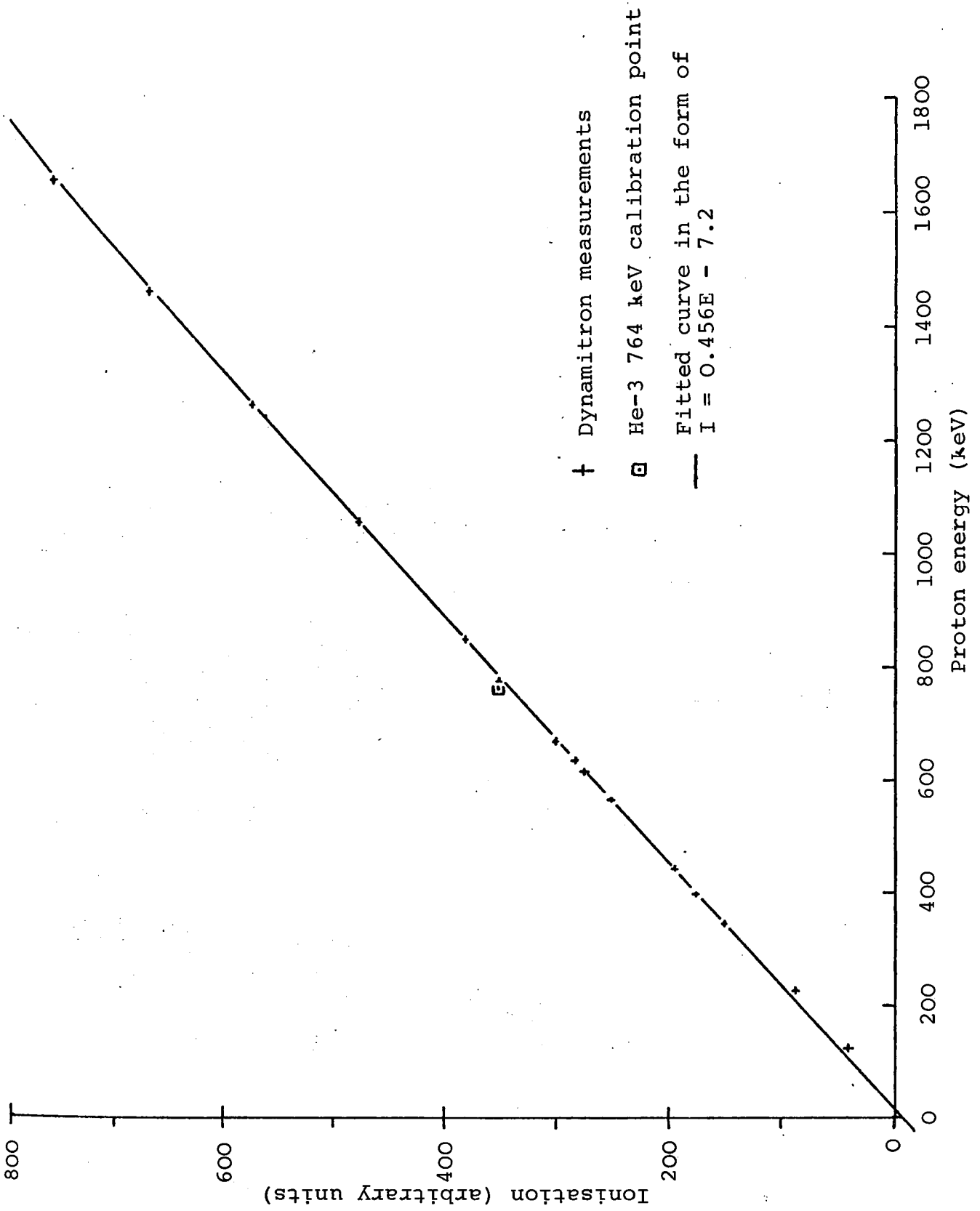
Figure 3.7: Energy-Ionisation Relationship for the 10 Atm Hydrogen Counter
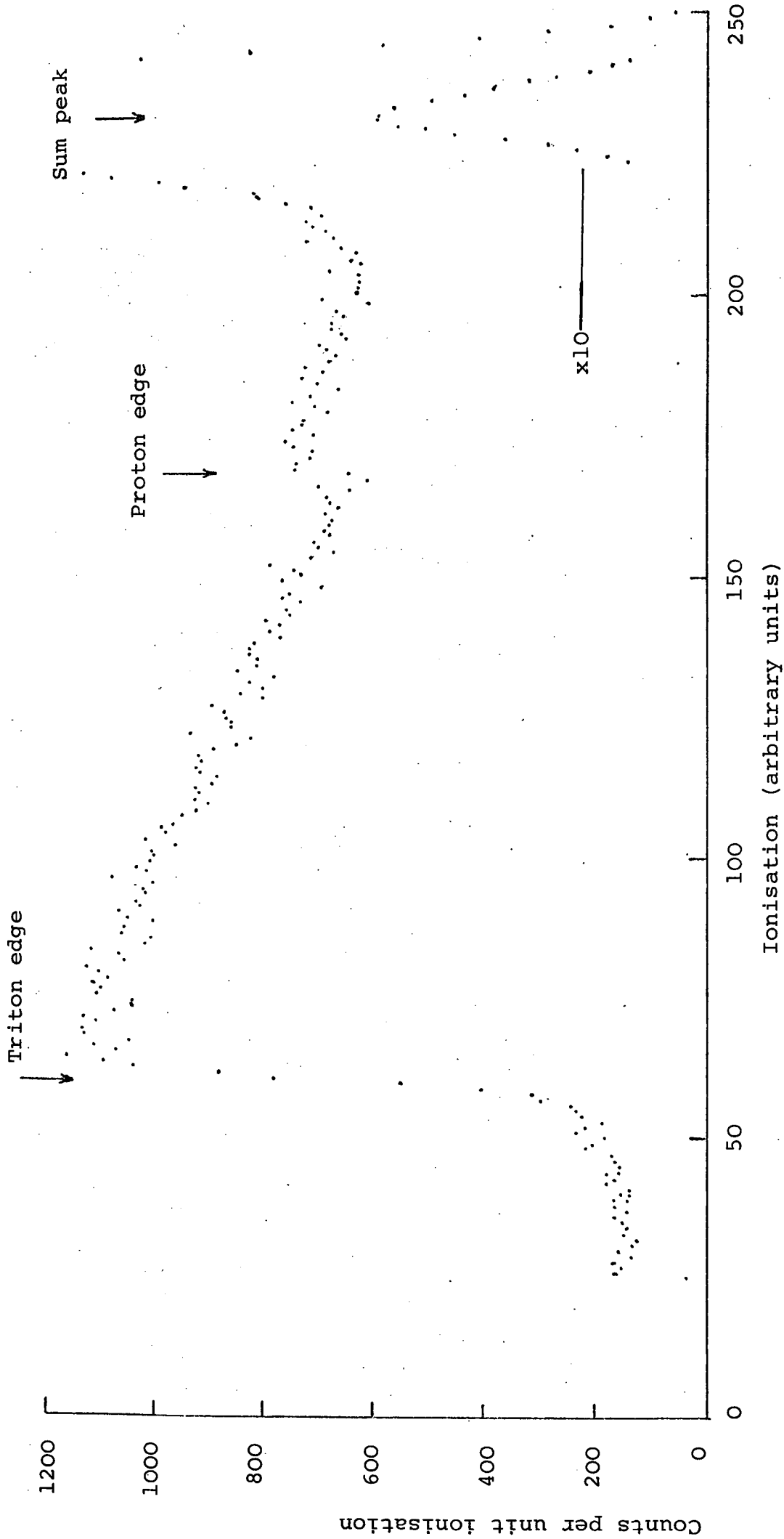
Figure 3.8: Ionisation spectrum of the helium-3 reaction in the 2.5 Atm counter
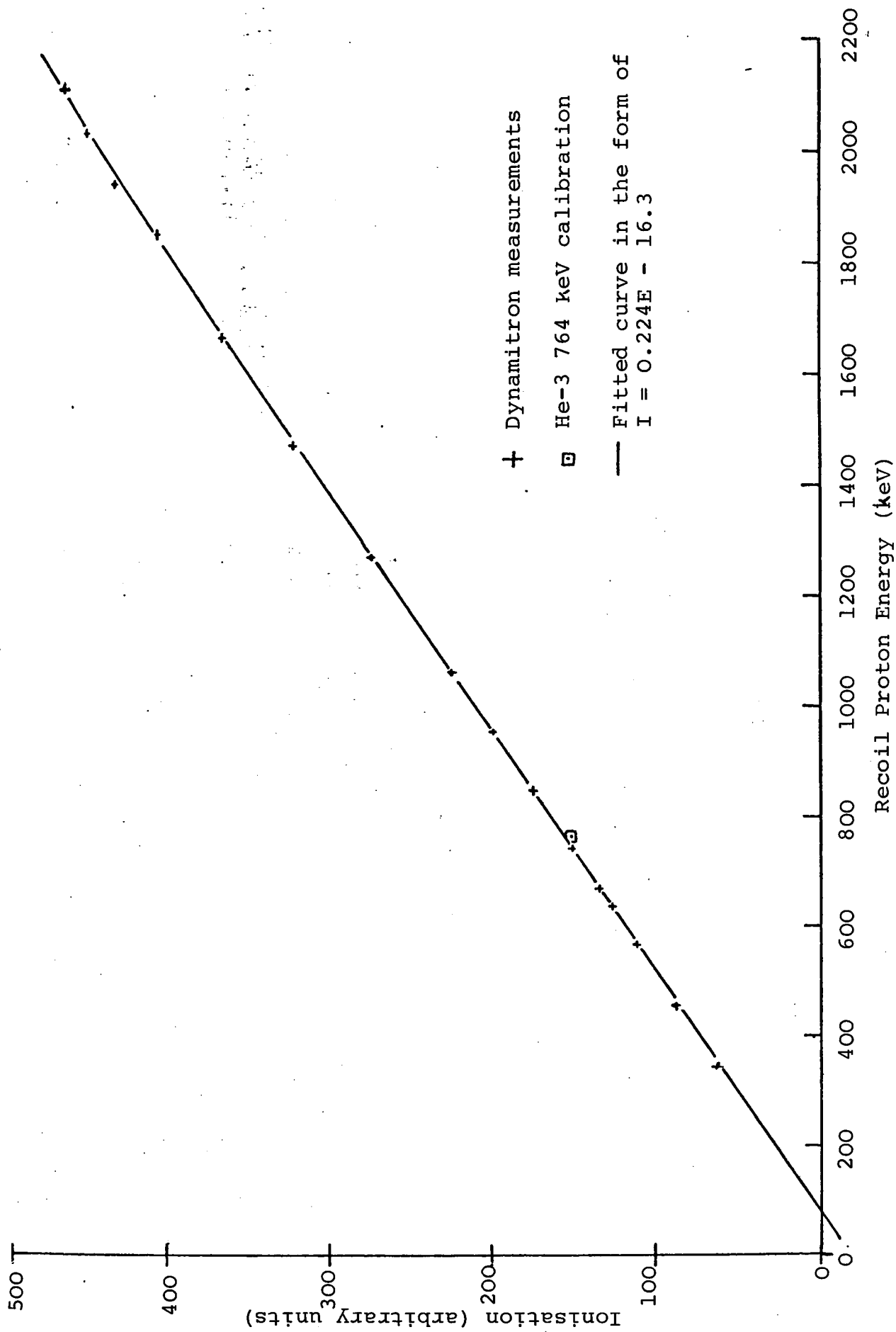
Figure 3.9: Energy-Ionisation Relationship for the Hydrogen-Argon Counter

Figure 3.10: Response function of the 2.5 Atm hydrogen counter to 584 keV

Neutron energy 584 keV
range over radius 0.79

— Snidow and Warren predicted curve

90°

Ionisation (arbitrary units)

Counters per unit ionisation

2048

1536

1024

572

0   100   200   300   400
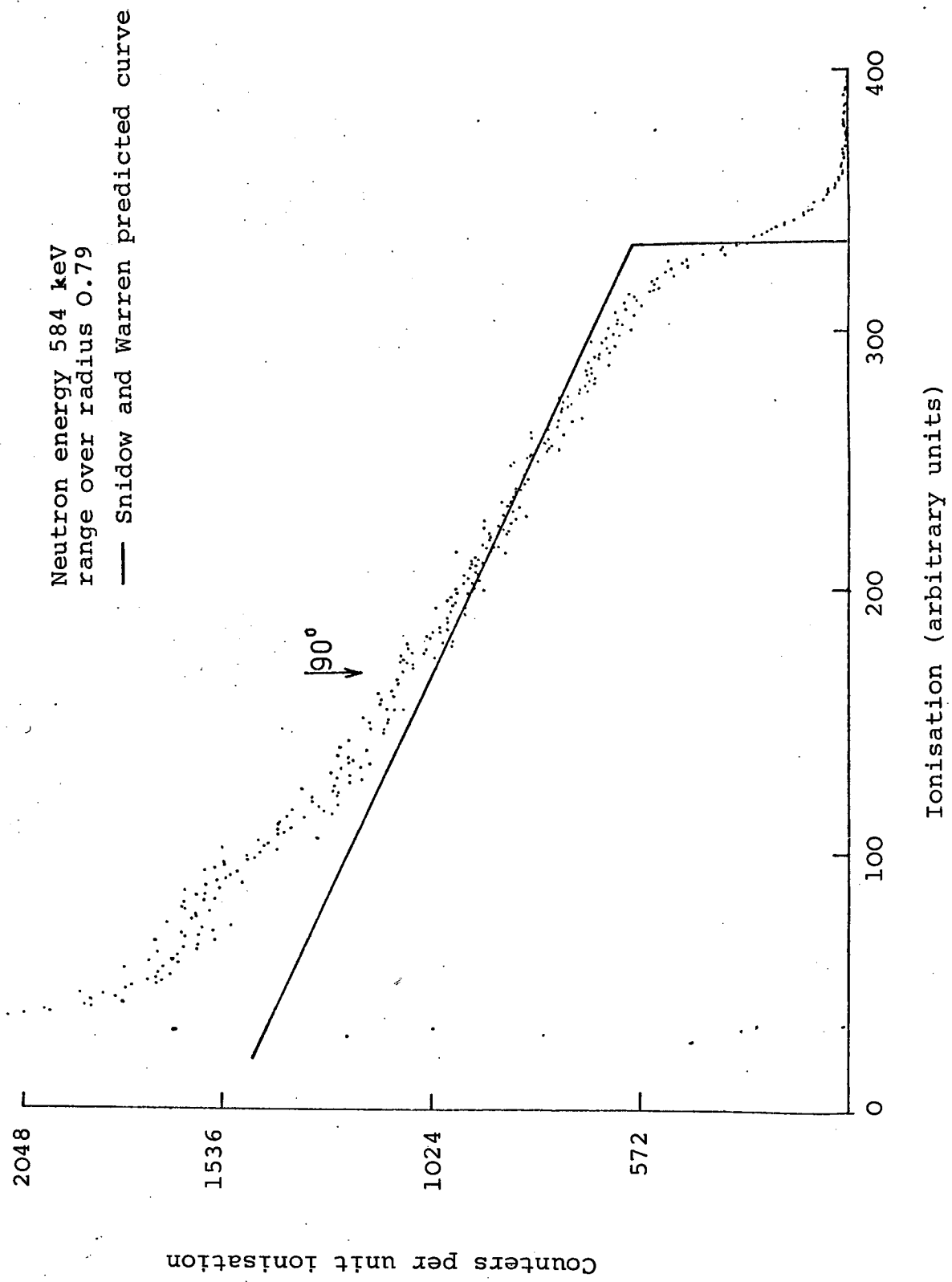
Figure 3.11: Response function of the 2.5 Atm hydrogen counter to 473 keV neutrons
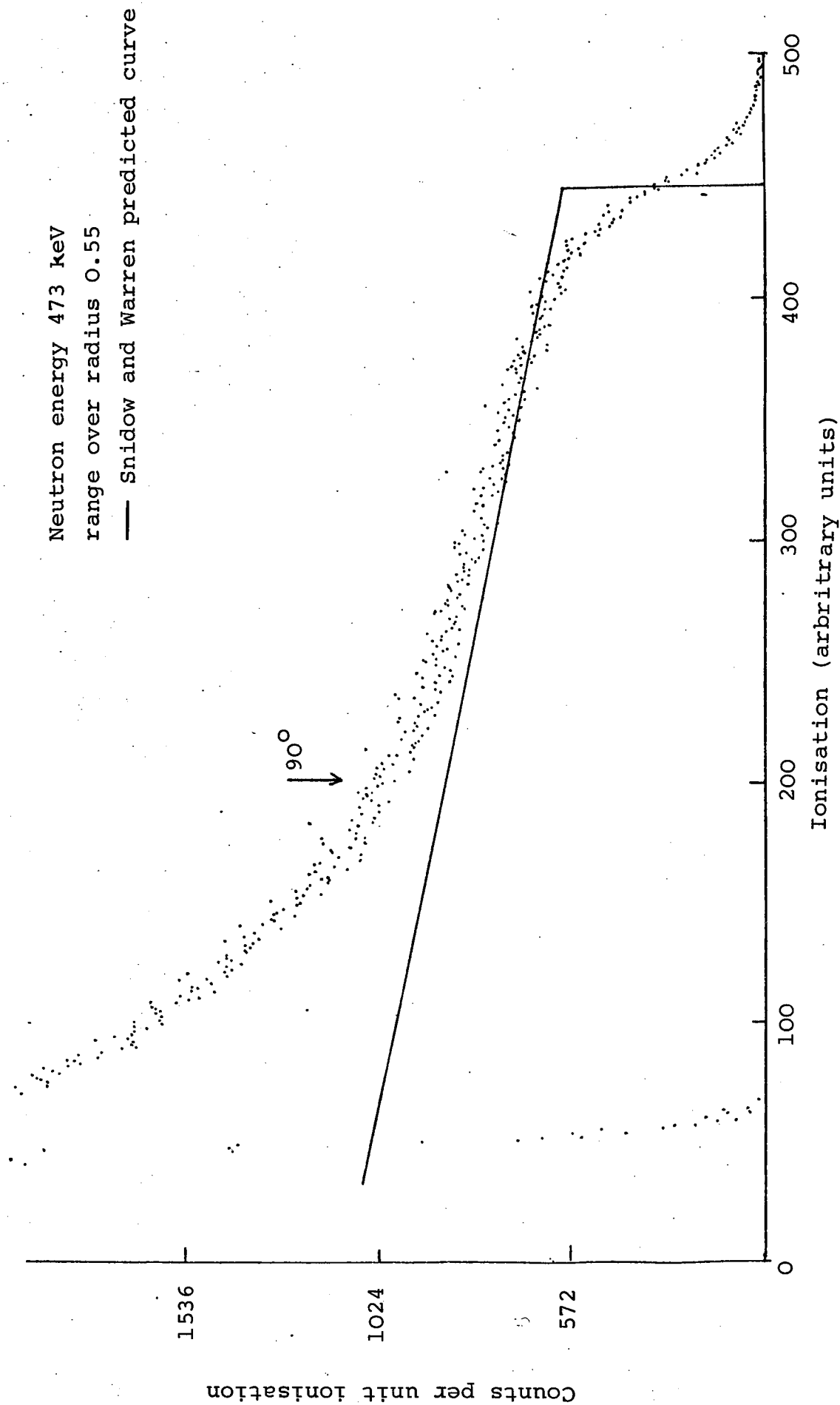
Figure 3.12: Response function of the 2.5 Atm hydrogen counter to 697 keV neutrons
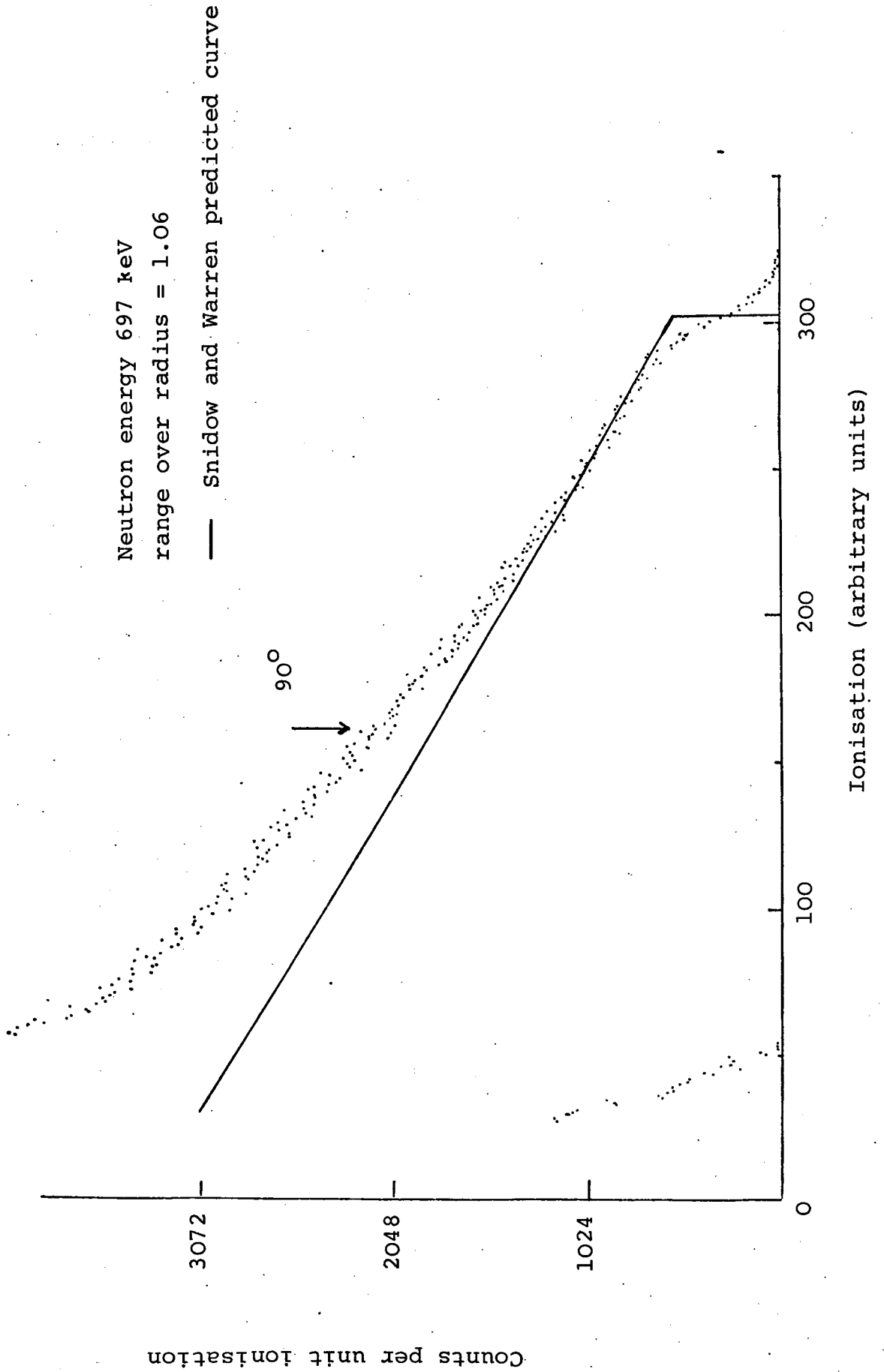
Figure 3.13: Response function of the 10 Atm hydrogen counter to 851 KeV neutrons

Neutron energy = 0.851 MeV

range over radius = 0.38

—— Snidow and Warren predicted curve

Figure 3.14: Response function of the 10 Atm hydrogen counter to 1.061 MeV neutrons

Neutron energy 1.061 MeV
range over radius = 0.54

—— Snidow and Warren predicted curve
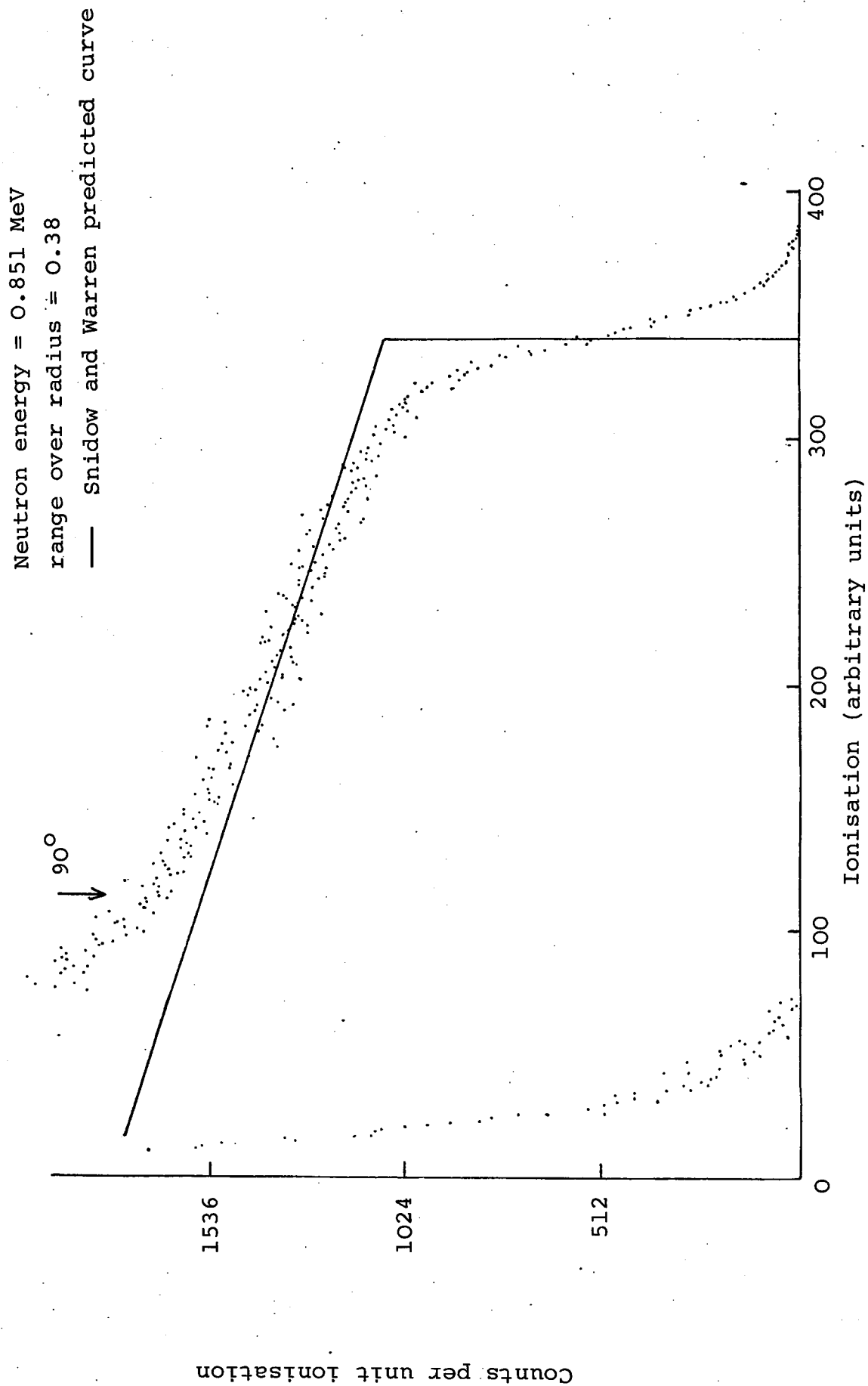
Figure 3.15: Response function of the argon hydrogen counter to 1.065 MeV neutrons

Neutron energy 1.065 MeV
range over radius = 0.166
—— Snidow and Warren predicted curve

90°

Ionisation (arbitrary units)

Counts per unit ionisation

768   572   256
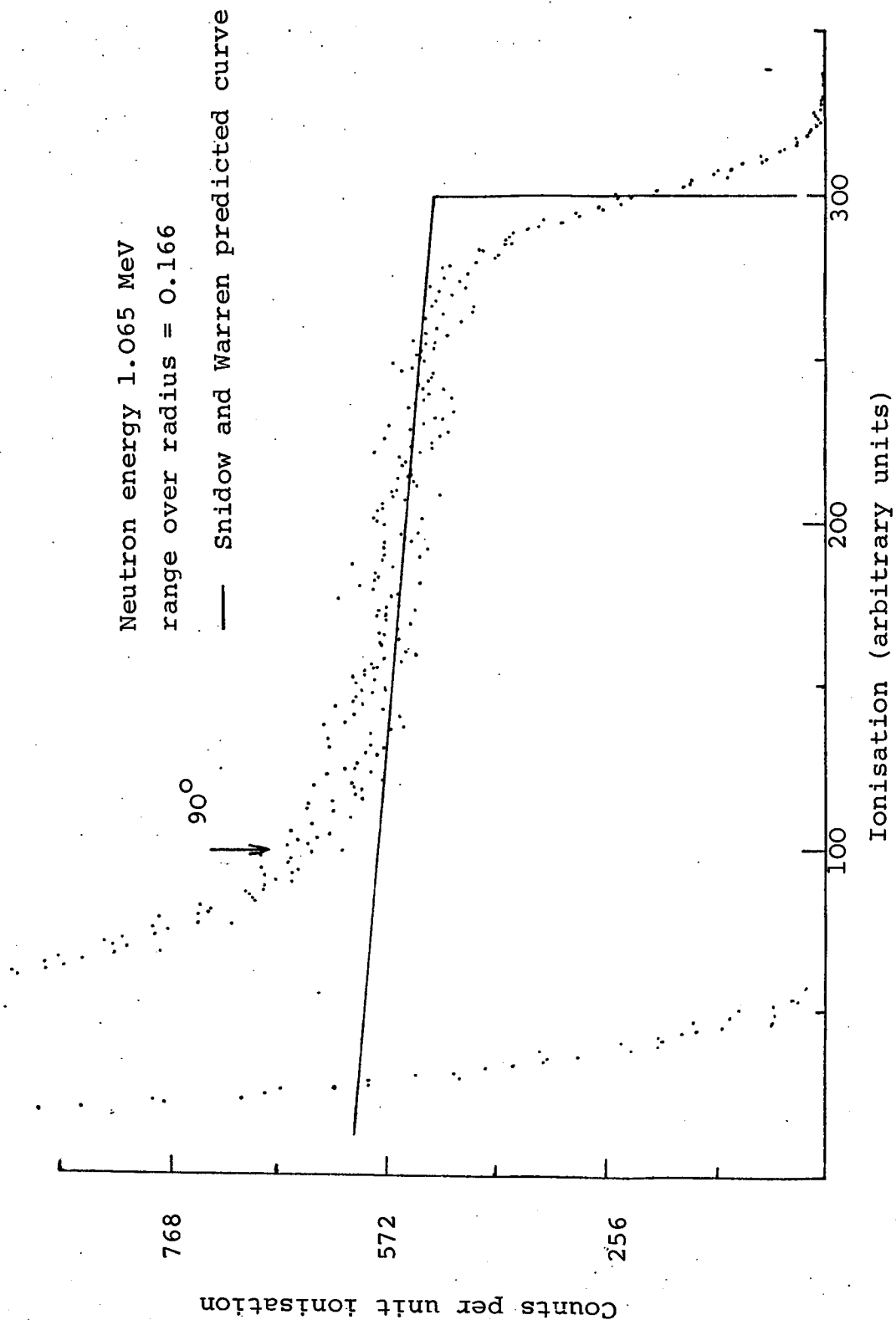
Figure 3.16: Response function of the argon-hydrogen counter for 1.675 MeV neutrons

Neutron energy 1.675 MeV
range over radius = 0.34

—— Snidow and Warren predicted curve

90°

Ionisation (arbitrary units)

Counts per unit ionisation
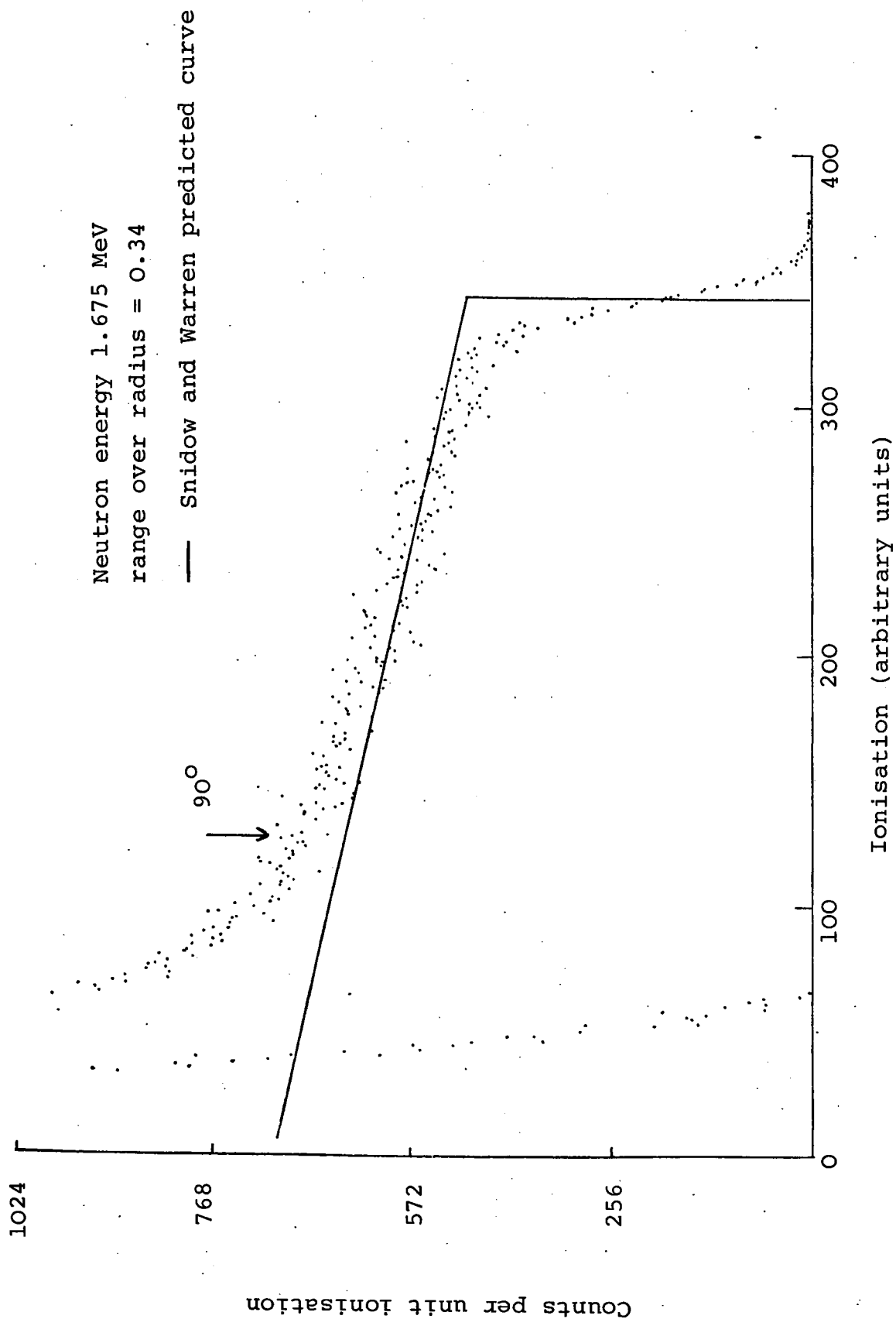
Figure 3.17: Response function of the argon-hydrogen counter to 1.959 MeV neutrons
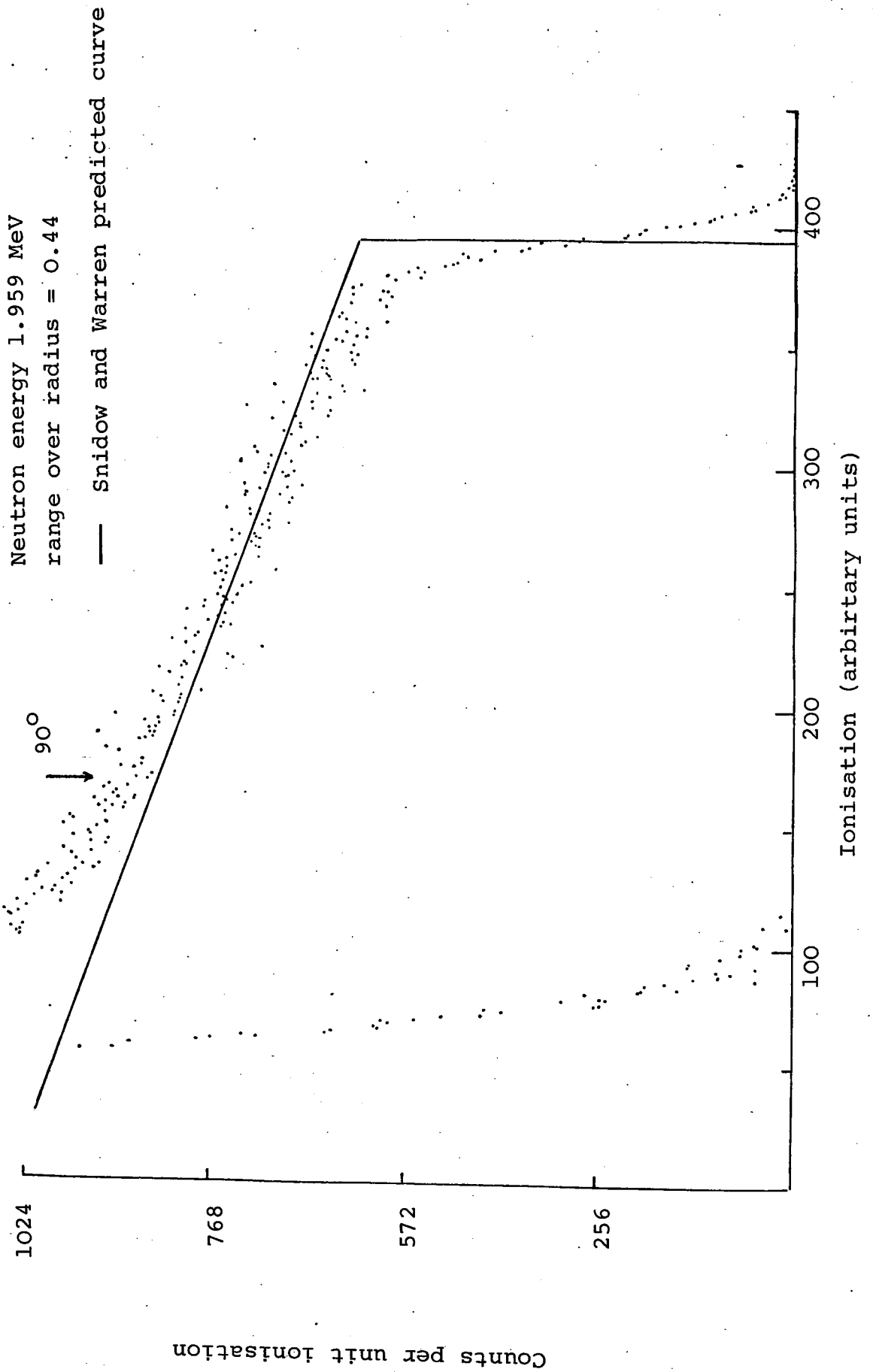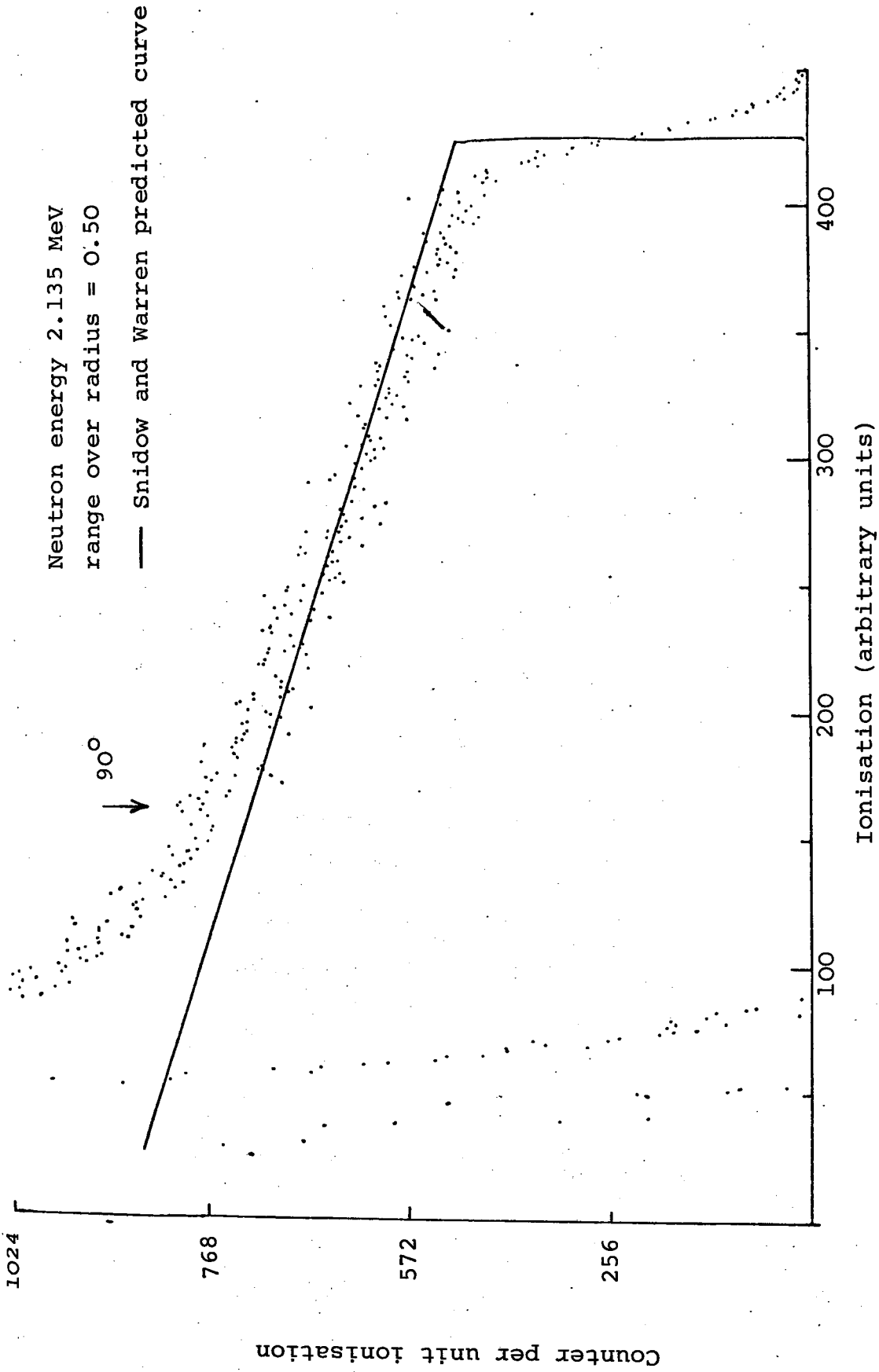
Figure 3.18: Response function of the argon hydrogen counter to 2.135 MeV neutrons
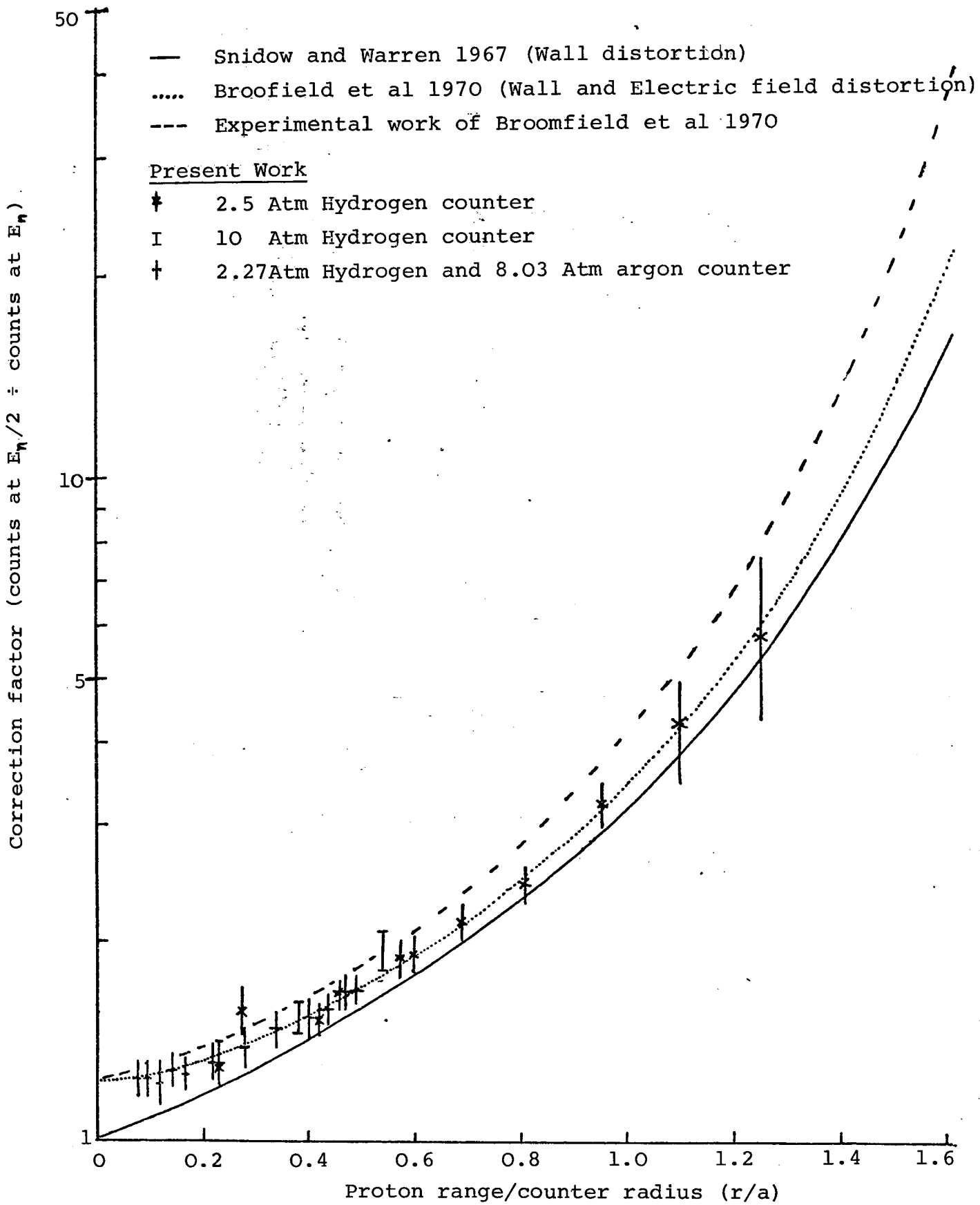
Figure 3.19: Experimental and Calculated Distortion of Response Functions

Neutron energy 800 KeV
range over radius = 1.35

——— response for mean neutron energy of
800 KeV and FWHM of 46 KeV

· · · respose for monoenergetic neutrons
of 800 KeV

90°

normalisation
point

Proton energy (KeV)

400   800

O

Counts per unit energy (arbitrary units)
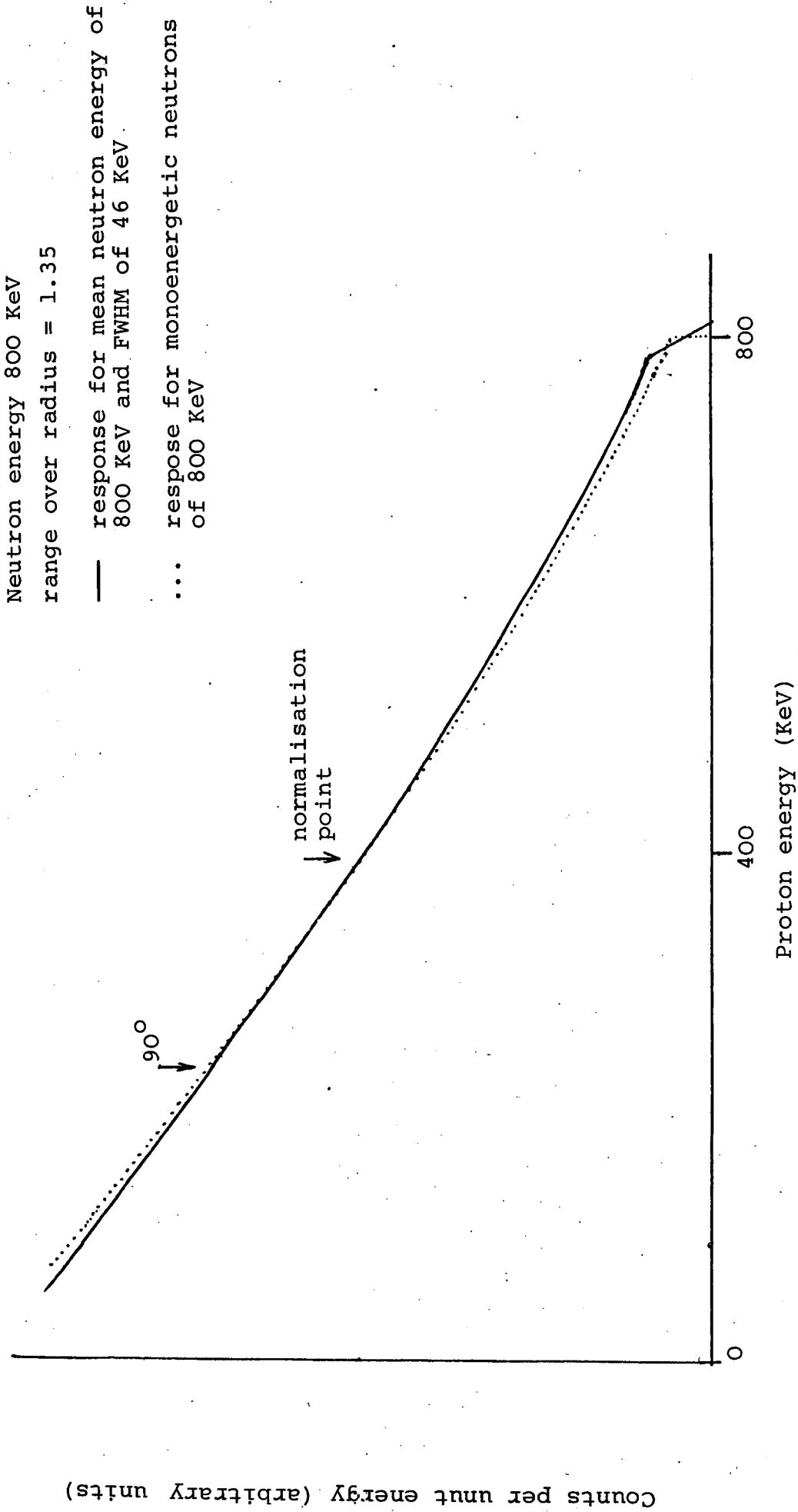
Figure 3.20: Response functions of 2.5 Atm hydrogen counter to neutrons of mean energy 800 KeV
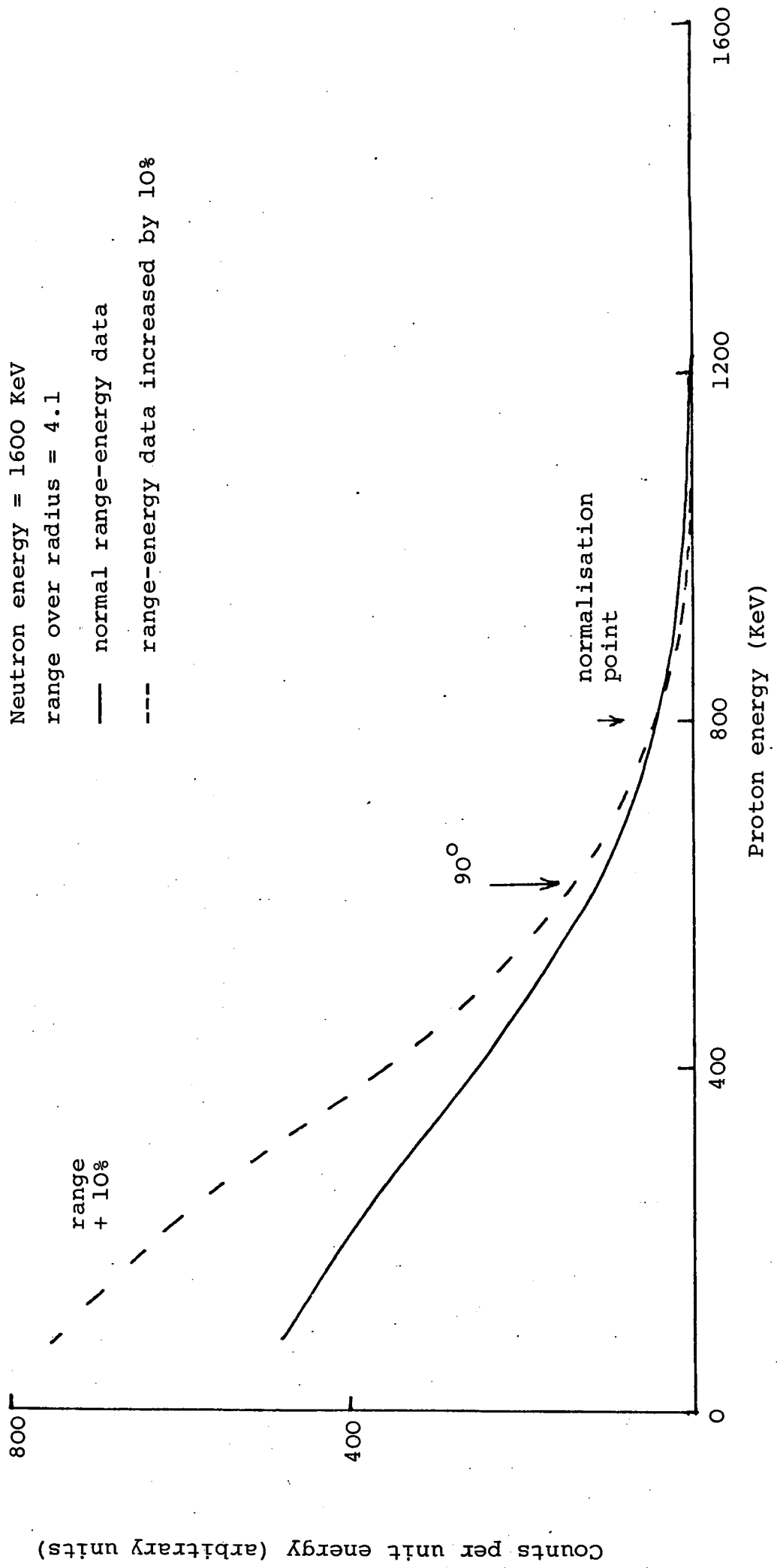
Figure 3.21: Response function for 1600 KeV neutrons and 2.5 Atm hydrogen counter
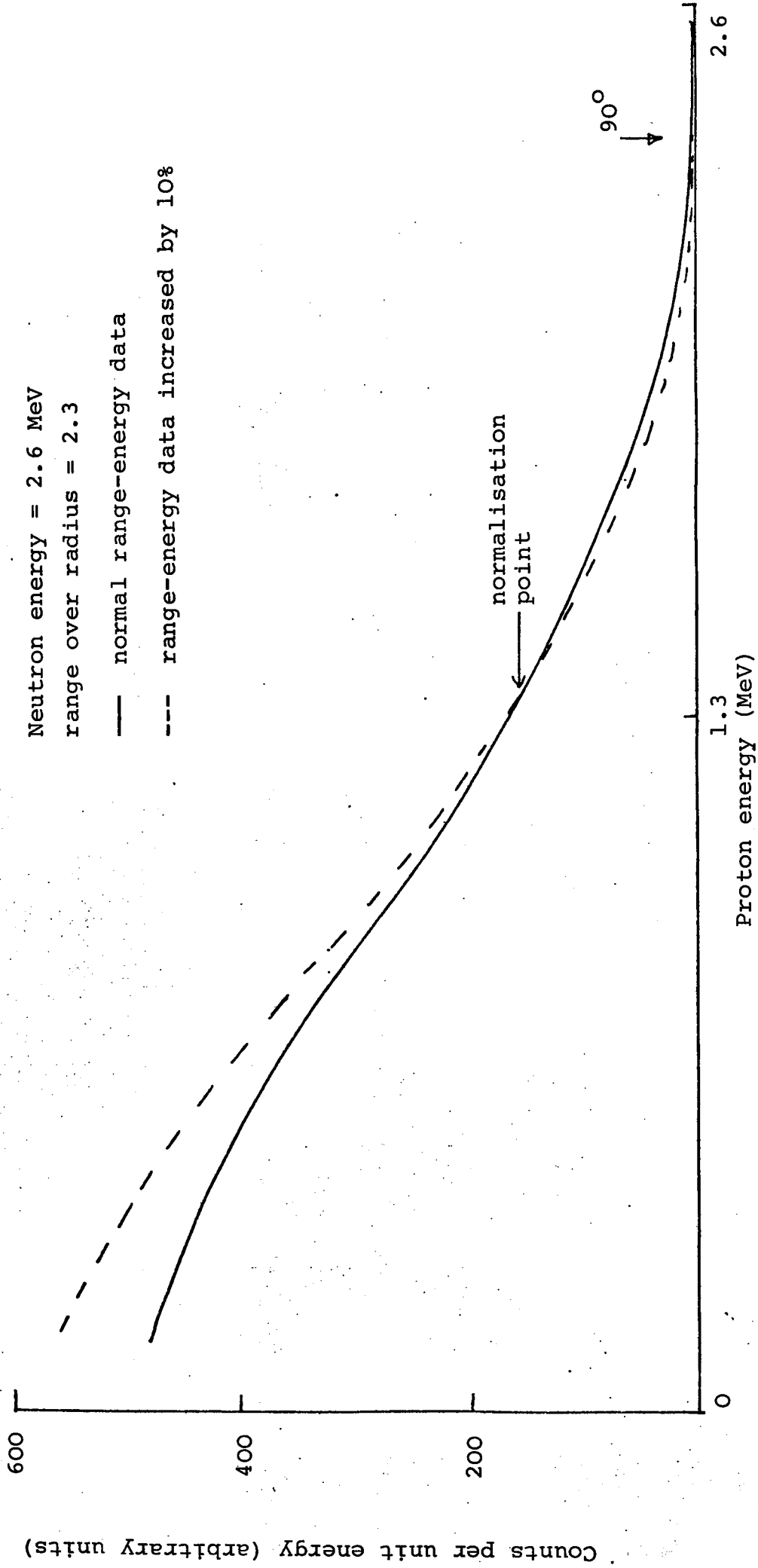
Figure 3.22: Response functions at 2.6 MeV and 10 Atm hydrogen
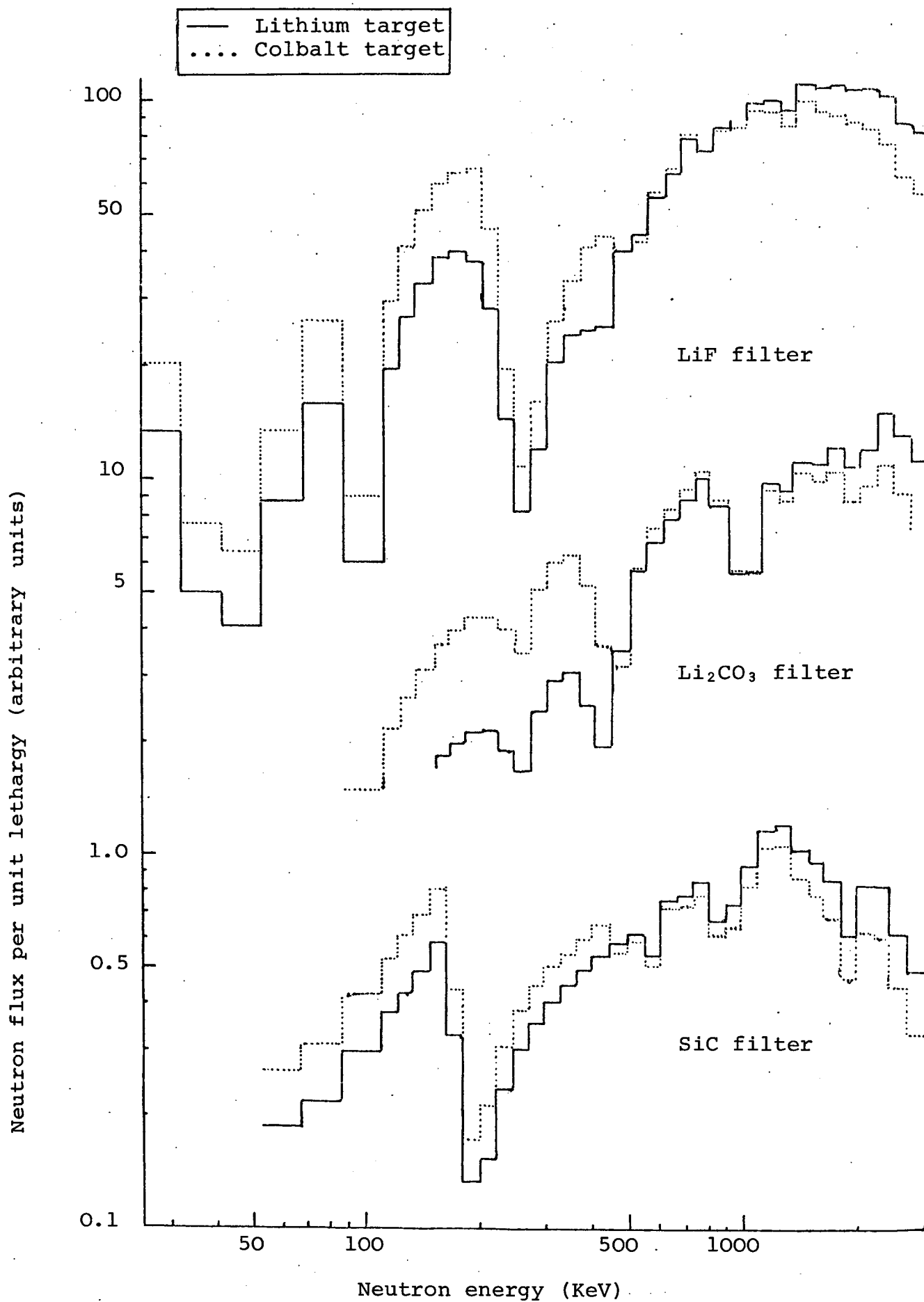
Figure 3.23: Theoretical neutron filter spectra
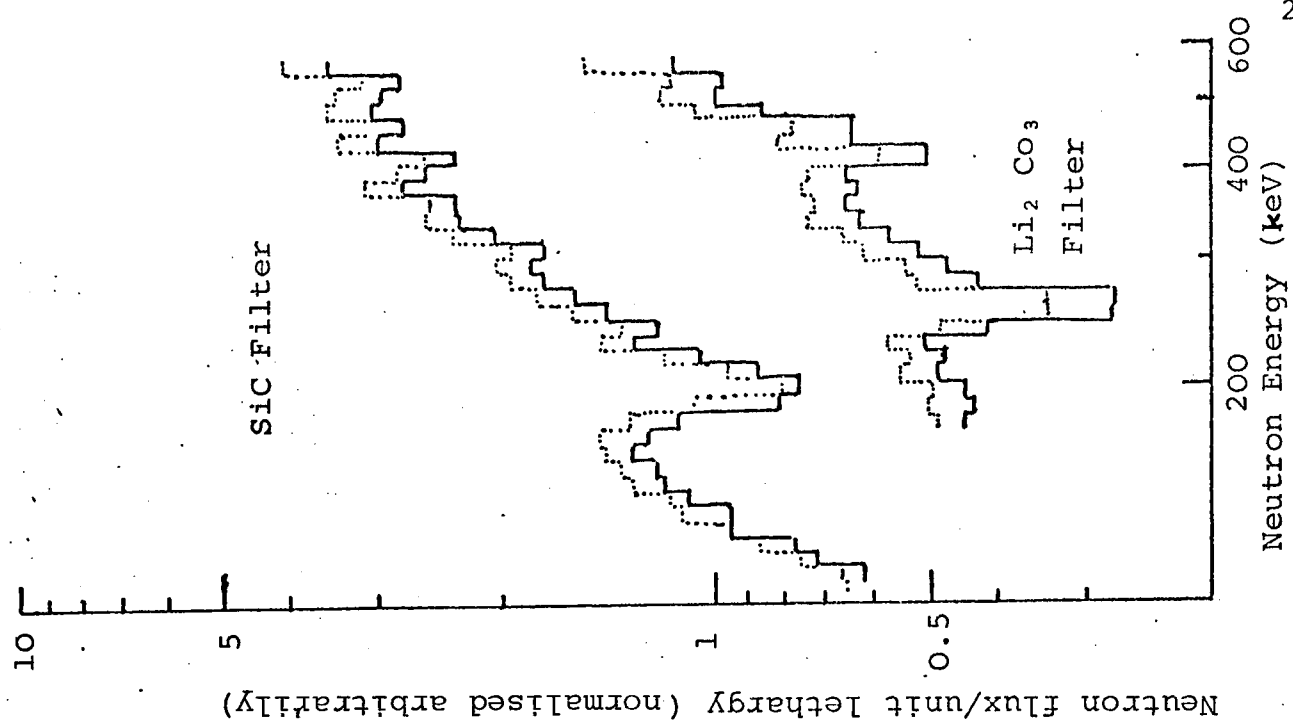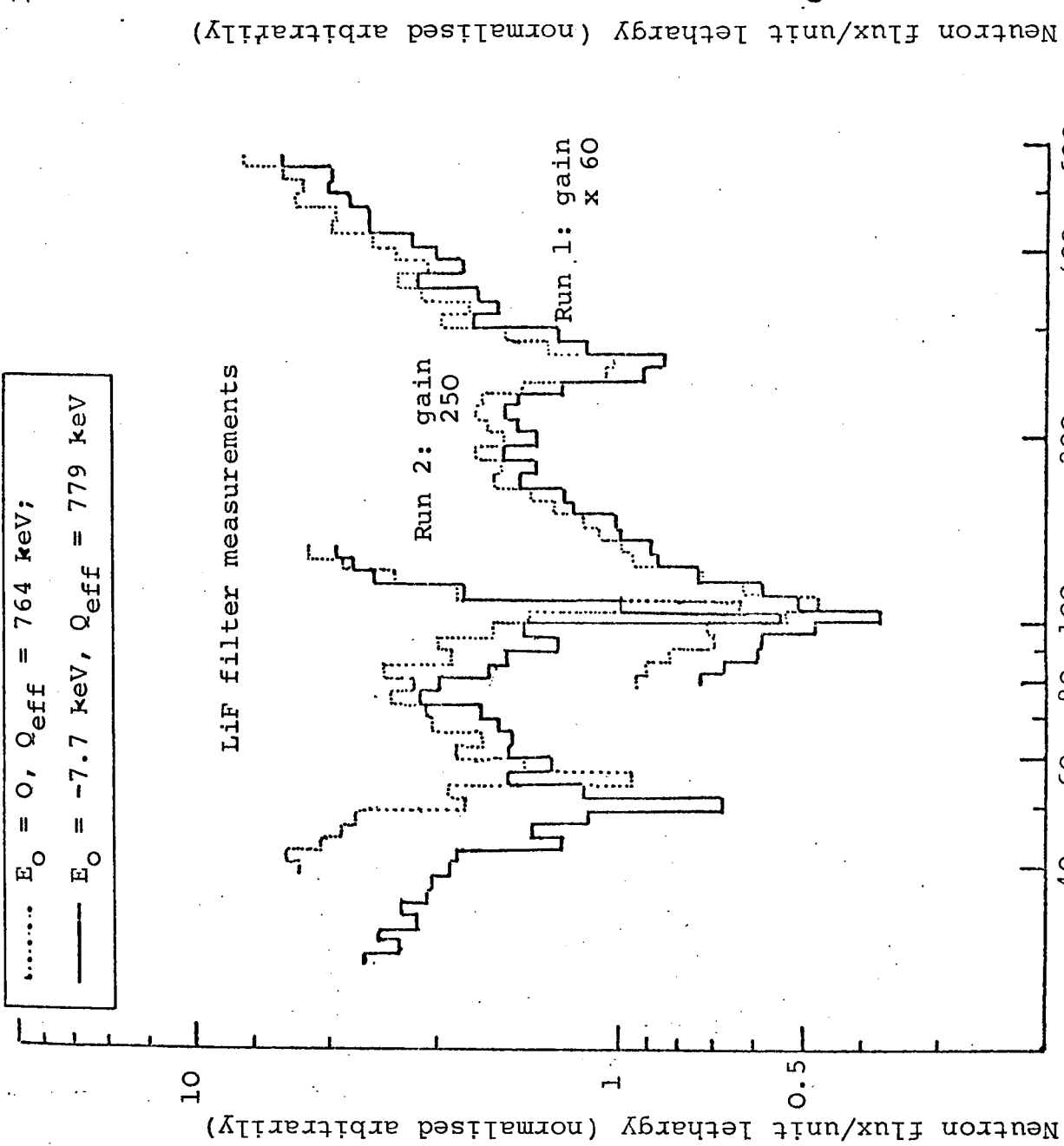
Figure 3.24: Filter measurements made with the 2.5 Atm counter
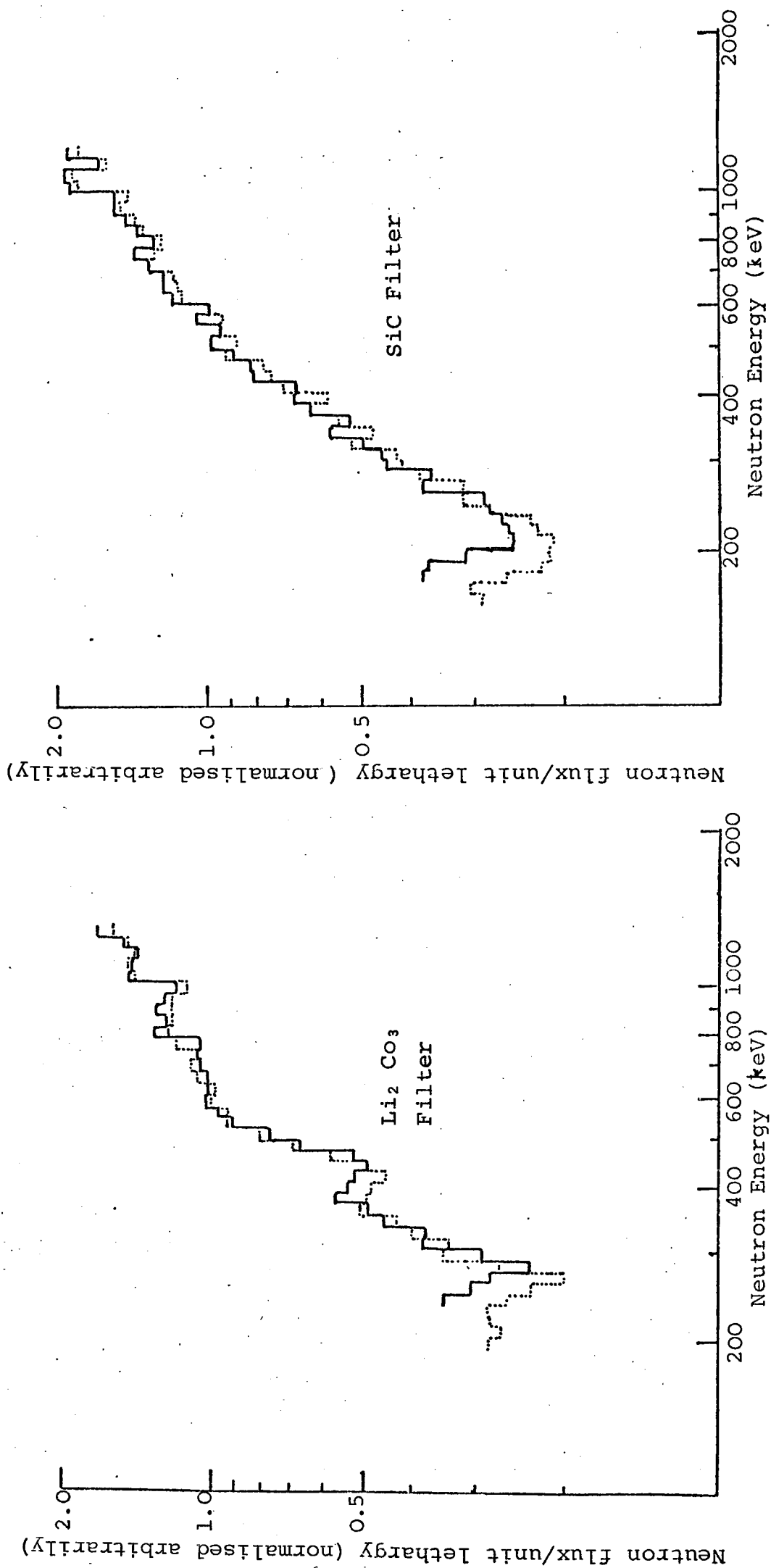
Figure 3.25: Resonance filter measurements for the 10 Atm hydrogen counter

.... $E_o = 0$, $Q_{eff} = 764$ keV; —— $E_o = 15.7$ keV, $Q_{eff} = 784$ keV

# Figure 3.26: Filter measurements with the argon-hydrogen counter
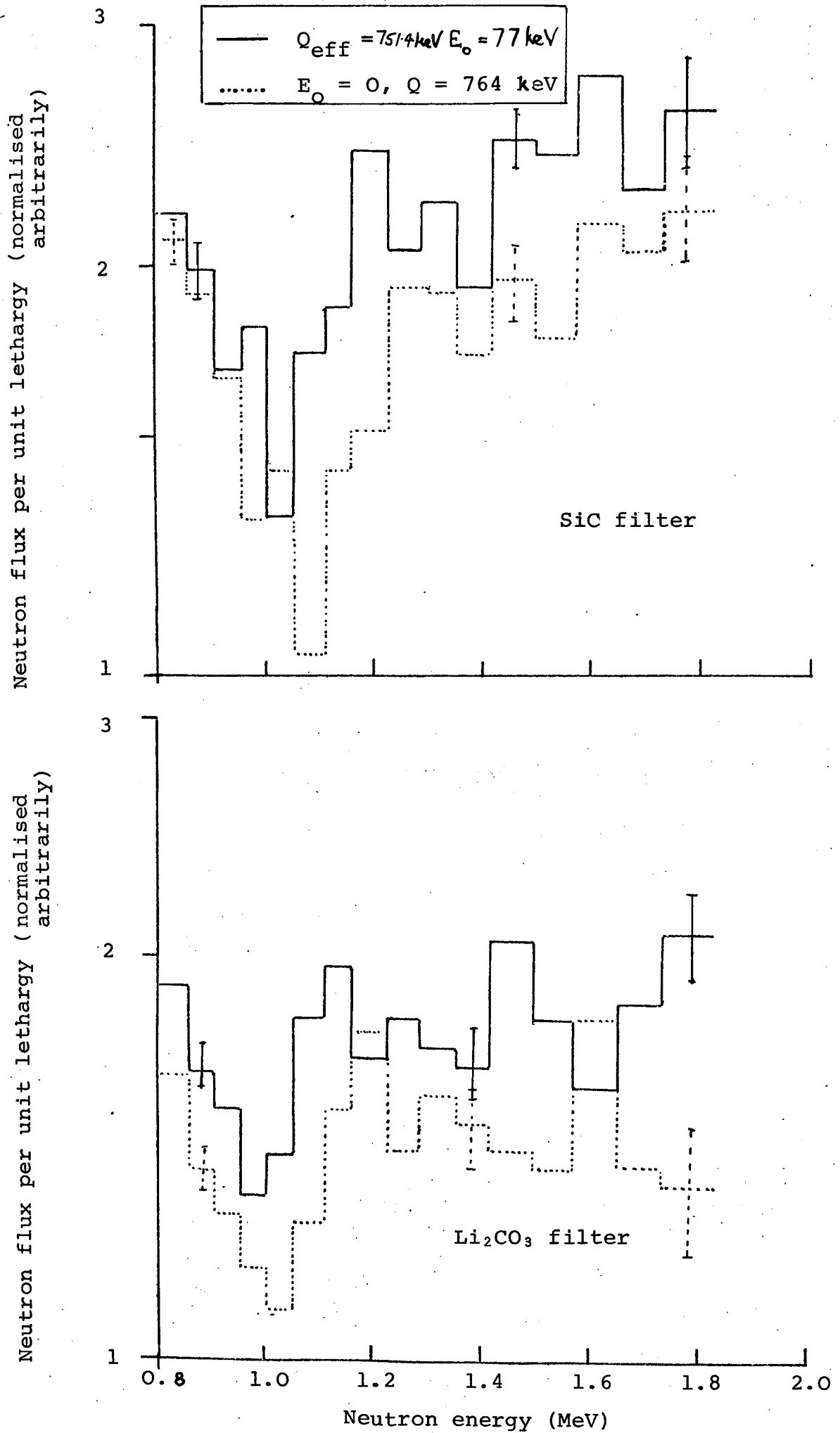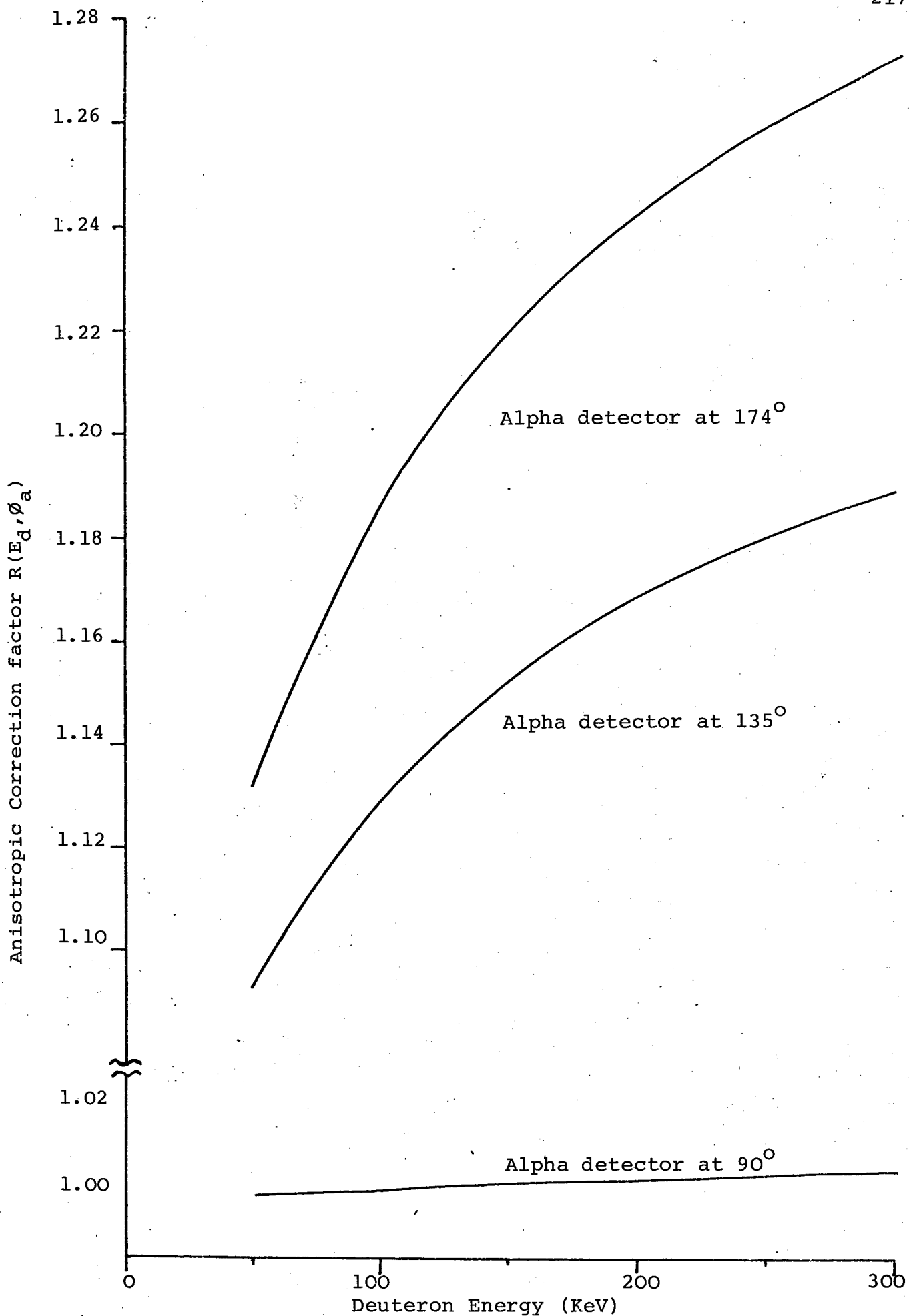
Figure 4.1: Anisotropic Correction factor versus deuteron energy for alpha detector angles of 90°, 135° and 174°
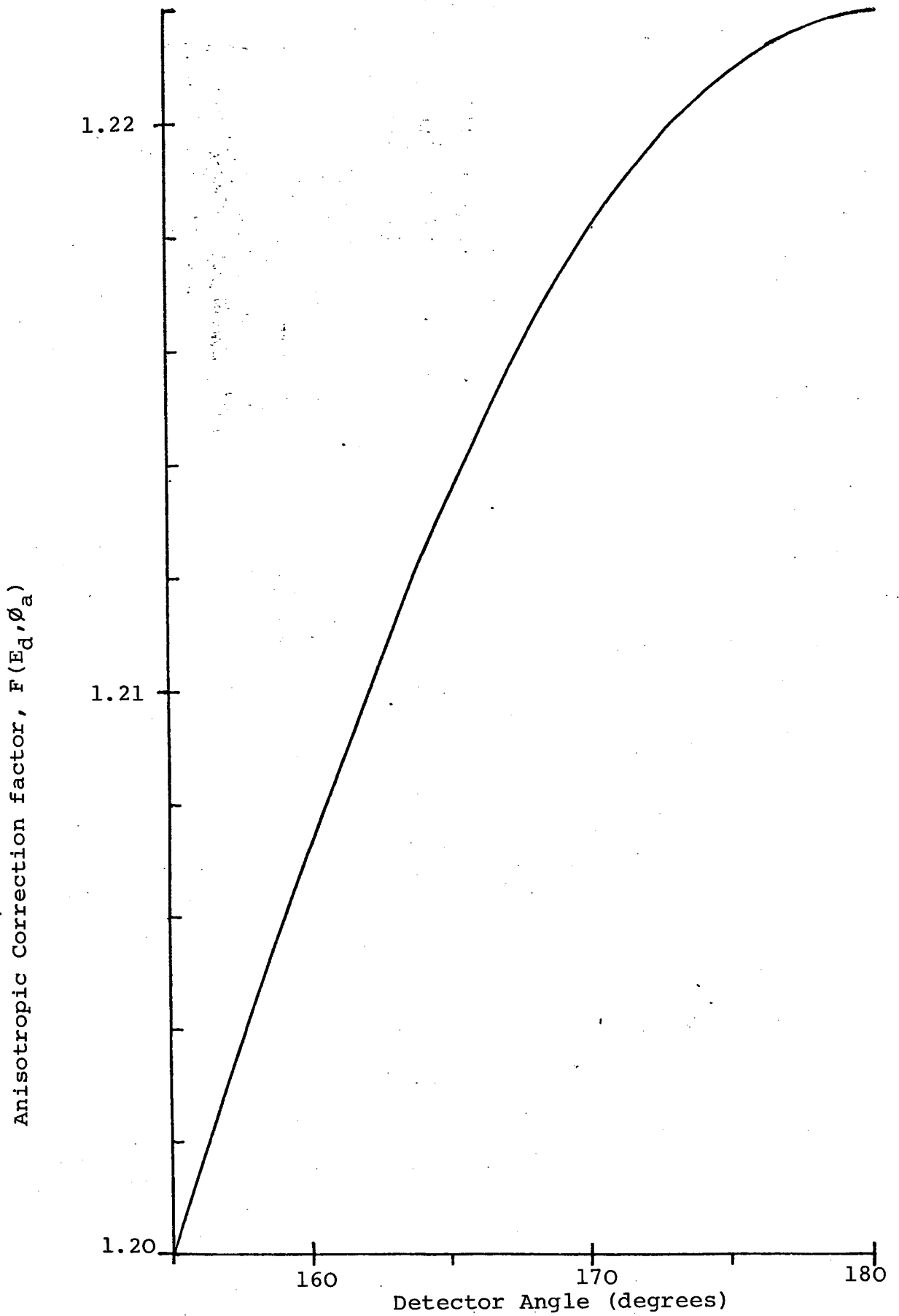
Figure 4.2: Anisotropic Correction factor versus Alpha Detector Angle for a Deuteron Energy of 150 KeV

Figure 4.3: Tritium surface distribution

(light areas indicate abundance of tritium)
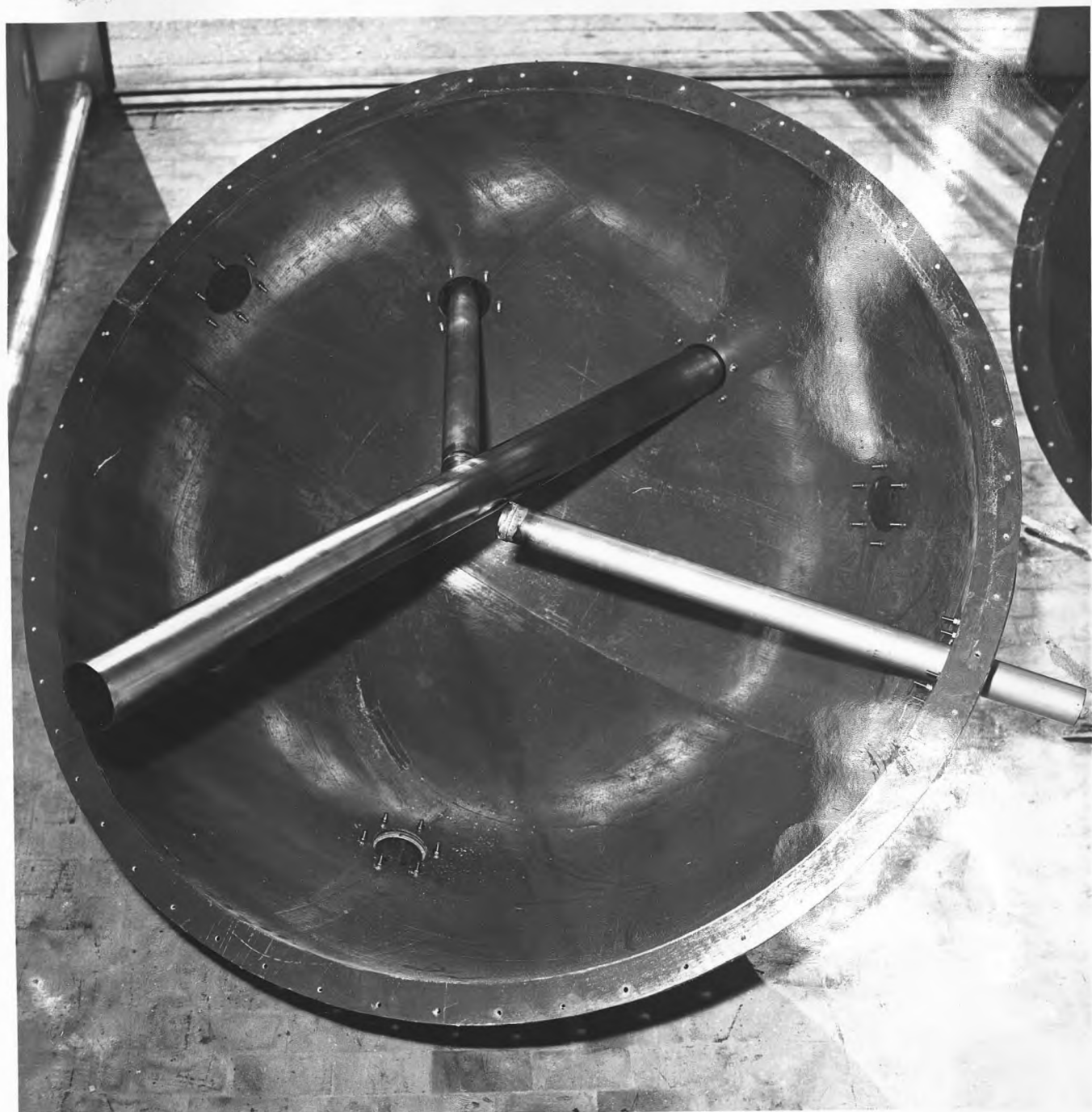
Figure 5.1:   Beam tube and measurement tubes in the lithium
              fluoride sphere

Neutron source tube
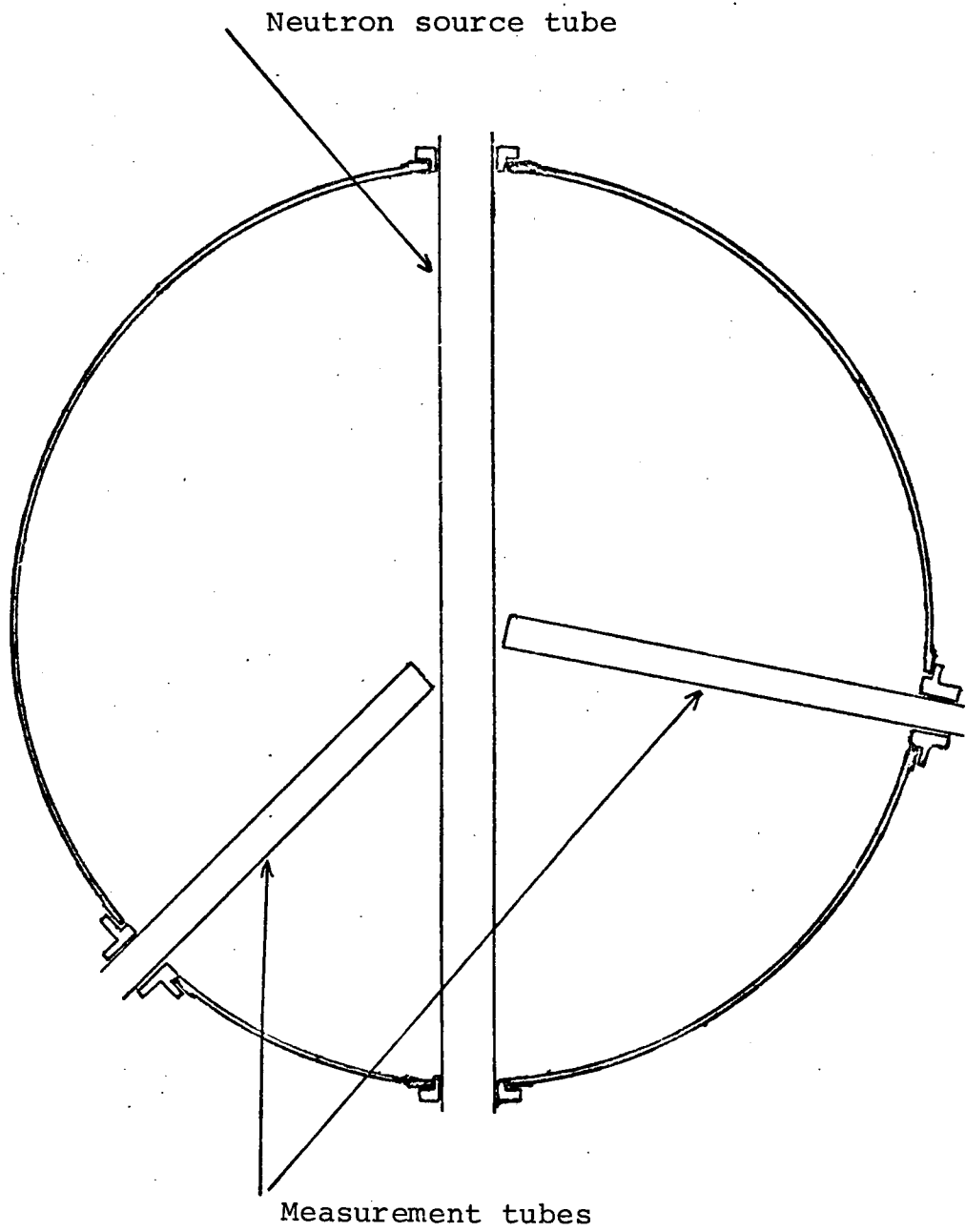
Measurement tubes

Figure 5.2: Schematic diagram of the neutron source
and measurement tubes in the LiF assembly

222
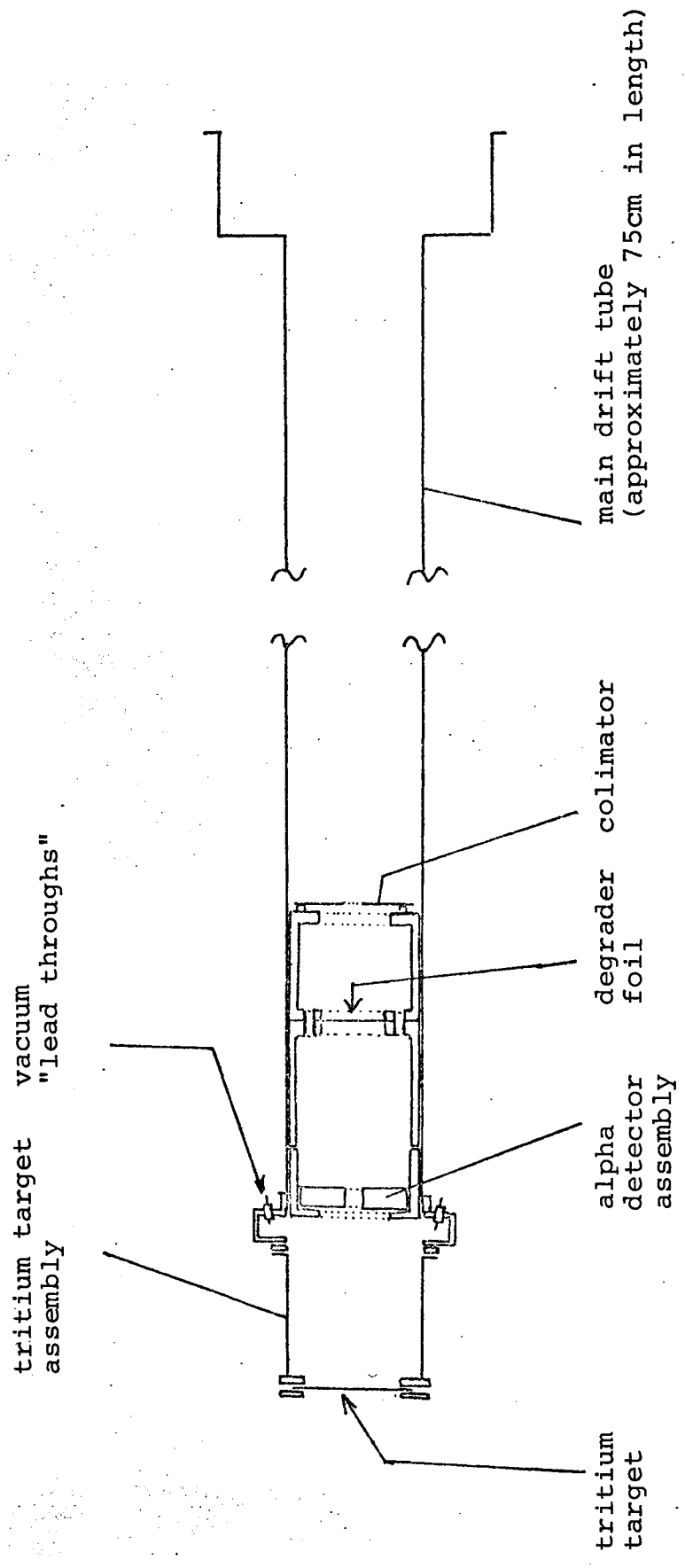
Figure 5.3: Schematic diagram of the vanadium bath target assembly

Figure 5.4: Vanadium bath target and counter assembly
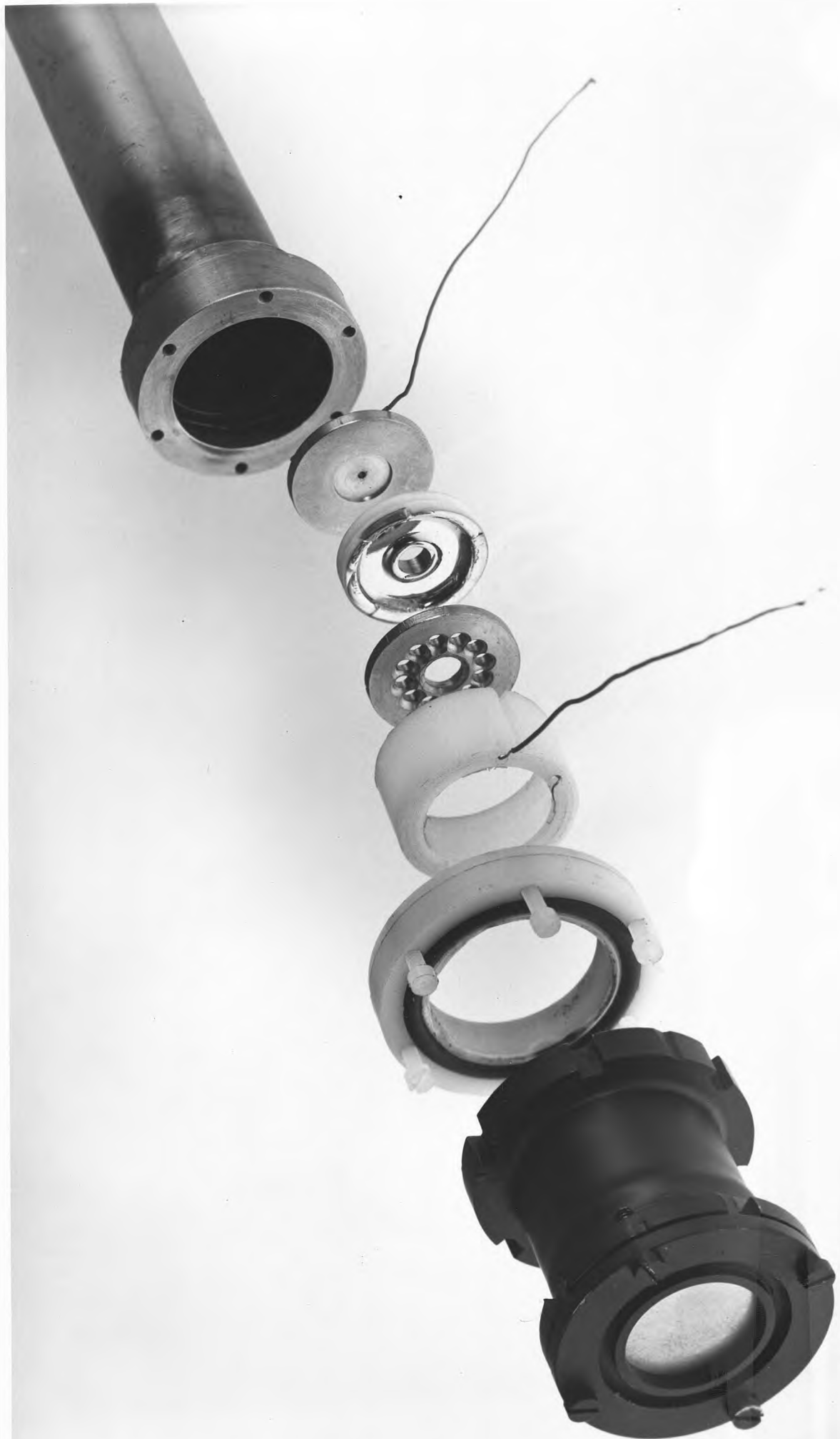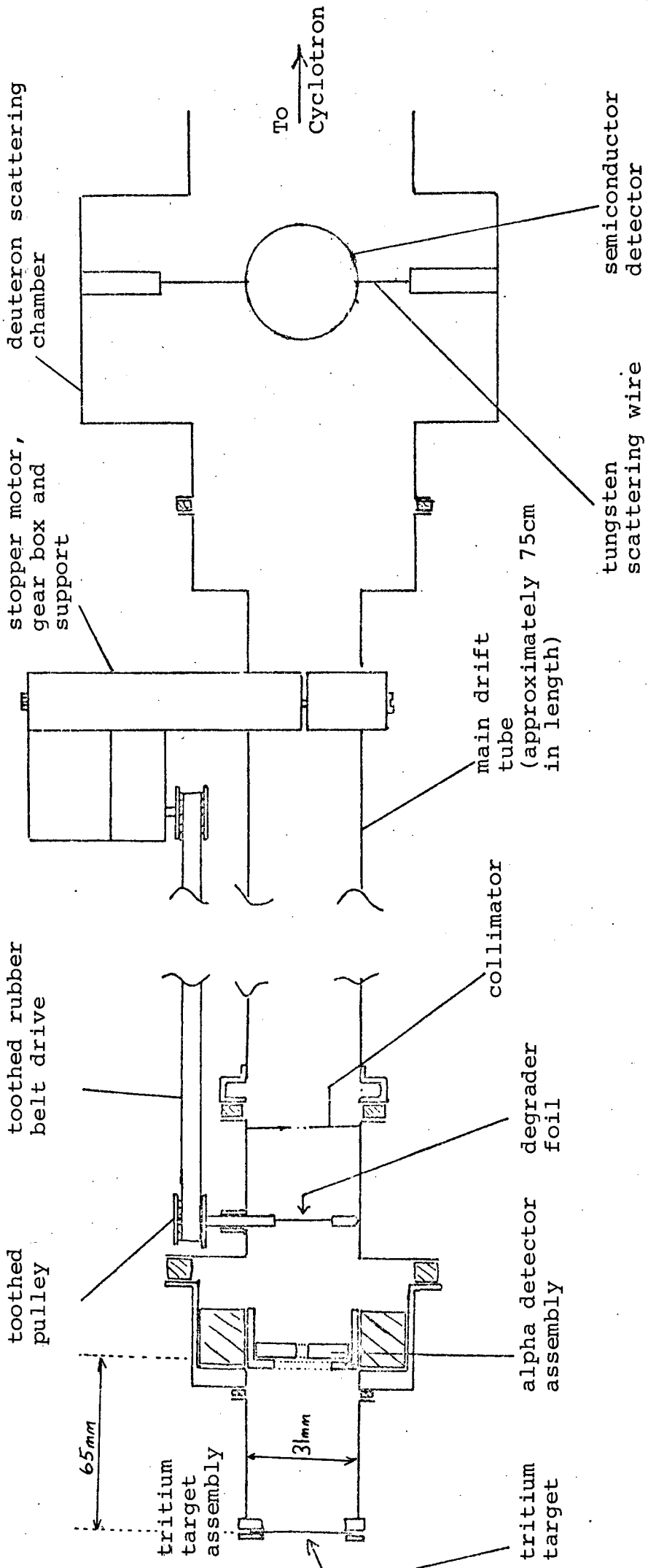
Figure 5.5: Schematic diagram of the LiF target assembly
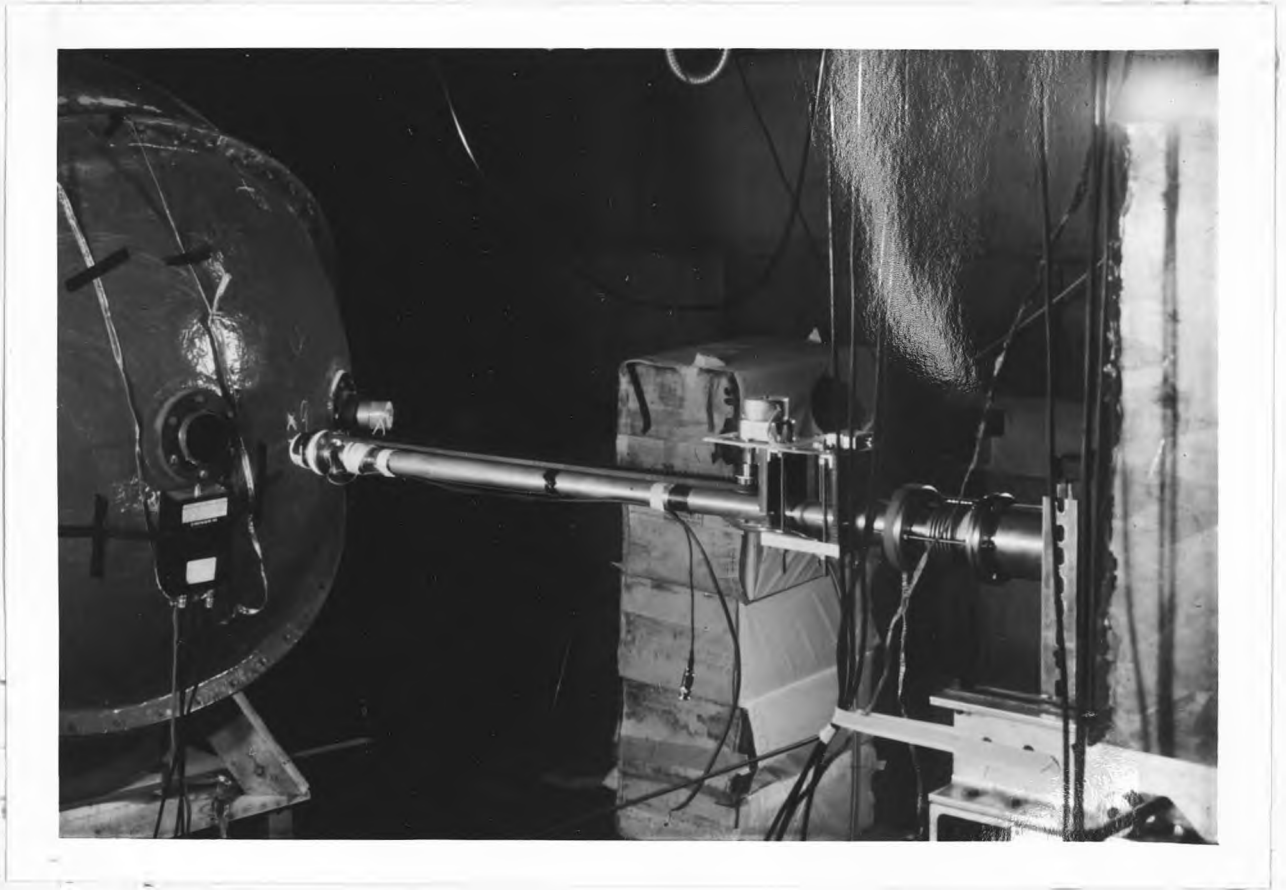
Figure 5.6: Drift tube and the lithium fluoride
assembly
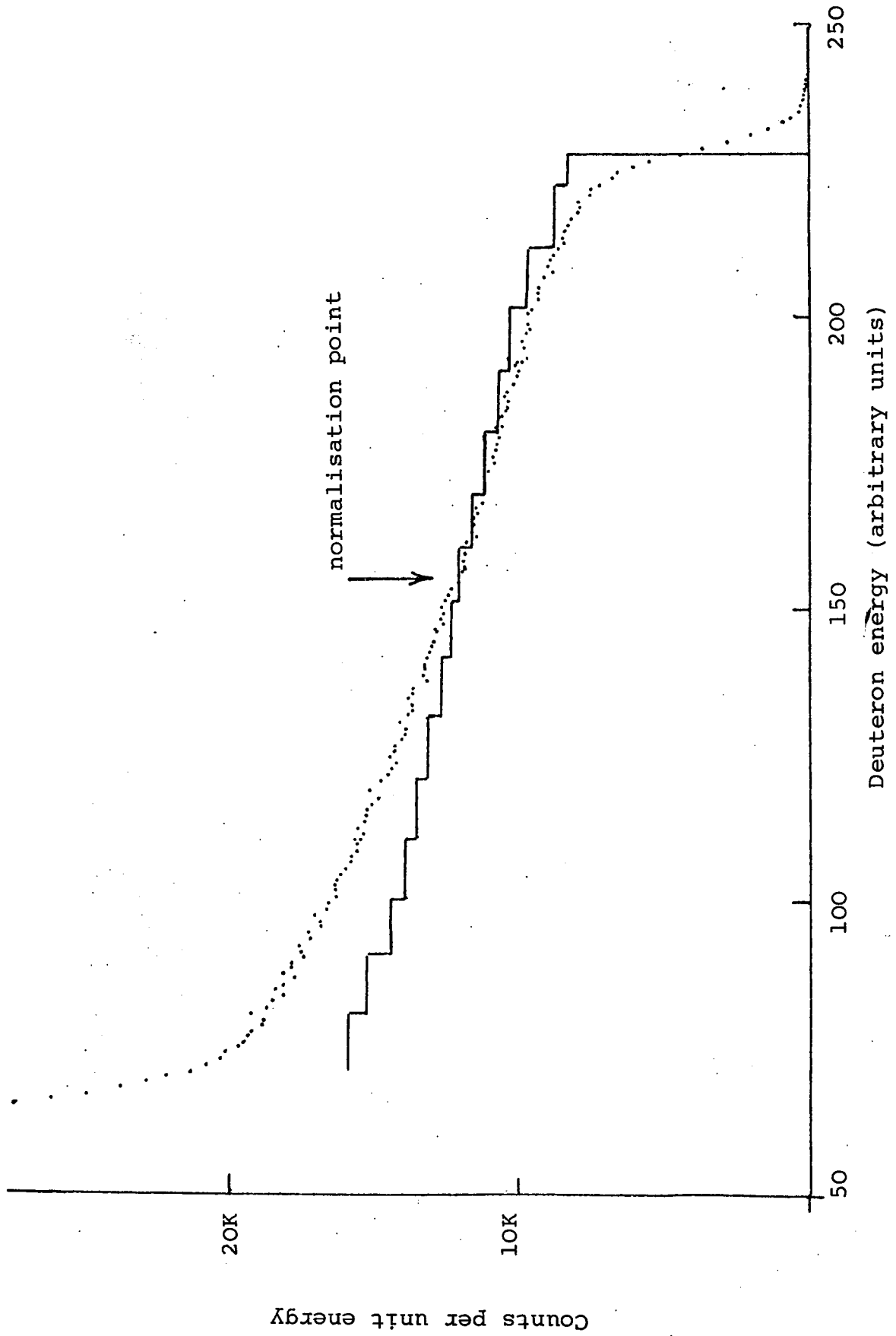
Figure 5.7: Experimental and calculated scattered deuteron spectra
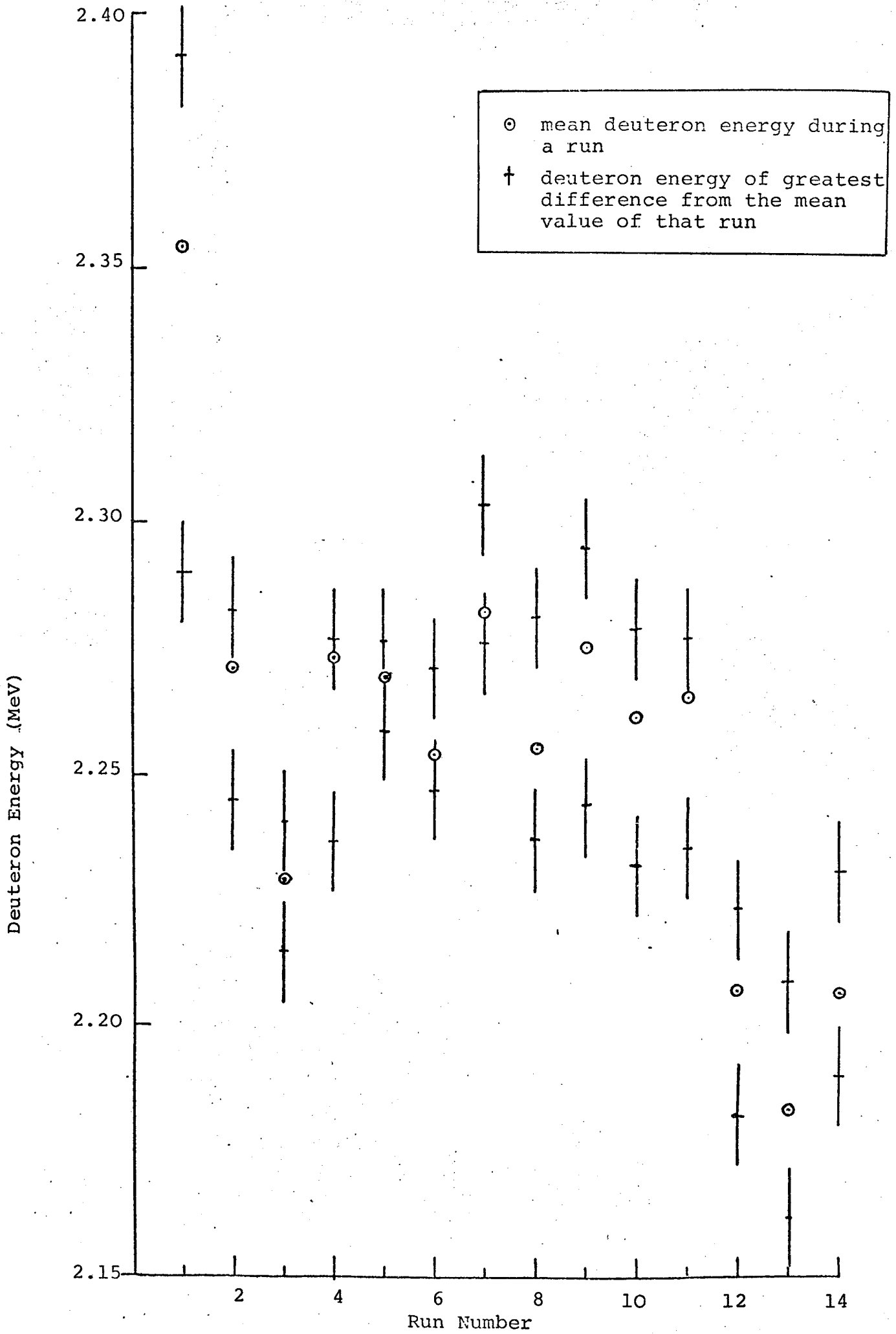
Figure 5.8:   Mean Deuteron Energies
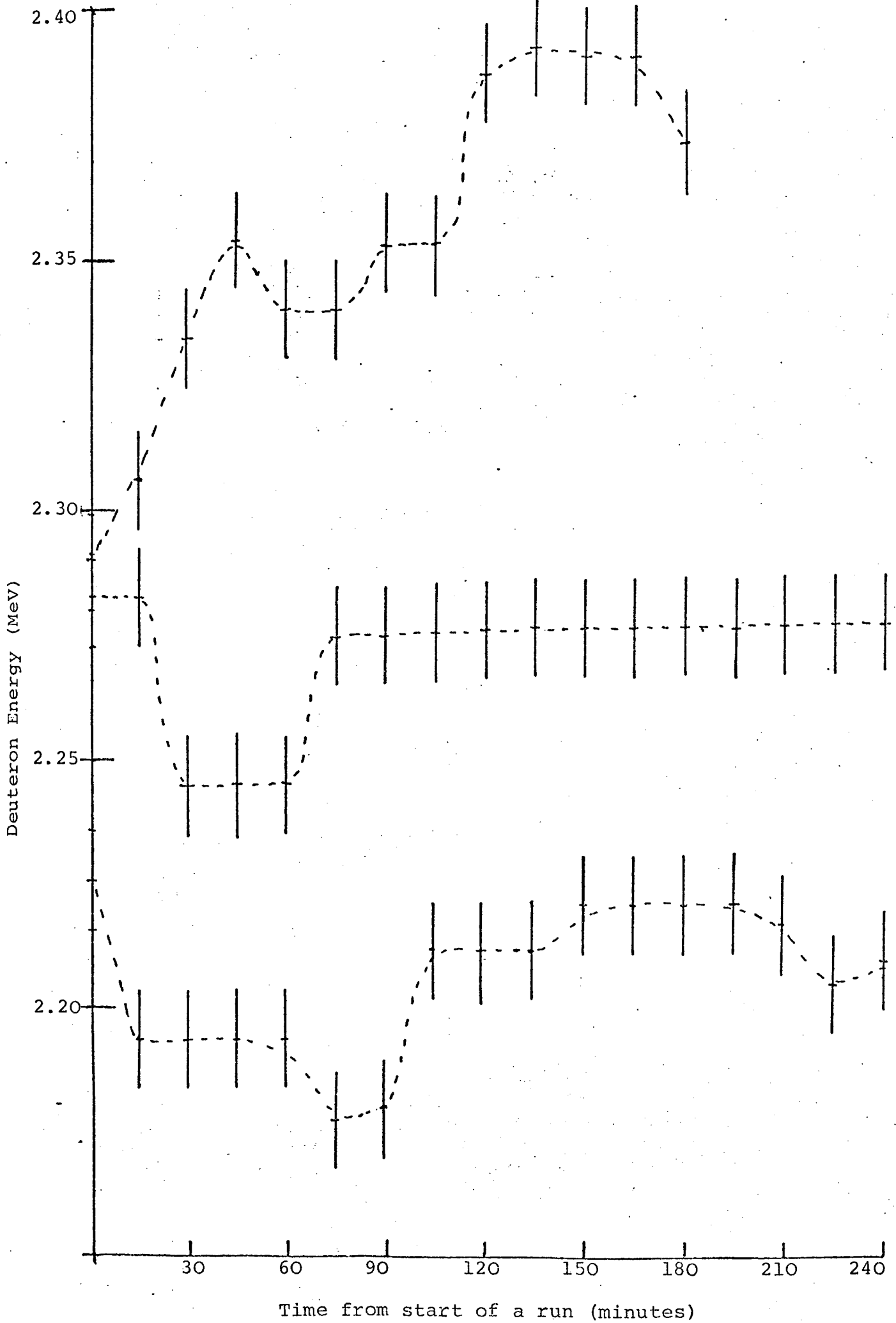
Figure 5.9: Variation of deuteron energy with time
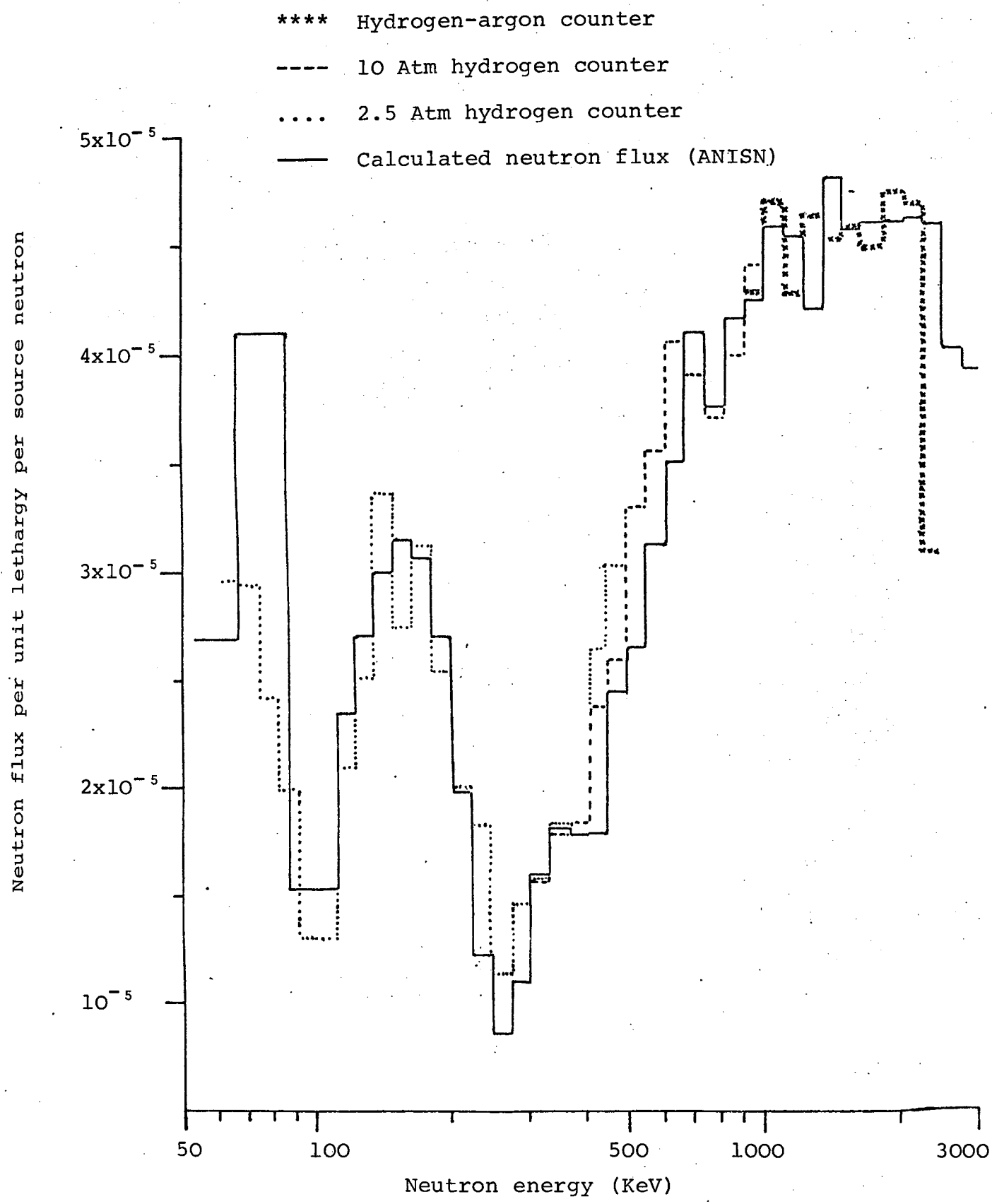
Figure 5.10:   Neutron spectrum at 27 cm

xxxx   Hydrogen-argon counter
----   10 Atm hydrogen counter
....   2.5 Atm hydrogen counter
———   Calculated neutron spectrum (ANISN)
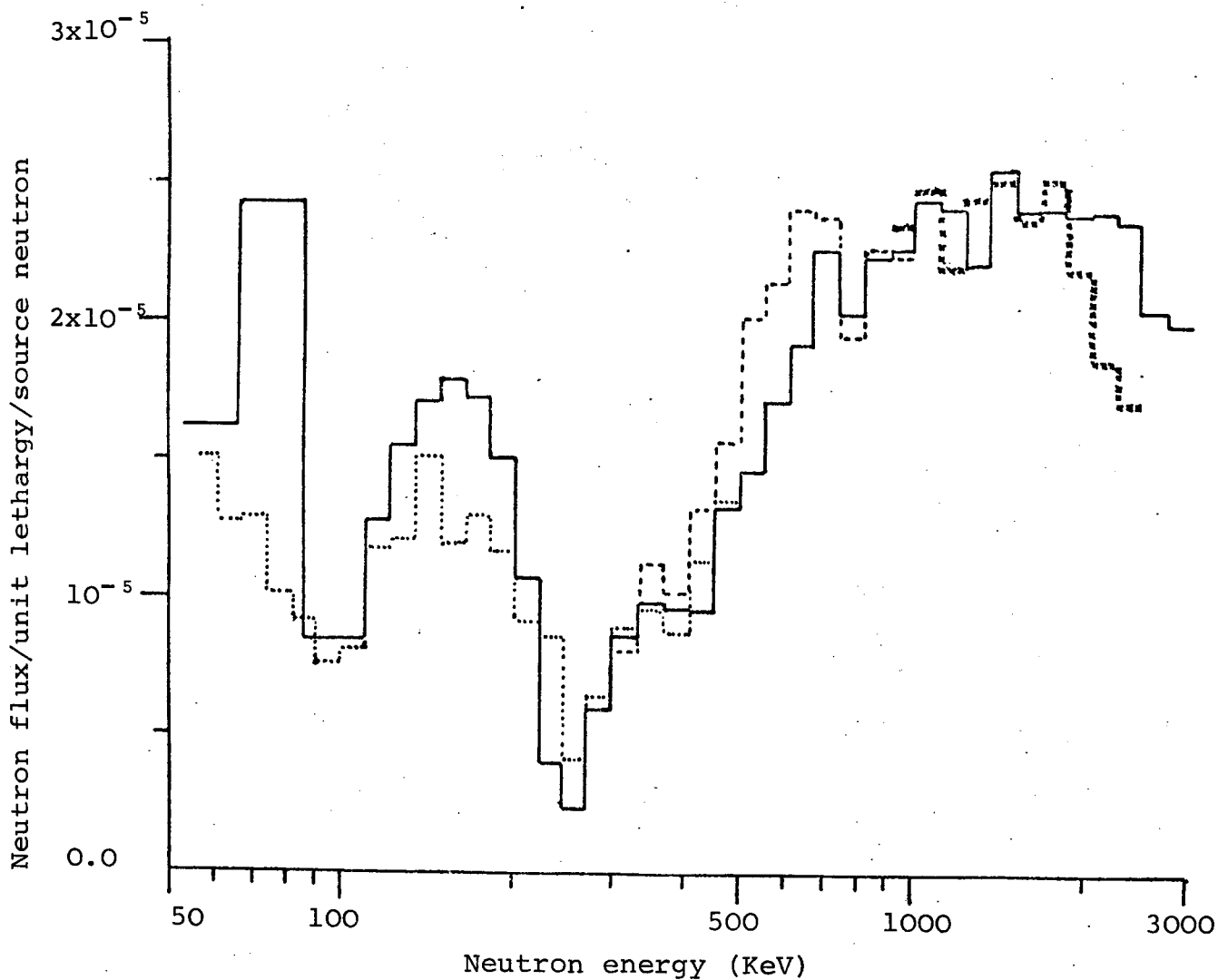
Figure 5.11:   Neutron spectrum at 37 cm
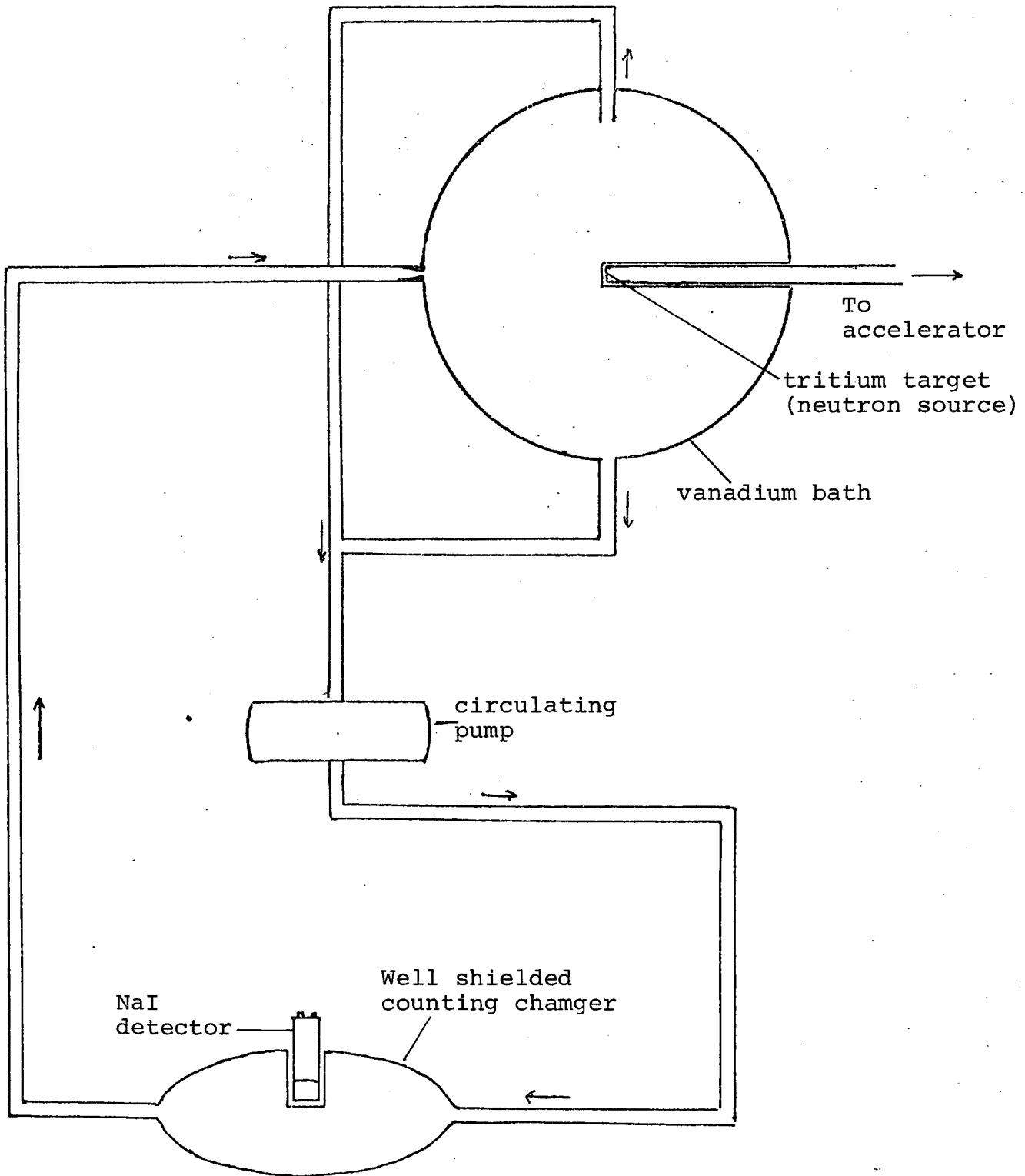
Figure 5.12:   Schematic diagram of the vanadium bath
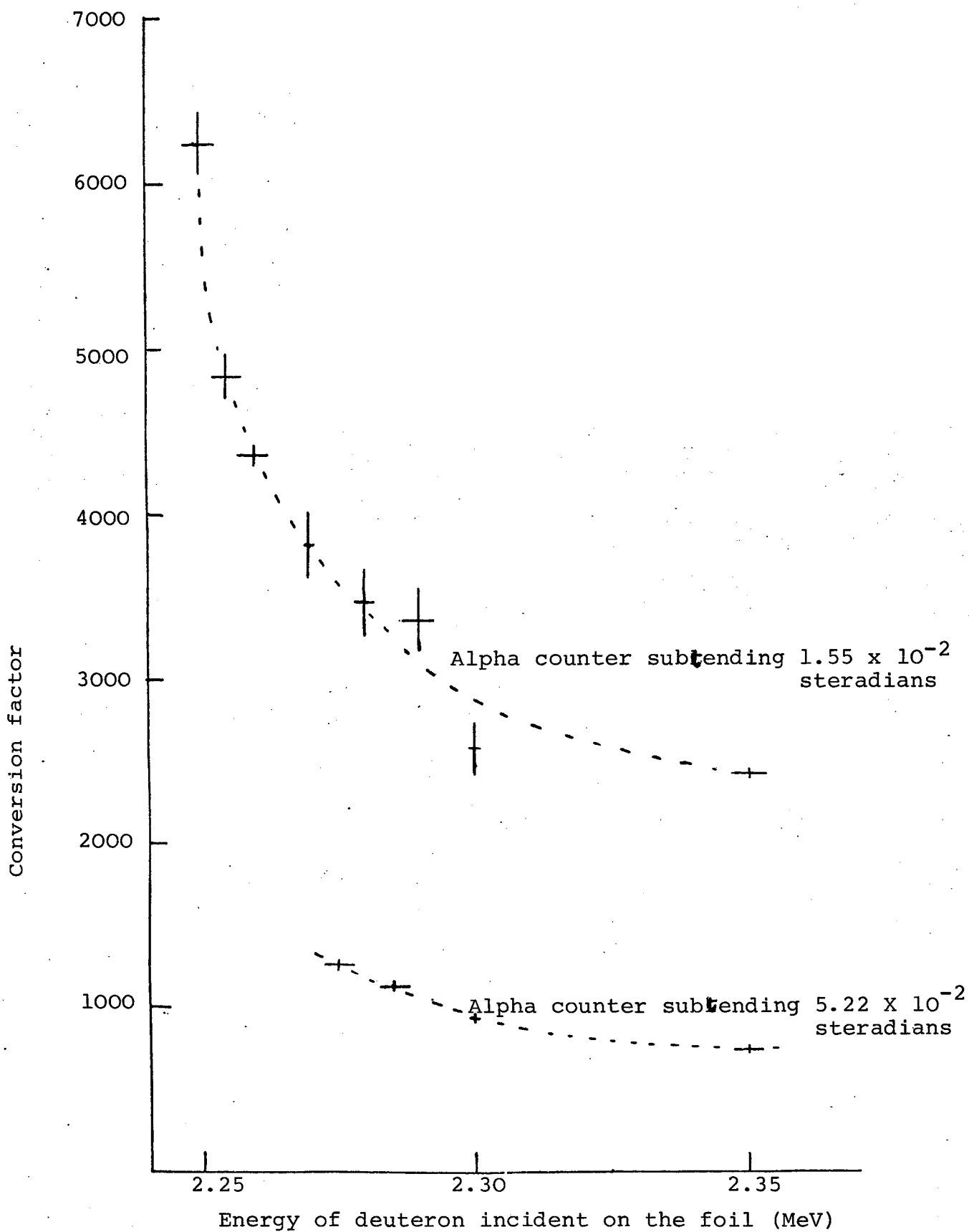
Figure 5.13: Conversion factor versus deuteron energy
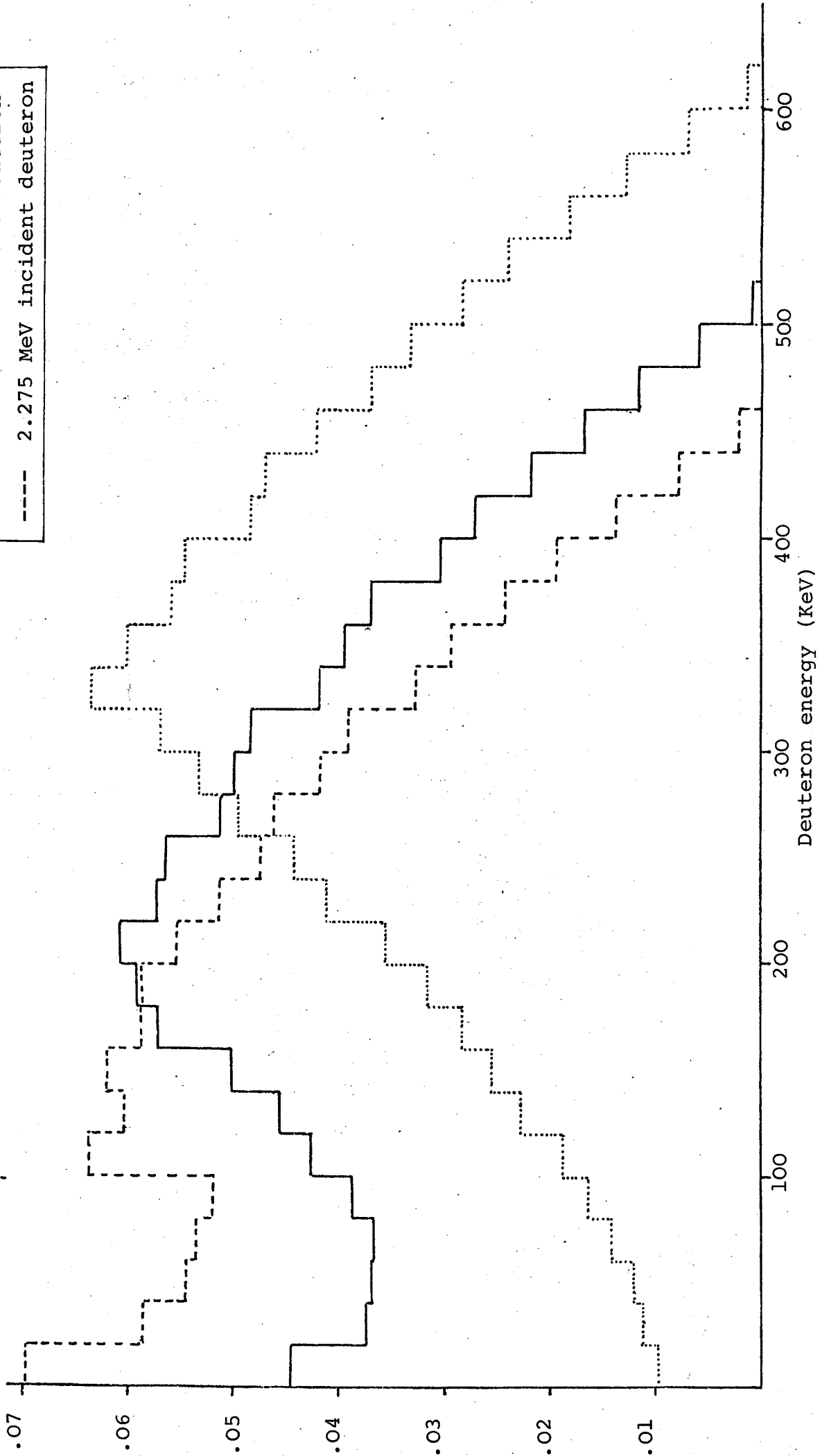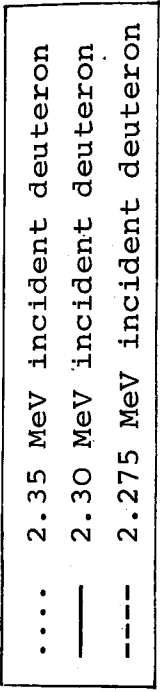
Figure 5.14: Emerging deuteron energy distributions from a foil of mean thickness 33.7 μm

KEY TO FIGURES 6.1 TO 6.3

1	Roughing pump
2	Activated alumina trap
3	Molecular sieve trap
4	Thermocouple gauge head
5	Liquid nitrogen cold trap
6	2" diffusion pump
7	Penning or ionisation gauge head
8	6" gauge section
9	6" gauge, 0 - 300 psig
10	Vertical storage section
11	Argon gas cylinder (research grade)
12	Methane gas cylinder (research grade)
13	Molecular sieve (type 3A) purifier
14	Horizontal storage section
15	Catalyst purifier
16	8" gauge, -15 to +200 psig
17	Counter section
18	Counter
19	Helium-3 section
20	Helium-3 storage cylinder
21	Palladium barrier
22	Hydrogen gas cylinder
23	Oxygen free nitrogen gas cylinder

⊗ ½" diaphragm valve   ⊛ Packless control valve

◍ 1/4" diaphragm valve   O Gas regulator

□ 1/8" needle valve

▨ Hone miniature instrument valve
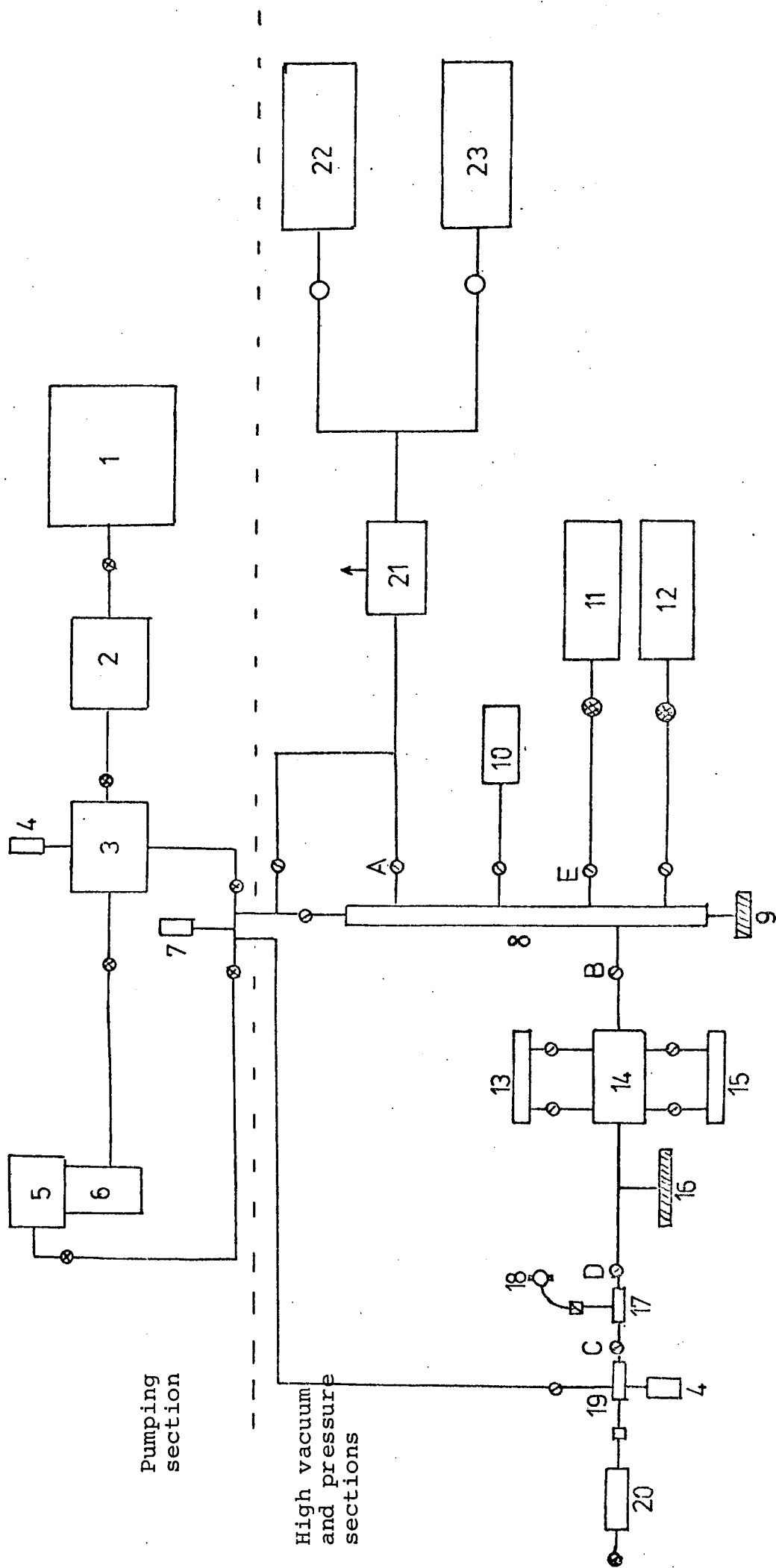
Figure 6.1: Counter filling rig
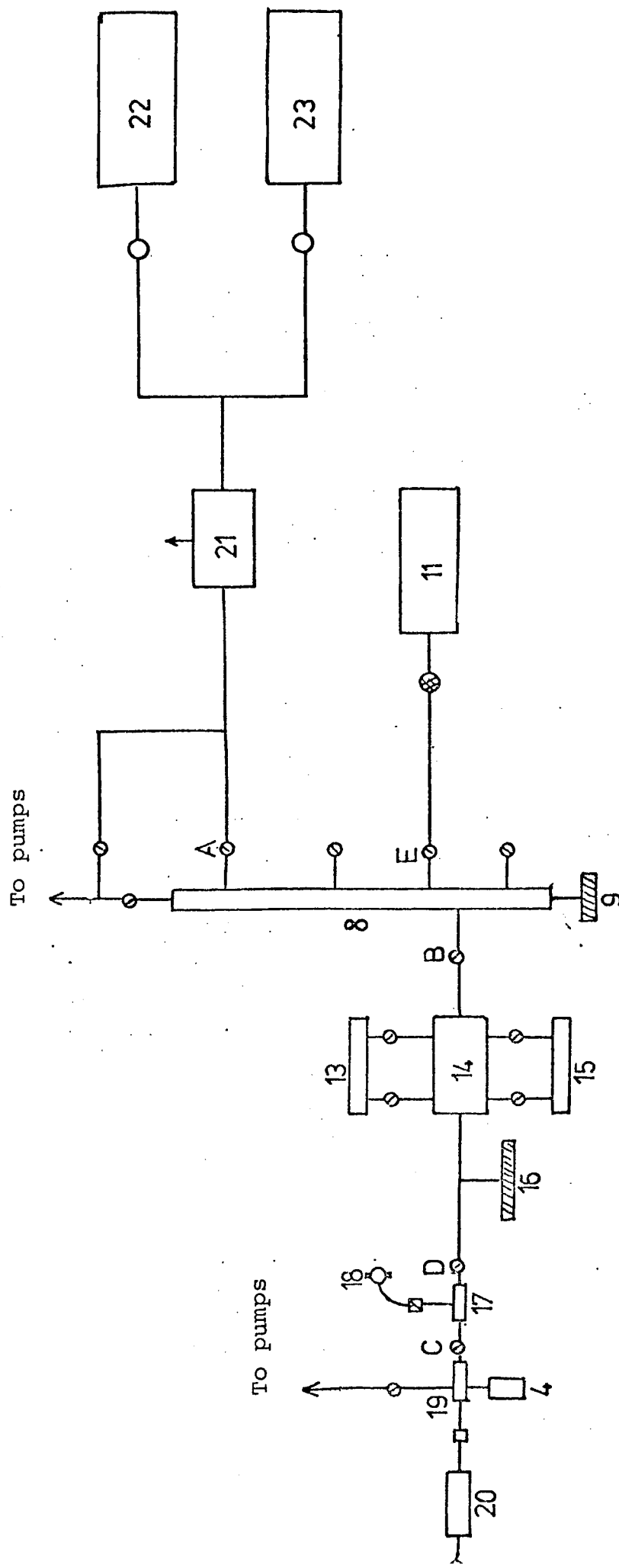
Figure 6.2: Sections used in a hydrogen gas filling
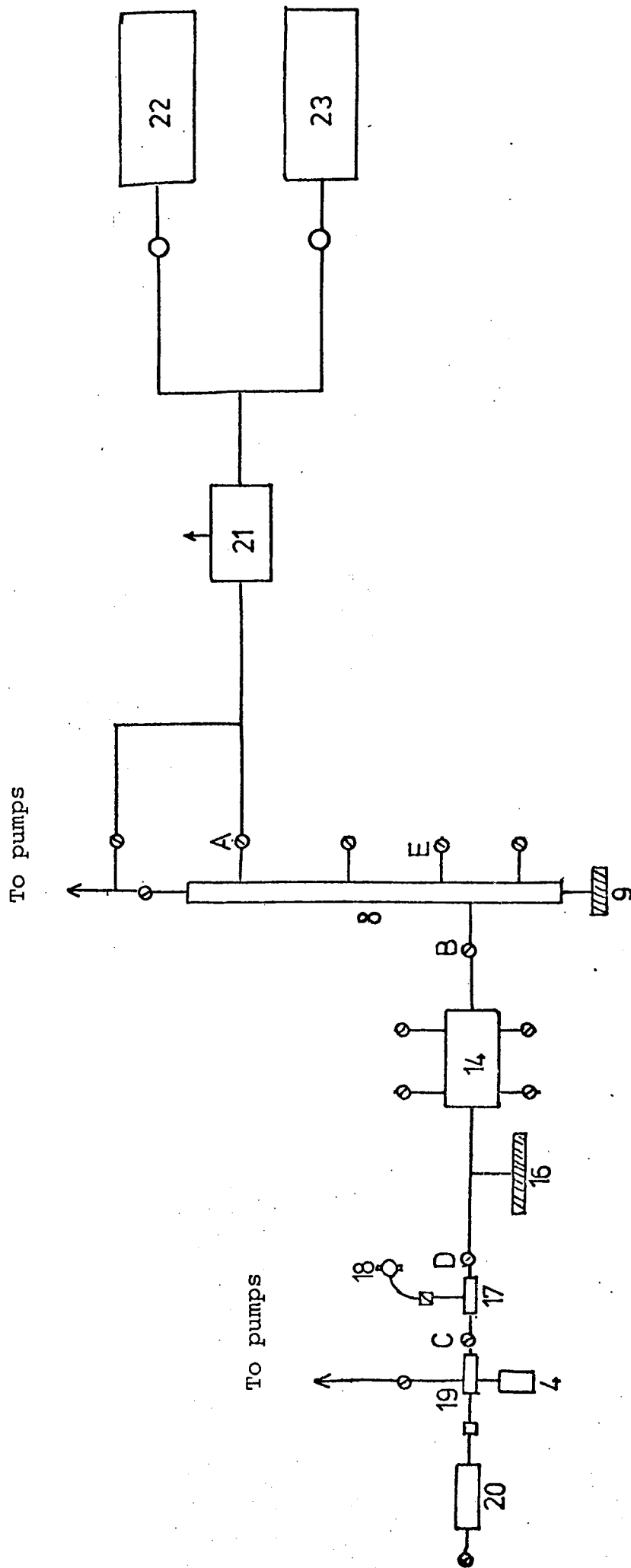
Figure 6.3: Sections used in an argon hydrogen gas filling

APPENDIX I: THE INSTRUMENTAL VARIABLE ESTIMATOR

In the case where a linear relationship between two variables ($y = \beta_1 + \beta_2 x$) is to be estimated from n observations on y and x, a least squares estimator (L.S.E.) is often used. The reason for this is that under the assumptions of the standard linear model the L.S.E. is not only unbiased and consistent but can be proved to be the best in the class of linear unbiased estimators in the sense that it has minimum variance.   (This result is known as the Gauss-Markov theorem and a proof is given by Johnston, 1963).   Consider the above problem rewritten in matrix notation then:

$$Y = X\beta + U \qquad\qquad (A1.1)$$

where

$$Y = \begin{bmatrix} y_1 \\ y_2 \\ \vdots \\ y_i \\ \vdots \\ y_n \end{bmatrix}, \quad X = \begin{bmatrix} x_1 \\ x_2 \\ \vdots \\ x_i \\ \vdots \\ x_n \end{bmatrix}, \quad \beta = \begin{bmatrix} \beta_1 \\ \beta_2 \end{bmatrix}, \quad U = \begin{bmatrix} u_1 \\ u_2 \\ \vdots \\ u_i \\ \vdots \\ u_n \end{bmatrix}$$

and so y_i is the ith observation on the dependent variable and u_i is the extent to which y_i falls short of or exceeds $\beta_1 + \beta_2 x_i$. Then the assumptions of the standard linear model are:

(1) $E(U) = O$

(2) $E(UU^1) = \sigma^2 I_n$

(3)   X is non-stochastic, which implies $E(X^1U) = O$

(4)   the number of observations exceeds the number of parameters to be estimated (i.e. n > 2 here).

Where E denotes the expected value and U^1 is the transpose of U.

The first and second assumptions imply that the u_i are

uncorrelated random variables, each with mean zero and with the same variance, σ^2. The third assumption, that the x_i are non-stochastic, implies that the x_i are measured without error.

However, in many situations X cannot be observed without error, so X is stochastic and in these cases the L.S.E. can be shown (see for example Johnston, 1963) to give a biased estimate of β. Furthermore the bias will not disapper as $n \to \infty$ i.e. the estimates are inconsistent. In fact, in this case the slope coefficient, β_2, is underestimated by Least Squares in large samples.

Let us consider the case where both the y_i and x_i are measured with error, thus:

$$y_i = y_i{}^* + w_i \qquad\qquad (A1.2)$$

and $\qquad x_i = x_i{}^* + v_i \qquad\qquad (A1.3)$

where y_i and x_i are the observed values as before and $y_i{}^*$ and $x_i{}^*$ are the true values. Therefore, w_i and v_i are the errors in the observations. If the true relationship is given by

$$y_i{}^* = \beta_1 + \beta_2 x_i{}^* \qquad\qquad (A1.4)$$

then substituting from (A1.2) and (A1.3) yields

$$y_i = \beta_1 + \beta_2 x_i + \bar{u}_i \qquad\qquad (A1.5)$$

where $\qquad \bar{u}_i = w_i - \beta_2 v_i \qquad\qquad (A1.6)$

or in matrix notation:

$$Y = X \beta + \bar{U} \qquad\qquad (A1.7)$$

where $\qquad \bar{U} = \begin{bmatrix} \bar{u}_1 & \bar{u}_2 & \ldots & \bar{u}_i & \ldots & \bar{u}_n \end{bmatrix}^1$

Suppose that a matrix Z of order (nx2) can be found such that the columns of Z are observations on two "instrumental variables" which are independent of (minimally uncorrelated with) the error terms of the system and correlated (presumably highly) with the explanatory variables (X). So premultiplying (A1.7) by

Z^I/n yields:

$$\frac{Z^1 Y}{n} = \frac{Z^1 X \beta}{n} + \frac{Z^1 \overline{U}}{n}$$

(A1.8)

and from the above assumptions

$$\plim_{n \to \infty} \left[\frac{Z^1 \overline{U}}{n} \right] = 0$$

(A1.9)

As the last term in (A1.8) vanishes in probability, one may obviously consider instead:

$$\frac{Z^1 Y}{n} = \frac{Z^1 X}{n} \beta$$

(A1.10)

and hence derive the instrumental variable estimator (I.V.E.)

$$\hat{\beta} = (Z^1 X)^{-1} Z^1 Y$$

(A1.11)

It should be noted that replacing Z by X in equation (A1.11) gives the L.S.E. The I.V.E. can be shown to give a consistent estimate of β in the case where errors exist in the measured y_i and x_i, unlike the L.S.E. which is both biased and inconsistent in this case. The variance of the I.V.E. is greater than that of the L.S.E., but the difference in the variances decreases as the correlation between Z and X increases. Clearly, it is desirable to choose a matrix of instrumentable variables that is as highly correlated as possible with X, while still being uncorrelated with $\overline{U}$. One of the difficulties of the I.V. approach is the arbitrary nature of the instrumental variables chosen, leading possibly to large variations in the resultant estimates depending on the instrumental variables chosen. Secondly, it may be difficult to check that the instrumental variables are uncorrelated with the errors, $\overline{U}$.

In the work in chapter III the matrix Z was chosen to be of the form:

$$Z = \begin{bmatrix} 1 & z_1 \\ 1 & z_2 \\ \vdots & \vdots \\ 1 & z_i \\ \vdots & \vdots \\ 1 & z_n \end{bmatrix}$$

Clearly, the correlation between the first column of Z and the first column of X is maximised. Several sets of z_i were tried to gain experience in the variation of the estimates of β by arbitrarily chosing different sets of z_i. As the X observations increased $(x_i < x_{i+1})$ an increasing z_i is desired for high correlation between Z and X. Finally, a simple rank I.V., $z_i = i$ was chosen. With the energy-ionisation data of chapter III, this Z and X were fairly highly correlated and the chi-square test indicated that the I.V.E. gave a better fit to the data than the L.S.E., whose estimate of β_2 was biased downwards, as expected, when compared with the I.V. estimate of β_2.

```
                        ( Start )
                            |
                            v
    \ I/P Range-energy data, Neutron flux above EMAX, /
     \         Response Correction factors,          /  <---+
      \        A.D.C. and counter parameters        /       |
                            |                                |
                            v                                |
      \      O/P Neutron flux above EMAX         /           |
       \     and A.D.C. and counter parameters  /            |
                            |                                |
                            v                                |
                          is                                 |
                      EMAX on          No                    |
                   A.D.C. Scale  ----------->  ------------->+
                            |
                          Yes
                            |
                            v
   +---------------------------------------------------+
   | Generate: range-energy table for counter filling  |
   | Generate: matrix of differentiated response       |
   | functions weighted by counter efficiency.         |
   +---------------------------------------------------+
                            |
                            v
   +---------------------------------------------------+
   | Calculate: ionisation spectrum due to neutrons    |
   |                  above EMAX                        |
   +---------------------------------------------------+
                            |
                            v
    \     I/P Recoil proton ionisation spectrum       /
                            |
                            v
   +---------------------------------------------------+
   | Subtract from recoil ionisation spectrum contribution |
   |          due to neutrons above EMAX               |
   |     Divide by monitor counts and ω to obtain      |
   |     recoil proton spectrum per monitor count      |
   +---------------------------------------------------+
                            |
                            v
   +---------------------------------------------------+
   | Calculate: grouped spectrum of slopes of recoil proton |
   |          spectrum and estimate errors             |
   +---------------------------------------------------+
                            |
                            v
   +---------------------------------------------------+
   |     Calculate: fluxes per monitor count           |
   +---------------------------------------------------+
                            |
                            v
    \ O/P fluxes per monitor count, energy groups /
     \          and errors                       /
                            |
                            v
                        ( Stop )
```

Figure A2.1:   Flow diagram of the computer programme   SPEC4

I/P   Input

O/P   Output

APPENDIX II: FORTRAN PROGRAMME SPEC4

This appendix outlines the computer programme, SPEC4,
used to unfold the neutron flux from the recoil proton data in
chapters III and V.   The version used in this work is modified
from the listing given by Kemshall, 1973.   The main
modifications have been the segmentation of the programme and
alteration of some array sizes   to enable the programme to be
run in the mini-computer in the Birmingham Radiation Centre.
This computer is linked to the satellite computer which stores
and displays the incoming experimental nuclear data, enabling
rapid and efficient transfer and analysis of the recoil proton
data.   Other modifications are mainly associated with
controlling the input (I/P) or output (O/P) statements and
options.

A simplified version of the flow diagram representing the
programme SPEC4 is given in figure A2.1.   The simplification
has been to remove some input (I/P) or output (O/P) options for
clarity.

In SPEC4 the response functions are calculated by the
subroutine SNIDOW, using the Snidow and Warren expressions, 1967,
and then their slopes are modified using the experimental response
correction factors to take account of the extra response
distortion caused by the non-uniform electric-field in the
counter.   The neutron flux above EMAX (the upper energy boundary
of the highest energy group to be analysed) must be obtained from
either theoretical calculations or from a neutron spectrometer
which has a higher energy range.   The contribution of neutrons
above EMAX is calculated by generating the response function due

to a particular energy above EMAX and weighting this with the neutron flux and counter efficiency at that energy.   This is repeated for all other neutron energies above EMAX and their individual contributions are summed.   The resultant contribution is normalised to the recoil ionisation data in the region of EMAX to 1.05 EMAX so that the number of events are equal and then the normalised contribution is subtracted from the recoil ionisation data.

In section 2.1 it was shown that the recoil ionisation spectrum per unit ionisation may be transformed to the recoil proton spectrum per unit energy by

$$M(E) = M(I)/\omega \qquad\qquad (A2.1)$$

where $\omega = dE/dI$, the specific energy per unit of ionisation.

In SPEC4 it was assumed that ω was constant and the energy scale was therefore given by $E = \omega(I+I_o)$ where I_o is the additional A.D.C. backbias caused by the non-zero energy intercept, E_o.

The neutron flux was obtained by back substitution in the following equation given in section 2.1:

$$DM^i = \sum_{j=i}^{i} DN_o^{ij} \, \phi^j \qquad\qquad (A2.2)$$

where M^i are the discrete observations of $M(E)$ and D denotes differentiation with respect to E.   In this, $D\,N_o^{ij}$ is the integral of $d(N_{oj}(E))/dE$ over the energy group $E_{i+1} \leqslant E \leqslant E_i$ and is given by:

$$D\,N_o^{ij} = N_{oj}(E_i) - N_{oj}(E_{i+1}) \qquad\qquad (A2.3)$$

where $N_{oj}(E)$ has been assumed to vary slowly with E and is defined by:

$$N_{oj} = \frac{1}{E_j - E_{j+1}} \int_{E_{j+1}}^{E_j} N_o(E,E^1) \, dE^1 \qquad (A2.4)$$

where $N_o(E,E^1)$ is the recoil proton distribution arising from monoenergetic neutrons of energy E^1.

In SPEC4 the equation (A2.2) is solved by back substitution to give the neutron flux per group starting, first, at the energy group whose upper bound is EMAX and then decreasing in energy group by group. It should be noted that equation (A2.2) is not valid where both the neutron flux, Φ, and the response function shape are rapidly changing functions of energy in the region of EMAX.